

Advances in Civil Engineering

# Artificial Intelligence Applications in Civil Engineering

Lead Guest Editor: Tayfun Dede

Guest Editors: Murat Kankal, Ali R. Vosoughi, Maksym Grzywinski,  
and Moacir Kripka





---

# **Artificial Intelligence Applications in Civil Engineering**

Advances in Civil Engineering

---

## **Artificial Intelligence Applications in Civil Engineering**

Lead Guest Editor: Tayfun Dede

Guest Editors: Murat Kankal, Ali R. Vosoughi,  
Maksym Grzywinski, and Moacir Kripka



---

Copyright © 2019 Hindawi. All rights reserved.

This is a special issue published in “Advances in Civil Engineering.” All articles are open access articles distributed under the Creative Commons Attribution License, which permits unrestricted use, distribution, and reproduction in any medium, provided the original work is properly cited.

## Editorial Board

- Khalid Abdel-Rahman, Germany  
José Aguiar, Portugal  
Reza Akhavian, USA  
Maria Cruz Alonso, Spain  
Serji N. Amirkhanian, USA  
P. Ch. Anastasopoulos, USA  
Venu G. M. Annamdas, Singapore  
Mehrdad Arashpour, Australia  
Pedro Arias-Sánchez, Spain  
Farhad Aslani, Australia  
Daniele Baraldi, Italy  
Emilio Bastidas-Arteaga, France  
Chiara Bedon, Italy  
Rafik Belarbi, France  
Rafael J. Bergillos, Spain  
Giovanni Biondi, Italy  
Hugo C. Biscaia, Portugal  
Giosuè Boscato, Italy  
Melina Bosco, Italy  
Jorge Branco, Portugal  
Emanuele Brunesi, Italy  
Alberto Campisano, Italy  
Francesco Canestrari, Italy  
Paolo Castaldo, Italy  
Giulio Castori, Italy  
Robert Černý, Czech Republic  
Constantin Chalioris, Greece  
Noel Challamel, France  
Daniel W.M. Chan, Hong Kong  
Edwin H W Chan, Hong Kong  
Carlos Chastre, Portugal  
Ghassan Chehab, Lebanon  
Wensu Chen, Australia  
Nicholas Chileshe, Australia  
Heap-Yih (John) Chong, Australia  
Francesco Colangelo, Italy  
Ottavia Corbi, Italy  
Marco Corradi, Italy  
Mario D'Aniello, Italy  
Jorge de Brito, Portugal  
Gianmarco de Felice, Italy  
Stefano de Miranda, Italy  
Tayfun Dede, Turkey  
Angelo Di Egidio, Italy
- Luigi Di Sarno, Italy  
Giulio Dondi, Italy  
Mohamed ElGawady, USA  
Ahmed Elghazouli, UK  
Behzad Esmaeili, USA  
Flora Faleschini, Italy  
Harry Far, Australia  
Antonio Formisano, Italy  
Giovanni Garcea, Italy  
Emilio García-Taengua, UK  
Elhem Ghorbel, France  
Agathoklis Giaralis, UK  
Rodrigo Gonçalves, Portugal  
Arturo Gonzalez, Ireland  
Belén González-Fonteboa, Spain  
Salvatore Grasso, Italy  
Fan Gu, UK  
Kirk Hatfield, USA  
Khandaker Hossain, Canada  
Zahid Hossain, USA  
M. R. Hosseini, Australia  
Bon-Gang Hwang, Singapore  
Dong-Sheng Jeng, Australia  
Jian Ji, China  
Andreas Lampropoulos, UK  
Raffaele Landolfo, Italy  
Eul-Bum Lee, Republic of Korea  
Chun-Qing Li, Australia  
Dongsheng Li, China  
Li Li, Canada  
Xuemei Liu, Australia  
Zaobao Liu, China  
Davide Lo Presti, UK  
Cristiano Loss, Canada  
Sui Pheng Low, Singapore  
Lyan-Ywan Lu, Taiwan  
Eric Lui, USA  
Zhongguo John Ma, USA  
Lorenzo Macorini, UK  
Yann Malecot, France  
John Mander, USA  
Giuseppe Carlo Marano, Italy  
Fabio Mazza, Italy  
Claudio Mazzotti, Italy
- Ahmed Mebarki, France  
Shazim A. Memon, Kazakhstan  
Giovanni Minafò, Italy  
Hossein Moayed, Iran  
Abbas Mohajerani, Australia  
Fabrizio Mollaioli, Italy  
Rosario Montuori, Italy  
Ayman S. Mosallam, USA  
Roberto Nascimbene, Italy  
Luís C. Neves, UK  
Trung Ngo, Australia  
Sanjay Nimbalkar, Australia  
Giuseppe Oliveto, Italy  
Alejandro Orfila, Spain  
Togay Ozbakkaloglu, UK  
Hayri Baytan Ozmen, Turkey  
Alessandro Palmeri, UK  
Fabrizio Paolacci, Italy  
Fulvio Parisi, Italy  
Arnaud Perrot, France  
Christophe Petit, France  
Giuseppe Piccardo, Italy  
Prodromos Psarropoulos, Greece  
Giuseppe Quaranta, Italy  
Carlo Rainieri, Italy  
Damien Rangeard, France  
Dimitris Rizos, USA  
Geoffrey W. Rodgers, New Zealand  
Hugo Rodrigues, Portugal  
Hamid Reza Ronagh, Australia  
Pier Paolo Rossi, Italy  
Lukasz Sadowski, Poland  
Anna Saetta, Italy  
Timo Saksala, Finland  
Evangelos J. Sapountzakis, Greece  
Vasilis Sarhosis, UK  
Halil Sezen, USA  
M. Shahria Alam, Canada  
Faiz U.A. Shaikh, Australia  
Mostafa Sharifzadeh, Australia  
Sanjay Kumar Shukla, Australia  
Amir Si Larbi, France  
Stefano Sorace, Italy  
Flavio Stochino, Italy



---

Claudio Tamagnini, Italy  
Yaya Tan, China  
Patrick W.C. Tang, Australia  
Yinshan Tang, UK  
Huu-Tai Thai, Australia  
Filippo Ubertini, Italy  
Humberto Varum, Portugal  
Castorina S. Vieira, Portugal  
C. Vipulanandan, USA  
Claudia Vitone, Italy  
Hao Wang, USA

Lei Wang, USA  
Linbing Wang, USA  
Wayne Yu Wang, UK  
Roman Wan-Wendner, Austria  
Bo Xia, Australia  
Wei-Chau Xie, Canada  
Michael Yam, Hong Kong  
Libo Yan, Germany  
Jian Yang, China  
Xu Yang, Australia  
Hui Yao, China

Victor Yepes, Spain  
Gürol Yildirim, Turkey  
Qingliang Yu, Netherlands  
Mariano Angelo Zanini, Italy  
Xiong Zhang, USA  
Yuqing Zhang, UK  
Dong Zhao, USA  
Xianbo Zhao, Australia  
Annan Zhou, Australia  
Abdul Aziz bin Abdul Samad, Malaysia

# Contents

## **Artificial Intelligence Applications in Civil Engineering**

Tayfun Dede , Murat Kankal, Ali Reza Vosoughi, Maksym Grzywiński, and Moacir Kripka   
Editorial (3 pages), Article ID 8384523, Volume 2019 (2019)

## **Risk Assessment Method for Cable System Construction of Long-Span Suspension Bridge Based on Cloud Model**

Zhifang Lu , Chaofan Wei, Muyu Liu , and Xiaoguang Deng   
Research Article (9 pages), Article ID 5720637, Volume 2019 (2019)

## **Implementation of Process-Based and Data-Driven Models for Early Prediction of Construction Time**

Silvana Petrusseva , Valentina Zileska-Pancovska, and Diana Car-Pušić   
Research Article (12 pages), Article ID 7405863, Volume 2019 (2019)

## **Application of Artificial Neural Network(s) in Predicting Formwork Labour Productivity**

Sasan Golnaraghi, Zahra Zangenehmadar , Osama Moselhi, and Sabah Alkass  
Research Article (11 pages), Article ID 5972620, Volume 2019 (2019)

## **Optimization of Headways and Departure Times in Urban Bus Networks: A Case Study of Çorlu, Turkey**

Huseyin Ceylan  and Tayfun Ozcan   
Research Article (12 pages), Article ID 7094504, Volume 2018 (2019)

## **Damage Identification by the Data Expansion and Substructuring Methods**

Eun-Taik Lee and Hee-Chang Eun   
Research Article (12 pages), Article ID 1867562, Volume 2018 (2019)

## **Modeling of Energy Efficiency for Residential Buildings Using Artificial Neuronal Networks**

José Antonio Álvarez, Juan Ramón Rabuñal , Dolores García-Vidaurrázaga, Alberto Alvarellos , and Alejandro Pazos  
Research Article (10 pages), Article ID 7612623, Volume 2018 (2019)

## **Predicting Shear Capacity of FRP-Reinforced Concrete Beams without Stirrups by Artificial Neural Networks, Gene Expression Programming, and Regression Analysis**

Ghazi Bahroz Jumaa  and Ali Ramadhan Yousif  
Research Article (16 pages), Article ID 5157824, Volume 2018 (2019)

## **Applicability of Artificial Neural Networks to Predict Mechanical and Permeability Properties of Volcanic Scoria-Based Concrete**

Aref M. al-Swaidani  and Waed T. Khwies  
Research Article (16 pages), Article ID 5207962, Volume 2018 (2019)

## **A Novel Dynamic Multicriteria Decision-Making Approach for Low-Carbon Supplier Selection of Low-Carbon Buildings Based on Interval-Valued Triangular Fuzzy Numbers**

Xia Cao, Zeyu Xing , Yuqi Sun, and Shi Yin   
Research Article (16 pages), Article ID 7456830, Volume 2018 (2019)

**A Computer-Aided Approach to Pozzolanic Concrete Mix Design**

Ching-Yun Kao , Chin-Hung Shen, Jing-Chi Jan, and Shih-Lin Hung 

Research Article (15 pages), Article ID 4398017, Volume 2018 (2019)

**Fast Local Laplacian-Based Steerable and Sobel Filters Integrated with Adaptive Boosting Classification Tree for Automatic Recognition of Asphalt Pavement Cracks**

Nhat-Duc Hoang  and Quoc-Lam Nguyen

Research Article (17 pages), Article ID 5989246, Volume 2018 (2019)

**An Artificial Intelligence Method for Asphalt Pavement Pothole Detection Using Least Squares Support Vector Machine and Neural Network with Steerable Filter-Based Feature Extraction**

Nhat-Duc Hoang 

Research Article (12 pages), Article ID 7419058, Volume 2018 (2019)

## Editorial

# Artificial Intelligence Applications in Civil Engineering

**Tayfun Dede** <sup>1</sup>, **Murat Kankal**,<sup>2</sup> **Ali Reza Vosoughi**,<sup>3</sup> **Maksym Grzywiński**,<sup>4</sup>  
and **Moacir Kripka** <sup>5</sup>

<sup>1</sup>Department of Civil Engineering, Karadeniz Technical University, Trabzon, Turkey

<sup>2</sup>Department of Civil Engineering, Uludağ University, Bursa, Turkey

<sup>3</sup>Department of Civil Engineering, Shiraz University, Shiraz, Iran

<sup>4</sup>Department of Civil Engineering, Czestochowa University of Technology, Czestochowa, Poland

<sup>5</sup>Department of Civil Engineering, Universidade de Passo Fundo, 99001-970 Passo Fundo, RS, Brazil

Correspondence should be addressed to Tayfun Dede; tayfundede@gmail.com

Received 9 April 2019; Accepted 10 April 2019; Published 2 May 2019

Copyright © 2019 Tayfun Dede et al. This is an open access article distributed under the Creative Commons Attribution License, which permits unrestricted use, distribution, and reproduction in any medium, provided the original work is properly cited.

With a great pleasure, we introduce this special edition of the *Journal of Advances in Civil Engineering*, the result of the joint effort of authors, editors, and reviewers.

Artificial intelligence is to develop the machine elements that analyze the human's thinking system and reflect the same to reality. In recent years, artificial intelligence applications have found a wide range of applications in civil engineering and the other engineering branches. The increase in artificial intelligence studies with great acceleration shows that the use of artificial intelligence in engineering branches will increase in the coming years.

The focus of this special issue is on applications of artificial intelligence approaches in civil engineering. Especially hybrid artificial intelligence studies in the fields of structural engineering, construction management, hydrology, hydraulic engineering, geotechnical engineering, environmental engineering, transportation engineering, coastal and ocean engineering, and materials of construction form the basis of this special issue. Besides, review articles including applications of civil engineering using branches of artificial intelligence techniques (ANN, fuzzy system, expert system, and swarm intelligence) is covered by this special issue.

During the call for submissions, more than 40 papers were received, focusing on several aspects related to the application of artificial intelligence in civil engineering. Twelve of these papers were accepted by the referee and the editor. This rigorous revision process can be seen as an indicative of the high quality of the accepted works. The

details about the published papers are given in the sequence.

The first accepted paper prepared by Lu et al. presenting a risk assessment method for cable system construction of suspension bridges was based on the cloud model. The proposed model can combine randomness and fuzziness of risk information effectively. At the end of their study, the authors concluded that the risk assessment method can provide safety assurance and technical support for cable system construction of the long-span suspension bridge.

S. Petrusseva et al. presented a hybrid method for predicting construction time in the early project phase. They used many ANN techniques such as General Regression Neural Network (GRNN), Backpropagation Neural Network (BNN), and Radial Base Function Neural Network (RBFNN). Their study shows that the BNN technique is better than the other techniques when they compared the results obtained. But, their developed model is not suitable for the higher, more intensive risk factors impact during the construction period.

H. Ceylan and T. Ozcan presented a case study on the optimization of headways and departure times in urban bus networks. The authors used the metaheuristic harmony search optimization method to evaluate the user and operator costs. This study gives Pareto solutions in terms of the user and operator benefits. At the end of the study, the authors concluded that total travel time and total service km could be reduced by 4.8% and 9.8%, respectively, compared with the current bus network.

E.-T. Lee and H.-C. Eun investigated damage detection methods using the stress or stiffness variation rate of the truss element before and after the damage. To predict damaged elements depending on complete and incomplete measurement, the authors of this study consider some methods such as the substructuring method, damage detection methods, and static-based and dynamic-based substructuring method. The detailed knowledge about these methods can be found from the paper submitted to this special issue.

G. B. Jumaa and A. R. Yousif proposed three prediction models by using ANN. They are ANN, gene expression programming (GEP), and nonlinear regression analysis (NLR). The authors used a large database including 269 shear test results and the genetic programming to predict the shear capacity of FRP-reinforced concrete beams without stirrups. Their parametric study indicated that the ANN model defines accurately the interaction of all parameters on shear capacity prediction.

C.-Y. Kao et al. develops a two-step computer-aided approach for pozzolanic concrete mix design. The first step is establishing a dataset of pozzolanic concrete mixture proportioning which conforms to American Concrete Institute Code. In the first step, ANNs are employed to establish the prediction models of compressive strength and the slump of the concrete. Sensitivity analysis of the ANN is used to evaluate the effect of inputs on the output of the ANN. The two ANN models are tested using data of experimental specimens made in a laboratory for twelve different mixtures. The second step is classifying the dataset of pozzolanic concrete mixture proportioning. A classification method is utilized to categorize the dataset into 360 classes based on compressive strength, pozzolanic admixture replacement rate, and material cost. Thus, one can easily obtain mix solutions based on these factors. The results show that the proposed computer-aided approach is convenient for pozzolanic concrete mix design and practical for engineering applications.

N.-D. Hoang's research establishes an automatic approach for asphalt pavement pothole detection. Image processing techniques including Gaussian filter (GF), steerable filter (SF), and integral projection (IP) are used synergistically to extract features from pavement digital images. Two levels of GF are utilized as an image denoising technique. SF assisted by GF is used to generate a pothole resilient map. IP analysis based on such map is performed to numerically present the feature of an image with the particular interest in pothole recognition. A simple moving average technique is put forward to reduce the number of the extracted features from 300 to 60. Based on the image features, two artificial intelligence (AI) approaches of ANN and the least squares support vector machine (LS-SVM) have been employed to construct classification models to predict the existence of pothole on the pavement surface. Experimental results with a repeated subsampling procedure with 20 runs confirm that ANN and LS-SVM are capable AI methods for pothole detection. It is because the classification accuracy rates (CARs) of both methods are higher than 85% and the area under the curve (AUC) values surpass 0.9.

Moreover, LS-SVM has been identified as the better approach for the task of pothole detection with a desired accuracy of approximately 89%.

S. Golnaraghi et al. used four different ANN methods: Backpropagation Neural Network (BNN), Radial Basis Network (RBF), Generalized Regression Neural Network (GRNN), and Adaptive Neuro-Fuzzy Inference System (ANFIS) to model labour productivity. Weather (temperature, humidity, wind speed, and precipitation), crew (gang size and labour percentage) and project (work type, floor level, and work method) data were selected as inputs in the models. According to  $R^2$  values, the best result in the models was obtained from BNN with 0.98 for the training set and from RBF with 0.85 for the test set. In the three methods other than RBF, it was determined that temperature was the most important parameter affecting labour productivity. It was determined that the best model BNN obtained as a result of this study can help save time and cost associated with quantifying loss of productivity.

J. A. Alvarez et al. predicted energy performance of a house using ANN models to evaluate building energy efficiency. The dataset obtained from 453 buildings located in the northern area of Spain with a total usable area of 570,438.30 m<sup>2</sup> was used in the models. The data were divided into two: 90% of them were training set, and 10% of them were validation set. Together with this study, it is possible to estimate the energy efficiency of a building in a certain region by using some characteristics belonging to that building with high accuracy without interfering with the building or using any measuring device.

A. M. al-Swaidani and W. T. Khwies applied the ANN and multilinear regression (MLR) models to estimate 2, 7, 28, 90, and 180 days compressive strength, water permeability, and porosity of concretes containing volcanic scoria as cement replacement. Cement content, volcanic scoria content, water content, superplasticizer content, and curing time were used as model inputs. The data used in the ANN models were divided into 70% training, 15% testing, and 15% validation pattern, respectively. Sensitivity analysis showed that all parameters used as an input in this study have significant effects on the properties of concrete containing volcanic scoria as cement replacement. The results showed that ANN models were much more accurate than MLR models and that ANN can be used successfully to predict the investigated concrete properties.

X. Cao et al. developed a new dynamic multicriteria decision-making approach for low-carbon supplier selection in low-carbon building construction projects. This approach includes interval-valued triangular fuzzy numbers intuitionistic fuzzy. According to the demand from the constructors during the considered projects, 5 main criteria and 17 subcriteria were established for the selection of low-carbon suppliers in the construction sector. In conclusion, the authors revealed that the proposed model can be easily extended to analyze other management decision problems as a structural model.

N.-D. Hoang and Q.-L. Nguyen suggest a hybrid model that includes image processing and machine learning approaches for automatic pavement crack recognition. They

used advanced image processing techniques (fast local Laplacian filter, Sobel filter, SF, and IP) to extract digital properties from digital images. They benefited from the adaptive boosting classification tree to perform pavement crack recognition tasks. To generate and validate the performance of the adaptive boosting classification tree, a set of image samples consisting of five classes, crocodile cracks, diagonal cracks, longitudinal cracks, no cracks, and cross cracks, were collected. The results of the study revealed that the crack classification accuracy of the proposed approach was approximately 90%. It is considered that the model can be used in the assessment of the pavement condition of the transportation agencies.

### **Conflicts of Interest**

The guest editors have no conflicts of interest regarding the publication of this special issue.

### **Acknowledgments**

We would like to thank the authors who have submitted manuscripts to this special issue. We would also like to thank the reviewers for their valuable comments about the submitted paper to this special issue. We hope that the accepted papers for this special issue will lead to the future works related to the advances in optimization techniques. The lead guest editor thanks all the editors for their contribution in reviewing and assigning reviews for the submitted manuscripts. At last, the authors would like to express their gratitude to the journal *Advances in Civil Engineering* for the opportunity to contribute to an important field of research.

*Tayfun Dede*  
*Murat Kankal*  
*Ali Reza Vosoughi*  
*Maksym Grzywiński*  
*Moacir Kripka*

## Research Article

# Risk Assessment Method for Cable System Construction of Long-Span Suspension Bridge Based on Cloud Model

Zhifang Lu , Chaofan Wei, Muyu Liu , and Xiaoguang Deng 

Hubei Key Laboratory of Roadway Bridge and Structure Engineering, Wuhan University of Technology, Wuhan 430070, China

Correspondence should be addressed to Xiaoguang Deng; [dengxiaoguang0825@163.com](mailto:dengxiaoguang0825@163.com)

Received 2 August 2018; Revised 17 January 2019; Accepted 30 January 2019; Published 1 April 2019

Guest Editor: Moacir Kripka

Copyright © 2019 Zhifang Lu et al. This is an open access article distributed under the Creative Commons Attribution License, which permits unrestricted use, distribution, and reproduction in any medium, provided the original work is properly cited.

Cable system construction is one of the most risky construction stages of long-span suspension bridges, and a reliable risk assessment is an important means to ensure the construction safety. This study proposes a risk assessment method for cable system construction of suspension bridges based on the cloud model, which can combine randomness and fuzziness of risk information effectively. First, a multilevel evaluation index system is built by disassembling the process of cable system construction. Next, the index weights are calculated by the uncertain analytic hierarchy process (AHP). Then, according to the cloud model, a risk assessment model for cable system construction of the suspension bridge is established by realizing the mutual transformation between qualitative language and quantified data. Finally, an illustrative example concerning the risk of cable system construction of Wuhan Yang-Si-Gang Yangtze River Bridge is provided to demonstrate the feasibility and objectivity of the proposed method.

## 1. Introduction

Long-span suspension bridges are a construction project with large investment, long cycle, and many uncertain factors. The problem of safety accidents during construction is very prominent. Cable system construction is the construction stage with the maximal risk of suspension bridge construction. Once the accidents occur, it will cause huge economic losses, even casualties and bad social impact. Therefore, it is important to propose an objective and effective risk assessment theory of bridge construction and to carry out risk management control on cable system construction.

At present, many scholars have proposed different evaluation methods in the risk assessment field of bridge construction. Nieto-Morote and Ruz-Vila [1] combined fuzzy theory with analytic hierarchy process to evaluate the risk of a bridge during construction period. Based on neural network finite element Monte Carlo simulation, Gong [2] proposed a risk assessment method of long-span cable-stayed bridge construction. Chen et al. [3] built a construction risk assessment system for building bridges from

three aspects of occupational health, safety, and environment (HSE), and the work decomposition structure-risk decomposition structure and the analytic hierarchy process were used to establish and apply to the evaluation model. Ding et al. [4] identified the main risk factors of the bridge construction stage, constructed the evaluation index system, and established the bridge construction risk assessment model based on the Monte Carlo method. Liu et al. [5] studied the construction risk of double-wall steel cofferdam piers and applied fuzzy fault tree theory to propose a fuzzy fault tree-based risk assessment method. To propose the principal component analysis method of bridge open caisson foundation construction risk, Liu et al. [6] studied the construction risk of open caisson foundation by using principal component analysis method. In summary, the current risk assessment methods have been well applied in the field of bridge construction risk assessment, but there are still some shortcomings; for example, the evaluation steps are cumbersome, and the analysis results are much more subjective. How to determine the membership function of a fuzzy concept accurately becomes the key problems in the risk assessment.

The cloud model, which can represent the fuzziness and randomness as well as their relations of uncertain concepts well by giving the random determination of the sample points [7], has been applied in the field of safety evaluation and decision analysis in recent years. Wang et al. [8] applied a synthetical cloud in the effectiveness evaluation method for the shortcomings of the cloud gravity center method and cloud model method and justified the capability through a simple example. The research team of Wang and Liu [9, 10] proposed a decision-making method based on cloud model to solve the multicriteria group decision-making problems and also applied the cloud model into the game problems, online recommendation approach, and sustainable energy crop selection problems [11–13]. The results were observed to demonstrate the cloud model could combine the randomness and fuzziness of an uncertain concept effectively.

In view of the above advantages, in order to provide an objective and effective risk assessment for cable system construction, this paper applies the cloud model into the risk assessment and proposes a new risk assessment method for cable system construction of suspension bridge based on the cloud model.

## 2. The Index System of Cable System Construction

*2.1. Determination of Risk Index of Cable System Construction for Long-Span Suspension Bridge.* According to the principles of scientificity, system, orientation, feasibility, and relative independence between index, the characteristics and actual conditions of cable system construction for large suspension bridges are analyzed, and the risk factors of the suspension bridge in the construction process are identified. The risk sources in the construction of the cable system are identified to determine the construction risk indicators, mainly including the following:

- (1) Saddle installation risk: during the installation process of the saddle, it is prone to hoisting damage, falling from a high altitude, etc. The mounting bracket is an important force structure when the saddle is installed, and its instability is also likely to cause serious safety accidents.
- (2) Traction system installation and catwalks construction risks: during the installation of the traction system and the catwalks construction process, frequent high-altitude operations and water above operations are prone to cause accidents such as machine failure, drowning, and falling from high altitude. Gale weather will also have a great impact on catwalks construction.
- (3) Main cable erection and cable tightening construction risk: one mistake in the erection of the cable can cause safety accidents such as slipping, lifting damage, and improper machine coordination.
- (4) Cable clamp and sling installation risk: there are risks such as sling high-altitude slings, cable clamp deformation, and cable strand extrusion.

*2.2. Construction of Evaluation Index System.* According to the aforesaid established construction risk index, a multi-level suspension bridge cable system construction risk evaluation index system including 20 secondary evaluation indicators such as “saddle installation risk” and 20 three-level evaluation indicators such as “high-altitude falling objects” is established in Figure 1, so the foundation for the construction risk assessment is settled.

*2.3. Cable System Construction Risk Assessment Criteria.* Combined with corresponding engineering data, on-site investigation, expert experience, and standard [14, 15], the risk assessment level standard for the cable system construction of the long-span suspension bridge is established and [7, 8] is used for all index. The evaluation value, from large to small, is a trend in which the risk gradually decreases. Five standard trust clouds are generated by the expert opinion in the interval, corresponding to different risk levels. The risk level of the comment set is {lower risk, low risk, medium risk, high risk, higher risk}, use the golden section method to calculate the cloud model parameters, and set the superentropy  $He$  according to the golden section method [8, 9]. Since the value of the domain is  $\{0, 10\}$ , the value of the superentropy  $He$  of the cloud corresponding to the intermediate value of “medium risk” is 0.05, and the calculation results of the values in the standard cloud model of each risk level are shown in Table 1, and the cloud model is shown in Figure 2.

## 3. Construction Risk Assessment of Suspension Bridge Cable System

In 1995, Li Deyi, an academician of the Chinese Academy of Engineering, proposed the concept and theory of the cloud and unified the randomness, ambiguity, and correlation between these two by giving the random determination of the sample points. Based on this research the cloud model was proposed based on. It has been applied in the field of safety evaluation and decision analysis.

*3.1. Cable System Risk Assessment Cloud Model.* The cloud model theory is to establish the uncertainty conversion model between a qualitative concept and its quantification expressed by natural language values and fully express the ambiguity and randomness of the qualitative concept evaluation information expressed by experts in natural language. It is also a group decision-making individual preference representation method based on natural language evaluation information. The cloud model includes tools such as virtual clouds, forward and reverse cloud generators, and cloud uncertainty prediction. This paper mainly applies forward and reverse cloud generators.

Let  $U$  be a domain expressed by exact numerical values. For any element  $X$  in the domain, there is a stable random number  $Y = U(X)$  as the degree of concept determination of  $X$ , the distribution of  $X$  on the domain is called the cloud model or simplified as cloud, and each  $(X, Y)$  is called a cloud

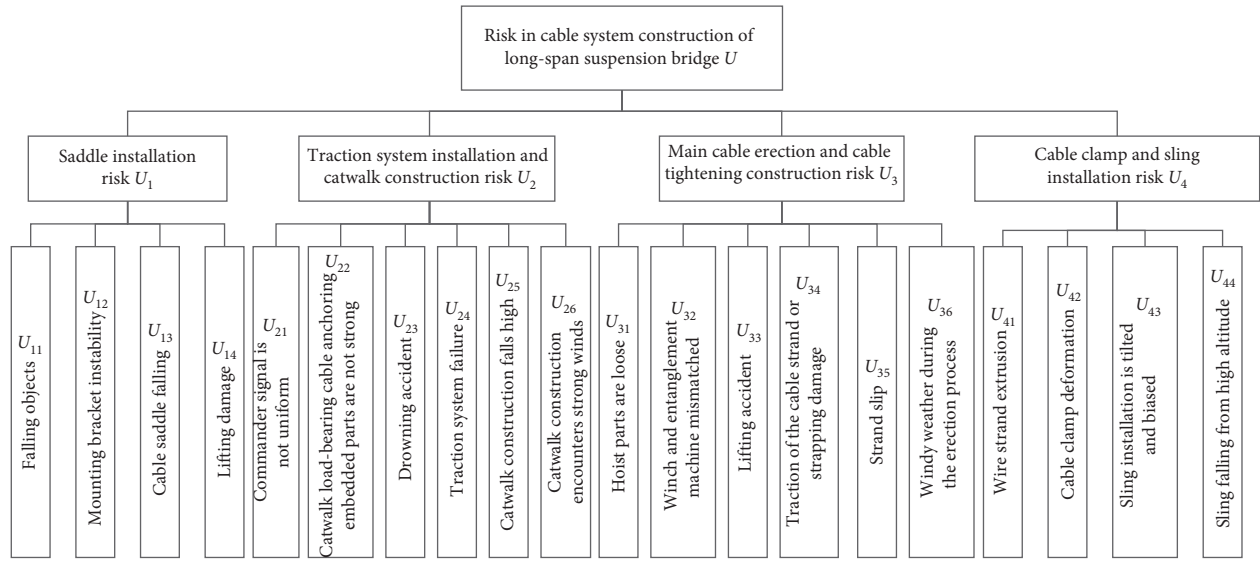


FIGURE 1: Cable system construction risk evaluation index system of the suspension bridge.

TABLE 1: Value form of risk-level reliance cloud.

Risk level	Ex	En	He
Lower risk	0	1.0302	0.1309
Low risk	3.0900	0.6367	0.0809
Medium risk	5.0000	0.3935	0.0500
High risk	6.9100	0.6367	0.0809
Higher risk	10.0000	1.0302	0.1309

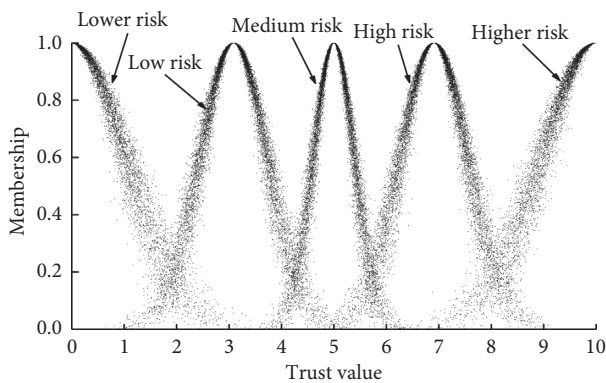


FIGURE 2: Cloud model of each risk level.

drop. If the domain  $U$  is defined as an  $n$ -dimensional space, it can be extended to an  $n$ -dimensional cloud.

The cloud consists of a large number of cloud droplets, each of which represents a specific implementation of this qualitative concept in the number domain space with uncertainty. Separate cloud droplets may not be trivial, but the shape of a large number of cloud droplets can reflect the basic characteristics of the qualitative concept [7].

The digital characteristics of the cloud are mainly represented by Ex (expected value), En (entropy), and He (hyper entropy). A schematic diagram of the one-dimensional cloud model is shown in Figure 3 with  $Ex = 5$ ,  $En = 1$ , and  $He = 0.05$ .

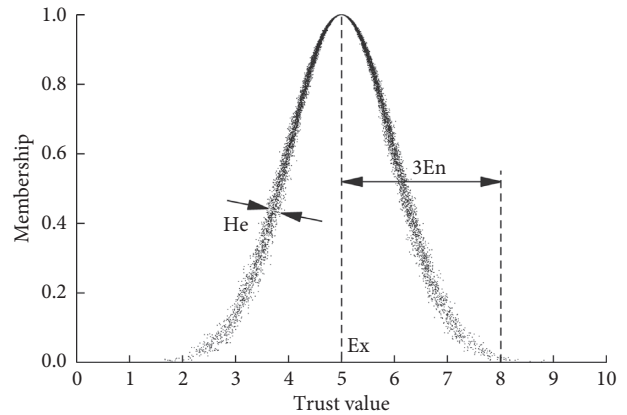


FIGURE 3: Diagram of the cloud model.

Ex: the value that best represents this qualitative concept, usually corresponding to the value of cloud center, reflecting the information center value of the corresponding qualitative concept.

En: the measure of the ambiguity of the qualitative concept. The number of elements that can be accepted of the qualitative concept in the domain is directly affected by the entropy value, which reflects the margin of the qualitative concept.

He: entropy of entropy, reflecting the degree of dispersion of the cloud, that is, the thickness of the cloud. The greater the thickness shows the greater the randomness of the membership.

3.2. Weight Determination of Risk Indicator. By the interval form, the two-two importance comparison of the indicators is given. The interval scale is still the 9 scale of the analytic hierarchy process, as shown in Table 2.

- (1) It is assumed that there are  $n$  evaluation indicators in a subindicator system of the cable construction risk

TABLE 2: Implication of index evaluation scale.

Scale	Implication
1	Indicator $i$ is as important as indicator $j$
3	Indicator $i$ is slightly more important than indicator $j$
5	Indicator $i$ is more important than indicator $j$
7	Indicator $i$ is significantly more important than indicator $j$
9	Indicator $i$ is far more important than indicator $j$
2, 4, 6, 8	The intermediate values of two adjacent judgments mentioned above
Reciprocal	The comparison result between index $i$ and index $j$ is the reciprocal of the comparison between index $j$ and index $i$

assessment system, which constitutes a set  $U = \{U_1, U_2, \dots, U_n\}$ , invites experts whose number is  $q$  to compare the importance of the two pairs of evaluation indicators in the set (according to the scale of 1~9), and gives a specific comparison interval. Then the judgment interval of the expert whose sequence is  $k$  for the indicator  $U_i$  and the indicator  $U_j$  is as follows:

$$A_k = (a_{ij})_{n \times n} = [a_{ij}^l, a_{ij}^u]. \quad (1)$$

- (2) The judgment matrix based on the uncertain AHP method is

$$A = \begin{bmatrix} [1, 1] & [a_{12}^l, a_{12}^u] & \cdots & [a_{1n}^l, a_{1n}^u] \\ \left[\frac{1}{a_{12}^u}, \frac{1}{a_{12}^l}\right] & [1, 1] & \cdots & [a_{2n}^l, a_{2n}^u] \\ \vdots & \vdots & \ddots & \vdots \\ \left[\frac{1}{a_{1n}^u}, \frac{1}{a_{1n}^l}\right] & \left[\frac{1}{a_{2n}^u}, \frac{1}{a_{2n}^l}\right] & \cdots & [1, 1] \end{bmatrix}. \quad (2)$$

The derived vector of the definition matrix is as follows:

$$\text{vec}(A_k) = \left( a_{11}^l, \dots, a_{n1}^l, a_{12}^l, \dots, a_{n2}^l, \dots, a_{1n}^l, \dots, a_{nm}^l, \dots, a_{11}^u, \dots, a_{n1}^u, a_{12}^u, \dots, a_{n2}^u, \dots, a_{1n}^u, \dots, a_{nm}^u \right). \quad (3)$$

Calculate the angle cosine  $V_k$  of the derived vector between matrices, and normalize  $V_k$  to obtain the similarity between the two judgment matrices by defining  $V_k = \sum_{i \neq k, i=1}^q V_{ik}$ :

$$\lambda_k = \frac{V_k}{\sum_{i=1}^q V_i}. \quad (4)$$

- (3) For the calculation of the difference between the judgment matrices, first use  $e_k$  to represent the sum of the absolute values of the elements in the

evaluation matrix of the  $k$ th expert and all the experts and then normalize the  $e_k$  to obtain the  $k$ th expert. The difference between the judgment and other experts' judgment is given as follows:

$$W_k = \frac{e_k}{\sum_{i=1}^q e_i}. \quad (5)$$

The similarity and difference of the judgment matrix are taken as important parameters, and the expert credibility  $r_k$  is calculated:

$$r_k = \begin{cases} \lambda_k, & \sum_{i=1}^q \lambda_i \cdot W_i = 1, \\ \frac{\lambda_k(1-W_k)}{1 - \sum_{i=1}^q \lambda_i \cdot W_i}, & \sum_{i=1}^q \lambda_i \cdot W_i \neq 1, \end{cases} \quad k = 1, 2, \dots, q. \quad (6)$$

- (4) The calculation of weighted sorting interval is an important part of the uncertain AHP method [16]. Firstly, the judgment matrix is uniformly approximated, and the matrix  $M = (m_{ij})_{n \times n}$  is constructed:

$$m_{ij} = \sqrt[2n]{\prod_{k=1}^n \frac{a_{jk}^l a_{jk}^u}{a_{ik}^l a_{ik}^u}}. \quad (7)$$

Weight vector of matrix  $M$  is  $w = (w_1, w_2, \dots, w_n)^T$ :

$$w_j = \frac{1}{\sum_{i=1}^n m_{ij}} = \frac{\left[ \prod_{k=1}^n a_{jk}^l a_{jk}^u \right]^{1/2n}}{\sum_{i=1}^n \left[ \prod_{k=1}^n a_{ik}^l a_{ik}^u \right]^{1/2n}}, \quad j \in N \quad (8)$$

Construct the level difference matrix  $\Delta M_1$  and  $\Delta M_2$  and its matrix weight vector:

$$\begin{aligned} \Delta M_1 &= (m_{ij} - a_{ij}^l)_{n \times n} = \Delta_1 m_{ij}, \\ \Delta M_2 &= (a_{ij}^u - m_{ij})_{n \times n} = \Delta_2 m_{ij}, \end{aligned} \quad (9)$$

$$(\Delta_k w_j)^2 = \frac{\sum_{i=1}^n (\Delta_k m_{ij})^2}{\left[ \sum_{i=1}^n m_{ij} \right]^4}, \quad k = 1, 2.$$

The weighting interval of the judgment matrix is

$$w'_j = (w_j - \Delta_1 w_j, w_j - \Delta_2 w_j) = (u_1, u_2). \quad (10)$$

- (5) The subjective weight  $w_{i1}$  based on the expert credibility risk factor is determined by the expert's judgment matrix. The weighted interval of the determined judgment matrix is processed by the fuzzy set-valued statistical method to obtain the subjective weight of the risk factor:

$$w_{i1} = \frac{1}{2} \cdot \frac{\sum_{k=1}^q r_k \left[ (u_2^k)^2 - (u_1^k)^2 \right]}{\sum_{k=1}^q r_k \left[ (u_2^k) - (u_1^k) \right]}. \quad (11)$$

The objective weight mainly reflects the degree of grasp and objectivity of the expert on the risk factor. The objective weight  $w_{i2}$  is

$$\begin{cases} w_{i2} = \frac{b_{di}}{\sum_{i=1}^n b_{di}}, & i = 1, 2, \dots, n, \\ b_{di} = \frac{1}{1 + g_i}, \\ g_i = \frac{1}{3} \cdot \sum_{k=1}^q r_k \frac{[u_2^k - w_{i1}]^3 - [u_1^k - w_{i1}]^3}{u_2^k - u_1^k}. \end{cases} \quad (12)$$

(6) Finally, the subjective weight  $w_{i1}$  and the objective weight  $w_{i2}$  are combined to obtain the final weight of the risk factor:

$$w_i = \frac{w_{i1} \cdot w_{i2}}{\sum_{i=1}^q w_{i1} \cdot w_{i2}}, \quad i = 1, 2, \dots, n. \quad (13)$$

**3.3. Risk Assessment of Cable System Construction Based on Cloud Model.** According to the evaluation index system, the uncertain analytic hierarchy process- (AHP-) based weighting method is combined with the cloud model to propose a suspension cable system construction risk assessment model. The specific steps are as follows:

- (1) Establish a risk assessment index system for cable systems of long-span suspension bridges
- (2) Identify the review set and generate a corresponding standard cloud model for different levels of reviews
- (3) Calculate the weight  $w_i$  of each indicator by using the weighting method based on the uncertain AHP
- (4) Collect the expert evaluation data, and the trust attribute cloud of the evaluation index is calculated by the undetermined reverse cloud algorithm [17], and the three characteristic values of the risk trust cloud are calculated by the indicator weight:

$$\begin{aligned} Ex &= \sum_{i=1}^n (Ex_i \times w_i), \\ En &= \sqrt{\sum_{i=1}^n (En_i^2 \times w_i)}, \\ He &= \sum_{i=1}^n (He_i \times w_i). \end{aligned} \quad (14)$$

(5) Calculate the similarity between the risk trust cloud and the trust clouds of each level. The specific steps are as follows:

- (1) Enter the risk trust cloud STC1 and standard trust cloud STC.

- (2) Generate a normal random number  $En'_i = \text{NORM}(En_i, He_i^2)$  with  $En_i$  as the expectation and  $He_i^2$  as the variance in the risk trust cloud STC1.
- (3) Generate a normal random number  $x_i = \text{NORM}(Ex_i, En_i'^2)$  with  $Ex_i$  as the expectation and  $En_i'^2$  as the variance in risk trust cloud STC1.
- (4) Substitute the normal random number  $x_i$  into the expected equation of the standard trust cloud STC, and calculate  $\delta'_i = \exp(-(x_i - Ex)^2 / 2(En)^2)$ .
- (5) Repeat steps (1)~(3) until  $\delta'_i$  are generated with number as  $n$ .
- (6) Calculate  $\delta = (1/n) \sum_{i=1}^n \delta'_i$  and  $\delta$  is the similarity sought.
- (7) Determination of the level of risk. The calculated risk trust cloud is sorted with the similarity degree of the standard trust cloud of different risk levels, and the risk level of the evaluation index is obtained.

## 4. Case Analysis of Cable Construction Risk of Suspension Bridge

**4.1. Engineering Background.** Wuhan Yang-Si-Gang Yangtze River Bridge is a double-layer suspension bridge connecting Hanyang and Wuchang. The total length of the bridge is 4134 m, as shown in Figure 4. The length of main span is 1700 m, the side span is 465 m, and the rise-span ratio is 1/9. The design load is 47 tons per meter, the main cable tension is 65,000 tons, and the sling tension is 500 tons, which are the largest in the world. It is necessary to carry out cable system construction risk analysis and propose corresponding risk prevention measures.

**4.2. Cable System Risk Index System of the Suspension Bridge.** Based on the construction risk index of the cable system of the long-span suspension bridge, the risk evaluation index system for the cable system of the Yang-Si-Gang Yangtze River Bridge in Wuhan is constructed, as shown in Figure 1.

**4.3. Determination of Indicator Weight.** Five experts were invited to compare the importance of each level of the indicators, and the interval number was scored to form the judgment matrix of each expert. The calculation was carried out by using Matlab software programming.

Take the “main cable erection and tight cable entanglement construction risk  $U_3$ ” of the criterion layer as an example. The six evaluation indicators are “hoist parts are loose  $U_{31}$ ,” “winch and entanglement machine mismatch  $U_{32}$ ,” “lifting accident  $U_{33}$ ,” “traction of the cable strand or strapping damage  $U_{34}$ ,” “strand slip  $U_{35}$ ,” and “windy weather during the process of erection process  $U_{36}$ ,” and five experts compare their importance and get the judgment matrix as follows:

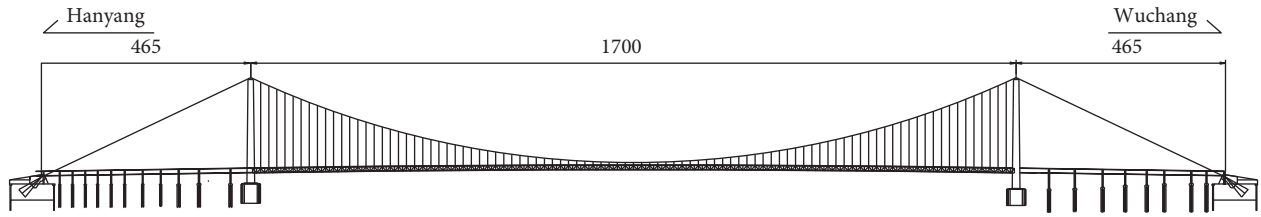


FIGURE 4: General arrangement diagram of main bridge.

$$\begin{aligned}
 A^{(1)} &= \begin{pmatrix} [1, 1] & [1, 2] & [2, 3] & \left[\frac{1}{3}, \frac{1}{2}\right] & \left[\frac{1}{4}, \frac{1}{2}\right] & \left[\frac{1}{4}, \frac{1}{3}\right] \\ \left[\frac{1}{2}, 1\right] & [1, 1] & [1, 2] & \left[\frac{1}{5}, \frac{1}{4}\right] & \left[\frac{1}{6}, \frac{1}{5}\right] & \left[\frac{1}{5}, \frac{1}{3}\right] \\ \left[\frac{1}{3}, \frac{1}{2}\right] & \left[\frac{1}{2}, 1\right] & [1, 1] & \left[\frac{1}{5}, \frac{1}{4}\right] & \left[\frac{1}{7}, \frac{1}{6}\right] & \left[\frac{1}{6}, \frac{1}{5}\right] \\ [2, 3] & [2, 4] & [4, 5] & [1, 1] & \left[\frac{1}{4}, \frac{1}{2}\right] & \left[\frac{1}{3}, 1\right] \\ [2, 4] & [5, 6] & [6, 7] & [2, 4] & [1, 1] & [1, 3] \\ [3, 4] & [3, 5] & [5, 6] & [1, 3] & \left[\frac{1}{3}, 1\right] & [1, 1] \end{pmatrix}, & A^{(4)} &= \begin{pmatrix} [1, 1] & [1, 3] & [2, 4] & \left[\frac{1}{3}, \frac{1}{2}\right] & \left[\frac{1}{4}, \frac{1}{2}\right] & \left[\frac{1}{4}, \frac{1}{2}\right] \\ \left[\frac{1}{3}, 1\right] & [1, 1] & [1, 2] & \left[\frac{1}{4}, \frac{1}{3}\right] & \left[\frac{1}{6}, \frac{1}{5}\right] & \left[\frac{1}{6}, \frac{1}{4}\right] \\ \left[\frac{1}{4}, \frac{1}{2}\right] & \left[\frac{1}{2}, 1\right] & [1, 1] & \left[\frac{1}{5}, \frac{1}{3}\right] & \left[\frac{1}{8}, \frac{1}{6}\right] & \left[\frac{1}{6}, \frac{1}{4}\right] \\ [2, 3] & [3, 4] & [3, 5] & [1, 1] & \left[\frac{1}{3}, \frac{1}{2}\right] & \left[\frac{1}{2}, 1\right] \\ [2, 4] & [5, 6] & [6, 8] & [2, 3] & [1, 1] & [1, 2] \\ [2, 4] & [4, 6] & [4, 6] & [1, 2] & \left[\frac{1}{2}, 1\right] & [1, 1] \end{pmatrix}, \\
 A^{(2)} &= \begin{pmatrix} [1, 1] & [1, 2] & [2, 4] & \left[\frac{1}{3}, \frac{1}{2}\right] & \left[\frac{1}{3}, \frac{1}{2}\right] & \left[\frac{1}{4}, \frac{1}{2}\right] \\ \left[\frac{1}{2}, 1\right] & [1, 1] & [1, 3] & \left[\frac{1}{5}, \frac{1}{3}\right] & \left[\frac{1}{6}, \frac{1}{5}\right] & \left[\frac{1}{5}, \frac{1}{4}\right] \\ \left[\frac{1}{4}, \frac{1}{2}\right] & \left[\frac{1}{3}, 1\right] & [1, 1] & \left[\frac{1}{5}, \frac{1}{4}\right] & \left[\frac{1}{7}, \frac{1}{5}\right] & \left[\frac{1}{6}, \frac{1}{5}\right] \\ [2, 3] & [3, 5] & [4, 5] & [1, 1] & \left[\frac{1}{3}, \frac{1}{2}\right] & \left[\frac{1}{4}, 1\right] \\ [2, 3] & [5, 6] & [5, 7] & [2, 3] & [1, 1] & [1, 2] \\ [2, 4] & [4, 6] & [5, 6] & [1, 4] & \left[\frac{1}{3}, 1\right] & [1, 1] \end{pmatrix}, & A^{(5)} &= \begin{pmatrix} [1, 1] & [1, 2] & [2, 5] & \left[\frac{1}{3}, \frac{1}{2}\right] & \left[\frac{1}{4}, \frac{1}{2}\right] & \left[\frac{1}{5}, \frac{1}{3}\right] \\ \left[\frac{1}{2}, 1\right] & [1, 1] & [1, 4] & \left[\frac{1}{4}, \frac{1}{3}\right] & \left[\frac{1}{8}, \frac{1}{5}\right] & \left[\frac{1}{6}, \frac{1}{4}\right] \\ \left[\frac{1}{5}, \frac{1}{2}\right] & \left[\frac{1}{4}, 1\right] & [1, 1] & \left[\frac{1}{5}, \frac{1}{3}\right] & \left[\frac{1}{7}, \frac{1}{5}\right] & \left[\frac{1}{7}, \frac{1}{3}\right] \\ [2, 3] & [3, 4] & [3, 5] & [1, 1] & \left[\frac{1}{5}, \frac{1}{2}\right] & \left[\frac{1}{3}, 1\right] \\ [2, 4] & [5, 8] & [6, 7] & [2, 5] & [1, 1] & [1, 3] \\ [3, 5] & [4, 6] & [3, 7] & [1, 3] & \left[\frac{1}{3}, 1\right] & [1, 1] \end{pmatrix}. & (15)
 \end{aligned}$$

Calculate the similarity between each expert's judgment matrix according to equations (3) and (4):

$$\lambda_k = \{0.2002, 0.2000, 0.2005, 0.2000, 0.1990\}. \quad (16)$$

The degree of difference between the judgment matrices is

$$W_k = \{0.1889, 0.1956, 0.1719, 0.1973, 0.2463\}. \quad (17)$$

Expert credibility is

$$r_k = \{0.2030, 0.2012, 0.2076, 0.2007, 0.1875\}. \quad (18)$$

Based on the expert credibility, the weights of uncertain AHP are calculated. Firstly, the judgment matrix is uniformly approximated, and the consistency matrix  $M$  is constructed with calculating weight vector (each column corresponds to the weight vector of each expert):

$$w_j = \begin{pmatrix} 0.0929 & 0.1013 & 0.1033 & 0.1023 & 0.0934 \\ 0.0648 & 0.0615 & 0.0612 & 0.0586 & 0.0612 \\ 0.0448 & 0.0431 & 0.0432 & 0.0454 & 0.0420 \\ 0.1745 & 0.1846 & 0.1703 & 0.1876 & 0.1696 \\ 0.3604 & 0.3286 & 0.3402 & 0.3457 & 0.3690 \\ 0.2625 & 0.2809 & 0.2818 & 0.2604 & 0.2649 \end{pmatrix}. \quad (19)$$

$$w'_j = \begin{pmatrix} (0.0764, 0.1072) & (0.0860, 0.1194) & (0.0874, 0.1238) & (0.0864, 0.1234) & (0.0760, 0.1151) \\ (0.0587, 0.0724) & (0.0577, 0.0712) & (0.0570, 0.0665) & (0.0541, 0.0660) & (0.0563, 0.0721) \\ (0.0403, 0.0486) & (0.0374, 0.0478) & (0.0386, 0.0474) & (0.0399, 0.0498) & (0.0341, 0.0496) \\ (0.1573, 0.2490) & (0.1635, 0.2789) & (0.1495, 0.2413) & (0.1709, 0.2338) & (0.1513, 0.2609) \\ (0.3007, 0.4081) & (0.2828, 0.3564) & (0.2922, 0.3709) & (0.3061, 0.3847) & (0.3054, 0.4210) \\ (0.2273, 0.3773) & (0.2448, 0.3528) & (0.2531, 0.3523) & (0.2316, 0.3106) & (0.2280, 0.3811) \end{pmatrix}. \quad (20)$$

The risk factor weights include the subjective weight  $w_{i1}$  and the objective weight  $w_{i2}$  of each element:

$$\begin{aligned} w_{i1} &= (0.1004, 0.0634, 0.0432, 0.2066, 0.3451, 0.2980), \\ w_{i2} &= (0.1668, 0.1668, 0.1668, 0.1666, 0.1665, 0.1663). \end{aligned} \quad (21)$$

Through the coupling of subjective weight and objective weight by using equation (13), the final weights of the six risk factors in the construction risk of main cable erection and tight cable entanglement construction risk are as follows:

$$w_i = (0.0952, 0.0601, 0.0409, 0.1956, 0.3266, 0.2817). \quad (22)$$

Due to the limited space, the weight calculation methods of the other indicator layers and the criterion layer are the same as above, and the calculation results are shown in Table 3.

**4.4. Comprehensive Synthesis of Risk Trust Clouds.** Based on the actual situation of the Yang-Si-Gang Yangtze River Bridge, and considering the risk occurrence probability and the degree of risk impact comprehensively, the five experts give a score to the indicators at the index level. According to these scores, the reversed cloud calculation is carried out, and the index layer attributes are synthesized based on formula (14). Then, the characteristic value of the criterion layer cloud model can be obtained, as shown as Table 4.

The criterion layer is synthesized again to obtain the characteristic value of the risk trust cloud of the target layer:

$$\begin{aligned} Ex &= 4.8514, \\ En &= 0.7258, \\ He &= 0.3083. \end{aligned} \quad (23)$$

**4.5. Comprehensive Evaluation of Cable System Construction Risk.** According to the similarity calculation method between the cloud models in Section 2.3, the similarity between

After constructing the level difference matrixes  $\Delta M_1$  and  $\Delta M_2$ , calculate the weight vectors  $\Delta_1 w$  and  $\Delta_2 w$  and determine the weight interval of the judgment matrix as

the risk trust cloud and each standard trust clouds of every level is calculated and sorted. The cloud model is shown in Figure 5, and the calculation results are shown in Table 5.

Table 5 shows that the risk trust cloud has the greatest similarity with the medium-risk standard trust cloud. Therefore, the comprehensive judgment result of the cable system construction risk of the Yang-Si-Gang Yangtze River Bridge is “medium risk”. According to the construction risk decision criteria, the risk level is subject to conditional acceptance, but further risk management measures are needed to improve project safety.

**4.6. Construction Risk Prevention Measures.** According to the calculation results of the characteristic values of each attribute cloud in the criterion layer in Table 5, the corresponding risk prevention measures are proposed for the cable saddle construction, the traction system and catwalk construction, the main cable erection and the cable tightening construction. The risk of cable clamp and sling installation construction is low and no need to take precautions.

**4.6.1. Saddle Construction Safety Measures.** The tower top construction platform shall be provided with protective railings and safety nets, and operators shall strictly wear safe labor insurance products. Before the sling is lifted, a special project should be formulated for demonstration.

**4.6.2. Risk Prevention Measures for Catwalk Construction and Traction System.** Before construction, the quality of the cable should be strictly checked. Wire breaking and rust is strictly forbidden. The impact of bad weather should be regarded. It is strictly forbidden to carry out the construction of the catwalk and the main cable under high wind conditions.

TABLE 3: Index weight of the cable system construction risk evaluation system.

Criteria layer	Weights	Indicator layer	Weights	Comprehensive weight
Saddle installation risk $U_1$	0.2734	Falling objects $U_{11}$	0.0801	0.0219
		Mounting bracket instability $U_{12}$	0.2696	0.0737
		Cable saddle falling $U_{13}$	0.5004	0.1368
		Lifting damage $U_{14}$	0.1499	0.0410
Traction system installation and catwalk construction risk $U_2$	0.3678	Commander signal is not uniform $U_{21}$	0.0413	0.0152
		Catwalk load-bearing cable anchoring embedded parts are not strong $U_{22}$	0.0594	0.0218
		Drowning accident $U_{23}$	0.0967	0.0356
		Traction system failure $U_{24}$	0.2081	0.0765
		Catwalk construction falls high $U_{25}$	0.2660	0.0978
		Catwalk construction encounters strong winds $U_{26}$	0.3285	0.1208
Main cable erection and cable tightening construction risk $U_3$	0.2980	Hoist parts are loose $U_{31}$	0.0952	0.0284
		Winch and entanglement machine mismatched $U_{32}$	0.0601	0.0179
		Lifting accident $U_{33}$	0.0409	0.0122
		Traction of the cable strand or strapping damage $U_{34}$	0.1956	0.0583
		Strand slip $U_{35}$	0.3266	0.0973
		Windy weather during the erection process $U_{36}$	0.2817	0.0839
Cable clamp and sling installation risk $U_4$	0.0608	Wire strand extrusion $U_{41}$	0.0660	0.0040
		Cable clamp deformation $U_{42}$	0.1277	0.0078
		Sling installation is tilted and biased $U_{43}$	0.3423	0.0208
		Sling falling from high altitude $U_{44}$	0.4640	0.0282

TABLE 4: Calculation results of the criterion layer attribute cloud characteristic value.

Criterion layer	Ex	En	He
Saddle installation risk $U_1$	5.0600	0.5738	0.2977
Traction system installation and catwalk construction risk $U_2$	4.9907	0.7981	0.3483
Main cable erection and cable tightening construction risk $U_3$	4.6661	0.7564	0.2771
Cable clamp and sling installation risk $U_4$	3.9789	0.7252	0.2666

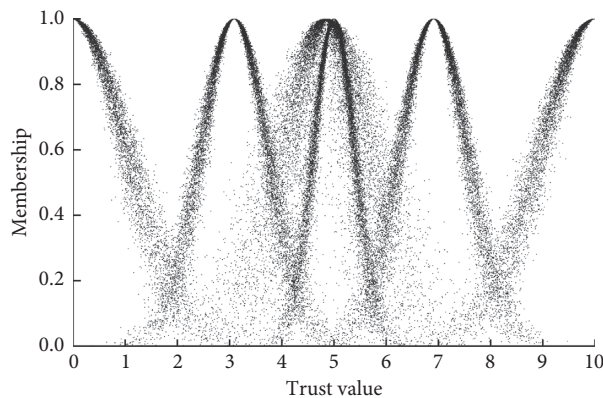


FIGURE 5: Diagram of the risk reliance cloud and criterion reliance cloud of each risk level.

TABLE 5: Similarity between criterion reliance cloud of each risk level and risk reliance cloud.

Risk level	Lower risk	Low risk	Medium risk	High risk	Higher risk
Connection number	$2.3417 \times 10^{-4}$	0.0841	0.5869	0.0389	$8.5316 \times 10^{-4}$

4.6.3. Risk Prevention Measures of Main Cable Erection and Cable Tightening Construction. Pay attention to monitoring the displacement of the main tower during construction. The

displacement should be adjusted in time and always within the allowable range. The wire bundle should be tracked and inspected during the traction process to prevent the wire

bundle from twisting, wearing, bulging, or breaking the bandage.

## 5. Conclusion

To solve the problems that the common risk assessment methods have their limitations with complicated operation and insufficient objectivity at present, this paper proposes a risk assessment method for cable system construction of suspension bridge based on the cloud model, and the research results are as follows. First, through the decomposition of the cable system construction and the identity of risk sources, a multilevel evaluation index systems including 4 secondary evaluation indicators and 20 three-level evaluation indicators is established. Second, according to the index weights determined by the uncertain AHP weighting method, as well as the expert evaluation data, the three characteristic values of risk trust cloud are calculated by using the undetermined reverse cloud algorithm, consequently the risk evaluation model based on cloud model is obtained. Finally, an illustrative example concerning the risk of cable system construction of Wuhan Yang-Si-Gang Yangtze River Bridge is provided, and the results show that the risk grade of the cable system is “medium risk”; simultaneously, the preventive measures for each construction risk are proposed accordingly. In conclusion, the risk assessment method proposed in this study can provide safety assurance and technical support for cable system construction of long-span suspension bridge feasibly and objectively.

## Data Availability

The data used to support the findings of this study are available from the corresponding author upon request.

## Conflicts of Interest

The authors declare that there are no conflicts of interests regarding the publication of the paper.

## Acknowledgments

This paper was financially supported by the Natural Science Fund of Hubei Province (no. 2016CFA074) and The Technological Innovation Project of Hubei Province (no. 2018AAA001-04). These supports are gratefully acknowledged.

## Supplementary Materials

The construction of Wuhan YangSiGang Yangtze River Bridge. (*Supplementary Materials*)

## References

- [1] A. Nieto-Morote and F. Ruz-Vila, “A fuzzy approach to construction project risk assessment,” *International Journal of Project Management*, vol. 29, no. 4, pp. 220–231, 1999.
- [2] C. Gong, *Construction Risk Analysis and Counter Measures Research of Long-Span Cable-Stayed Bridges*, Tongji University, Shanghai, China, 2006.
- [3] G. Chen, W. Wu, S. Xu et al., “Assessment HSE risk of during sea-crossing bridges project construction based on WBS-RBS and AHP,” *China Safety Science Journal*, vol. 23, no. 9, pp. 51–57, 2013.
- [4] S. Ding, X. Liu, Y. Wang et al., “Risk assessment of bridge construction stage based on monte carlo method,” *Safety and Environmental Engineering*, vol. 20, no. 6, pp. 121–125, 2013.
- [5] M. Liu, J. Wu, and R. Zhang, “Analysis of construction risk for water piers and foundations with double-wall steel cofferdam based on the fuzzy fault tree theory,” *Journal of Civil, Architectural & Environmental Engineering*, vol. 36, no. 6, pp. 34–40, 2014.
- [6] M. Liu, K. Chen, and J. Wu, “Principal component analysis method of construction risk of open caisson foundation in a bridge,” *Journal of Wuhan University of Technology (Transportation Science & Engineering)*, vol. 39, no. 1, pp. 1–4, 2015.
- [7] D. Li and C. Liu, “Study on the universality of the normal cloud model,” *Engineering Science*, vol. 6, no. 8, pp. 28–34, 2004.
- [8] J. Wang, W. Xiao, S. Wang et al., “An improved effectiveness evaluation method based on cloud model,” *Fire Control & Command Control*, vol. 35, no. 7, pp. 139–142, 2010.
- [9] J. Wang and T. Liu, “Uncertain linguistic multi-criteria group decision-making approach based on integrated cloud,” *Control and Decision*, vol. 27, no. 8, pp. 1185–1190, 2012.
- [10] H.-G. Peng and J.-Q. Wang, “A multicriteria group decision-making method based on the normal cloud model with zadeh’s,” *IEEE Transactions on Fuzzy Systems*, vol. 26, no. 6, pp. 3246–3260, 2018.
- [11] H. G. Peng, X. K. Wang, T. L. Wang et al., “Multi-criteria game model based on the pairwise comparisons of strategies with Z-numbers,” *Applied Soft Computing*, vol. 74, pp. 451–465, 2018.
- [12] M. X. Wang and J. Q. Wang, “New online recommendation approach based on unbalanced linguistic label with integrated cloud,” *Kybernetes*, vol. 47, no. 7, pp. 1325–1347, 2018.
- [13] H. G. Peng and J. Q. Wang, “Cloud decision model for selecting sustainable energy crop based on linguistic intuitionistic information,” *International Journal of Systems Science*, vol. 48, no. 15, pp. 3316–3333, 2017.
- [14] Ministry of Transport of the People’s Republic of China, *Guide for Safety Risk Assessment of Highway Bridges and Tunnels*, Ministry of Transport of the People’s Republic of China, Beijing, China, 2011.
- [15] C. Xiao, L. Jia, and R. Xiao, “Risk assessment of long-span suspension bridge during construction period,” *Journal of Shandong Jiaotong University*, vol. 24, no. 1, pp. 47–52, 2016.
- [16] Z. Fan and D. Pan, “How to establish the database and the mathematical model of materials’ compositions and their functions,” *System Engineering*, vol. 14, no. 2, pp. 56–60, 1996.
- [17] H. Chen, B. Li, and C. Liu, “An algorithm of backward cloud without certainty degree,” *Journal of Chinese Computer Systems*, vol. 36, no. 3, pp. 544–549, 2015.

## Research Article

# Implementation of Process-Based and Data-Driven Models for Early Prediction of Construction Time

Silvana Petrusева <sup>1</sup>, Valentina Zileska-Pancovska,<sup>1</sup> and Diana Car-Pušić <sup>2</sup>

<sup>1</sup>“Ss Cyril and Methodius” University, Faculty of Civil Engineering, Partizanski Odredi 24, 1000 Skopje, Macedonia

<sup>2</sup>University of Rijeka, Faculty of Civil Engineering, Radmile Matejčić 3, Rijeka 51 000, Croatia

Correspondence should be addressed to Silvana Petrusева; [silvana@gf.ukim.edu.mk](mailto:silvana@gf.ukim.edu.mk)

Received 5 October 2018; Accepted 23 December 2018; Published 23 January 2019

Guest Editor: Moacir Kripka

Copyright © 2019 Silvana Petrusева et al. This is an open access article distributed under the Creative Commons Attribution License, which permits unrestricted use, distribution, and reproduction in any medium, provided the original work is properly cited.

The need of respecting the construction time as one of the construction contract elements points out that early prediction of construction time is of crucial importance for the construction project participants' business. Thus, having a model for early prediction of construction time is useful not only for the participants involved in the construction contracting process, but also for other participants in the construction project realization. Regarding that, this paper aims to present a hybrid method for predicting construction time in the early project phase, which is a combination of process-based and data-driven models. Five hybrid models have been developed, and the most accurate one was the BTC-GRNN model, which uses Bromilow's time-cost (BTC) model as a process-based model and the general regression neural network (GRNN) as a data-driven model. For evaluating the quality of the models, the 10-fold cross-validation method has been used. The mean absolute percentage error (MAPE) of the BTC-GRNN is 3.34% and the coefficient of determination  $R^2$ , which reflects the global fit of the model, is 93.17%. These results show a drastic improvement of the accuracy in comparison to the model when only data-driven model (GRNN) has been used, where MAPE was 31.8% and  $R^2$  was 75.64%. This model can be useful to the investors, the contractors, the project managers, and other project participants for construction time prediction in the early project phases, especially in the phases of bidding and contracting, when many factors, that can determine the construction project realization, are unknown.

## 1. Introduction

Construction time is one of the key elements at the early phases of the construction project, particularly in bidding and contracting processes [1]. The problem arises precisely from the need to make a more accurate estimation of building time in those early phases of the project. There is, then, a high degree of uncertainty and often a lack of information required for a satisfactory accurate time assessment. Two elements are important for solving problems, collecting and systematically storing information, and developing new and improving existing models of time estimates, which will use such information. The accumulated legacy information in the information systems could improve decision-making [2]. Business decisions regarding the duration of construction projects can be considered among the most important because of the potential impact

on the final business results of the investor and the contractor.

While the problem of systematic storage and use of information can be solved by an appropriate information system [2], the development and improvement of appropriate assessment models are the result of scientific research. Moreover, addressing modern challenges and developmental trends in civil engineering [3–5], the information system should also include prediction time models that would use data system resources and supply it with new data. The next step further is that this information system time frame should be a segment of the unique construction information management system. Watson [5] classifies the “fragmented structure” into one of the “underlying, inherent construction industry problems.” Solutions that bring integrated management information systems have a synergistic potential with the ability to

enhance significantly the operational, functional, economic, management, and quality dimensions of the construction.

Problem of construction time prediction is a very complex and demanding task because the construction time is influenced by numerous factors such as project sector, building type, procurement route, construction materials, machines, and equipment; resources that will be used; methods used for work performance; project complexity and cost; site conditions; and many other factors [1, 6]. As a result, construction time prediction is a serious, difficult, and complex process [7].

During the construction period, the construction time is influenced by changes of its determining factors. Thus, many construction projects have not met the contracted time and have been finished with significant construction time overrun [6, 8–17]. Consequently, reaching the contracted construction time is an important problem worldwide. Project closure in the contracted time has become a project participant's challenge and an important factor that should be considered in each construction project [8, 9, 18].

Regarding the above-mentioned, construction time prediction is among the issues that are highly pronounced in the construction practice [19, 20]. As stated by Kenley [21], there are investigations focusing on predicting construction duration and cost, mostly due to cash flow modelling. However, there are also limited investigations that cover all aspects of their relation. Thus, Kenley [21] stated that the focus of researcher investigations are relations between project time and value in order to develop models for a rapid prediction of project time (using budgeted cost and current indices of cost as inputs). Additional investigations are related to exploiting and modelling time-cost relationship and its impact on important industry issues such as productivity improvement and industry efficiency.

As stated in [13], Bromilow, from Australia, was the first who investigated time and financial execution for buildings constructed in Australia between 1963 and 1967. Using simple linear regression analysis as the mathematical method, the research resulted in establishing the so-called "time-cost" model or BTC model:  $Y = aX^b$ , where  $Y$  is the construction time,  $X$  is the construction price, and  $a$  and  $b$  are constants.  $a$  is the coefficient that expresses the average time needed for construction of a monetary value, and  $b$  is the coefficient that indicates the sensitivity of the project duration regarding its value. BTC model has been tested and proven in additional investigations [17, 22].

The study [22] tested the plausibility of BTC model on construction projects realized in Australia in the period from 1991 to 1998. The suitability of BTC model was tested and proven with its implementation on different types of structures. It was proven that different types of projects need the explicit estimation of parameters. The investigation has also shown that the construction time for small industrial structures is shorter than the construction time for small educational and residential buildings. Two models were developed: the first for industrial and the second for non-industrial projects. It was concluded that different client sectors, contractor selection methods, and contractual

arrangements did not have influence on parameter change. At the same time, constants  $a$  and  $b$  were influenced by the characteristics of the region, economic characteristics, structure type, etc. Hence, the construction time prediction is more accurate if the model is developed for structures with similar characteristics, for a particular country or even a region.

Regarding the above-mentioned, researchers worldwide have developed regression models for different types of structures for different countries and even regions [17, 23–30]. For Malaysia, Chan [23] developed a "time-cost" model for building projects and proved its plausibility. Kaka and Price [12] developed such models for buildings and road construction in the UK, and the "time-cost" relation was confirmed once again.

Kumaraswamy and Chan [31] proved that the model can be applied in Hong Kong for buildings and construction structures. Similarly, Car-Pušić and Radujković [14] proved that the "time-cost" function can be used also in Croatia and consequently developed respective models for buildings, roads, and road structures.

The relationship between the initial estimated and the final achieved construction time was investigated by Ayodeji et al. [32]. The authors used linear regression analysis to investigate the relationship between the initial and actual construction time for public and private building projects in South Africa. It was determined that approximately 35% additional time needs to be added to the amount of the initial contract time in order to estimate the final, real contract time.

The next stage of research was to develop models based on the BTC, but with different predictors, as well as with two predictors. The main motivational factor was to obtain a more accurate time prediction because the time is influenced by numerous factors and not only by the project cost. Regarding this, Chan and Kumaraswamy [15] analyzed the government and private buildings construction duration in Hong Kong. Using BTC model as an initial model, they developed and tested new construction time prediction models as a function of one different independent variable, i.e., the total gross floor area in  $m^2$  as well as the number of floors. Additionally, they developed and tested a model with two independent variables: the cost and the total gross floor area.

Following further model development, an increase in predictor numbers can be noticed. As stated by Car-Pušić [17], one of the starting problems for developing more variable models was the appropriate method selection. Numerous studies have proven the suitability of multilinear regression analysis. [12, 20, 29, 33, 34].

The models described above can be grouped into two main groups. The first group consists of models oriented to groups of activities, whereas the second group consists of models oriented to project characteristics [17]. Thus, in [10], the developed regression model for time prediction is oriented on groups of activities and their sequential start-start lag times. In the model, 12 independent variables (i.e., gross floor area, area of ground floor, approximate excavated volume, building height, etc.) have been used. A similar

model was developed by Chan and Kumaraswamy [15, 33] for public housing projects in Hong Kong by modelling work packages and their respective sequential start-start lag times. Chan APC and Chan DWM [29] developed similar benchmark time prognostic model for public housing projects in Hong Kong. What is interesting to point out is that the model was developed in order to formulate “benchmark measures of industry norms for construction period of public housing projects” in Hong Kong.

Regarding models oriented to project characteristics, there are numerous useful studies worth attention. Khosrowshahi and Kaka [34] stated that the project time and cost were influenced by different variables, separate or in combination. Their research was oriented on housing projects in the UK. The most influential variables were determined. The relationship between these variables and project duration, as well as the total cost, was defined, and finally, prognostic models developed.

Dissanayaka and Kumaraswamy [11] developed a time index regression model for building projects in Hong Kong considering a set of procurement and nonprocurement variables. They concluded that the project complexity representative value, programme duration, and client type, i.e., nonprocurement variables, are more significant than the procurement ones.

Žujo and Car-Pušić [35] developed regression models for construction time overrun. The construction time of building projects was considered as the function of risk factors based on the data for the buildings constructed in Federation BiH. Models for two groups of buildings, new construction and reconstruction, were established. It has been concluded that for new buildings, the most significant risk factors are weather conditions, technical documentation disadvantages, and law aspects, which means local regulations. Regarding reconstructions, the most significant risk factors are contractual and also technical documentation disadvantages. These models are applicable when an increased influence of risk factors is expected.

Similarly, Abu Hammad et al. [36] developed prediction models for construction duration for private and governmental projects in Jordan, classified according to the type of object. With 95% of probability, the proposed models predict the project duration with a precision of  $\pm 0.35\%$  of the mean time.

Skitmore and Ng [27] developed several prediction models for the actual construction time based on the data of Australian construction projects. The cross-validation regression analysis was used to develop models when client sector, contractor selection method, contractual arrangement, project type, contract period, and contract sum are known. They also investigated models with the estimated contract period and contract cost.

Artificial neural networks (ANNs) are also used for time prediction modelling. In fact, ANNs have the prediction ability to solve numerous problems that appear in the construction industry [37].

Vahdani et al. [38] developed ANNs prediction model for construction project time prediction. The model is based on a new neuro-fuzzy algorithm. Furthermore, Petrusseva

et al. [39] developed a multilayer perceptron (MLP) neural network model for construction time prediction. The model is based on real data. Bromilow’s “time-cost” model was implemented in two predictive models: linear regression (LR) and MLP. The results showed that using MLP significantly improves the accuracy of MLP model compared with the LR model.

Naik and Radhika [37] developed ANNs models for predicting the construction time duration for highway road construction using two completed projects. They obtained excellent results using the neural network fitting tool (Nftool) and neural network data manager (Nntool) approaches with the software MATLAB R2013a. In addition, they propose this approach to contractors for making much easier decisions.

Attarzadeh and Ow [40] propose the ANN model that improves the prediction accuracy of time by applying novel soft computing model. The model is characterized by good generalization and adaptation capability. It was shown that applying the good features of ANNs on algorithmic estimation model results in improvement of time prediction accuracy.

A model for construction time prediction using general regression neural network is presented by Petrusseva et al. [41]. The coefficient of correlation between the predicted and the actual time values is around 0.999, and the error of the model is about 2.19%.

Neural networks have been used by Mensah et al. [42] to develop a hybrid model for predicting the duration of bridge construction projects in Ghana, using artificial neural network (ANN) and multilayer perceptron (MLP). Data were collected from the department of feeder roads for 18 completed bridge construction projects and included the number of lanes of the bridge components, their weights, and bridge span (20 to 54 m). The authors have shown that bridge project duration strongly depends on the bridge span and formwork used for reinforced in situ concrete. They have obtained good accuracy of the model with MAPE 4.05% and coefficient of determination  $R^2 = 0.998$ , making it suitable for predicting the duration of bridge construction projects.

Yousefi et al. [43] proposed a neural network model to predict time and cost claims in construction projects. By using the proposed model, the rate of possible claims in a particular construction project can be obtained.

Gab Allah et al. [44] developed the ANN time predictive model for building projects using MATLAB program as a model development environment. They used data for 130 building projects constructed in Egypt. Obtained accuracy of the model was with a maximum error of 14%.

Related to computing in civil and building engineering, many authors [3–5] point out the importance of digital information modelling as one of the guidelines and challenges for further research and development.

A relatively new predictive modelling research area is hybrid modelling, which combines two or more techniques, resulting in improvement in strength and performances of the model. The point is in using the good characteristics of each technique involved.

Regarding the above-mentioned, Roberts et al. [45] compared predictions of a process-based crop model, a data-driven model, and a hybrid model, i.e., a combination of both models, and found that the hybrid model performs much better than the other two models.

The authors in [46] proposed a hybrid model combining process-based and data-driven models in order to predict system remaining useful life applied on lithium ion battery. Drastically better accuracy was obtained when compared with the classical particle filter method. The conclusion was that by using the strengths of the data-driven and process-based methods together, the proposed hybrid prognostic framework bridges the gap between data-driven and process-based prognostics when abundant historical data and knowledge about the physical degradation process are available.

In this paper, a hybrid model, which includes process-based and data-driven models, is presented. As the result, a drastic improvement of the accuracy of the time prediction is obtained.

Issues discussed above lead to the conclusion that fast prediction of construction time, particularly at the early project phase when accurate and adequate information is limited, is not only difficult but also an important and necessary process.

Considering the fact that the construction time is influenced by a range of parameters that could not be accurately predicted, it is impossible to acknowledge all of them during the time prediction in early project phase [41]. This results in little accuracy of construction time [40] and points out the need and significance of future research in early construction time prediction. For this reason, the research has been carried out and its results are presented in this paper. The development of a more reliable model for early and fast construction time prediction, which would be used as a decision support tool at an early phase of the project, was the focus of this research.

Regarding that, data about construction duration from previous projects have been collected. Two methods, a process-based model and a data-driven model, have been used for predicting the construction duration. It should be highlighted that this is a relatively new research approach, demonstrating better results than using only one of these methods. Bromilow's time-cost model is used as a process-based model because of its simplicity and worldwide usage for time prediction. As the data-driven model, GRNN (general regression neural network) is used. Hybrid models usually combine the best characteristics of different tools in order to improve the performance of the hybrid model.

## 2. Materials and Methods

**2.1. Data Collection.** A questionnaire was developed by the authors of the paper to provide historical data relevant for the purpose of the research. The questionnaire was distributed in construction companies through personal visits of authors, meetings with company representatives, and construction site visits. Historical data, relevant for construction time prediction, were collected for a total of 116

different types of structures built since 2000. Database consists of road sections (27), petrol stations (4), bridges (7), education facilities (5), business buildings (28), residential-business buildings (10), sport halls (5), water tanks (4), residential buildings (4), water supply system sections (7), bridges (7), an overpass (1), a tunnel (1), traffic arteries (5), and other (8). The collected data refer to the structure type—purpose, year of construction, region of its location, contracted construction time and cost, and realized construction time and cost.

**2.2. Process-Based and Data-Driven Models.** *Process-based models* describe the process by examining two basic phases: *mathematical modelling* (mathematical equations) and *numerical solution*. In the mathematical modelling phase, the process is described by mathematical equations. After that, an accurate and efficient *numerical solution* of these equations follows. Process-based models have a wide range of applications because they are based on the theoretical understanding of relevant process and offer explicitly stated assumptions about the functioning of the process; therefore, they are used to guide the management decision under conditions of rapid global changes [47].

In order to develop process-based models, a very good understanding of the process is needed, together with accurate data that describe the process. In situations when process-based models cannot be built due to the lack of knowledge about the process which should be modelled, then *data-driven* models can be built. In such cases, some of the variables, which characterize the process are measured, and the data representing the input-output relationship describing the process should be available. Data-driven models (DDMs) can make it possible to predict some output variables. DDMs do not require a priori knowledge about the process and the laws under which the variables included in the process are connected. The only required knowledge is the factors that influence the process in order to identify which variables are relevant for the analysis. DDMs can supply important information extracted from the available data about the relationship of the variables in the process.

Recent developments in artificial intelligence, particularly computation intelligence and machine learning, have widened the capabilities of data-driven (empirical) modelling. Other research fields, which have contributed very much to improving conventional empirical (data-driven) modelling, are soft computing, data mining, and intelligent data analysis.

When process-based models are not adequate to model a particular situation or when the estimation of the parameters in the process-based models is difficult to obtain or is not precise enough, and when there are not enough data to train data-driven models, then a combination of models of different types can be an efficient solution. The research of hybrid modelling is trying to develop algorithms to obtain an efficient combination of data-driven and process-based models. This is a relatively new area of research, which has been examined in the last several years, giving important results.

Corzo et al. [48] have used a combination of process-based and data-driven models. They have obtained model performance improvement by reducing the error and increasing the model efficiency in hydrology at river flow simulation.

The authors Zhou et al. [49] have made a comparison of data-driven and process-based models for simulating HVAC (heating, ventilation, and air-conditioning) systems, analyzing their differences, and showing that the both models perform almost equally well for energy efficient control.

Computational intelligence and machine learning methods have developed the data-driven models, making them suitable for complementing or replacing the process-based models. The authors in [50] have shown that the data-driven method can sometimes outperform the process-based method because of the fact that in reality each process-based model is an approximation of the reality. The authors Rajabi et al. [51] have also shown in their research that the data-driven model RBFLN (based on RBFNN) has demonstrated best predictive accuracy in comparison with two knowledge-driven methods: Fuzzy AHP\_OWA and Fuzzy GIS-based method.

Machine learning algorithms are used to determine the relationship between input and output of the system (predictors and target variable) using data set for training, which should be most representative for the behavior of the system. After training the model, it is tested on independent data set for validating how well it will generalize to new unknown data. The most important way for providing generalization to unknown data is choosing the most representative sample from the data set, which will present the whole behavior of the process [52]. In the last several years, the methods of artificial intelligence modelling have been used for improving and generating new and better process-based models from empirical data [53]. The combination of process-based and data-driven models, used in this paper for predicting construction time, is presented below.

**2.2.1. Process-Based Model.** Bromilow's "time-cost" model is used as a process-based model, giving the relation between the construction price and construction time (Eq. (1)) [54].

$$Y = a \cdot X^b, \quad (1)$$

$Y$  is a construction time,  $X$  is a construction price,  $a$  is a parameter that expresses the average time needed for construction of a monetary value, and  $b$  is a model parameter that expresses the dependence of the time on the cost change [54].

This model has been tested, verified, and confirmed by many authors from many different countries around the world [13–15, 25]. According to Žujo et al. [13], one of the significant "time-cost" model limitations is that it can be applied only in the area or country of its origin because of specific economic characteristics, which are reflected on the value of model constants. Therefore, the existing models are not universally applicable and must be defined according to structure categories for each country separately. Consequently, similar studies have been conducted in many

countries in order to obtain adequate and corresponding time assessment models [15, 18, 35, 55, 56].

The most representative variables that influence the construction duration are as follows: type of structure, contracted time, real construction time, contracted price, and real construction price; these were chosen for building the model. Bromilow's "time-cost" model (Eq. (1)) is applied for contracted (planned) time and contracted (planned) price (Eq. (2)), and also for real price and real time of construction (Eq. (3)):

$$Y_1 = a_1 \cdot X_1^{b_1}, \quad (2)$$

$$Y_2 = a_2 \cdot X_2^{b_2}, \quad (3)$$

$Y_1$  is the planned (contracted) time for construction and  $X_1$  is the contracted construction price, and  $Y_2$  and  $X_2$  are the real construction time and real construction price, respectively.

These equations ((2) and (3)) shall be logarithmized (Eq. (4) and Eq. (5)):

$$\ln(Y_1) = \ln(a_1) + b_1 \ln(X_1), \quad (4)$$

$$\ln(Y_2) = \ln(a_2) + b_2 \ln(X_2), \quad (5)$$

and  $Y_2$  shall be expressed from Eqs. (4) and (5), by their summing (Eq. (6)):

$$\ln(Y_1) + \ln(Y_2) = \ln(a_1) + b_1 \ln(X_1) + \ln(a_2) + b_2 \ln(X_2), \quad (6)$$

$$\ln(Y_2) = \ln(a_1) + b_1 \ln(X_1) + \ln(a_2) + b_2 \ln(X_2) - \ln(Y_1). \quad (7)$$

Eq. (7) was used as a basic idea for the implementation of Bromilow's model in this research because it is linear in terms of the coefficients  $b_1$  and  $b_2$  and more suitable for the implementation in comparison with equations (2) and (3). Consequently, as input variables for the general regression neural network (GRNN),  $\ln Y_1$ ,  $\ln Y_2$ ,  $\ln X_1$ , and  $\ln X_2$  were used, and not their actual values  $Y_1$ ,  $Y_2$ ,  $X_1$ , and  $X_2$ . In this way, Bromilow's time-cost model was implemented as input in the GRNN.

The importance of using Bromilow's time-cost model as a process-based model, which significantly improved the accuracy of the new hybrid model, should once more be pointed out.

**2.2.2. Data-Driven Model.** General regression neural network (GRNN) is used as a data-driven model using the process-based Bromilow model.

Neural networks (NN), as data-driven models, have proven their applicability in civil engineering in the last almost three decades, demonstrating very good solutions to many problems of civil engineering. NN are computational, biologically inspired models. Simulating the way of brain functioning, they learn from the experience. Using interconnected neurons, they perform input-output mapping.

The data enter the network through the neurons from the input layer. Then, they are fed forward through the middle (hidden) layer to the last output layer. The inputs are the variables that are the most representative for the process. NN capture the relationship between the actual input and output variables. NN are successful in solving a specific problem or modelling a particular process if substantial amount of data that describes the problem is available. Moreover, there should be no significant changes to the system or process that is being modelled [54]. For solving any problem with NN, the appropriate type of NN architecture should be selected because for different types of problems and available data, different types of NN architecture or data-driven model will be applicable.

For our investigation, several NN and other data-driven models were tried: linear regression, multilayer perceptron (MLP), support vector machine (SVM), RBFNN (radial basis NN), and GRNN. The most appropriate for our data was GRNN, performing the most accurate predicting.

General regression neural network (GRNN) can be applied for solving control problems, prediction, mapping, and any nonlinear regression problem [57]. The main characteristics that make it very applicable in practice are that in most of the cases, it is very accurate and it needs only several training samples to converge to the optimal solution. However, to store the model, it takes quite a lot of memory space. Some of the advantages of GRNN in comparison with other nonlinear regression models are that GRNN can generalize from the input data as soon as they are stored, learning in one pass through the data. Simulation of the GRNN algorithm is very simple, and because of the local minima of the error criterion, GRNN can converge to good solutions [58]. Figure 1 shows the architecture of GRNN.

The input layer has the same number of neurons as the number of predictors. The values of the predictors from the input neurons are fed to the neurons in the next pattern layer. The neurons from the pattern layer store the data for the rows from the training data set, each neuron for one row (case), and in this layer, for each new test case, Euclidean distance from the neuron's center is computed, RBF kernel function is applied, and that value is fed to the summation layer. The summation layer has two neurons: numerator summation unit and denominator summation unit. The numerator unit adds up the weight values multiplied by the actual value of the dependent (target) variable from each neuron from the pattern layer, and the denominator unit adds up the weight values from the neurons from the pattern layer. In the final decision layer (output unit), the predicted value of the target variable is computed by dividing the value from the numerator unit with the value from the denominator unit [57, 59].

GRNN implements the following equation (Eq. (8)) [57]:

$$y(X) = E\left[\frac{y}{X}\right] = \frac{\int_{-\infty}^{\infty} y f(X, y) dy}{\int_{-\infty}^{\infty} f(X, y) dy}. \quad (8)$$

$E[y/X]$  is the conditional expectation of the output (target variable)  $y$  for the given input  $X$  and  $f(X, y)$  is the joint probability density function (jpdf) of the input vector  $X$

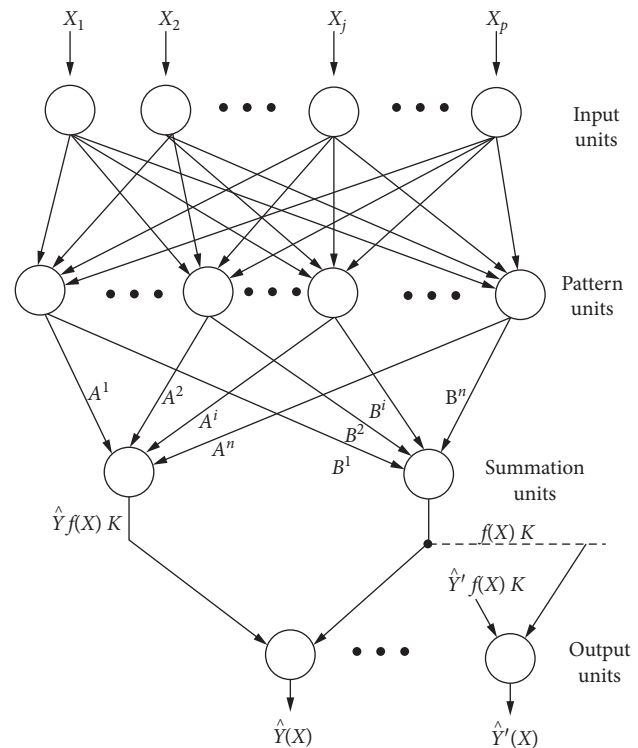


FIGURE 1: GRNN [57].

and the output  $y$ . When the function  $f(X, y)$  is not known, Parzen estimators [60] are used for its estimation from the set of observations of  $X$  and  $y$ .

Specht [61], the author of GRNN, has made improvement of his first GRNN version, applying hybrid combination of three techniques: clustering, kernel regression with adaptive parameters, and the second level of clustering with the formation of a binary decision tree. These techniques have greatly improved the speed for training, the speed for readout and testing, and also the accuracy. These improvements have contributed to making GRNN useful for high-dimensional problems and for noisy data, too.

Hybrid modelling became very significant last several years, demonstrating very good predictive results.

Xiaojun et al. [58] proposed the Tree-Structure Ensemble GRNN (TSE GRNN), which consists of ensemble modelling methods using GRNN for predicting molten steel temperature in a ladle furnace, solving the larger scale issue. They obtained very good predictive results in comparison with other temperature models.

Lee et al. [62] present hybrid model developed for the classification of noisy data. The model, called GRNNFA, unites GRNN and a fuzzy adaptive (FA) resonance theory. It has been used for predicting the occurrence of the flashover in compartment fires and has demonstrated a very accurate prediction in comparison with other ANN models.

### 3. Results

Predicting modelling software DTREG [59, 63] has been used for modelling and predicting the construction time.

For building the predictive models in this research, among all available data, the purpose of structure, real time of construction, planned time of construction, planned price, and real price of construction have been chosen as the most representative. “Purpose of structure” is the categorical variable and the others are numerical ones.

At first, a data-driven model using only GRNN for predicting real time of construction has been developed. The real time of construction has been used as a target variable and the rest of the variables have been used as predictors. The accuracy of the model expressed by MAPE was around 30%.

After that, five new hybrid models implementing Bromilow’s TCM have been developed, and the most accurate among them was BTC-GRNN, combining Bromilow’s TCM and GRNN. According to the discussion in Section 2.2.1 (Eq. (7)), for all these five hybrid models, as numerical variables (predictors and target variable), logarithm of their values:  $\ln$  (real time),  $\ln$  (planned time),  $\ln$  (real costs), and  $\ln$  (planned costs) have been used, not their actual values. Equation (7) is used because it is more appropriate for implementation than Eqs. (2) and (3) because of its linearity in terms of the coefficients  $b_1$  and  $b_2$  which express the dependency of the time of construction (planned and real time, accordingly) on cost change (planned and real cost, accordingly).

Target variable is  $\ln$  (real time) and predictors are the remaining variables. The prices of all structures have been converted into euros, and the planned and real construction time for all structures has been expressed in working days. DTREG software operates with categorical variables, considering them as strings.

Usually, the data should be normalized before making the model and running the NN, but there was no need for normalizing the input data because the software DTREG does it for each predictive model.

DTREG software offers three methods for validation and testing of the model: the standard V-fold cross-validation, random percent validation, and “leave one out” (LOO) validation. DTREG also has an option for model optimization by removing unnecessary neurons from the NN. In this research, the model BTC-GRNN has been tested by three methods: first, by 10-fold cross validation, second, by using the option of “reducing number of neurons” with random percent, and third, by using LOO validation.

The accuracy of the model BTC-GRNN for the training and validation data using the 10-fold cross-validation method is presented in Table 1. The most frequently used estimators of the accuracy are MAPE, i.e., mean absolute percentage error and the coefficient of determination  $R^2$ , which reflects the global fit of the model. For the BTC-GRNN model, MAPE is 3.34% and the coefficient of determination  $R^2$  is 0.9317, which means that around 93.17% of the variation of the predicted target variable can be explained by the chosen predictors, whereas the remaining around 7% can be ascribed by some unknown variables or inherent variability. The coefficient of correlation between the actual and the predicted target values is 0.97.

The dependence between the actual and the predicted values for this model is presented in Figure 2 [63].

TABLE 1: Model accuracy results for BTC-GRNN model for (a) training data and (b) validating data (using 10-fold cross-validation) [63].

(a) Training data	
Mean target value for input data	5.1452765
Mean target value for predicted values	5.1456292
Variance in input data	1.1319931
Residual (unexplained) variance after model fit	0.0031972
<i>Proportion of variance explained by model (<math>R^2</math>)</i>	<b>0.99718</b> <b>(99.718%)</b>
Coefficient of variation (CV)	0.010989
Normalized mean square error (NMSE)	0.002824
<i>Correlation between actual and predicted target values</i>	<b>0.998588</b>
Maximum error	0.2234627
RMSE (root mean squared error)	0.0565438
MSE (mean squared error)	0.0031972
MAE (mean absolute error)	0.0310945
<i>MAPE (mean absolute percentage error)</i>	<b>0.6133842</b>
(b) Validation data	
Mean target value for input data	5.1452765
Mean target value for predicted values	5.1156255
Variance in input data	1.1319931
Residual (unexplained) variance after model fit	0.0772845
<i>Proportion of variance explained by model (<math>R^2</math>)</i>	<b>0.93173</b> <b>(93.173%)</b>
Coefficient of variation (CV)	0.054030
Normalized mean square error (NMSE)	0.068273
<i>Correlation between actual and predicted target values</i>	<b>0.965664</b>
Maximum error	1.2041075
RMSE (root mean squared error)	0.2780008
MSE (mean squared error)	0.0772845
MAE (mean absolute error)	0.1727287
<i>MAPE (mean absolute percentage error)</i>	<b>3.34113</b>

The model BTC-GRNN has also been tested by using the optimization option by reducing the number of neurons. In this case, for validation, the model random percent (16%) and the LOO method have been used. The optimal model has been obtained with only 70 neurons. The results for the estimators, i.e., MAPE and  $R^2$ , using these 3 validation methods are presented in Table 2.

The accuracy of the other four hybrid models and the data-driven GRNN model shall be discussed in the next section.

For the numerical variables, DTREG computes their minimal, maximal, mean value and their standard deviation (Table 3) [63].

For each predictor, DTREG computes its importance for the quality of the model (Table 4) [63].

DTREG computes the target mean value for each different value of the predictors. Table 5 [63] shows the mean target values for only three different values of 4 predictors: purpose of facility,  $\ln$ (planned costs),  $\ln$ (real costs), and  $\ln$ (planned time). The first row for the predictor, “purpose of facility,” means that 4 rows, which is 3.45% of all 116 rows, have the same mean target value of 3.8491. The target value is  $\ln$ (real time), and the mean value for the real time in days can be easily computed. For the predictor  $\ln$ (planned time),

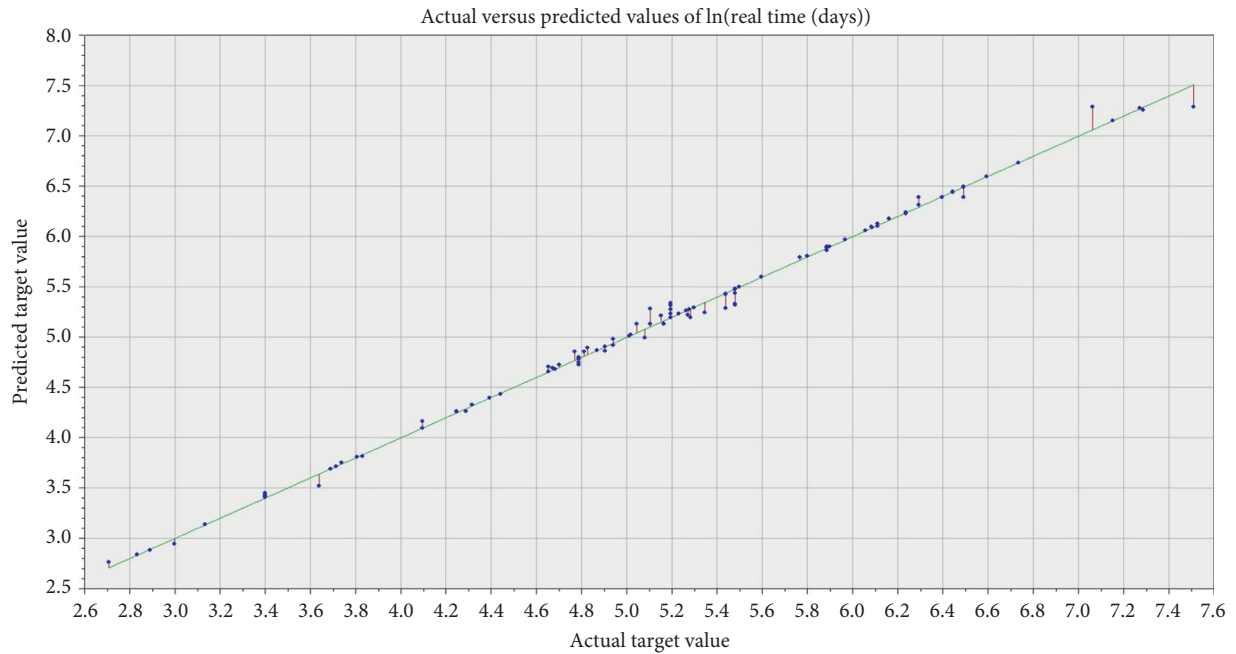


FIGURE 2: Dependence between actual and predicted values for the BTC-GRNN model.

TABLE 2: Accuracy results for the hybrid model BTC-GRNN using three validation methods.

Method for validation and testing	MAPE (%)	$R^2$ (%)	Coefficient of correlation between actual and predicted target values
10-fold cross-validation	3.34	93.17	0.966
Random percent (16%) (when using the optimization option by reducing the number of neurons)	3.76	93.72	0.970
LOO (when using the optimization option by reducing the number of neurons)	2.596	95.70	0.979

TABLE 3: Minimal, maximal, mean value, and standard deviation of input numerical variables for the BTC-GRNN model.

Variable	Rows	Minimum	Maximum	Mean	Standard deviation
ln(planned costs, euro)	116	9.05358	18.36511	13.27770	2.06661
ln(real costs, euro)	116	9.09459	18.51599	13.35837	2.11371
ln(planned time, days)	116	2.70805	6.81619	5.07076	1.04090
ln(real time, days)	116	2.70805	7.50934	5.14528	1.06395

TABLE 4: Overall Importance of variables for the BTC-GRNN model [63].

Variable	Importance
ln(planned time, days)	100.000
ln(real costs, euro)	28.396
Purpose of the facility	3.432
ln(planned costs, euro)	0.010

the first row means that two rows, which is 1.72%, of all 116 rows, have the same value of 2.70805, and their mean target value (ln(real time)) is 2.8519. For each predictor, only the first three rows are shown.

DTREG has a separate file from which the predicted values for the target variable can be read for each value of the predictors.

## 4. Discussion

As other neural networks, the GRNN learns from the input data, so their quality and quantity influence the prediction error. In this paper, the emphasis is on the importance of using the process-based Bromilow time-cost model combined with the data-driven model (GRNN). The reason is in the accuracy of the model that has been drastically improved. Moreover, for the model BTC-GRNN proposed in this paper, there was no need for computing the parameters of Bromilow's model.

Without using Bromilow's model and using only the actual values of the input variables: real time and planned time of construction and real price and planned price of construction as input data to GRNN, the model accuracy was tested by using three validation methods. Using the 10-

TABLE 5: Target mean values for three different predictor values [63].

Predictors			Target variable: ln(real time, days)
Purpose of the facility			Target mean
4	3.45%	Petrol station	3.8491
5	4.31%	Education	6.6249
7	6.03%	Bridge	4.5354
ln(planned costs, euro)			Target mean
1	0.86%	9.05358	3.6889
1	0.86%	9.35037	2.9957
1	0.86%	9.44293	2.8332
ln(real costs, euro)			Target mean
1	0.86%	9.09459	3.6889
1	0.86%	9.35037	2.9957
1	0.86%	9.44293	2.8332
ln(planned time, days)			Target mean
2	1.72%	2.708050	2.8519
2	1.72%	2.995732	2.8618
1	0.86%	3.218876	3.1355

fold cross-validation method, MAPE was 31.8,  $R^2 = 75.64\%$ , and the coefficient of correlation was 0.879 (Table 6). The other two validation methods, random percent (16%) validation and LOO validation, were used when the option for optimizing the model with reducing the number of neurons was applied. The results for the model accuracy, expressed by the most used estimators MAPE and  $R^2$ , obtained by using these three validation methods are summarized in Table 7.

After developing the data-driven GRNN model, five hybrid models which implement process-based and data-driven models have been developed: BTC-SVM, BTC-LR, BTC-RBFNN, BTC-MLPNN, and BTC-GRNN, which combine Bromilow's TCM and SVM (support vector machine), LR (linear regression, RBFNN (radial basis function NN), MLPNN (multilayer perceptron NN), and GRNN, respectively.

The results for the obtained accuracy, expressed by MAPE and  $R^2$ , using 10-fold cross-validation, are presented in Table 8. The most accurate was the BTC-GRNN model, as discussed in the previous section.

The model proposed in this paper has some limitations. Namely, the model is not applicable for higher, more intensive risk factors impact during the construction period (e.g., longer period with bad weather conditions, economic crisis, and high inflation). The project documentation is expected to be completed and corrected before the construction begins. It should be noted that some researches [17, 25] have shown that the problems with technical documentation (e.g., incompleteness and inaccuracy) sometimes cause delays in the construction process. It can be said that the model is applicable for the "normal" level of expected risk factors.

## 5. Conclusion

Construction time is one of the key elements in the bidding process and decision-making at the early phase of the construction project. However, at the same time, in this phase, the construction time prediction is a complex,

TABLE 6: Model accuracy results for (a) training and (b) validating data by using only data-driven GRNN model (using the 10-fold cross-validation method) [63].

(a) Training data	
Mean target value for input data	286.90647
Mean target value for predicted values	286.19978
Variance in input data	99430.392
Residual (unexplained) variance after model fit	2319.0624
<i>Proportion of variance explained by model (<math>R^2</math>)</i>	0.97668 (97.668%)
Coefficient of variation (CV)	0.167848
Normalized mean square error (NMSE)	0.023323
<i>Correlation between actual and predicted target values</i>	0.988279
Maximum error	300.05113
RMSE (root mean squared error)	48.156644
MSE (mean squared error)	2319.0624
MAE (mean absolute error)	21.681144
<i>MAPE (mean absolute percentage error)</i>	19.471364
(b) Validation data	
Mean target value for input data	286.90647
Mean target value for predicted values	285.08662
Variance in input data	99430.392
Residual (unexplained) variance after model fit	24222.689
<i>Proportion of variance explained by model (<math>R^2</math>)</i>	<b>0.75639</b> <b>(75.639%)</b>
Coefficient of variation (CV)	0.542464
Normalized mean square error (NMSE)	0.243615
<i>Correlation between actual and predicted target values</i>	<b>0.879069</b>
Maximum error	1002
RMSE (root mean squared error)	155.6364
MSE (mean squared error)	24222.689
MAE (mean absolute error)	74.291454
<i>MAPE (mean absolute percentage error)</i>	<b>31.79981</b>

demanding task for project participants. Available project information is limited. Hence, using data from previous projects is of particular interest.

This paper presents research results of hybrid model development for early and fast construction time predicting using historical data. The model implements a combination of process-based model (Bromilow's time-cost model) and data-driven model (GRNN). Using 10-fold cross-validation, the mean absolute percentage error (MAPE) of the model is 3.34% and the coefficient of determination  $R^2$ , which reflects the global fit of the model, is 93.17%. These results point to the drastic improvement of the accuracy when using only the data-driven GRNN model when MAPE is 31.8% and  $R^2$  is 75.64%.

Such improved model can be successfully used at early project phases for a preliminary prediction of project duration with satisfactory accuracy. As such, it is not a substitution of detailed construction time planning.

For future researches, it is suggested to develop separate models for different types of structures and different projects characteristics (e.g., type of client, procurement characteristics, and type of contract). Homogeneous database will probably lead to improving the accuracy of the models. Moreover, the latest research and achievements in the area of

TABLE 7: Model accuracy results for validation data by using only data-driven GRNN model (using three methods).

Method for validation and testing	MAPE (%)	R <sup>2</sup> (%)	Coefficient of correlation between actual and predicted target values
10-fold cross-validation	31.8	75.64	0.879
Random percent (16%) (when using the optimization option by reducing the number of neurons)	32.47	83.75	0.952
LOO (when using the optimization option by reducing the number of neurons)	31.59	83.37	0.924

TABLE 8: Comparison of the accuracy of the five new hybrid models using 10-fold cross-validation.

Type of the predictive hybrid model	MAPE (%)	R <sup>2</sup> (%)	Coefficient of correlation between actual and predicted target values
BTC-SVM	3.9	91.63	0.958
BTC-LR	4.5	89.39	0.950
BTC-RBFNN	4.31	90.65	0.953
BTC-MLPNN	4.28	89.91	0.948
BTC-GRNN	3.34	93.17	0.966

the artificial intelligence, obtained by combining the process-based and data-driven models, can be of great significance for improving the accuracy of the predictive models.

Additionally, such models should be, in future research, considered as the part of integral building management information system. The reason lies in their characteristics and developmental potential. This would significantly solve the problems of wrong project decisions as the result of the initial faulty project time estimation.

## Data Availability

The data used to support the findings of this study are available from the corresponding author upon request.

## Conflicts of Interest

The authors declare that there are no conflicts of interest regarding the publication of this paper.

## Acknowledgments

The authors want to express their gratitude to Prof. Vojislav Kecman from the University of Virginia (USA) and Phil Sherrod, the author of the software DTREG, for their valuable consultations. This work was partly supported by the University of Rijeka (Grant number: 13.05.1.3.10).

## References

- [1] H. M. Günaydin and S. Z. Doğan, "A neural network approach for early cost estimation of structural systems of buildings," *International Journal of Project Management*, vol. 22, no. 7, pp. 595–602, 2004.
- [2] Z. Ma, N. Lu, and S. Wu, "Identification and representation of information resources for construction firms," *Advanced Engineering Informatics*, vol. 25, no. 4, pp. 612–624, 2011.
- [3] W. Tiziani and M. J. Mawdesley, "Advances and challenges in computing in civil and building engineering," *Advanced Engineering Informatics*, vol. 25, no. 4, pp. 569–572, 2011.
- [4] R. J. Scherer and S.-E. Schapke, "A distributed multi-model-based Management Information System for simulation and decision-making on construction projects," *Advanced Engineering Informatics*, vol. 25, no. 4, pp. 582–599, 2011.
- [5] A. Watson, "Digital buildings—challenges and opportunities," *Advanced Engineering Informatics*, vol. 25, no. 4, pp. 573–581, 2011.
- [6] M. Joe, T. B. Keoughan, and I. Pegg, "Predicting construction duration of building projects," in *TS 28—Construction Economics I, Shaping the Change*, pp. 1–13, XXIII FIG Congress, Munich, Germany, 2006.
- [7] B. Dimitrov and V. Zileska-Pančovska, "Structure of price elements for construction works on water engineering systems," *Journal Gradjevinar*, vol. 67, pp. 363–368, 2015.
- [8] P. González, V. González, K. Molenaar, and F. Orozco, "Analysis of causes of delay and time performance in construction projects," *Journal of Construction Engineering and Management*, vol. 140, no. 1, 2014.
- [9] Y. A. Olawale and M. Sun, "Cost and time control of construction projects: inhibiting factors and mitigating measures in practice," *Construction Management and Economics*, vol. 28, no. 5, pp. 509–526, 2010.
- [10] R. N. Nkado, "Construction time information system for the building industry," *Construction Management and Economics*, vol. 10, no. 6, pp. 489–509, 1992.
- [11] S. M. Dissanayaka and M. M. Kumaraswamy, "Comparing contributors to time and cost performance in building projects," *Building and Environment*, vol. 34, no. 1, pp. 31–42, 1998.
- [12] A. Kaka and A. D. F. Price, "Relationship between value and duration of construction projects," *Construction Management and Economics*, vol. 9, no. 4, pp. 383–400, 2006.
- [13] V. Žujo, D. Car-Pušić, V. Zileska-Pančovska, and M. Čeček, "Time and cost interdependence in water supply system construction projects," *Technological and Economic Development of Economy*, vol. 23, pp. 895–914, 2017.
- [14] D. Car-Pušić and M. Radujković, "Modeli za brzu procjenu održivog, vremena gradnja," *Gradjevinar*, vol. 58, pp. 559–568, 2006.
- [15] D. W. M. Chan and M. M. Kumaraswamy, "A study of the factors affecting construction durations in Hong Kong," *Construction Management and Economics*, vol. 13, no. 4, pp. 319–333, 1995.

- [16] K. Petlíková and Č. Jarský, "Modeling of the time structure of construction processes using neural networks," *Organization, Technology and Management in Construction: an International Journal*, vol. 9, no. 1, pp. 1559–1564, 2017.
- [17] D. Car-Pušić, "Methodology of planning the sustainable construction time," Dissertation, Faculty of Civil Engineering, University of Zagreb, Zagreb, Croatia, 2004, in Croatian.
- [18] H. P. Moura, J. C. Teixeira, and B. Pires, "Dealing with cost and time in the Portuguese construction industry," in *Proceedings of CIB World Building Congress*, pp. 1252–1265, Cape Town, South Africa, May 2007.
- [19] Y. Zhang and S. T. Ng, "An ant colony system based decision support system for construction time-cost optimization," *Journal of Civil Engineering and Management*, vol. 18, no. 4, pp. 580–589, 2012.
- [20] A. P. C. Chan and D. W. M. Chan, "Developing a benchmark model for project construction time performance in Hong Kong," *Building and Environment*, vol. 39, no. 3, pp. 339–349, 2004.
- [21] R. Kenley, *Financing Construction: Cash Flows and Cash Farming. The Time-Cost Relationship* Routledge, pp. 138–160, Taylor and Francis Group, London, UK, 2013.
- [22] S. Ng Thomas, M. M. Y. Mak, R. M. Skitmore, K. C. Lam, and M. Varnam, "The predictive ability of Bromilow's time-cost model," *Construction Management and Economics*, vol. 19, no. 2, pp. 165–173, 2001.
- [23] A. P. C. Chan, "Time-cost relationship of public sector projects in Malaysia," *International Journal of Project Management*, vol. 19, no. 4, pp. 223–229, 2001.
- [24] I. Choudhury and S. S. Rajan, *Time-Cost Relationship for Residential Construction in Texas*, Construction Informatics Digital Library, University of Ljubljana, Ljubljana, Slovenia, 2003.
- [25] D. Car-Pušić and M. Radujković, "Construction time-cost model in Croatia," *International Journal for Engineering Modelling*, vol. 22, pp. 63–70, 2009.
- [26] D. Mačková and R. Bašková, "Applicability of Bromilow's time-cost model for residential projects in Slovakia," *Selected Scientific Papers—Journal of Civil Engineering*, vol. 9, no. 2, pp. 5–12, 2014.
- [27] R. M. Skitmore and S. T. Ng, "Forecast models for actual construction time and cost," *Building and Environment*, vol. 38, no. 8, pp. 1075–1083, 2003.
- [28] R. M. Skitmore and S. T. Ng, "Australian project time-cost analysis: statistical analysis of intertemporal trends," *Construction Management and Economics*, vol. 19, no. 5, pp. 455–458, 2001.
- [29] A. P. C. Chan and D. W. M. Chan, "A benchmark model for construction duration in public housing developments," *International Journal of Construction Management*, vol. 3, no. 1, pp. 1–14, 2003.
- [30] J. F. Shr and W. T. Chen, "Functional model of cost and time for highway construction projects," *Journal of Marine Science and Technology*, vol. 14, pp. 127–138, 2006.
- [31] M. M. Kumaraswamy and D. W. M. Chan, "Determinants of construction duration," *Construction Management and Economics*, vol. 13, pp. 209–217, 1995.
- [32] A. O. Ayodeji, J. Smallwood, and W. Shakantu, "A linear regression modelling of the relationship between initial estimated and final achieved construction time in South Africa," *Acta Structilia*, vol. 19, pp. 39–56, 2012.
- [33] D. W. M. Chan and M. M. Kumaraswamy, "Forecasting construction durations for public housing projects: a Hong Kong perspective," *Building and Environment*, vol. 34, no. 5, pp. 633–646, 1999.
- [34] F. Khosrowshahi and A. P. Kaka, "Estimation of project total cost and duration for housing projects in UK," *Building and Environment*, vol. 31, no. 4, pp. 373–383, 1996.
- [35] V. Žujo and D. Car-Pušić, "Prekoračenje ugovorenog roka građenja kao funkcija rizičnih faktora," *Građevinar: Časopis Hrvatskog Saveza Građevinskih Inženjera*, vol. 61, pp. 721–729, 2009, in Croatian.
- [36] A. A. Abu Hammad, S. M. Alhaj Ali, J. S. Ghaleb, and A. Bashir, "Prediction model for construction cost and duration in Jordan," *Jordan Journal of Civil Engineering*, vol. 2, pp. 250–266, 2008.
- [37] M. G. Naik and V. S. B. Radhika, "Time and cost analysis for highway road construction project using artificial neural networks," *Journal of Construction Engineering and Project Management*, vol. 5, no. 1, pp. 26–31, 2015.
- [38] B. Vahdani, S. M. Mousavi, M. Mousakhani, and H. Hashemi, "Time prediction using a neuro-fuzzy model for projects in the construction industry," *Journal of Optimization in Industrial Engineering*, vol. 19, pp. 97–103, 2016.
- [39] S. Petruseva, V. Zujo, and V. Zileska-Pancovska, "Neural network prediction model for construction project duration," *International Journal of Engineering Research and Technology*, vol. 2, pp. 1646–1654, 2013.
- [40] I. Attarzadeh and S. H. Ow, "Software development cost and time forecasting using a high performance artificial neural network model," in *Intelligent Computing and Information Science: Communications in Computer and Information Science*, R. Chen, Ed., pp. 18–26, Springer, Berlin, Germany, 2011.
- [41] S. Petruseva, D. Car-Pusic, and V. Zileska Pancovska, "Model for predicting construction time by using general regression neural network," in *Proceedings of People Buildings and Environment, International Scientific Conference (PBE 2016)*, p. 31, Luhačovice, Czech Republic, September–October 2016.
- [42] I. Mensah, G. Nani, and T. Adjei-Kumi, "Development of a model for estimating the duration of bridge construction projects in Ghana," *International Journal of Construction Engineering and Management*, vol. 5, pp. 55–64, 2016.
- [43] V. Yousefi, S. Haji Yakhchali, M. Khanzadi, E. Mehrabanfar, and J. Šaparauskas, "Proposing a neural network model to predict time and cost claims in construction projects," *Journal of Civil Engineering and Management*, vol. 22, no. 7, pp. 967–978, 2016.
- [44] A. A. Gab Allah, A. H. Ibrahim, and O. A. Hagra, "Predicting the construction duration of building projects using artificial neural networks," *International Journal of Applied Management Science*, vol. 7, no. 2, pp. 123–141, 2015.
- [45] M. J. Roberts, N. O. Braun, T. R. Sinclair, D. B. Lobell, W. Schlenker, and W. Schlenker, "Comparing and combining process-based crop models and statistical models with some implications for climate change," *Environmental Research Letters*, vol. 12, no. 9, article 095010, 2017.
- [46] L. Liao and F. Köttig, "A hybrid framework combining data-driven and model-based methods for system remaining useful life prediction," *Applied Soft Computing*, vol. 44, pp. 191–199, 2016.
- [47] K. Cuddington, M. J. Forth, L. R. Gerber et al., "Process-based models are required to manage ecological systems in a changing world," *Ecosphere*, vol. 4, no. 2, pp. 1–12, 2013.
- [48] G. A. Corzo, D. P. Solomatine, M. Hidayat et al., "Combining semi-distributed process-based and data-driven models in flow simulation: a case study of the Meuse river basin," *Hydrology and Earth System Sciences*, vol. 13, no. 9, pp. 1619–1634, 2009.

- [49] D. Zhou, Q. Hu, and C. Tomlin, "Model comparison of a data-driven and a physical model for simulating HVAC systems," 2016, <https://arxiv.org/abs/1603.05951>.
- [50] S. Formentin, K. Heusden, and A. Karimi, "A comparison of model-based and data-driven controller tuning," *International Journal of Adaptive Control and Signal processing*, pp. 1–16, 2012.
- [51] M. Rajabi, A. Mansourian, P. Pilesjö, F. Hedefalk, R. Groth, and A. Bazmani, "Comparing knowledge-driven and data-driven modelling methods for susceptibility mapping in spatial epidemiology: a case study in Visceral Leishmaniasis," in *Proceedings of the AGILE 2014, International Conference on Geographic Information Science*, Castellon, Spain, June 2014.
- [52] R. J. Abrahart, L. M. See, and D. P. Solomatine, *Practical Hydroinformatics: Water Science and Technology Library*, Springer-Verlag, Berlin, Germany, 2008.
- [53] K. Manhart, *Artificial Intelligence Modelling: Data Driven and Theory Driven Approaches (Revised Version of a Contribution Published in, Social Science Micro Simulation*, U. Troitzsch, U. Muller, G. Nigel, and J. E. Doran, Eds., Springer, Berlin 1996, Springer, Munchen, Germany, 2007.
- [54] F. J. Bromilow, "Contract time performance expectations and reality," *Building forum*, vol. 1, pp. 70–80, 1969.
- [55] O. Durson and C. Stoy, "Time-cost relationship of building projects: statistical adequacy of categorization with respect to project location," *Construction Management and Economics*, vol. 29, no. 1, pp. 97–106, 2011.
- [56] C. Sun and J. Xu, "Estimation of time for Wenchuan Earthquake reconstruction in China," *Journal of Construction Engineering and Management*, vol. 137, no. 3, pp. 179–187, 2011.
- [57] D. F. Specht, "A general regression neural network," *IEEE Transactions on neural networks*, vol. 2, no. 6, pp. 568–576, 1991.
- [58] W. Xiaojun, Y. Mingshuang, M. Zhizhong, and Y. Ping, "Tree-structure ensemble general regression neural networks applied to predict the molten steel temperature in Ladle Furnace," *Advanced Engineering Informatics*, vol. 30, no. 3, pp. 368–375, 2016.
- [59] P. Sherrod, "Predictive modelling software-tutorial," 2013, <http://www.dtreg.com>.
- [60] E. Parzen, "On estimation of a probability density function and mode," *Annals of Mathematical Statistics*, vol. 33, no. 3, pp. 1065–1076, 1962.
- [61] D. F. Specht, "GRNN with double clustering," in *Proceedings of the International Joint Conference on Neural Networks*, Vancouver, Canada, July 2006.
- [62] E. W. M. Lee, Y. Y. Lee, C. P. Lim, and C. Y. Tang, "Application of a noisy data classification technique to determine the occurrence of flashover in compartment fires," *Advanced Engineering Informatics*, vol. 20, no. 2, pp. 213–222, 2006.
- [63] P. Sherrod, "Predictive Modelling Software," 2013, <http://www.dtreg.com>.

## Research Article

# Application of Artificial Neural Network(s) in Predicting Formwork Labour Productivity

Sasan Golnaraghi, Zahra Zangenehmadar , Osama Moselhi, and Sabah Alkass

*Department of Building, Civil and Environmental Engineering, Concordia University, Montréal, Canada*

Correspondence should be addressed to Zahra Zangenehmadar; [z\\_zange@encs.concordia.ca](mailto:z_zange@encs.concordia.ca)

Received 2 August 2018; Revised 5 October 2018; Accepted 19 November 2018; Published 2 January 2019

Guest Editor: Ali R. Vosoughi

Copyright © 2019 Sasan Golnaraghi et al. This is an open access article distributed under the Creative Commons Attribution License, which permits unrestricted use, distribution, and reproduction in any medium, provided the original work is properly cited.

Productivity is described as the quantitative measure between the number of resources used and the output produced, generally referred to man-hours required to produce the final product in comparison to planned man-hours. Productivity is a key element in determining the success and failure of any construction project. Construction as a labour-driven industry is a major contributor to the gross domestic product of an economy and variations in labour productivity have a significant impact on the economy. Attaining a holistic view of labour productivity is not an easy task because productivity is a function of manageable and unmanageable factors. Compound irregularity is a significant issue in modeling construction labour productivity. Artificial Neural Network (ANN) techniques that use supervised learning algorithms have proved to be more useful than statistical regression techniques considering factors like modeling ease and prediction accuracy. In this study, the expected productivity considering environmental and operational variables was modeled. Various ANN techniques were used including General Regression Neural Network (GRNN), Backpropagation Neural Network (BNN), Radial Base Function Neural Network (RBFNN), and Adaptive Neuro-Fuzzy Inference System (ANFIS) to compare their respective results in order to choose the best method for estimating expected productivity. Results show that BNN outperforms other techniques for modeling construction labour productivity.

## 1. Introduction

Artificial Intelligence (AI) has been a powerful tool in the construction industry over the past decade. Several AI modeling techniques have been employed in the construction industry such as expert systems (ES) and Artificial Neural Network (ANN). Modeling labour productivity is challenging as it requires the quantification of substantial factors that affect labour productivity and consideration of influential factor interdependencies. Productivity is a delicate aspect of any construction project. Unquestionably, arriving at a definition of construction productivity can cause confusion because of the various different ways at defining it. Strictly speaking, productivity is a component of cost and is not a method for estimating the cost of resources; rather, it is a quantitative assessment of the correlation among the number of resources used and the amount of output made [1]. Productivity in construction is considered

as a measure of output achieved by a combination of inputs. Considering this perspective, two concepts for measuring productivity described in the literature are total factor productivity and circulating capital [2]. Total factor productivity is the most common construction productivity measurement technique where the output is measured against all inputs. Partial factor productivity is referred to as single-factor productivity, in which the output is measured against a single input or selected inputs. Partial factor productivity is a cost-effective model and very advantageous for developing strategy and assessing the state of the economy; however, it is not beneficial for contractors [2]. Circulating capital is any kind of capital that will be depleted during the course of a project, such as material and operating expenses, whereas fixed capital refers to any kind of capital that is not exhausted during the course of a project.

Productivity modeling has been a topic of interest for many researchers and the various models being developed

today can be classified into two major groups: statistical and AI. Regression analysis is the most common statistical method for modeling labour productivity. The main advantage to regression analysis is that a productivity model can be developed to reach anticipated clarification or forecasting levels with as few predictor variables as possible. However, for regression methods, the degree of relationship (linear and nonlinear) needs to be selected prior to model development. In AI modeling, ANN models are the most common for developing labour construction productivity. Unlike regression methods, the degree of relationship is not a concern in ANN modeling. Those studies that have applied various ANN methods to predict different types of productivity are discussed in the next section.

Lu et al. [3] estimated construction labour productivity using real historical data from local construction companies. They applied a Probability Inference Neural Network (PINN) model and compared it to a feed-forward back-propagation neural network model. AbouRizk et al. [4] developed a two-stage ANN model for predicting labour productivity rates. They stated that understanding input factors and having a sufficient historical database are the most important parts in productivity prediction. Later, [5] introduced a neural network model for defining the impact of a change order on labour productivity and found that the ANN model shows better performance in comparison to other techniques. Ezledin and Sharara [6] established an ANN model for productivity prediction in formwork activity, steel fixing, and concrete-pouring activities. Ok and Sinha [7] applied ANN to estimate the daily productivity of earthmoving equipment. Song and AbouRizk [8] presented a productivity model for steel drafting and fabrication productivity through ANN and discrete-event simulation using actual data. Oral and Oral [9] utilized a Self Organizing Map (SOM) to analyze the relationship between construction crew productivity and different factors. They also predicted productivity in given situations for ready-mixed concrete, formwork, and reinforcement crew. Data were collected randomly from a construction site in Turkey. They concluded that SOM can predict productivity better than regression methods due to its complexity. Muqem et al. [10] predicted production rate values for installation of beam formwork using ANN. Meanwhile, Mohammed et al. [11] predicted the productivity of ceramic wall construction using data from general contractor companies. They applied ANN since analysis required performing complex mapping of environment and management factors to productivity. AL-Zwainy et al. [12] developed a model for estimating construction labour productivity in marble finishing works. They used multilayer perceptron training through a BNN algorithm. Moselhi and Khan [13] ranked labour productivity-influencing parameters in construction using Fuzzy Subtractive Clustering, Neural Network Modeling, and Stepwise Variable Selection. They determined that work type, floor level, and temperature were the parameters with a larger effect on productivity. Heravi and Eslamdoost [14] considered 15 important factors in the motivation of labour, supervision sufficiency, and competency and suggested a model for labour productivity rate estimation. Aswed [15]

applied ANN for estimating the bricklayer (builder) productivity and modeled 13 productivity-influencing factors. El-Gohary et al. [16] proposed a framework to document, control, and predict contractor labour productivity using ANN and hyperbolic tan function. They considered factors at micro and macro/microlevels and applied the models to construction crafts, carpentry, and fixing reinforcing steel bars.

A considerable issue in the construction industry is that a lot of problems such as last-minute bids, design under pressure, and so on are analogy-based in form. Thus, ANN techniques as compared to other conventional practices are more appropriate in modeling construction industry problems that demand analogy-based resolutions [17]. There are four major steps for modeling analogy-based problems using ANN: (i) gathering historical data, (ii) building and configuring relevant network, (iii) initializing weights and biases, and (iv) training and validation step. In this research, four types of ANN were applied for modeling labour productivity. These were Backpropagation Neural Network (BNN), Radial Basis Network (RBF), Generalized Regression Neural Network (GRNN), and Adaptive Neuro-Fuzzy Inference System (ANFIS). A detailed explanation of all the applied modeling techniques will be discussed along with the data collection procedure in the following sections.

## 2. ANN Model Development

Construction projects are highly dynamic with many challenges in the areas of costs, delays and disruptions, impaired productivity, quality issues, safety aspects, materials unavailability, and escalation among others. These challenges are highly complicated in nature and information related to these challenges is vague. Therefore, construction projects are within the purview of ANN in which the given ambiguous information can be effectively interpreted in order to arrive at meaningful conclusions. In other words, because of ANN's capability to draw the relationships between input and output provided via a training dataset, ANN is suitable for nonlinear problems where vague information, subjective judgment, experience, and surrounding conditions are key features, and traditional approaches are insufficient to calculate the complex input-output relationship necessary for predicting construction labour productivity. This paper reviews the application of various ANNs in predicting construction labour productivity for formwork assembly with a limited given dataset. Figure 1 shows the overall flowchart of the research. The first step in the model development process was the choice of inputs from the available data and appropriate model outputs. Then, the data were processed through normalization and for handling missing data. The data were divided into training and testing, and the BNN, RBF, ANFIS, and GRNN AI models were applied to the datasets. The models were calibrated via a performance evaluation and were compared using a determination coefficient ( $R$ -squared), Mean Squared Error (MSE), and Mean Absolute Error (MAE). Ultimately, the best AI model was selected. Development of each model and their results is presented in the following sections.

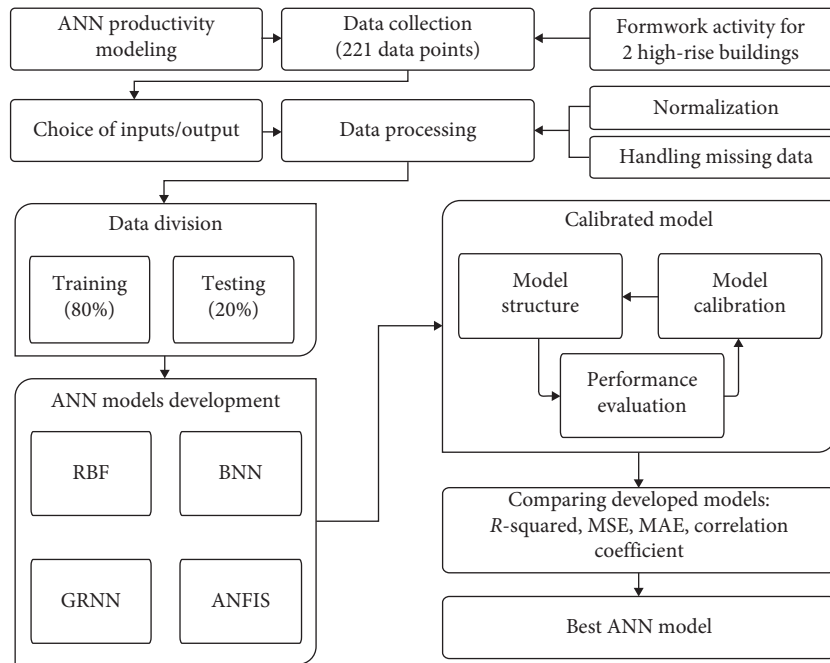


FIGURE 1: Overall flowchart of the study.

**2.1. Data Collection.** The dataset used for modeling labour productivity in this research was gathered by Khan [1] and collected from field observations and data collection from two high-rise buildings located in downtown Montreal over a period of eighteen months. The buildings were 17 and 16 floors. The first building is a concrete, mainly flat slab structure with Roller Compacted Concrete (RCC) construction and several typical levels with a surface of 68,000 m<sup>2</sup>. The project was constructed over three years. The second building also has a similar structure system and is a flat slab building. Two hundred and twenty-one data points were collected from both projects for formwork activity. The collected data was classified into three groups of weather, crew, and project. Data related to temperature, humidity, wind speed, and precipitation were classified into weather data while gang size and labour percentage as crew. Floor level, work type, and method were the parameters used in the project category. These variables were selected because they cause variations in productivity on a daily basis [1]. Data of nine factors classified into three major categories were available, as shown in Table 1, for performing the task.

These variables were chosen since they can cause differences in productivity on a daily basis or in the short-term. Short-term influence means that factors change value every day and do not have a cumulated or ripple effect impact on other activities. Thus, it is worthwhile to consider the abovementioned labour productivity factors for modeling labour productivity. Table 2 shows the descriptive statistics of the collected data which can provide a summary of the dataset.

The Pearson correlation coefficient is used to examine the strength and direction of a linear relationship between two variables in a database. A correlation coefficient ranges between  $-1$  and  $+1$ . A larger absolute coefficient value results in a stronger relationship between variables. In the case of a

TABLE 1: Labour productivity factors.

Weather	Crew	Project
Temperature (T)	Gang size (GS)	Work type (WT)
Humidity (H)	Labour percentage (LP)	Floor level (FL)
Wind speed (WS)		Work method (WM)
Precipitation (P)		

Temperature: based on an average of eight working hours a day (°C). Humidity: average humidity of eight working hours a day in percentage form. Precipitation: includes four numerical value terms assigned as: no precipitation = 0, light rain = 1, snow = 2, and rain = 3. Wind speed: average wind speed for eight working hours a day and included in the calculation in terms of km/h. Height: related to the floor being worked on and included in terms of the number of floors. Work type: three different types of formwork installation included as slabs = 1, walls = 2, and columns = 3. Work method: covers two techniques built in place (BIP) and flying forms (FF). BIP was coded as 1 and FF was coded as 2. Gang size: number of persons in a crew. Labour percentage: the ratio of labour to gang size obtained from the following equation:  $(\text{labour}\% = \text{labour size}/\text{gang size}) \times 100$ .

TABLE 2: Collected data descriptive statistics.

Variable	Mean	SE mean	Std. dev	Min.	Median	Max.
Temperature	4.08	0.81	12.03	-26	3	25
Humidity	66.34	1.05	15.67	18	67	97
Precipitation	0.28	0.04	0.6	0	0	3
Wind speed	15.42	0.57	8.46	3	14	43
Gang size	16.03	0.34	5.07	8	18	24
Labour percentage	35.49	0.26	3.79	29	36	47
Work type	1.43	0.03	0.51	1	1	3
Floor level	11.38	0.25	3.75	1	12	17
Work method	1.44	0.03	0.5	1	1	2
Productivity	1.57	0.02	0.35	0.82	1.51	2.53

Pearson correlation, an absolute value of 1 specifies a perfect linear relationship and a value of 0 indicates nonlinear relationship between variables. Table 3 shows that the

TABLE 3: Pearson correlation matrix for input and output parameters.

Variables	T	H	P	WS	GS	LP	WT	FL	WM	Productivity
T	1	0.151	-0.093	-0.122	0.390	-0.120	-0.122	0.358	0.078	0.589
H	0.151	1	0.338	0.026	-0.167	0.219	-0.110	0.048	0.176	0.090
P	-0.093	0.338	1	0.076	0.065	-0.063	-0.037	-0.288	-0.057	-0.175
WS	-0.122	0.026	0.076	1	-0.415	0.051	0.065	0.235	0.030	-0.202
GS	0.390	-0.167	0.065	-0.415	1	-0.310	-0.175	-0.352	-0.036	0.183
LP	-0.120	0.219	-0.063	0.051	-0.310	1	-0.135	0.142	0.177	-0.053
WT	-0.122	-0.110	-0.037	0.065	-0.175	-0.135	1	-0.052	-0.761	-0.353
FL	0.358	0.048	-0.288	0.235	-0.352	0.142	-0.052	1	0.225	0.301
WM	0.078	0.176	-0.057	0.030	-0.036	0.177	-0.761	0.225	1	0.328
Productivity	0.589	0.090	-0.175	-0.202	0.183	-0.053	-0.353	0.301	0.328	1

correlation between parameters most of the time is an approximate near 0. Consequently, none of the correlates very much and there is no over-estimation phenomenon. The Pearson  $p$ -values and  $R$ -squared prove the same the inputs and output behaviour.

**2.2. Backpropagation Productivity Modeling.** In this section, BNN was applied to model labour productivity. BNN is mostly used for unknown function approximation. As described in the literature review, a key BNN feature is its learning ability. It can be trained by historical datasets to find the accurate relation between inputs and outputs as well as predict the output(s) for new inputs. In this research, BNN models were developed, trained, validated, and tested in MATLAB 2017a with 221 data points. The dataset was randomly divided into 80% and 20% groups used for training and testing results, respectively. Several BNN models were developed which were different in three aspects: number of neurons in hidden layer varied between five and 100, random groups of datasets, and the number of hidden layers of one and two.

Bayesian Regularization (BR) algorithm was used for data training. BR is commonly used in noisy and small problems. The algorithms attempted to minimize the sum of the squared errors by updating the network's bias and weight. Training sets were used to adjust the network structure based on the associated errors until the best structure was reached. Validation sets were utilized to measure network generalization capabilities and to pause training when generalization stopped improvement. After training, testing sets provided an independent network performance index. For each BNN model, trials were performed to reach lowest error. Model performance was assessed based on  $R$ -squared and MSE developed through MATLAB coding according to the following equations, where " $t_i$ " is the target value while " $o_i$ " is the output value:

$$R^2 = 1 - \frac{\sum_i (t_i - o_i)^2}{\sum_i (t_i - (1/n)\sum_i t_i)^2}, \quad (1)$$

$$MSE = \frac{1}{n} \sum_i (t_i - o_i)^2. \quad (2)$$

$R$ -squared is often used in statistical analysis since it is easy to calculate and understand. It fluctuates between [0, 1]

and evaluates the percentage of total differences between estimated and target values with respect to the average. Several BNN models with different numbers of neurons and hidden layers were developed to find the best model for identifying labour productivity. The number of hidden layers varied between one and two and the models were trained by five, ten, . . . , 100 neurons. Considering the differences in the number of neurons and the hidden layer, 32 different models were developed and their results compared.

Figures 2 and 3 display the effect the number of neurons has on the  $R$ -squared for one and two hidden layers. As can be seen from Figure 2,  $R$ -squared values are mostly between 90 and 100% for the training phase and 70–90% for the testing phase. The model with one hidden layer and 50 neurons shows maximum accuracy. For the two hidden layers' models, the model with 20 neurons in each layer showed the best performance in predicting labour productivity.

Increasing the number of hidden layers resulted in better performance; however, this approach takes more computational time and does not change model accuracy in any significant way. In this research, the maximum number of neurons that could be considered in the ANN model was set at 60 due to the extreme computational time needed for what is an insignificant improvement to model accuracy. Figures 4 and 5 show that the MSE value was the smallest in the models with two hidden layers and 20 neurons and one hidden layer and 50 neurons.

It should be mentioned that no performance index was available during the validation phase while the given datasets were trained by the BR algorithm because the algorithm does not validate data and the datasets were randomly divided into trained and tested datasets only.

Model performances were assessed based on  $R^2$  and MSE, as summarized in Table 4 for one hidden layer and Table 5 for two hidden layers. As can be seen, the final model was the one with two hidden layers and 20 neurons, which showed the highest accuracy for identifying labour productivity. The model had MSE and  $R^2$  performance value indices of 0.0054 and 0.949, respectively. Therefore, this model was considered for comparison with the ANIFS model in the next sections.

The error histogram of the final model with two hidden layers and 20 neurons demonstrates that most of the errors oscillate between  $-0.55$  and  $0.75$  in all training and testing

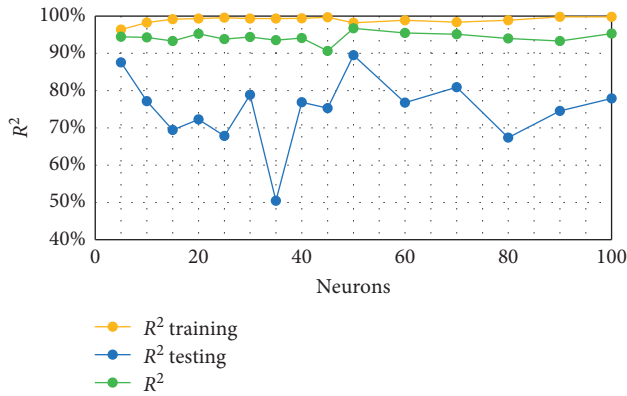


FIGURE 2:  $R^2$  values of ANN models using BP algorithm with 1 HL.

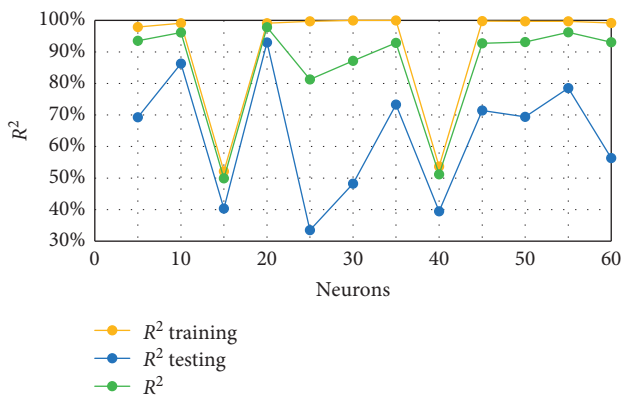


FIGURE 3:  $R^2$  values of ANN models using BP algorithm with 2 HL.

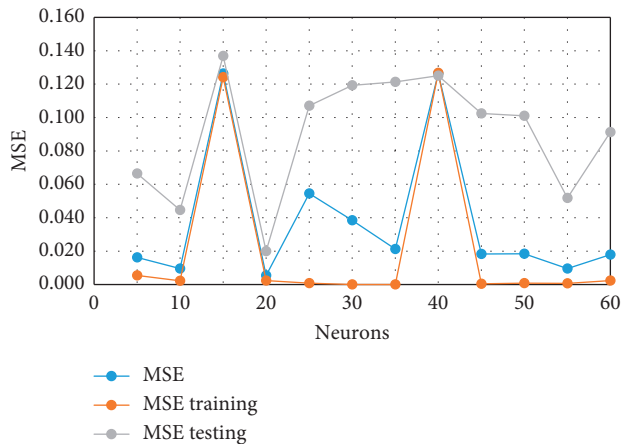


FIGURE 4: MSE values of ANN models in 1HL for distinct phases of ANN.

phases. The concentration of errors was 0.003, which is a small error for prediction. The  $R$ -squared in the selected model shows the fitted line for all data as output =  $0.97 \times$  target + 0.099 and an  $R^2$  value of 97.68% in the training dataset, demonstrating that the outputs are very close to target values. The  $R^2$  value for testing was 83.27%, proof that the model is able to predict 83% of future outcomes accurately. The applied method is able to rank predictor variables

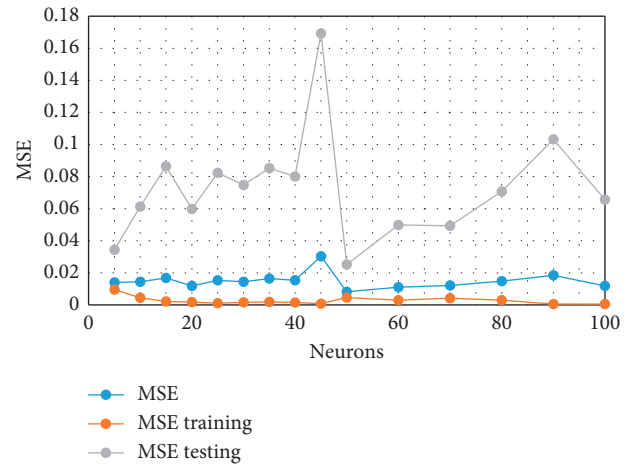


FIGURE 5: MSE values of ANN models in 2HL for different phases of ANN.

for the selected model as shown in Figure 6. The model shows that temperature and floor level are the most important factors in labour productivity.

**2.3. RBF Productivity Modeling.** RBF is a three-layer forward network applied for modeling science and engineering problems fast and precisely. RBF is a branch of ANN first introduced in the late eighties. RBFNN architecture is simple and includes one hidden layer and output. The RBF was selected to model labour productivity because of its feed-forward training done on a layer-by-layer basis in default of having input signals going through convoluted and time consuming multihidden layer developments. Thus, as compared to other ANN techniques, RBFNN is faster and has application flexibility [18].

Because of the abovementioned advantages, an effort was made in this research to model the nine predictor variables' convoluted relations and target based on actual datasets gathered from two high-rise buildings using RBFNN. The RBFNN model was trained using a BP algorithm to minimize MSE with selected predictor variables. The RBF neural network included three layers: input, hidden, and summation.

In this model, there is one neuron in the input layer for each predictor variable, where  $N$  is the number of categories and  $N-1$  the neurons used. Input neurons normalize a range of the values by subtracting the median and dividing it by an interquartile range. The input neurons feed the values to each of the neurons in the hidden layer. The hidden layer has a changing number of neurons (the optimal number is determined by the training process). Each neuron contains a radial basis function centered on a point with the dimensions equal to predictor variables. The radius of a RBF function is different for each dimension. Here, the training process determined the centers and spreads. A hidden neuron measured the Euclidean distance of the test case from the neuron's center point and then applied a RBF kernel function to this distance using the spread values when presented with the  $x$  vector of input values from the input

TABLE 4: Performance indices for models with one hidden layer.

Neurons	5	10	15	20	25	30	35	40	45	50	60
MSE	0.014	0.014	0.017	0.012	0.015	0.014	0.017	0.015	0.030	0.008	0.011
MSE train	0.010	0.004	0.002	0.002	0.001	0.002	0.002	0.002	0.001	0.005	0.003
MSE test	0.034	0.061	0.086	0.060	0.082	0.075	0.085	0.080	0.069	0.025	0.050
$R^2$	0.94	0.94	0.93	0.95	0.94	0.94	0.94	0.94	0.91	0.97	0.96
$R^2$ train	0.96	0.98	0.99	0.99	1	0.99	0.99	0.99	1	0.98	0.99
$R^2$ test	0.88	0.77	0.69	0.72	0.68	0.79	0.5	0.77	0.75	0.89	0.77

TABLE 5: Performance indices for models with two hidden layers.

Neurons	5	10	15	20	25	30	35	40	45	50	60
MSE	0.0162	0.0096	0.1264	<b>0.0215</b>	0.0545	0.0384	0.0212	0.1264	0.0183	0.0184	0.0096
MSE train	0.0055	0.0022	0.1242	<b>0.0200</b>	0.0008	0.0000	0.0000	0.1267	0.0005	0.0008	0.0007
MSE test	0.0665	0.0446	0.1369	<b>0.0230</b>	0.1071	0.1193	0.1213	0.1251	0.1024	0.1010	0.0518
$R^2$	0.935	0.942	0.499	<b>0.949</b>	0.813	0.872	0.929	0.512	0.927	0.932	0.962
$R^2$ train	0.979	0.981	0.522	<b>0.976</b>	0.997	1	1	0.537	0.998	0.997	0.997
$R^2$ test	0.693	0.693	0.403	<b>0.832</b>	0.335	0.482	0.733	0.395	0.714	0.694	0.785

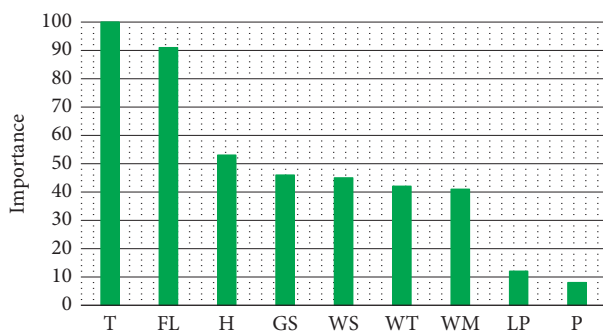


FIGURE 6: BNN model relative variable importance.

layer. The resulting value was handed to the summation layer. The coming out value of a neuron in the hidden layer was multiplied by a weight associated with the neuron ( $W_1, W_2, \dots, W_n$ ) and passed to the summation which added up the weighted values and presented this sum as the output of the network. A bias value of 1.0 was multiplied by a weight ( $W_0$ ) and fed into the summation layer. For classification reasons, there was one output along with a separate set of weights and summation unit for each target category. The output value of a category equaled to the probability that the evaluated case has that category.

In order to develop a reliable model, the dataset was randomly divided into two separate training and testing subsets. Eighty percent of the dataset was considered for network training and 20% of data was used for network reliability and to avoiding overfitting. It should be noted that RBF was developed using DTREG predictive modeling software. One of the key advantages of using DTREG for RBF development is that DTREG uses an evolutionary method called Repeating Weighted Boosting Search (RWBS) for building neural networks. In DTREG, a population of candidate neurons is first built with random centers and spreads which is limited by the minimum and maximum specified radius. The population size parameter controls how many candidate neurons are created. If there are many

variables, increasing the population size is recommended. Increasing the population size helps to prevent local minima and find the optimal global solution. In addition, DTREG lets the user modify the network and neuron parameters as well as the testing and validation percentage, select how to handle missing predictor variable values, and select one of four options for target categories' prior probabilities. Another interesting option available to the user is that the software can compute predictor variables' importance [19].

To train the DTREG algorithm, sequential orthogonal training developed by [20] was used. This algorithm uses an evolutionary approach to determine the optimal center points and spreads for each neuron. It also determines when to stop adding neurons to the network by monitoring the estimated Leave-One-Out (LOO) error and terminating when the LOO error begins to increase due to overfitting. Optimal weight computation between the neurons in the hidden layer and the summation layer was done using ridge regression. An iterative procedure was used to compute the optimal regularization Lambda parameter that minimizes generalized cross-validation (GCV) error [20]. During training, it was found that model errors can be reduced sufficiently to a lower level after incorporating 11 neurons and the model reached a steady state with 47 neurons. Thus, 47 neurons were used to model labour productivity. The RBF network with 47 neurons developed in this research has  $R$ -squared values of 0.91 and 0.67 for training and testing, respectively. Table 6 shows the developed model performance indicators. The RBF network algorithm ranked humidity, floor level, and temperature as the most important variables, as shown in Figure 7.

**2.4. GRNN Productivity Modeling.** GRNN, proposed by Donald F. Specht in 1990, is often used for nonlinear function approximation. It has a special linear and radial basis layer which makes it different from radial basis networks. GRNN is a neural network model that mimics nonlinear relations between a target variable and a set of

TABLE 6: Performances indices for RBF.

Performance index	$R^2$	MSE	RMSE	MAE
Training	91.30%	0.0103	0.1026	0.0756
Testing	85.84%	0.0471	0.1531	0.1421

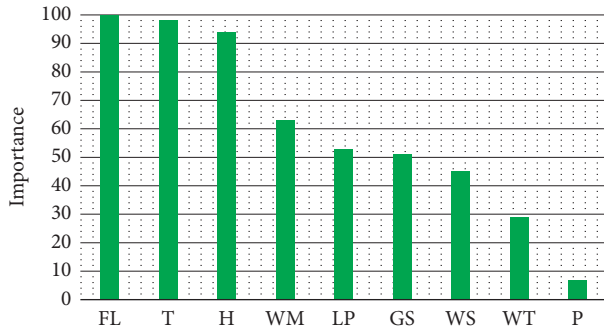


FIGURE 7: Relative importance of variables in the RBFNN model.

predictor variables. GRNN falls into the class of probabilistic neural networks and requires less training samples in comparison to a BNN. A GRNN's main advantage is that since available datasets for developing neural networks are not usually sufficient, probabilistic neural networks are more attractive for modeling. In other words, GRNN can solve any function approximation problem in case sufficient data is available in abbreviated time.

In GRNN, the target value of the predictor is achieved by considering the weighted average of the values of its neighbouring points. Target neighbour variable distance plays a key role in predicting target value. Neighbouring points close to target points have a greater impact on target value; distant points, on the other hand, are not influential as much as close neighbouring points. A radius base function is used for calculating the neighbouring point influence level. As mentioned, GRNN is able to build a model with a relatively small dataset and has the capability to handle outliers [21]. There are two main disadvantages associated with GRNN; it needs considerable calculations to evaluate new points and is not able to ignore unrelated inputs without assistance and needs major algorithm modifications. Consequently, this method is not a choice for problems with a substantial number of predictor variables. A GRNN algorithm can be enhanced by advancing GRNN in two ways: using clustering versions of GRNN and applying parallel calculations to take advantage of GRNN structure characteristics [22].

In addition to the abovementioned drawbacks, GRNN models can be large due to having one neuron for each training row. In the developed GRNN model, DTREG was utilized; thus, after the model was constructed, DTREG provided an option for facilitating the removal of unnecessary neurons from the model. By removing unnecessary neurons, computational time was reduced and it became possible to improve model accuracy. DTREG was utilized in order to select the best possible model. Three criteria available for guiding the removal of neurons are

minimizing error, minimizing the number of neurons, and limiting the number of neurons to a certain number.

The developed GRNN model's accuracy was compared with other models' using the same dataset. Therefore, 80% of the dataset was selected randomly as the training set, which corresponded to 177 input-output pairs. Twenty percent of the data were kept unused for testing, which corresponds to 44 input-output pairs. Note that all techniques used for modeling labour productivity in this study used the same training and testing datasets for a proper comparison approach.

In addition, a Gaussian kernel function type was selected as it is the best function among other kernel functions, and a single sigma for the whole model was selected to reduce computational time. Using a trial and error approach to select the best model, three models were developed based on three options provided by the software: remove unnecessary neurons, minimize error, and the constant number of neuron. Table 7 summarizes various statistical indices for the developed models.

The models with 34 and 10 neurons had overfitting in their training process since there was a large difference between the  $R^2$  in the training and testing phases. Therefore, the best GRNN model was found to have 107 nodes with the  $R^2$  value of 87.87%, which is higher than the two other approaches. Like the RBF neural network, GRNN is able to rank predictor variables for the selected model as shown in Figure 8. Here, temperature and floor levels were the significant factors found for modeling productivity.

**2.5. ANFIS Productivity Modeling.** ANFIS is used in various engineering fields such as environmental, civil, electrical, etc. [23–25]. ANFIS utilizes a hybrid learning algorithm which can model the relationship between predictor variables and respond variables based on expert knowledge by using neural network capabilities. It represents expert knowledge in the form of fuzzy “if-then” rules with an approximation of membership functions from given predictors and response datasets. Fuzzy logic handles the vagueness and uncertainty associated with the system being modeled, whereas the neural network provides model adaptability. By combining the learning abilities of a neural work with the reasoning capacities of fuzzy logic into a unified platform, ANFIS can be considered an enhanced prediction tool in comparison with a single methodology one. ANFIS can adjust membership function (MF) parameters and linguistic rules directly from neural network training capabilities with respect to refining model performance. ANFIS is able to capture expert knowledge regarding a nonlinear system and its behaviour in a qualitative model without quantitative descriptions of the system. Fuzzy inference system (FIS) is a knowledge interpretation technique based on the concept of fuzzy set theory, fuzzy “if-then” rules, and fuzzy reasoning, where each fuzzy rule characterizes a state of the system. ANFIS uses a Sugeno FIS for a structured approach to generate fuzzy rules by using a given dataset [26]. Training and testing data are matrices with ten columns where the

TABLE 7: Performances indices for GRNN.

Performance index	Number of neuron	$R^2$ train (%)	$R^2$ test (%)	MSE train	MSE test	RMSE train	RMSE test	MAE train	MAE test
Minimize error	107	87.87	75.32	0.0103	0.0475	0.1108	0.2219	0.0651	0.1421
Minimize number of neurons	34	85.84	48.70	0.0172	0.0716	0.1311	0.2676	0.0984	0.1785
Number of neurons	10	64.82	41.07	0.0427	0.0823	0.2067	0.2868	0.1471	0.2164

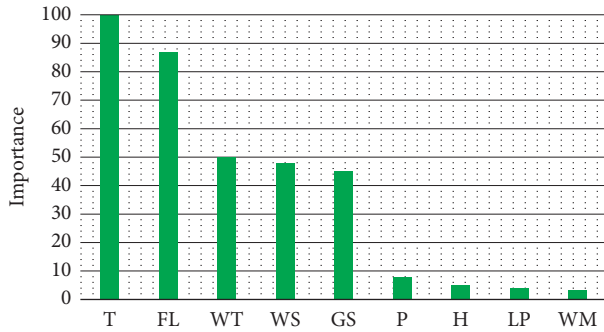


FIGURE 8: Relative importance of variables in the selected GRNN model.

first nine columns contain data for each FIS predictor variable and the last column contains the response data. It should be noted that the same 177 data points were used for training and the other 44 for testing purposes. Then, the FIS model structure was generated by choosing the subtractive clustering technique. Subtractive clustering technique is faster than grid partitioning and with a satisfactory result for justifying use. Based on the selected parameters of subtractive clustering, 63 clusters were detected as the most suitable MF number. Here, the number of clusters and MFs were equal. The hybrid method was selected for training the MF because it generates better results rather than BP. The hybrid method includes BP and least squares for MF parameter estimation, BP for estimating input MF parameters, and least square for MF parameters. ANFIS parameters were selected to reach higher accuracy with less computational time, as shown in Table 8.

Figure 9 shows the predicted daily productivity against corresponding actual values, and Table 9 summarizes the dataset various statistical indices using the developed ANFIS model.

ANFIS is also able to rank predictor variables for the selected model as shown in Figure 10. Temperature and floor level are the important factors in modeling productivity. Table 10 summarizes the performance indices of  $R^2$  Train,  $R^2$  Test, MSE Train, and MSE Test for the four models. BNN shows the highest  $R$ -squared in the training phase followed by RBF, ANFIS, and GRNN. Moreover, BNN shows the highest  $R$ -squared in testing phases followed by RBF, ANFIS, and GRNN. GRNN is the least accurate technique among all the techniques for the given dataset in both training and testing phases. BNN has the lowest MSE of the techniques in the training phase followed by RBF. ANFIS and BNN show the lowest MSE in the testing phase followed by RBF and GRNN.

TABLE 8: ANFIS parameters for modeling labour productivity.

ANFIS parameters	
Number of input variables	9
Training data points	177
Testing data points	44
Number of layers	5
Operator	Subtractive
Number of membership functions (MF)	63
MF type	Bell shape
Transfer function of output layer	Linear
Training algorithm	Hybrid
Error tolerance	0
Number of epochs	1000

To recognize which algorithm is the best method to be utilized in modeling construction labour productivity, analysis of variance (ANOVA) was applied to demonstrate the significant superiority of the BNN algorithm over other algorithms, which had the lowest  $F$ -Value.

Furthermore, the results of the model were compared with the SOM model developed by [9] and results show that for formwork productivity prediction, BNN performs better in comparison to SOM. The correlation of coefficient and the MSE for the available database were 94.9% and 0.0215 for backpropagation method while it was 89.25% and 0.07 for SOM.

Both regression and AI techniques have merits and demerits. Three statistical methods, namely, best subset, stepwise, and Evolutionary Polynomial Regression (EPR), were applied to the available database, and the coefficient of correlation and MSE were calculated and are presented in Table 11. EPR predicted the data better than best subset and stepwise. However, BNN outperformed and achieved a better fit and forecast with the given dataset than the regression models due to the nonlinearity of the dataset in modeling labour productivity for formwork. The statistical performance of those models is far behind BNN. The analysis of variance for different techniques is presented in Table 12.

### 3. Conclusions

One of the major strategic components in determining the success or failure of a construction project is the productivity rate, which has a relationship with different factors. This paper attempts to demonstrate a way to use AI models to predict labour productivity. These are effective tools for quantifying loss of productivity and can be used as a support method for actual loss of productivity calculations. GRNN, BNN, RBFNN, and ANFIS were tested against Khan's

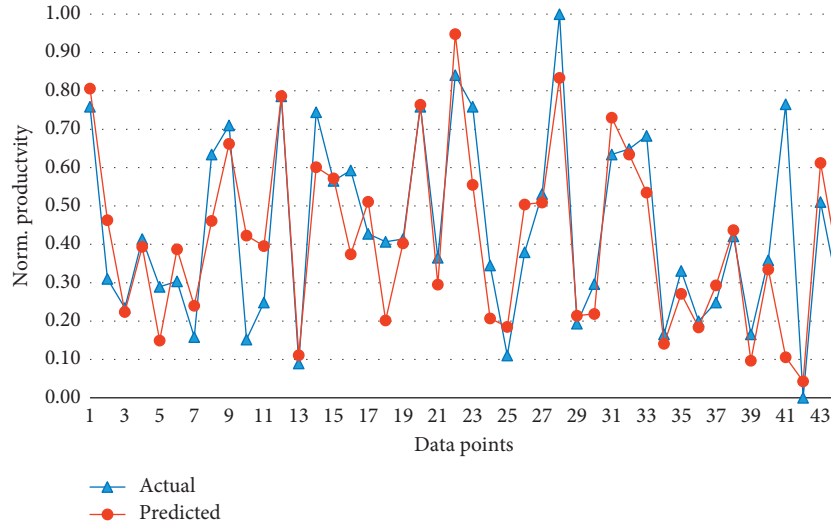


FIGURE 9: Actual vs predicted value using ANFIS.

TABLE 9: Statistical indicators of the developed ANFIS model.

Performance index	$R$ (%)	$R^2$ train (%)	$R^2$ test (%)	MSE train	MSE test	RMSE train	RMSE test	MAE train	MAE test
Value	81.1	89.3	66.2	0.01	0.02	0.114	0.146	0.017	0.097

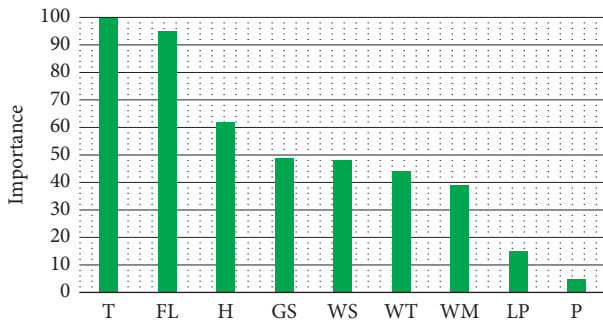


FIGURE 10: Relative importance of variables in ANFIS Model.

TABLE 10: Performance results comparison.

	$R^2$ train	$R^2$ test	MSE train	MSE test
BNN	0.98	0.83	0.0023	0.020
RBF	0.91	0.85	0.0096	0.018
GRNN	0.88	0.75	0.0103	0.047
ANFIS	0.89	0.66	0.0100	0.020

TABLE 11: Statistical performance of the regression methods.

Technique	$R^2$	MSE	Time (sec)	Number of variables
Best subset	46.8	0.259	~2	8
Stepwise	48.61	0.259	~2	7
EPR	52.69	0.057	1140	8

datasets of two high-rise buildings related to formwork operation. From the comparisons, BNN showed the best performance among the techniques. However, BNN can be considered a black box approach and is prone to overfitting, which can be the result of network architecture

TABLE 12: Analysis of variance for different techniques.

	Source	DF	Adj. SS	Adj. MS	$F$ -value	$P$ -value
BNN	Actual	37	2.14235	0.05790	4.42	0.034
	Error	6	0.07864	0.01311		
	Total	42	2.22099			
ANFIS	Actual	36	5.69202	0.15811	15.53	0.001
	Error	6	0.06108	0.01018		
	Total	42	5.75310			
RBF	Actual	34	3.4887	0.10261	6.67	0.004
	Error	8	0.1231	0.01539		
	Total	42	3.6118			
GRNN	Actual	37	5.59931	0.151333	31.89	0.002
	Error	4	0.01898	0.004745		
	Total	42	5.61829			

(i.e., decreasing the number of nodes), early training phase stopping, or weight decay use. Furthermore, the dataset used to develop the aforementioned models was a raw and unbalanced dataset. Studying the behaviour of the given datasets prior to feeding it to any AI techniques is required in order to have a robust model for modeling labour productivity.

Researchers have proved that supervised BNN models are more successful in predicting construction crew productivity in comparison to statistical methods like regression. Furthermore, if the causal relationship between input and output has a complex variability in areas other than construction, in most cases, the learning task is easier with unsupervised learning. Therefore, this study focuses on the application of supervised methods in formwork crew productivity data to compare the predicted results. This study focused on formwork installation operations since

they constitute a substantial part of the overall labour component of concrete framing in building construction. Results reveal that BNN shows superior performance in comparison to RFBNN, ANFIS, and GRNN for formwork productivity prediction in the following ways:

- (1) Selected input variables are those that cause variations in productivity in the short-term or daily basis. The developed models were compared based on statistical performances and BNN outperformed the techniques of RBF, ANFIS, and GRNN. The developed model of this research can be utilized in different ways.
- (2) The model can help to estimate formwork productivity by considering variables such as temperature, humidity, gang size, labour percentages, work type, etc. In addition, this study also found that productivity is not significantly correlated with precipitation, labour percentage, work method, and humidity. Within the scope of the conducted study, the number of parameters observed, and the range of their values, this study found temperature to have the most significant impact on productivity followed by floor level.
- (3) The model can also be useful for quantifying loss of productivity by considering the output of the developed model as the value for unimpacted productivity period since the identifying unimpacted period for quantifying loss of productivity is impossible to calculate sometimes. Therefore, BNN can help save time and cost associated with quantifying loss of productivity.

Ultimately, this study shows that the backpropagation model can be an alternative tool to supervised learning-based tools and can be used in various prediction applications. One limitation of this study is that the findings are limited to the collected data range and parameters considered in the study. It should be noted that the developed model does not involve any parameters that directly account for management strategies and skills or any project-specific conditions.

## Data Availability

The data used to support the findings of this study are available from the corresponding author upon request.

## Conflicts of Interest

The authors declare that they have no conflicts of interest.

## References

- [1] Z. U. Khan, "Modeling and parameter ranking of construction labor productivity," Doctoral Dissertation, Concordia University, Montreal, Canada, 2005.
- [2] W. Yi and A. P. C. Chan, "Critical review of labor productivity research in construction journals," *Journal of Management in Engineering*, vol. 30, no. 20, pp. 214–225, 2014.
- [3] M. Lu, S. M. AbouRizk, and U. H. Hermann, "Estimating labor productivity using probability inference neural network," *Journal of Computing in Civil Engineering*, vol. 14, no. 4, pp. 241–248, 2000.
- [4] S. AbouRizk, P. Knowles, and U. R. Hermann, "Estimating labor production rates for industrial construction activities," *Journal of Construction Engineering and Management*, vol. 127, no. 6, pp. 502–511, 2001.
- [5] O. Moselhi, I. Assem, and K. El-Rayes, "Change orders impact on labor productivity," *Journal of Construction Engineering and Management*, vol. 131, no. 3, pp. 354–359, 2005.
- [6] A. S. Ezeldin and L. M. Sharara, "Neural networks for estimating the productivity of concreting activities," *Journal of Construction Engineering and Management*, vol. 132, no. 6, pp. 650–656, 2006.
- [7] S. C. Ok and S. K. Sinha, "Construction equipment productivity estimation using artificial neural network model," *Construction Management and Economics*, vol. 24, no. 10, pp. 1029–1044, 2006.
- [8] L. Song and S. M. AbouRizk, "Measuring and modeling labor productivity using historical data," *Journal of Construction Engineering and Management*, vol. 134, no. 10, pp. 786–794, 2008.
- [9] E. L. Oral and M. Oral, "Predicting construction crew productivity by using self organizing maps," *Automation in Construction*, vol. 19, pp. 791–797, 2010.
- [10] S. Muqem, M. Idrus, and F. Khamidi, "Construction labor production rates modeling using artificial neural network," *Journal of Information Technology in Construction*, vol. 16, pp. 713–725, 2011.
- [11] S. Mohammed and A. Tofan, "Neural networks for estimating the ceramic productivity of walls," *Journal of Engineering*, vol. 17, no. 2, pp. 200–217, 2011.
- [12] F. M. S. AL-Zwainy, H. A. Rasheed, and H. F. Ibraheem, "Development of the construction productivity Estimation model using artificial neural network for finishing works for floors with marble," *ARNP Journal of Engineering and Applied Sciences*, vol. 7, no. 6, pp. 714–722, 2012.
- [13] O. Moselhi and Z. Khan, "Significance ranking of parameters impacting construction labour productivity," *Construction Innovation*, vol. 12, no. 3, pp. 272–296, 2012.
- [14] G. Heravi and E. Eslamdoost, "Applying artificial neural networks for measuring and predicting construction-labor productivity," *Journal of Construction Engineering and Management*, vol. 141, no. 10, article 04015032, 2015.
- [15] G. Aswed, "Productivity estimation model for bricklayer in construction projects using neural network," *Al-Qadisiyah Journal for Engineering Sciences*, vol. 9, no. 2, pp. 183–199, 2016.
- [16] K. M. El-Gohary, R. F. Aziz, and H. A. Abdel-Khalek, "Engineering approach using ANN to improve and predict construction labor productivity under different influences," *Journal of Construction Engineering and Management*, vol. 143, no. 8, article 04017045, 2017.
- [17] O. Moselhi, T. Hegazy, and P. Fazio, "Neural networks as tools in construction," *Journal of Construction Engineering and Management*, vol. 117, no. 4, pp. 606–625, 1991.
- [18] M. T. Musavi, W. Ahmed, K. H. Chan, K. B. Faris, and D. M. Hummels, "On the training of radial basis function classifiers," *Neural Networks*, vol. 5, no. 4, pp. 595–603, 1992.
- [19] P. Sherrod, "DTREG predictive modeling software," 2018, <http://www.dtreg.com>.
- [20] S. Chen, X. Hong, and C. J. Harris, *Orthogonal Forward Selection for Constructing the Radial Basis Function Network*

*with Tunable Nodes, in Lecture Notes in Computer Science, Vol. 3644, 2005.*

- [21] H.-I. Yip, H. Fan, and Y.-h. Chiang, "Predicting the maintenance cost of construction equipment: comparison between general regression neural network and Box-Jenkins time series models," *Automation in Construction*, vol. 38, pp. 30–38, 2014.
- [22] D. F. Specht, "Probabilistic neural networks," *Neural Networks*, vol. 3, no. 1, pp. 109–118, 1990.
- [23] H. Alasha'ary, B. Moghtaderi, A. Page, and H. Sugo, "A neuro-fuzzy model for prediction of the indoor temperature in typical Australian residential buildings," *Energy and Buildings*, vol. 41, no. 7, pp. 703–710, 2009.
- [24] A. Subasi, A. S. Yilmaz, and H. Binici, "Prediction of early heat of hydration of plain and blended cements using neuro-fuzzy modelling techniques," *Expert Systems with Applications*, vol. 36, no. 3, pp. 4940–4950, 2009.
- [25] L.-C. Ying and M.-C. Pan, "Using adaptive network based fuzzy inference system to forecast regional electricity loads," *Energy Conversion and Management*, vol. 49, no. 2, pp. 205–211, 2008.
- [26] M. Negnevitsky, *ANFIS: Adaptive Neruo-Fuzzy Inference System, Artificial Intelligence-A Guide to Intelligent Systems*, Pearson Education Limited, Essex, UK, 2nd edition, 2005.

## Research Article

# Optimization of Headways and Departure Times in Urban Bus Networks: A Case Study of Çorlu, Turkey

Huseyin Ceylan <sup>1</sup> and Tayfun Ozcan <sup>2</sup>

<sup>1</sup>Civil Engineering Department, Faculty of Engineering, Pamukkale University, Denizli 20160, Turkey

<sup>2</sup>Department of Construction Technologies, Yatağan Vocational School, Muğla Sıtkı Koçman University, Muğla 48500, Turkey

Correspondence should be addressed to Huseyin Ceylan; [hceylan@pau.edu.tr](mailto:hceylan@pau.edu.tr)

Received 4 October 2018; Accepted 25 November 2018; Published 27 December 2018

Guest Editor: Tayfun Dede

Copyright © 2018 Huseyin Ceylan and Tayfun Ozcan. This is an open access article distributed under the Creative Commons Attribution License, which permits unrestricted use, distribution, and reproduction in any medium, provided the original work is properly cited.

The traffic congestion, which has become one of the major problems of developed and developing countries, has led to a shift in the way public transport systems are viewed, and it has accelerated efforts to increase the efficiency of these systems. In recent studies, several approaches, in which both user and operator benefits are evaluated together in order to increase the demand for public transportation systems and to ensure the sustainability of these systems, are emphasized. In this study, a bilevel simulation/optimization model is developed to optimize service headways and departure times of first buses from the beginning of the routes in urban bus networks. At the upper level of the proposed model, a multiobjective function representing user and operator costs is evaluated using the metaheuristic harmony search (HS) optimization technique. The transit assignment problem, which represents the distribution of transit users over the routes, is handled at the lower level. In the proposed model, the transit assignment problem is solved by the timetable-based assignment approach with VISUM transport planning software. The timetable-based transit assignment is an approach in which the perception errors within the users' route choice are taken into consideration and the transfer wait times can be precisely calculated. The proposed model is applied to a real-life urban bus network of the Çorlu district (Tekirdağ, Turkey), and the effectiveness of the model on a medium-sized urban bus system has been demonstrated. The results show that the user and operator benefits can be simultaneously increased by adding an initial departure offset parameter to the problem.

## 1. Introduction

Traffic congestion due to increasing demand for private car use brings health and environmental problems, as well as imposes a heavy burden on the economies of developing and developed countries. Along with the increase in fuel consumption of motor vehicles in the heavy traffic, the harmful gases threaten human health by polluting the environment and trigger global warming by increasing the effect of greenhouse gases [1]. Behrens and Egenhofer [2] state that the transportation sector is responsible for a quarter of all greenhouse gas emissions in European countries. Therefore, it is important to organize public transportation systems which can be alternative to private cars in terms of safety, reliability, comfort, and economy criteria in order to avoid environmental and health problems and to minimize the amount of energy required in the transport sector. Central

and local governments trying to reduce traffic congestion by making public transportation services more attractive are investing in public transport systems in the direction of short- and long-term strategies as well as even taking measures to limit individual car sales [3]. However, public transportation systems, which are the most important solution to the traffic congestion, cannot meet the increasing travel demand due to poor planning, design, and management. In studies evaluating the performance of public transportation systems, it is revealed that the primary problem related to the transit services in developing countries is the lack of capacity during peak hours [4–6]. This problem can be solved by increasing the fleet size and service frequency during peak hours, which leads to an increase in operating costs that reduces the operator profit margins. However, in order to ensure the sustainability of transit services, not only the users' expectations but also the

operator's expectations must be met. In public transportation, operators aim to achieve a certain profitability by considering their limited budgets and available bus fleets, while users generally expect a combination of high service quality and minimum travel time. At this point, service quality can be considered as a function of comfort level and reliability, while travel time consists of in-vehicle time, waiting time, and transfer time. Therefore, the trade-off between user and operator objectives should carefully be considered in public transport planning. Considering that the conventional public transportation planning process includes route design, timetable preparation based on the available fleet of buses, and crew scheduling steps, accurately determined that frequencies of bus lines play an important role in this process. Oudheusden and Zhu [7] state that poorly prepared timetables lead to an overloading of buses. On the contrary, accurate timetables, which are determined based on optimized frequencies, may reduce operating costs and increase user benefits. In the relevant literature, several studies concerning the optimization of service frequencies in public transportation networks have focused on the transit network design problem (TNDP) [8–20]. In the TNDP, which is generally formulated as the minimization of the sum of user and operator costs, the optimal transit routes and associated frequencies are sought. On the contrary, there are few studies that deal with the service frequencies for fixed bus route configurations [7, 21, 22].

Baaj and Mahmassani [11] developed a Transit Routes Analyst (TRUST) program in order to solve the TNDP. In their study, the TNDP was formulated as the minimization of an overall cost measure including operator costs and user costs. The former was considered as total trip time of all services during the analysis period. On the contrary, user costs were taken into consideration as the total travel time for all transit users, which requires the assignment of the origin-destination (O-D) matrix to the transit routes. At this point, a lexicographic strategy, which was previously presented by Han and Wilson [23], was adopted in TRUST. In this strategy, it was assumed that the users avoid transfers when choosing their routes among competing ones between their origins and destinations. From this point of view, the number of transfers and trip times incurred on different alternative choices were evaluated during the assignment process. In this context, all travel demands were assigned to the route with the least number of transfers, while a “frequency share” rule, which was developed by Lampkin and Saalmans [8], was applied if there is at least one alternative whose trip time is within a threshold of the minimum trip time. In TRUST, total travel time of a journey with one transfer was calculated as the sum of waiting times for buses in the first and second routes, in-vehicle travel times, and a fixed transfer penalty. Note that the waiting time for a bus route was assumed to be half of the headway on the route, while the transfer penalty was 5 minutes of equivalent in-vehicle travel time. In another study by Baaj and Mahmassani [12], in which a route generation algorithm (RGA) was developed based on the framework of artificial intelligence/operations research hybrid solution approach, was also built on TRUST and its assumptions on transit

assignment problem. Chakroborty and Dwivedi [13] developed a genetic algorithm- (GA-) based solution technique to the solution of the TNDP. In the study, it was stated that, unlike previous studies concerning the route network design, an optimization tool was primarily used to minimize the reliance on heuristics. At the end of the study, a brief comparison with the results of the study by Mandl [9] and Baaj and Mahmassani [24] was provided to show the effectiveness of the proposed methodology. Szeto and Wu [14] proposed a hybrid solution method, in which GA was employed for the solution of the route design problem, while a neighbourhood search heuristic was used to search for the optimal set of frequencies. In the study, the average travel time was calculated based on the assumptions of the transit assignment in the study of Baaj and Mahmassani [11], and the proposed method was applied to the Tin Shui Wai (Hong Kong) bus network. The results showed that the total travel time could be reduced up to 23% in comparison with the current status of the Tin Shui Wai bus network. Nikolic and Teodorovic [15] solved the TNDP using the bee colony optimization (BCO) algorithm. In the study, three objective functions, which are total travel time, unsatisfied demand, and total number of buses required to meet the demand, were minimized. The transit assignment problem was solved based on the frequency share method, and the obtained results were compared with the previous models concerning the TNDP. Unlike the abovementioned studies, some researchers considered different assignment approaches. Mumford [16] assumed that the transit demand assigned to the routes with the shortest travel times and total travel time includes a constant transfer penalty and in-vehicle travel time. In the study, waiting times of users were ignored. Additionally, vehicle frequencies were not considered, and it was assumed that there were sufficient buses when solving the TNDP. Afandizadeh et al. [17] developed a GA-based model which is capable of optimizing bus assignment at depots. In the study, TNDP was formulated as a combination of user and operator costs. User costs were represented by the combination of total travel time and unsatisfied demand cost, while the operator cost included empty seat costs, dead-head trip costs, and total travel time cost. The transit assignment problem was solved based on the logit route choice model, in which waiting time was assumed to be half of the headway on the corresponding bus route. In a more recent study, Owais and Osman [18] employed GAs for the solution of the TNDP. Recently, Buba and Lee [19] applied the differential evolution approach to the solution of TNDP. In the study, the sum of total travel time and unmet demand is minimized. Ruano-Daza et al. [20] developed a global-best harmony search-based solution method for TNDP. The proposed model is applied to a real bus rapid transit system to minimize total network travel time and waste bus capacities simultaneously. Although the conventional TNDP has been considered as design of routes and setting of frequencies on a transit system, some researchers have handled the TNDP within the frequency setting, namely, the “bus scheduling” perspective. Kidwai et al. [21] presented a two-level method for vehicle scheduling. In the first level of the model, minimum service

frequencies were determined regarding the load feasibility constraint. On the contrary, the required fleet size was minimized using GA in the second level. In the study, the transit assignment problem was solved based on the procedure presented by Baaj and Mahmassani [11]. Ruisanchez et al. [22] developed a bilevel solution method for optimal bus sizes and frequencies in urban transit networks. At the upper level, a cost function representing the costs of users and operators was minimized. In the study, user cost function was formulated as a weighted sum of total transfer time, total access time, total in-vehicle time, and total waiting time. On the contrary, the transit assignment problem was solved using ESTRAUS™ traffic simulation software.

As can be seen from the literature review, the TNDP has been formulated as either both route design and frequency setting or only frequency setting in urban transit networks. Additionally, the frequency share method has widely been accepted for the solution of the transit assignment problem. It may be a reasonable approach to distribute the demand regarding the service frequencies. However, considering the exact waiting time at the origin, a transfer point may provide more realistic results instead of considering it as half of the headway since the passengers have better knowledge owing to the intelligent transportation systems and mobile applications nowadays. Doğan and Özuysal [25] state that excess waiting times in urban bus systems may lead to a change in transit users' route choice. Another widely accepted approach is the assumption of users' choice of routes with the shortest travel time. However, some users may choose some routes with longer travel times considering the level of service (i.e., comfort level and route environment), daily habits, or incomplete information. Therefore, it may be more appropriate to take the stochastic nature of users' route choice behaviour into consideration.

In this study, a bilevel simulation/optimization method is proposed to determine headways on bus routes and departure times of first buses from the beginning of the routes in urban bus networks. At the upper level, a multiobjective function representing the weighted sum of user and operator costs is minimized, while the transit assignment problem is solved using VISUM® transportation planning software at the lower level. Since headway and offset variables are integers, the TNDP is formulated as the integer programming problem, and the harmony search (HS) optimization algorithm is used for the solution. One of the novelties of our approach is the use of timetable-based assignment in which the actual transfer wait times, and the coordination of the timetable is taken into account. Moreover, by adding the offset parameter, which represents the departure time relationship between bus operations, effects of the coordination between bus operations are investigated.

Headway and departure offset optimization problem and related notations are given in the next section. Subsequently, the proposed model and the implementation of the HS algorithm are provided in Section 3. Section 4 presents some numerical applications on a medium-sized real bus network. Results and future directions are presented in the last section.

## 2. Problem Formulation

Effects of headways and departure times on transfer waiting time and total travel time are illustrated in Figure 1.

As can be seen from Figure 1(a), a user, who travels from the origin to destination, can directly complete his travel on Bus Line 1 (BL1). However, he may transfer to Bus Line 2 (BL2) at Stop Point (SP) to reach the destination. It can be seen in Figure 1(b) that the average speed of BL2 is higher than that of BL1. Thus, a user that boards on BL1 at 06:00 can arrive to the destination at 06:40 if he transfers to BL2 at SP; otherwise, he arrives at 06:55 via BL1. Therefore, it may be possible to reduce total travel time by transferring a faster transit line with a reasonable transfer waiting time, and each travel alternative can be called a "connection" [26]. At the second departure of BL1, there is not any transfer possibility. Thus, there is only one connection for a user who boards on BL1 at 06:55. Changes on headways and departure times of transit routes may lead to new connection alternatives or loss of some connections. Reducing headways of BL1 and BL2 provide shorter travel times for transit users. However, this leads to an undesirable situation from the operator's perspective due to the increasing fleet requirement and operational costs. Therefore, investigating the trade-off between user and operator costs is an important issue. In this section, a multiobjective optimization problem, which takes this issue into account, is proposed.

Considering the user and operator costs, the proposed optimization problem is formulated as a biobjective minimization problem as given in the following equations:

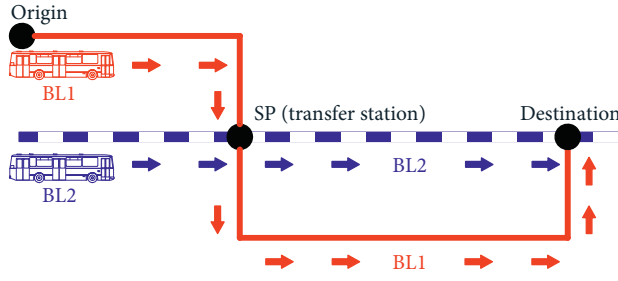
$$\begin{aligned} \min \quad Z = & D_1 \sum_{i \in O} \sum_{j \in V} \sum_{k \in G} (\text{OWT}_k^{ij} + \text{IVT}_k^{ij} + \text{TWT}_k^{ij}) \\ & + D_2 \sum_{i \in N} \left( \text{int} \left( \frac{T - \theta_i}{h_i} \right) l_i \right) + \sum_{i \in N} P_i, \end{aligned} \quad (1)$$

$$\text{subject to } h_{\min} \leq h_i \leq h_{\max}, \quad (2)$$

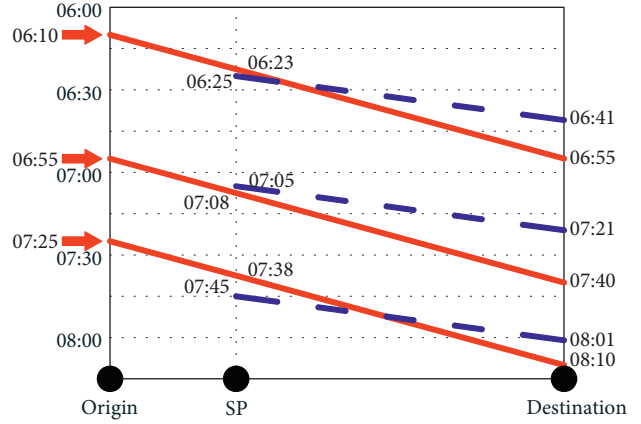
$$0 \leq \theta_i \leq h_i - 1, \quad (3)$$

$$\sum_{i \in N} \text{int} \left[ \frac{t_i}{h_i} \right] + 1 \leq W. \quad (4)$$

The objective of the proposed problem is to minimize the weighted sum of the total passengers' travel time (including in-vehicle travel time and transfer wait time), total service kilometres (service km) covered by transit vehicles and a penalty term. Herein, Constraint (2) ensures that the headways on each transit route should satisfy prespecified minimum and maximum allowable values. Constraint (3) ensures that the offset of the first departure on a particular route must be less than the departure headway on the same route. Constraint (4) ensures that the required fleet size cannot exceed the available fleet size. The third term on the right side in equation (1) represents a penalty value arising from the capacity violation on routes and it is formulated as follows:



(a)



(b)

FIGURE 1: An example of (a) bus network and (b) graphical timetable.

$$P_i = \begin{cases} \phi(u_i - x_{i,\max}), & \text{if } x_{i,\max} > u_i, \\ 0, & \text{otherwise.} \end{cases} \quad (5)$$

In order to calculate in-vehicle travel time, transfer wait time, and the penalty term, which is a function of maximum passenger loads on bus routes, in the objective function given in equations (1)–(4), distribution of passengers on the transit network must be calculated, which refers to the solution of the transit assignment problem. The general assumption is that transit users choose the route with the shortest travel time between O-D pairs. However, in reality, some routes with longer travel times may be chosen by some users based on their level of service expectations, daily habits, or by incomplete information. Furthermore, some travels with one transfer between a certain O-D pair may take a shorter time than a travel with a zero transfer (or direct) transit route serving between the same O-D pair. Therefore, it may be useful to employ an approach which is closer to reality than the lexicographic strategy represented by Han and Wilson [23]. In this study, the transit assignment problem is solved based on the timetable-based assignment approach of the VISUM transportation planning tool. This approach is similar to the stochastic traffic assignment that a small part of the travel demand is assigned to suboptimal routes based on the route choice model [26]. The timetable-based assignment consists of two parts. Possible connections are investigated using the branch-and-bound algorithm at the first stage, while the passenger assignment is carried out based on a connection choice model at the second stage. The major advantages of using a timetable-based assignment are that the coordination of the timetable is taken into account by calculating the actual transfer wait times, and actual decision of the passengers can be represented realistically. Furthermore, by creating a root function, passengers can be assumed to have better knowledge of timetables. Thus, a more factual origin wait time, which has widely been taken into account as half of the mean headway in previous research, can be determined. After completing the connection search process (see [26] for details), the passenger assignment can be carried out as explained below:

The number of passengers using each bus route can be calculated based on the following equation:

$$x_i = \sum_{i \in O} \sum_{j \in D} \sum_{k \in G} q^{ij} R_k^{ij} \delta_{ik}. \quad (6)$$

Choice probability of connection  $k$  between origin  $i$  and destination  $j$  can be calculated based on the following equation:

$$R_k^{ij} = \frac{B_k^{ij-\beta}}{\sum_{k \in G} B_k^{ij-\beta}}. \quad (7)$$

Impedance of connection  $k$  in a time interval  $a$  is calculated as follows:

$$B_k^a = \text{OWT}_k^{ij} + \text{IVT}_k^{ij} + \text{TWT}_k^{ij} + \gamma v_k^{ij}. \quad (8)$$

### 3. Model Development

In this study, a bilevel solution model is developed for optimizing timetables in urban bus networks considering the interaction between users and operators. In the last decades, several optimization algorithms have been developed to deal with complex engineering optimization problems. Among these algorithms, genetic algorithms, simulated annealing, particle swarm optimization, ant colony optimization, and harmony search are the most popular optimization techniques [27]. In this context, the proposed model is formulated within the solution framework of the metaheuristic HS optimization technique, which has been developed by Geem et al. [28] and has widely been used to the solution of complex civil engineering optimization problems [29–35]. The HS algorithm inspires from a spontaneous performance of a musical group. In an orchestra, each musician seeks for a note that leads to the most pleasing harmony when playing together. Similarly, particular values of decision variables, which lead the objective function to reach the global optimum solution, are sought in an optimization process. According to the basic assumption

of the HS technique, a musician can improvise a note in three different ways, which are as follows:

- (i) Playing a completely random note
- (ii) Reselecting any note that he has taken in his memory by playing so far
- (iii) Selecting a note from the neighbour of a note that he has played so far

Similarly, the value of a decision variable can be determined in three ways, which are as follows:

- (i) Selecting a value chosen randomly from the possible upper and lower bounds
- (ii) Selecting a value from harmony memory
- (iii) Assigning a value in a specific neighbourhood to a value selected from harmony memory

As can be seen above, while an orchestra improvises new harmonies during a musical performance, the HS algorithm generates new solution vectors during the optimization process. In this context, the general layout of the proposed HS-based model is illustrated in Figure 2.

It can be seen in Figure 2 that the solution of the bi-objective optimization problem is carried out at the upper level, while the transit assignment problem is solved at the lower level of the proposed bilevel model. The solution

procedure of the HS-based model consists of five steps, and its stepwise flowchart is given in Figure 3.

As can be seen in Figure 3, travel demand between O-D pairs, transit network characteristics (i.e., bus routes and travel speeds), fleet characteristics (i.e., size and bus capacities), HS algorithm parameters, and a stopping criterion are presented at Step 1. There are three HS parameters governing the performance of the algorithm. The first one is harmony memory size (HMS) that represents the number of solution vectors in harmony memory (HM). Secondly, harmony memory consideration rate (HMCR) determines the probability of considering the available solutions in the HM while generating a new solution vector. The third parameter is pitch adjustment rate (PAR), which is used when the harmony memory consideration is realized and represents the probability of slightly adjusting by moving to neighbouring values of a value selected from the HM. Values of three HS parameters are also initialized at Step 1.

At Step 2, an initial harmony memory is created by generating initial solution vectors with randomly generated headway and offset values considering the preset upper and lower limits. Subsequently, the transit assignment problem is solved using VISUM for each initial solution vector to obtain passenger loads on the bus routes. Thereafter, objective function values of the initial solution vectors are calculated by equations (1)–(4) and stored as given in the following equation:

$$\left[ \begin{array}{c} \text{Headways} \\ \hline h_1^1 \quad h_2^1 \quad \dots \quad h_{N-1}^1 \quad h_N^1 \\ h_1^2 \quad h_2^2 \quad \dots \quad h_{N-1}^2 \quad h_N^2 \\ \vdots \quad \vdots \quad \vdots \quad \vdots \quad \vdots \\ h_1^{\text{HMS}-1} \quad h_2^{\text{HMS}-1} \quad \dots \quad h_{N-1}^{\text{HMS}-1} \quad h_N^{\text{HMS}-1} \\ h_1^{\text{HMS}} \quad h_2^{\text{HMS}} \quad \dots \quad h_{N-1}^{\text{HMS}} \quad h_N^{\text{HMS}} \\ \hline \text{Offsets} \\ \hline \theta_1^1 \quad \theta_2^1 \quad \dots \quad \theta_{N-1}^1 \quad \theta_N^1 \\ \theta_2^2 \quad \theta_2^2 \quad \dots \quad \theta_{N-1}^2 \quad \theta_N^2 \\ \vdots \quad \vdots \quad \vdots \quad \vdots \quad \vdots \\ \theta_1^{\text{HMS}-1} \quad \theta_2^{\text{HMS}-1} \quad \dots \quad \theta_{N-1}^{\text{HMS}-1} \quad \theta_N^{\text{HMS}-1} \\ \theta_2^{\text{HMS}} \quad \theta_2^{\text{HMS}} \quad \dots \quad \theta_{N-1}^{\text{HMS}} \quad \theta_N^{\text{HMS}} \\ \hline \text{Solution vectors} \end{array} \right] \Rightarrow \left[ \begin{array}{c} \text{Objective} \\ \text{functions} \\ \hline Z(\mathbf{h}, \boldsymbol{\theta})^1 \\ Z(\mathbf{h}, \boldsymbol{\theta})^2 \\ \dots \\ Z(\mathbf{h}, \boldsymbol{\theta})^{\text{HMS}-1} \\ Z(\mathbf{h}, \boldsymbol{\theta})^{\text{HMS}} \end{array} \right]. \quad (9)$$

At Step 3, a new solution vector, which includes headway and offset variables, is generated based on HS rules in a similar manner with the improvisation of a new harmony with an orchestra. In this context, it is first decided whether a decision variable value is selected from the HM or not. This procedure is illustrated for a headway variable as follows:

$$h_i' = \begin{cases} h_i \in [h_{\min}, h_{\max}], & \text{with probability } (1 - \text{HMCR}), \\ h_i' \in \{h_i^1, h_i^2, h_i^3, \dots, h_i^{\text{HMS}}\}, & \text{with probability } (\text{HMCR}). \end{cases} \quad (10)$$

In equation (10), the value of the  $i^{\text{th}}$  headway variable in the new solution vector is either taken from the harmony memory or randomly generated between the possible value range with the probabilities of HMCR and  $(1 - \text{HMCR})$ , respectively. Similarly, the value of the  $i^{\text{th}}$

offset variable in the new solution vector is determined as follows:

$$\theta_i' = \begin{cases} \theta_i' \in [0, h_i - 1], & \text{with probability } (1 - \text{HMCR}), \\ \theta_i' \in \{\theta_i^1, \theta_i^2, \theta_i^3, \dots, \theta_i^{\text{HMS}}\}, & \text{with probability } (\text{HMCR}). \end{cases} \quad (11)$$

Once the value of a decision variable is selected from the harmony memory, it is decided whether a pitch adjustment is required or not. Considering the discrete set of decision variables (i.e., successive integers), the pitch adjusting process may be performed for headway and offset variables as given in the following equations:

$$h_i' = \begin{cases} h_i' \pm \text{int}[\text{Rand}(0, 1) \times \mu], & \text{with probability } \text{PAR}, \\ h_i', & \text{with probability } (1 - \text{PAR}), \end{cases} \quad (12)$$

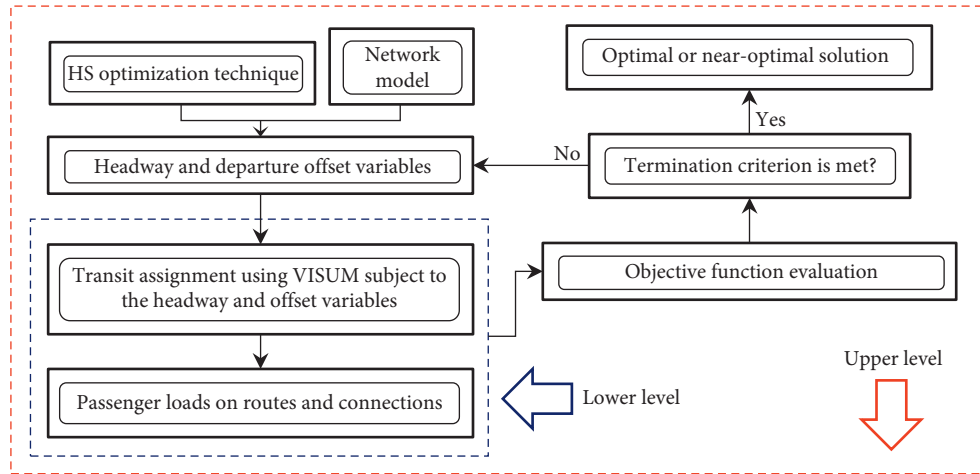


FIGURE 2: Layout of the proposed bilevel model.

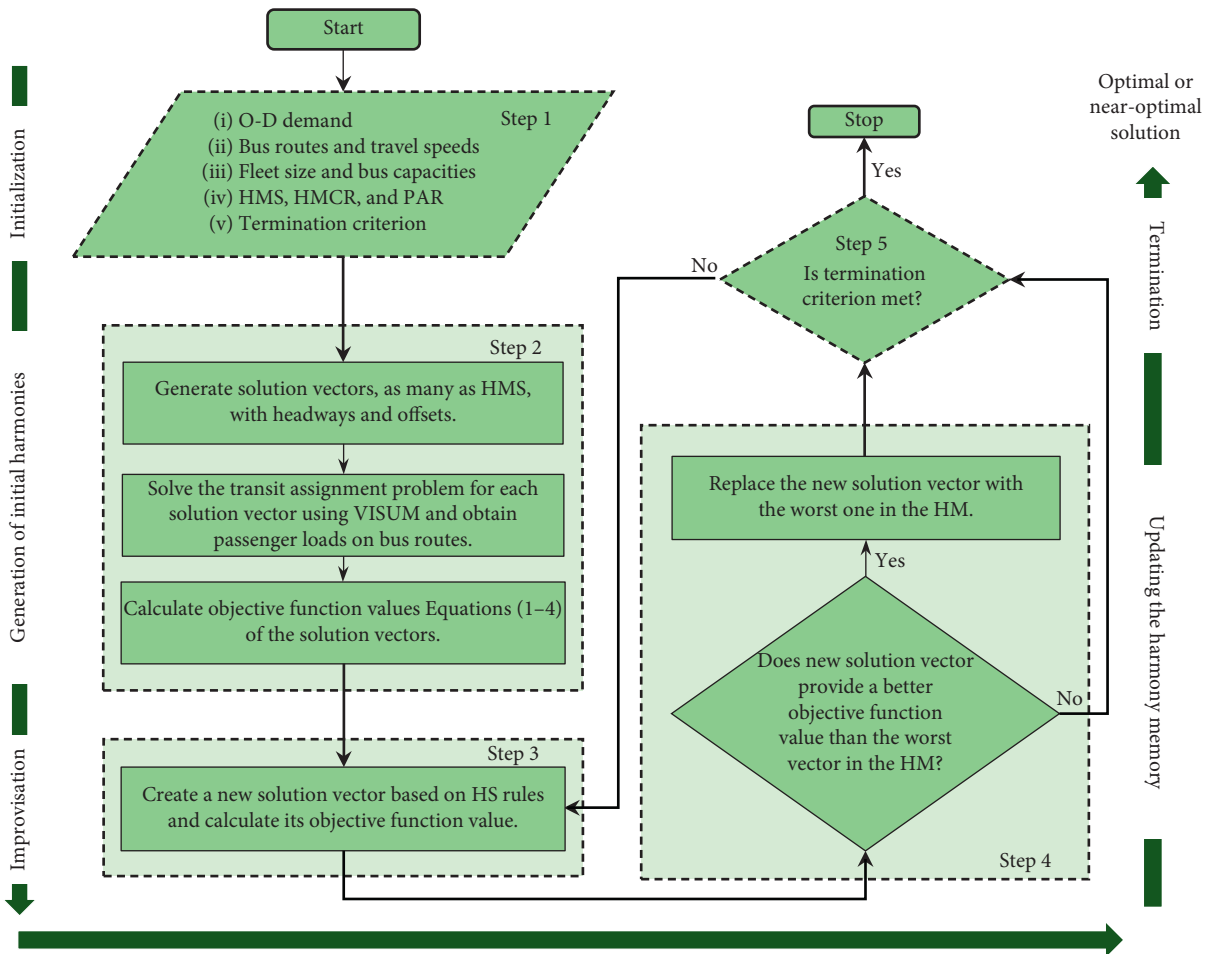


FIGURE 3: Flowchart of the HS-based model.

$$\theta'_i = \begin{cases} \theta_i \pm \text{int}[\text{Rand}(0, 1) \times \mu], & \text{with probability PAR,} \\ \theta_i, & \text{with probability } (1 - \text{PAR}). \end{cases} \quad (13)$$

Note that the procedure given in equations (10)–(13) is applied to all decision variables in the newly created solution

vector. At the end of Step 3, the transit assignment is carried out using VISUM for the new vector and its corresponding objective value is calculated by equations (1)–(4). At Step 4, a comparison is conducted between the worst solution vector in the HM and the newly created solution vector in terms of their objective function values. The one with a better objective value is kept in the HM. At the last step, the solution

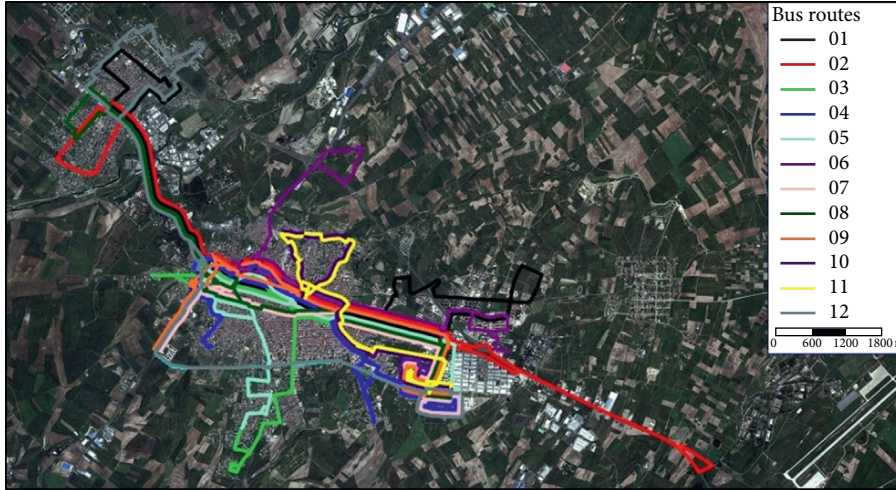


FIGURE 4: Layout of the studied bus network.

process is terminated if the termination criterion is satisfied. Otherwise, the computation is continued by iterating from Step 3 to Step 5.

#### 4. Numerical Application

In this section, a numerical application is carried out for the bus system of the Çorlu district (Tekirdağ, Turkey) in order to evaluate the performance of the proposed model. Çorlu, located within the boundaries of Tekirdağ province, is one of the largest settlement centres in the Thrace region of Turkey after Istanbul in terms of its spatial size and trade volume. Çorlu public transportation system consists of 12 bus routes providing regular transit services. In 2017, monthly average of 2.5 million passenger trips were made with a fleet size of 80 buses with capacities of 50, 70, and 100 passengers. Layout and the lengths and vehicle capacities of the bus routes are given in Figure 4 and Table 1, respectively.

During the model computations, penalty weight is set as  $\phi = 1$ , impedance sensitivity is set as  $\beta = 4$ , transfer penalty is set as  $\gamma = 5$  mins, HS parameters are set as  $HMS = 100$ ,  $HMCR = 0.85$ , and  $PAR = 0.05$ , and band width is set as  $\mu = 5$ . The model algorithm is terminated after  $3 \times 10^6$  iterations. Since 15% of all trips are between 07:00 and 09:00 in the morning in the Çorlu transit network, analyses are conducted for this period. Lower and upper bounds for headway variables are considered as 5 and 30 minutes, respectively. Since the objective weights  $D_1$  and  $D_2$  govern the trade-off between user and operator costs, the proposed multiobjective problem is solved with different weights. Owing to the vast search space of the proposed problem, Pareto efficient solutions are investigated by ignoring the offset variables, and only headway variables are taken into account. Thus, first buses on all bus routes departure at the beginning of the analysis period (i.e., 07:00 a.m.). Computational results for 11 cases with different objective weights are given in Table 2.

It can be seen in Table 2 that the total travel time is about 2217 hours for Case 1 where objective weights are  $D_1 = 0$  and  $D_2 = 1.0$ . In the consecutive cases, where objective

TABLE 1: Lengths and vehicle capacities of bus routes.

Route code	Length (km)	Bus capacity
01	25.46	100
02	30.31	50
03	15.58	50
04	17.17	50
05	20.52	50
06	19.29	50
07	16.75	70
08	21.95	70
09	16.92	50
10	14.04	50
11	13.10	50
12	27.62	50

weight  $D_1$  gradually increases, total travel time decreases and reaches to 2126 hours for Case 11 where  $D_1 = 1.0$  and  $D_2 = 0$ . Meanwhile, the total service km value increases from 1311 to 1423 kilometres. This reveals that the planner fully concentrates on total service km on the transit network for  $D_1 = 0$ , while only the total travel time is considered for  $D_1 = 1.0$ . When analysing the changes in both objective values, it can be seen that the percentage decrease in total travel time is relatively close to the percentage increase in total service km values except for Case 9 where total travel time decreases about 1.4% while total service km increases about 4.1%. This indicates that a small amount of gain in cost saving for users leads to a sudden spike in operator cost. Therefore, Case 8 can be considered as the optimal solution to the proposed biobjective problem, and optimal values for the objective weights  $D_1$  and  $D_2$  may be considered as 0.70 and 0.30, respectively. Figure 5 illustrates the Pareto efficient solutions for both objective functions.

In Table 3, proposed headways, maximum passenger loads, and capacities on bus routes are given for objective weights  $D_1 = 0.70$  and  $D_2 = 0.30$ . It can be seen in Table 3 that all headway values are between 5 and 30 minutes and there is no capacity violation on the transit network.

In order to investigate the effects of departure offsets in urban bus operations, the proposed problem was solved by

TABLE 2: Computational results for the proposed model without departure offsets.

Case	Objective weights		Total travel time (hour)	Total service km	Objective value	Change in the total travel time (%)	Change in the total service km (%)
	$D_1$	$D_2$					
1	0.00	1.00	2216.64	1310.88	1310.88	—	—
2	0.10	0.90	2216.64	1310.88	1401.45	0.00	0.00
3	0.20	0.80	2216.64	1310.88	1492.03	0.00	0.00
4	0.30	0.70	2212.47	1314.80	1584.10	-0.19	0.30
5	0.40	0.60	2206.81	1319.79	1674.60	-0.26	0.38
6	0.50	0.50	2199.70	1325.25	1762.48	-0.32	0.41
7	0.60	0.40	2191.76	1330.84	1847.39	-0.36	0.42
8	0.70	0.30	2177.95	1344.00	1927.77	-0.63	0.99
9	0.80	0.20	2147.70	1402.21	1998.60	-1.39	4.33
10	0.90	0.10	2127.55	1421.45	2055.54	-1.02	1.52
11	1.00	0.00	2125.76	1423.48	2125.76	0.00	0.00

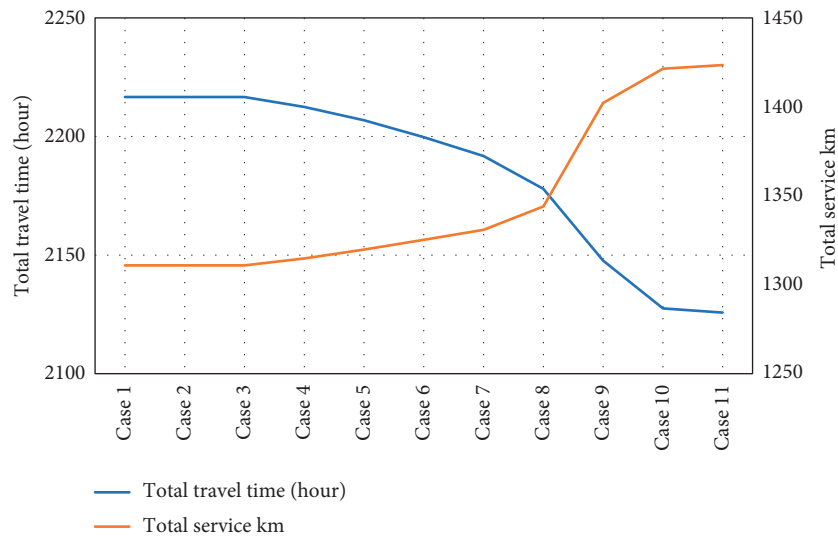


FIGURE 5: Pareto efficient solutions for both objectives.

TABLE 3: Proposed headways and their corresponding maximum load and capacity values.

Route code	Headway (minutes)	Maximum load (no. of passengers)	Capacity
01	21	413	500
02	14	439	450
03	29	217	250
04	24	299	300
05	19	337	350
06	23	276	300
07	16	489	490
08	26	234	250
09	30	194	200
10	29	97	200
11	30	108	200
12	30	72	200

considering both headway and offset variables for objective weights  $D_1 = 0.70$  and  $D_2 = 0.30$ . Convergence history of the solution process is illustrated in Figure 6.

It can be seen in Figure 6 that the model algorithm achieves a steady convergence after about  $1.2 \times 10^6$  iterations.

In order to illustrate the robustness of the proposed approach, the model was run 100 times with different initial solutions and random seeds. After the analyses, minimum, maximum, and average objective function values are obtained as 1901.87, 1920.28, and 1904.45, respectively. While the minimum objective function value was reached with 55% of all runs, standard deviation was calculated as 4.54. Computational results for the proposed model are given in Table 4.

It can be seen in Table 4 that the total travel time is about 2287 hours for the current bus network of Çorlu. It can also be seen that the headway optimization leads to a decrease of about 4.8% while both headway and departure offset optimization can reduce total travel time of about 5.4% in comparison with the current bus network. On the contrary, total distance covered by buses can be reduced about 9.8% by optimizing the headways on bus routes. Moreover, considering different departure times for the first buses on bus routes may reduce this value about 13.3%. In Table 5, comparison between the current and proposed bus networks is provided in terms of headway and capacity values. Additionally, departure offsets with

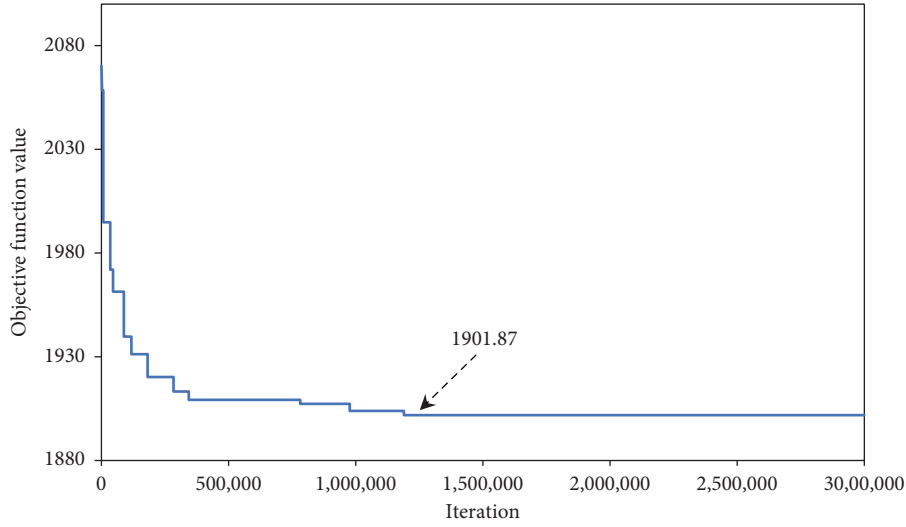


FIGURE 6: Convergence history of the proposed model with headway and offset variables.

TABLE 4: Computational results in comparison with the current bus network of Çorlu.

Case	Total travel time		Total service km	
	Value (hour)	Improvement (%)	Value (km)	Improvement (%)
Current bus network	2286.64	—	1490	—
Bus routes with optimal headways	2177.95	4.75	1344	9.80
Bus routes with optimal headways and departure offsets	2163.67	5.38	1291	13.36

TABLE 5: Model results.

Route code	Current bus network				Model results			
	Bus capacity (no. of passengers)	Headway (minutes)	Capacity (no. of passengers)	Headway (minutes)	Departure offset (minutes)	Maximum load (no. of passengers)	Capacity (no. of passengers)	
01	100	11	1100	21	0	413	600	
02	50	11	550	14	0	430	450	
03	50	15	400	27	16	200	200	
04	50	13	500	22	7	298	300	
05	50	15	400	17	1	354	400	
06	50	17	400	23	0	291	300	
07	70	15	560	18	9	477	490	
08	70	24	350	25	23	249	280	
09	50	24	250	30	12	184	200	
10	50	30	200	30	13	94	200	
11	50	30	200	25	5	137	250	
12	50	30	200	30	24	49	200	

their corresponding maximum passenger loads on bus routes are given for objective weights  $D_1 = 0.70$  and  $D_2 = 0.30$ . It can be seen in Table 5 that all headway values are between 5 and 30 minutes, all departure offset values are between possible bounds, and there is no capacity violation on the bus network according to the model outputs.

Number of trips observed for the current bus network and those calculated based on the proposed model are given in Table 6.

As can be seen in Table 6, 2934 and 169 trips are made with one and two transfers, respectively, during the analysis period on the current bus network of Çorlu. When optimal

headways are applied to the bus routes, the number of trips with both one and two transfers can be reduced up to 2461 and 116 trips, respectively. This reveals that the number of users that can complete their travels on a particular bus route can be increased by headway optimization. On the contrary, when optimal departure offsets are considered, the number of trips with one transfer increases in comparison to the bus network only with optimal headways. This increase indicates that optimal departure offsets may provide a coordination of bus services and shorter transfer wait times resulting in a reasonable reduction in total travel time and total distance covered by buses.

TABLE 6: Number of trips for the current bus network and modelling results.

Case	Number of trips		
	Without transfer	With one transfer	With two transfers
Current bus network	11234	2934	169
Bus routes with optimal headways	11488	2461	116
Bus routes with optimal headways and departure offsets	11456	2537	104

## 5. Conclusions

In this study, a multiobjective minimization problem, which was formulated as a weighted sum of total travel time of transit users and total distance covered by transit vehicles, was proposed. Subsequently, a bilevel simulation/optimization model was developed to optimize departure headway and offset variables in urban bus networks. At the upper level of the model, the proposed problem was solved based on the HS optimization algorithm solution framework. On the contrary, the transit assignment problem was solved using the timetable-based assignment approach of VISUM transport planning software at the lower level.

Owing to the multiobjective nature of the problem, investigating the trade-off between user and operator benefits is an important issue. In this context, the proposed model was first applied to a real-life transit network with different weights in order to analyse Pareto efficient solutions and determine the optimal values of objective weights. Those computations were made by ignoring departure offset values that require more computational efforts due to the vast search space of the multiobjective problem. It was found that the total travel time and total service km could be reduced by 4.8% and 9.8%, respectively, compared with the current bus network. Once the optimal values of the objective weights were determined, the proposed model was applied to the network by considering both departure headway and offset variables. The results showed that 5.4% and 13.3% improvements could be achieved by including departure offset variables in the model.

Fleet constraint considered in the proposed model ensures that the number of buses required on particular routes does not exceed the number of buses allocated to those routes. In future, a bus allocation algorithm will be integrated into the proposed model that can distribute a common fleet including buses with different types and capacities. Integrating a route construction algorithm into the proposed model is considered as another future direction.

## Abbreviations

### Sets/indices

- $N$ : Set of routes in the transit network  
 $O$ : Set of origins  
 $V$ : Set of destinations  
 $G$ : Set of connections  
 $i, j, k$ : Indices

### Parameters

- $IVT_k^{ij}$ : In-vehicle travel time on the connection  $k$  between origin  $i$  and destination  $j$   
 $OWT_k^{ij}$ : Origin wait time on the connection  $k$  between origin  $i$  and destination  $j$   
 $TWT_k^{ij}$ : Transfer wait time on the connection  $k$  between origin  $i$  and destination  $j$   
 $l_i$ : Length of route  $i$   
 $P_i$ : Value of the penalty arising from the capacity violation on route  $i$   
 $T$ : Length of the analysis period  
 $h_{\min}$ : Minimum headway  
 $h_{\max}$ : Maximum headway  
 $t_i$ : Single trip time of route  $i$   
 $W$ : Available bus fleet size  
 $x_i$ : Number of passengers on route  $i$   
 $x_{i,\max}$ : Maximum passenger load on route  $i$   
 $u_i$ : Vehicle capacity of route  $i$   
 $\phi$ : Penalty weight  
 $R_k^{ij}$ : Choice probability of connection  $k$  between origin  $i$  and destination  $j$   
 $\delta_{ik}$ : Element of route/connection incidence matrix that  $\delta_{ik} = 1$  if connection  $k$  uses route  $i$ , and  $\delta_{ik} = 0$  otherwise  
 $\beta$ : Parameter for modelling the impedance sensitivity  
 $B_k^{ij}$ : Impedance of connection  $k$  between origin  $i$  and destination  $j$   
 $B_k^a$ : Impedance of connection  $k$  in a time interval  $a$   
 $\mu$ : Arbitrary band width  
 $\text{Rand}(0, 1)$ : Uniform random number between 0 and 1  
 $v_k^{ij}$ : Number of transfers on connection  $k$  between origin  $i$  and destination  $j$   
 $\gamma$ : Transfer penalty  
 $q^{ij}$ : Travel demand between origin  $i$  and destination  $j$   
 $D_1$ : Weight for the total travel time  
 $D_2$ : Weight for the total service km

### Decision variable

- $h_i$ : Departure headway on route  $i$   
 $\theta_i$ : Departure offset for the first bus on route  $i$ .

## Data Availability

The data used to support the findings of this study may be released upon application to the Metropolitan Municipality of Tekirdağ, which can be contacted at [tbb@tekirdag.bel.tr](mailto:tbb@tekirdag.bel.tr).

## Conflicts of Interest

The authors declare that there are no conflicts of interest regarding the publication of this paper.

## Acknowledgments

The authors gratefully acknowledge the contribution of the PTV Traffic Mobility Logistics for the VISUM traffic planning software. The authors are also grateful to the Metropolitan Municipality of Tekirdağ for providing the

reference for the background of this paper. This research was supported by Scientific Research Projects Department of Pamukkale University with project no. 2018KRM002-233.

## References

- [1] M. M. Nesheli, A. Ceder, F. Ghavamirad, and S. Thacker, "Environmental impacts of public transport systems using real-time control method," *Transportation Research Part D: Transport and Environment*, vol. 51, pp. 216–226, 2017.
- [2] A. Behrens and C. Egenhofer, "Rethinking European Climate Change Policy," in *Toward a Common European Union Energy Policy*, V. L. Birchfield and J. S. Duffield, Eds., pp. 217–234, Palgrave Macmillan Press, New York, NY, USA, 2011.
- [3] A. Aravindan, "Singapore to halt car population growth from next year," 2017, <https://www.reuters.com/article/us-singapore-autos/singapore-to-halt-car-population-growth-from-next-year-idUSKBN1CS14K>.
- [4] J. Pucher and N. Korattyswaroopam, "The crisis of public transport in India: overwhelming needs but limited resources," *Journal of Public Transportation*, vol. 7, no. 4, pp. 1–20, 2004.
- [5] M. A. M. Ittyerah, P. N. Moeketsi, and V. Baloyi, "Increasing public transport market share in South Africa: the options," in *Proceedings of International Conference Series on Competition and Ownership in Land Passenger Transport*, Cape Town, South Africa, September 1999.
- [6] B. Finn and C. Mulley, "Urban bus services in developing countries and countries in transition: a framework for regulatory and institutional developments," *Journal of Public Transportation*, vol. 14, no. 4, pp. 89–107, 2011.
- [7] D. L. V. Oudheusden and W. Zhu, "Trip frequency scheduling for bus route management in Bangkok," *European Journal of Operational Research*, vol. 83, pp. 439–451, 1995.
- [8] W. Lampkin and P. D. Saalmans, "The design of routes, service frequencies, and schedules for a municipal bus undertaking: a case study," *Journal of the Operational Research Society*, vol. 18, pp. 375–397, 2017.
- [9] C. E. Mandl, "Evaluation and optimization of urban public transportation network," in *Proceedings of 3rd European Congress on Operation Research*, Amsterdam, Netherlands, April 1979.
- [10] A. Ceder and N. H. M. Wilson, "Bus network design," *Transportation Research Part B: Methodological*, vol. 20, no. 4, pp. 331–344, 1986.
- [11] M. H. Baaj and H. S. Mahmassani, "TRUST: a LISP program for the analysis of transit route configurations," *Transportation Research Record*, vol. 1283, pp. 125–135, 1990.
- [12] M. H. Baaj and H. S. Mahmassani, "Hybrid route generation heuristic algorithm for the design of transit networks," *Transportation Research Part C: Emerging Technologies*, vol. 3, no. 1, pp. 31–50, 1995.
- [13] P. Chakroborty and T. Wivedi, "Optimal route network design for transit systems using genetic algorithms," *Engineering Optimization*, vol. 34, no. 1, pp. 83–100, 2002.
- [14] W. Y. Szeto and Y. Wu, "A simultaneous bus route design and frequency setting problem for Tin Shui Wai, Hong Kong," *European Journal of Operational Research*, vol. 209, pp. 141–155, 2011.
- [15] M. Nikolic and D. Teodorovic, "A simultaneous transit network design and frequency settings: computing with bees," *Expert Systems with Applications*, vol. 41, no. 16, pp. 7200–7209, 2014.
- [16] C. L. Mumford, "New heuristic and evolutionary operators for the multi-objective urban transit routing problem," in *Proceedings of IEEE Congress on Evolutionary Computation*, pp. 939–946, Cancún, Mexico, June 2013.
- [17] S. Afandizadeh, H. Khaksar, and N. Kalantari, "Bus fleet optimization using genetic algorithm a case study of Mashhad," *International Journal of Civil Engineering*, vol. 11, no. 1, pp. 43–52, 2013.
- [18] M. Owais and M. K. Osman, "Complete hierarchical multi-objective genetic algorithm for transit network design problem," *Expert Systems with Applications*, vol. 114, no. 30, pp. 143–154, 2018.
- [19] A. T. Buba and L. S. Lee, "A differential evolution for simultaneous transit network design and frequency setting problem," *Expert Systems with Applications*, vol. 106, no. 15, pp. 277–289, 2018.
- [20] E. Ruano-Daza, C. Cobos, J. Torres-Jimenez, M. Mendoza, and A. Paz, "A multiobjective bilevel approach based on global-best harmony search for defining optimal routes and frequencies for bus rapid transit systems," *Applied Soft Computing*, vol. 67, pp. 567–583, 2018.
- [21] F. A. Kidwai, B. R. Marwah, K. Deb, and M. R. Karim, "A genetic algorithm based bus scheduling model for transit network," *Proceedings of the Eastern Asia Society for Transportation Studies*, vol. 5, pp. 477–489, 2005.
- [22] F. Ruisanchez, L. dell'Olio, and A. Ibeas, "Design of a tabu search algorithm for assigning optimal bus sizes and frequencies in urban transport services," *Journal of Advanced Transportation*, vol. 46, pp. 366–377, 2012.
- [23] A. F. Han and N. H. M. Wilson, "The allocation of buses in heavily utilized networks with overlapping routes," *Transportation Research Part B: Methodological*, vol. 16, no. 3, pp. 221–232, 1982.
- [24] M. H. Baaj and H. S. Mahmassani, "An AI-based approach for transit route system planning and design," *Journal of Advanced Transportation*, vol. 25, no. 2, pp. 187–209, 1991.
- [25] G. Doğan and M. Özuysal, "Toplu Ulaşımında Bekleme Süresini Etkileyen Faktörlerin İncelenmesi: Güvenilirlik, Yolcu Bilgilendirme Sistemi ve Fiziksel Koşullar," *Teknik Dergi*, vol. 28, no. 3, pp. 7927–7954, 2017.
- [26] PTV, *PTV Visum Manual*, PTV Traffic Mobility Logistics, Karlsruhe, Germany, 2015.
- [27] T. Dede, "Jaya algorithm to solve single objective size optimization problem for steel grillage structures," *Steel and Composite Structures*, vol. 26, no. 2, pp. 163–170, 2018.
- [28] Z. W. Geem, J. H. Kim, and G. V. Loganathan, "A new heuristic optimization algorithm: harmony search," *Simulation*, vol. 76, no. 2, pp. 60–68, 2001.
- [29] H. Ceylan, H. Ceylan, S. Haldenbilen, and O. Baskan, "Transport energy modeling with meta-heuristic harmony search algorithm, an application to Turkey," *Energy Policy*, vol. 36, pp. 2527–2535, 2008.
- [30] H. Ceylan and H. Ceylan, "A hybrid harmony search and TRANSYT hill climbing algorithm for signalized stochastic equilibrium transportation networks," *Transportation Research Part C: Emerging Technologies*, vol. 25, pp. 152–167, 2012.
- [31] M. Dell'Orco, O. Baskan, and M. Marinelli, "A harmony search algorithm approach for optimizing traffic signal Timings," *Journal of Traffic and Transportation*, vol. 25, no. 4, pp. 349–358, 2013.
- [32] S. Salcedo-Sanz, D. Manjarrés, Á. Pastor-Sánchez, J. A. Del Ser, and S. Gil-López, "One-way urban traffic reconfiguration

- using a multi-objective harmony search approach,” *Expert Systems with Applications*, vol. 40, pp. 3341–3350, 2013.
- [33] O. Baskan, “Harmony search algorithm for continuous network design problem with link capacity expansions,” *KSCE Journal of Civil Engineering*, vol. 18, no. 1, pp. 273–283, 2013.
- [34] K. Gao, Y. Zhang, A. Sadollah, and R. Su, “Optimizing urban traffic light scheduling problem using harmony search with ensemble of local search,” *Applied Soft Computing*, vol. 48, pp. 359–372, 2016.
- [35] H. Ceylan and T. Özcan, “Otobüs ağlarındaki sefer sıklıklarının Armoni Araştırması Algoritması ile optimizasyonu: Mandl test ağı üzerine bir uygulama,” *Pamukkale University Journal of Engineering Sciences*, vol. 24, no. 6, pp. 1107–1116, 2018.

## Research Article

# Damage Identification by the Data Expansion and Substructuring Methods

Eun-Taik Lee<sup>1</sup> and Hee-Chang Eun <sup>2</sup>

<sup>1</sup>Department of Architectural Engineering, Chung-Ang University, Seoul, Republic of Korea

<sup>2</sup>Department of Architectural Engineering, Kangwon National University, Chuncheon, Republic of Korea

Correspondence should be addressed to Hee-Chang Eun; [heechang@kangwon.ac.kr](mailto:heechang@kangwon.ac.kr)

Received 24 September 2018; Revised 29 October 2018; Accepted 18 November 2018; Published 11 December 2018

Guest Editor: Tayfun Dede

Copyright © 2018 Eun-Taik Lee and Hee-Chang Eun. This is an open access article distributed under the Creative Commons Attribution License, which permits unrestricted use, distribution, and reproduction in any medium, provided the original work is properly cited.

Structural damage can be detected by comparing the responses before and after the damage. The responses are transformed into curvature, strain, and stress, among others, which characterize the mechanical behavior of the structural members, and can be utilized as damage indices for damage detection. The damage of a truss structure can rarely be detected by the displacements only at nodes. This work investigates damage detection methods using the stress or stiffness variation rate of the truss element before and after the damage. This paper considers three different cases according to the number of measurement locations. If the complete responses at a full set of degrees of freedom are measured, the stiffness variation rates of the elements are calculated accurately, and the damage can be explicitly detected despite external noise. If the number of measured data points is fewer than the system order, the displacements are estimated by the data expansion method, and the damage-expected regions are predicted by the stiffness variation rates. Apart from the explicitly damaged elements, the substructuring approach is adopted for closer damage detection with several measurement sensors despite external noise. It is illustrated by the examples that three cases are compared numerically. The numerical examples compare and analyze the numerical results of the three cases.

## 1. Introduction

Structural maintenance has received significant attention in the construction industry. Existing structures have been diagnosed, repaired, reformed, and remodeled for improving the structural performance and durability. Structural health monitoring and nondestructive tests for evaluating structural performance have been developed with the advent of new measurement sensors and technologies, and techniques for structural health monitoring have been applied in the field.

The health state of a structure is evaluated by the response, internal strain, or internal stress, among others. Structural defects are detected in the process by comparing the responses before and after the structural performance deterioration. The measured responses are transformed into curvature, strain, and stress for damage detection. The measured displacements in the truss structure should be transformed into axial stresses for evaluating the existence of damage.

It is impractical to collect the responses at a full set of degrees of freedom (DOFs) because of the limited number of sensors. The number of measurement sensors is practically fewer than the system order. Thus, incomplete measurement data should be expanded, or the system order should be reduced.

The damage identification method has become a prominent research field. The identification of a global structure requires a large number of sensors and unknowns; however, the substructuring method needs only several sensors for response measurement.

Blachowski et al. [1] presented a damage quantification method for the truss structure without identifying modal parameters or solving a global optimization problem. The method quantifies the damage in a given substructure with only a small subset of sensors. Park and Reich [2] provided two complementary methods for model-based structural damage detection, based on changes in the localized flexibility and invariance properties of the elemental or

substructural transmission zeros. Xing and Mita [3] proposed a substructure approach for identifying localized damage on each substructure using only three sensors. Ugalde et al. [4] presented a substructuring approach to predict the health of each substructure by means of the vector autoregressive variation with the exogenous model. Hou et al. [5] proposed a substructure damage identification method using local free responses. Estimating additional unknown inputs by the algorithm, without measurements of the substructure interface DOFs, Lei et al. [6] applied the damage detection method by means of the degradation of the identified substructural element stiffness values. Lee and Eun [7] presented a model-based substructuring method for local damage detection using the frequency response function measured at the interfaces between the adjacent substructures. Li et al. [8] proposed a substructural damage identification approach based on dynamic response reconstruction and a dynamic response sensitivity-based method.

An et al. [9] presented a stochastic damage-locating vector method as a useful tool for damage localization in steel truss bridges. An et al. [10] proposed a damage localization approach for truss structures using the curvature difference method of strain waveform fractal dimensions. Yang and Jin [11] presented a damage detection method for truss structures using incompletely measured modes, with the aid of the eigenvalue perturbation method. Kaven and Zolghadr [12] proposed a damage detection method using the differences between structure characteristics, such as natural frequencies and mode shapes of truss structures. Xu and Wu [13] developed a damage detection technique based on strain data under ambient excitation using the environmental excitation incomplete strain mode. Artar and Daloglu [14] presented a damage identification method to update the numerical model and to predict damage location and severity in the space frame using genetic algorithms.

This study considers methods for predicting damaged elements depending on complete and incomplete measurement data, including the noise effect. The measured and estimated displacements are transformed into the internal stress of the elements, and the stiffness variation rate is used as a damage index. By dividing a full truss structure into several damage-expected substructures, this work proposes the substructuring method to estimate damaged elements. This method offers merits in reducing the model order and number of measurement locations by the static-based and dynamic-based data expansion method [15] and is insensitive to external noise. The damage detection methods using complete and incomplete measurements are investigated in numerical examples. The validity of the proposed static-based and dynamic-based substructuring method is illustrated in examples, depending on external noise.

## 2. Substructuring Method for Damage Detection

Structural diagnosis is conducted by means of the comparison of the response, strain, stress, and stiffness in healthy and unhealthy states, or the measurement data only in the damage-expected state without the baseline data. This

method is performed by a response comparison in both states. This work compares three damage detection methods, depending on the number of measurement locations to be causable in the structural performance evaluation. The three different cases are as follows: (1) damage detection using complete measurement data; (2) damage detection using the data to expand fewer measurement data than the model order; and (3) damage detection by measurement data and data expansion at the substructures to divide an entire structure. Moreover, the effect of the noise contained in the measurement data is examined. Figure 1 summarizes the flow of this study to detect damaged elements.

### 2.1. Static Approach

*2.1.1. Complete Measurement Data.* The equilibrium equation of a finite element model with  $n$  DOFs in the intact state can be expressed by

$$\mathbf{F} = \widehat{\mathbf{K}}\widehat{\mathbf{u}}, \quad (1)$$

where  $\widehat{\mathbf{K}}$  and  $\widehat{\mathbf{u}}$  denote the  $n \times n$  positive definite stiffness matrix and  $n \times 1$  displacement vector in the healthy state, respectively. Moreover,  $\mathbf{F}$  is the  $n \times 1$  external force vector. The displacement data at a full set of DOFs may be measured by measurement sensors or calculated by the finite element model for damage detection.

The truss structure is composed of axial members for carrying the axial load, and each member has axial displacement DOFs at both end nodes. The measured displacements are transformed into the axial stress related to the axial stiffness, and the damage can be detected by comparing the stresses or stiffness. This complete method exhibits the limitation of requiring the same number of measurement sensors as the system order.

*2.1.2. Incomplete Measurement Data.* It is not practical to measure the responses for the entire DOFs because of fewer measurement sensors than the system order. This indicates that the full set of displacements should be estimated by means of data expansion. Assuming that the static responses are taken as  $m$  ( $m < n$ ) DOFs, constraints must be implemented to describe the static behavior of the entire system. These can be written as

$$\mathbf{A}\mathbf{u} = \mathbf{b}, \quad (2)$$

where the  $m \times n$  coefficient matrix  $\mathbf{A}$  is a Boolean matrix for defining the measurement locations and the vectors  $\mathbf{u}$  and  $\mathbf{b}$  are the  $n \times 1$  actual displacement vector and  $m \times 1$  measured response vector, respectively.

Constraint forces for pulling the unconstrained path of the initial system into the constrained path are required. Combining equations (1) and (2), reference [15] derives the constrained equilibrium equation as follows:

$$\mathbf{u} = \widehat{\mathbf{u}} + \widehat{\mathbf{K}}^{-1/2} \left( \mathbf{A}\widehat{\mathbf{K}}^{-1/2} \right)^+ (\mathbf{b} - \mathbf{A}\widehat{\mathbf{u}}), \quad (3)$$

where “+” denotes the Moore–Penrose inverse. The displacements corresponding to the entire DOFs are estimated

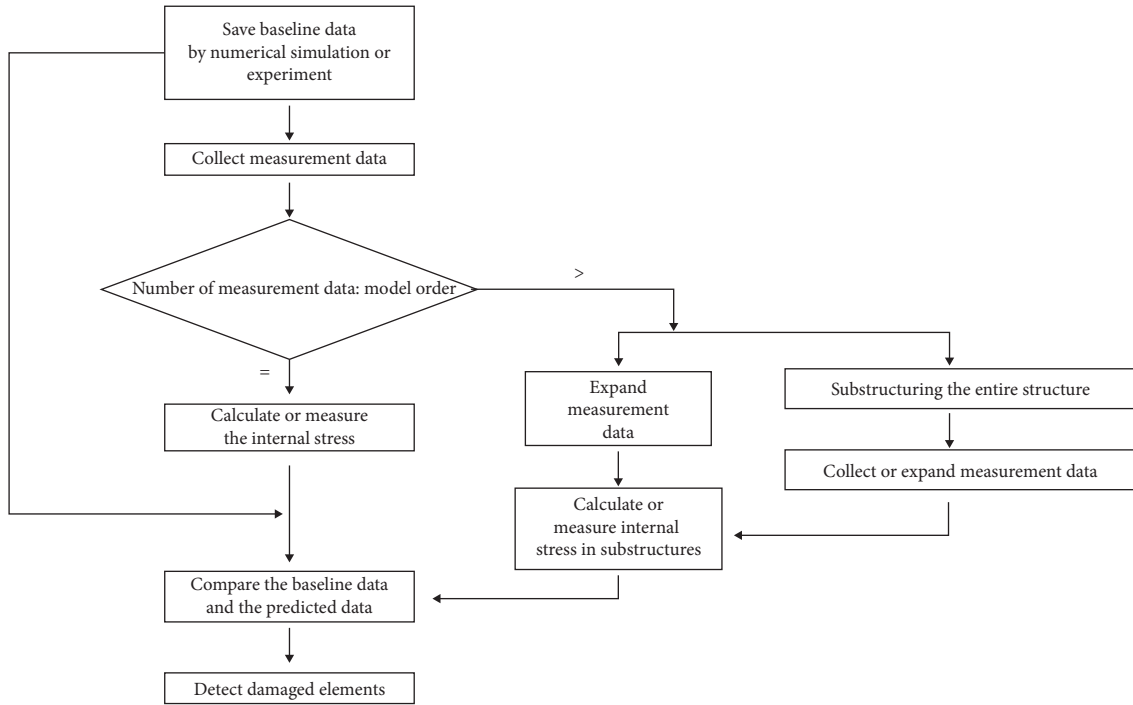


FIGURE 1: Flow chart of this work to detect damaged elements.

by using equation (3), satisfying the constraints of equation (2). The second term on the right-hand side of equation (3) represents the displacement variation deviating from the initially established trajectory. Moreover, by premultiplying the second term on the right-hand side of equation (3) by  $\hat{\mathbf{K}}$ , the constraint force vector  $\mathbf{F}^c$  is obtained by

$$\mathbf{F}^c = \hat{\mathbf{K}}^{1/2} \left( \mathbf{A} \hat{\mathbf{K}}^{-1/2} \right)^+ (\mathbf{b} - \mathbf{A} \hat{\mathbf{u}}). \quad (4)$$

The internal stresses of the truss structure can be calculated accurately by using the displacements and axial stiffness. However, the displacements for expanding the incomplete measurements rarely coincide with the accurate displacements. Moreover, the calculated internal stresses of the truss elements do not coincide with the exact values. The following example investigates the feasibility of the damage detection by comparing the internal stresses estimated by the expanded data with the initially established stresses.

*Example 1.* The adequacy of the estimated responses using equation (3) is investigated in the numerical example of a plane truss structure, as illustrated in Figure 2. In the figure, the nodal points and members are numbered. Each node has two DOFs of the horizontal and vertical responses  $u$  and  $v$ , respectively. The truss is composed of six nodes, nine members, and nine DOFs, except for boundary conditions. All members have the same elastic modulus of 200 GPa and cross-sectional area of  $2.5 \times 10^{-3} \text{ m}^2$ . The simply supported truss has a single span. Its length is 12 m, its height is 3 m, and each bay is 4 m long. The responses in the intact state can be calculated by the finite element method under the action of the external force of 10 N in the downward direction of

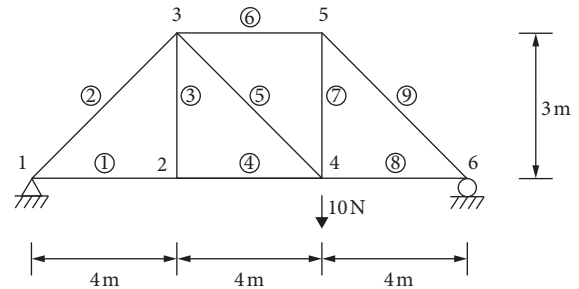


FIGURE 2: A three-bay truss structure.

node 4. The elemental stiffness matrices and responses in the initial state should be saved for subsequent analysis.

The truss exhibits a 20% section loss at element ④ and 30% section loss at element ⑧. The vertical displacements  $v_2$ ,  $v_3$ ,  $v_4$ , and  $v_5$ , numerically simulated in the damaged state, were utilized as measurement data. Inserting the equilibrium equation in the intact state and measurement data in the damaged state into equation (3), the displacements for the entire DOFs are estimated. The truss structure is composed of axial members and pin joints. Thus, unlike the beam, the truss structure represents discontinuous responses at the element nodes. The differences between the actual and estimated responses are displayed in Figure 3. The plots illustrate that the resulting responses coincide at measured DOFs, but a discrepancy of a very small magnitude is evident at the other DOFs. The expansion method does not describe the accurate responses, except for the constraint conditions. The utilization of inaccurately expanded data leads to incorrect analysis.

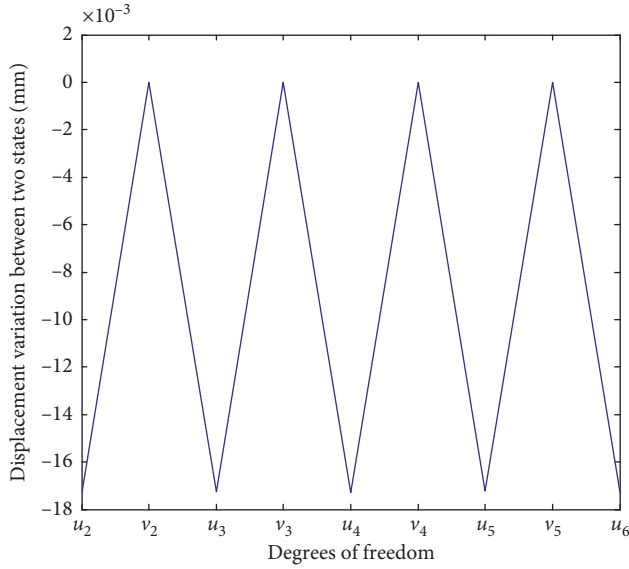


FIGURE 3: Difference between actual and estimated responses of the truss model.

The stress variation rate  $\alpha$ , defined as the stress variation with respect to the stress on an element in the damage state, can be calculated by

$$\alpha = \frac{\sigma_d - \sigma_u}{\sigma_d} \times 100 (\%) \quad (5)$$

where  $\sigma_u$  and  $\sigma_d$  denote the axial stresses in the undamaged and damaged states, respectively. Moreover,  $\sigma_d$  is calculated using the cross-sectional area and axial stiffness in the intact state and measurement data in the damaged state.

The stress variation rates in Figures 4(a) and 4(b) are obtained using the complete and incomplete measurement data, respectively. It is observed that accurate stress variation rates for the damaged elements can be obtained by using the complete measurement data. However, the plot using the incomplete measurement data exhibits very small variation rates, regardless of the damaged elements, and the damaged elements cannot be detected.

This expansion method exhibits the drawbacks of inaccurately estimating the expanded data and yielding inconsistent results depending on the sensor location and number. Thus, this work considers the analytical method for detecting the damage by dividing an entire structure into substructures in order to reduce the sensor number and detecting damage elements more reliably.

**2.1.3. Substructuring Method.** The limited number of sensors and unclearness of the damaged locations make a more detailed diagnosis method necessary. One precise diagnosis method may be the substructuring method, whereby an entire structure is divided into several substructures, as illustrated in Figure 5, and the damage is detected by measurements on each substructure. The damage detection in the substructure is carried out by means of a similar process to those of the previous

complete and incomplete methods, depending on the number of measurement locations. The measured or estimated displacement data are transformed into the stress of the truss structure.

The damage yields the variation in the element stress, and it may be utilized as a damage index for evaluating the structural performance. Assuming a constant mass before and after the damage, the stress variation rate in equation (5) can be applied for detecting the damage. The stress variation is related to the cross-sectional variation under a constant axial force. The axial stiffness  $k$  is also related to the variation in the cross-sectional area with the same elastic modulus and member length. Thus, equation (5) for the axial members can be expressed by

$$\alpha = \left( \frac{(E(A_d)/L) - (E(A_u)/L)}{(E(A_d)/L)} \right) \times 100 (\%) \quad (6)$$

$$= \left( \frac{k_d - k_u}{k_d} \right) \times 100 (\%),$$

where  $k_d$  and  $k_u$  represent the stiffness values in the damaged and undamaged states, respectively, while  $A_d$  and  $A_u$  are the cross-sectional areas in the damaged and undamaged states, respectively. It is observed that the stiffness variation of equation (6) has the same meaning as the stress variation of equation (5).

**2.2. Dynamic Approach.** In the dynamic approach, mode shape data are utilized as measurement data as with the static displacements. The measurement data may be a full set of displacement DOFs or the data expanded from incomplete measurements. The stress variation rates in the truss elements are calculated by equation (5), or the stiffness variation rate is predicted by equation (6). The damage is detected by the stiffness variation rate plots.

**Example 2.** The above methods are examined in the numerical example in order to detect the damaged elements of the plane truss structure displayed in Figure 6. The numbering of nodes and members is indicated in the figure. Each node has two DOFs of the horizontal and vertical responses  $u$  and  $v$ , respectively. The truss structure of 12 bays is simply supported and is composed of 24 nodes and 45 members. All members have the same elastic modulus of 200 GPa, cross-sectional area of  $2.5 \times 10^{-3} \text{ m}^2$ , and density of  $7,860 \text{ kg/m}^3$ , as in the previous example. The total length of the truss is 6 m, its height is 0.6 m, and each bay is 0.5 m long. The truss is subjected to an external force of 10 N in the downward direction of node 7. It has multiple damages of 20% section loss at elements 4, 14, and 42. The numerically simulated responses and stiffness values in the intact state are saved as baseline data for comparison with the numerical results in the damaged state. The above three static methods are compared, and one dynamic method is presented in this example. Moreover, each method evaluates the effect of the noise contained in the measured data.

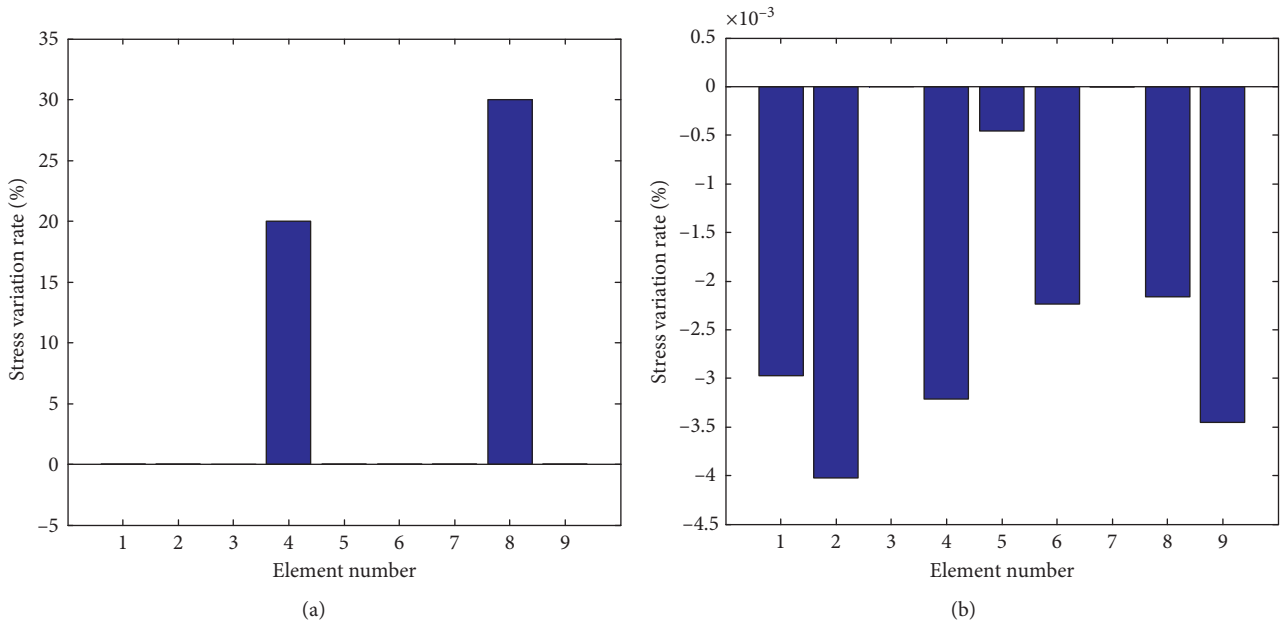


FIGURE 4: Stress variation rate of the truss model: (a) complete measurement data; (b) incomplete measurement data.

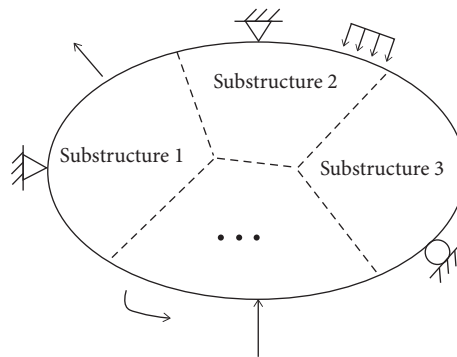


FIGURE 5: Substructuring of an entire structure.

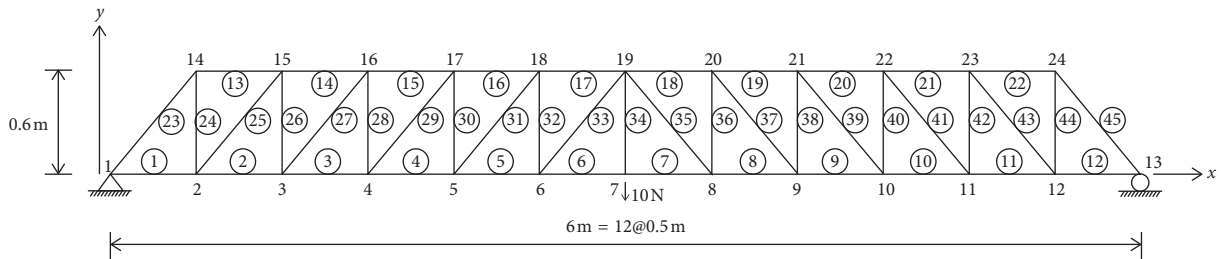


FIGURE 6: Numerical model of the truss structure for damage detection.

2.2.1. Complete Measurement Data. Figure 7 illustrates the numerical results calculated from the complete noise-free measurement data before and after the damage. Figure 7(a) represents the horizontal and vertical displacement variations before and after the damage. The plots display the abrupt changes at the node to move from the lower to the upper chords. The damage positions at the element represent the abrupt displacement variation owing to the stiffness deterioration. However, the continuous displacement plots

at the lower and upper chords do not provide any damage information without any additional considerations, such as flexural curvature. Figure 7(b) represents the stiffness variation rates calculated by equation (6), respectively. It is observed that abrupt stiffness variations are located at the damaged elements, and the variation rate coincides with the damage degree of 20%. The application indicates that the damage can be clearly detected if accurate information is provided on the completely measured displacements.

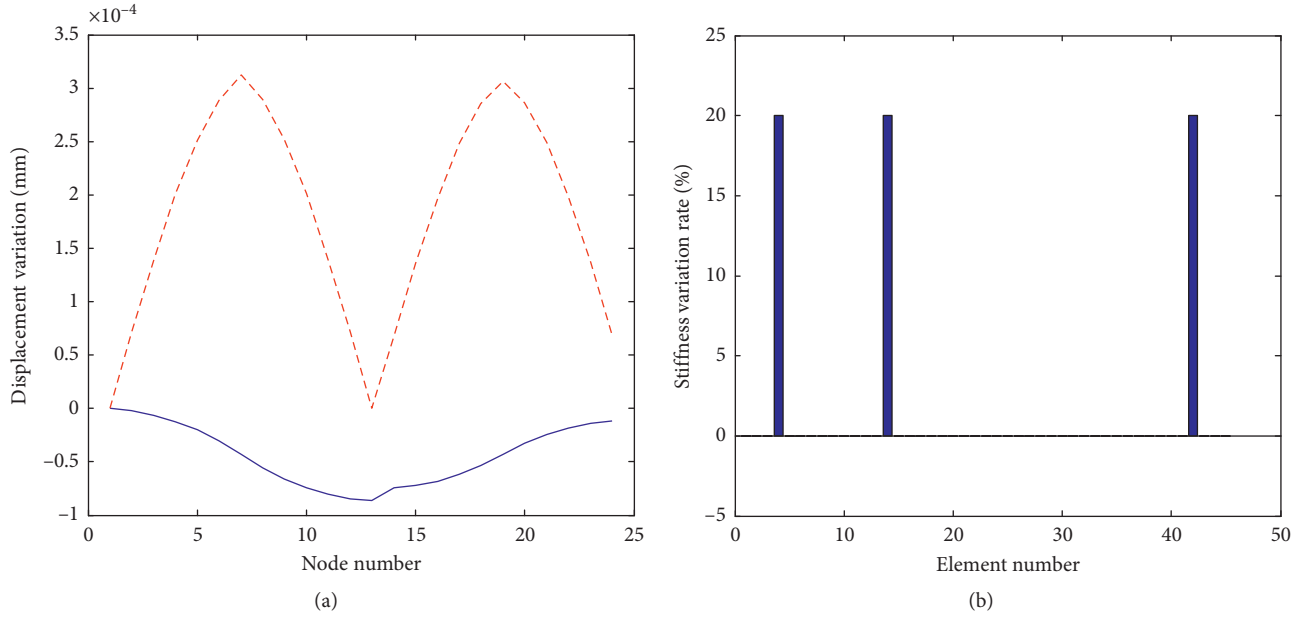


FIGURE 7: Numerical results using the complete noise-free measurement data: (a) displacement variations; (b) stiffness variation rate. In (a), the solid line indicates the horizontal displacement and the dashed line indicates the vertical displacement.

The presence of external noise leads to a slight variation in the displacements, deviating from the accurate trajectory. The measurement data contain errors contaminated by external noise. The  $i$ -th simulated or measurement dataset  $\psi_i$  is established as

$$\psi_i = \psi_{0,i}(1 + \gamma\xi_i), \quad (7)$$

where  $\gamma$  denotes the relative magnitude of the error,  $\xi_i$  is a random number variant in the range of  $[-1, 1]$ , and  $\psi_{0,i}$  is the  $i$ -th noise-free dataset. The applicability of the proposed method is investigated in the numerical example.

Figure 8(a) represents the displacement curves containing 1% noise. In order to reduce the effect owing to external noise, the mean values of 10 repeated numerical results were utilized as the measurement data for evaluating the validity of the method. It is observed that the plots in Figure 8(a) represent the displacement variations, do not indicate any peculiarity related to the damage, and exhibit difficulties in detecting the damage. Figure 8(b) displays the stiffness variation rate plot. The noise leads to irregular stiffness variations, unlike in the noise-free case. The damaged elements are clearly detected by the plots. The stiffness variation rates do not coincide with the actual damage degree owing to the noise. This example indicates that accurate damage detection is possible when accurate measurement data despite external noise are provided. It is demonstrated that the stiffness variation rate plots are almost the same except for the irregularities owing to noise.

**2.2.2. Incomplete Measurement Data.** At this time, we consider damage detection using measurement data with fewer DOFs than the system order. The vertical displacements at 22 nodes, except for support nodes 1 and 13, were

measured, and the mean values of 10 repeated results were recorded. By inserting the numerically simulated measurement data and equilibrium equation in the intact state into equation (3), the displacements for the entire DOFs are estimated. Figure 9(a) illustrates the noise-free displacement differences before and after the damage. It is observed that the curve is nearly similar to that of Figure 7(a), using the complete measurement data. The damage cannot be detected from the plots. The estimated displacements are used to predict the internal stresses of the truss members. Figures 9(b)–9(f) illustrate the stiffness variation rates in the lower and upper chord members, diagonal members, and vertical members before and after the damage. Overall, the plots exhibit very small variation rates, except for the lower chord members and vertical members, as indicated in Figure 9. This is the reason that the expanded method rarely describes accurate responses, and the lower chord members are affected by the external load. The slash lines in Figure 10 represent the elements with high stiffness variation rates by the members. It is indicated that the damages are located at the left half of the midspan rather than at the right half, representing higher stiffness variation rates. Moreover, higher internal stress rates are represented at the left half of the midspan than at the right half. The highest stiffness variation rates are concentrated on the left-end support and loading point. The abrupt stiffness change in vertical member 42 is also illustrated. It is expected that the damaged members will be positioned at the left half region of the midspan and at vertical member 42. Thus, the plots are merely used for estimation and do not clearly indicate the damaged elements. It can be concluded that this approach cannot detect the explicitly damaged elements.

This example also considers the noise effects included in the incomplete measurement data. The measurement data

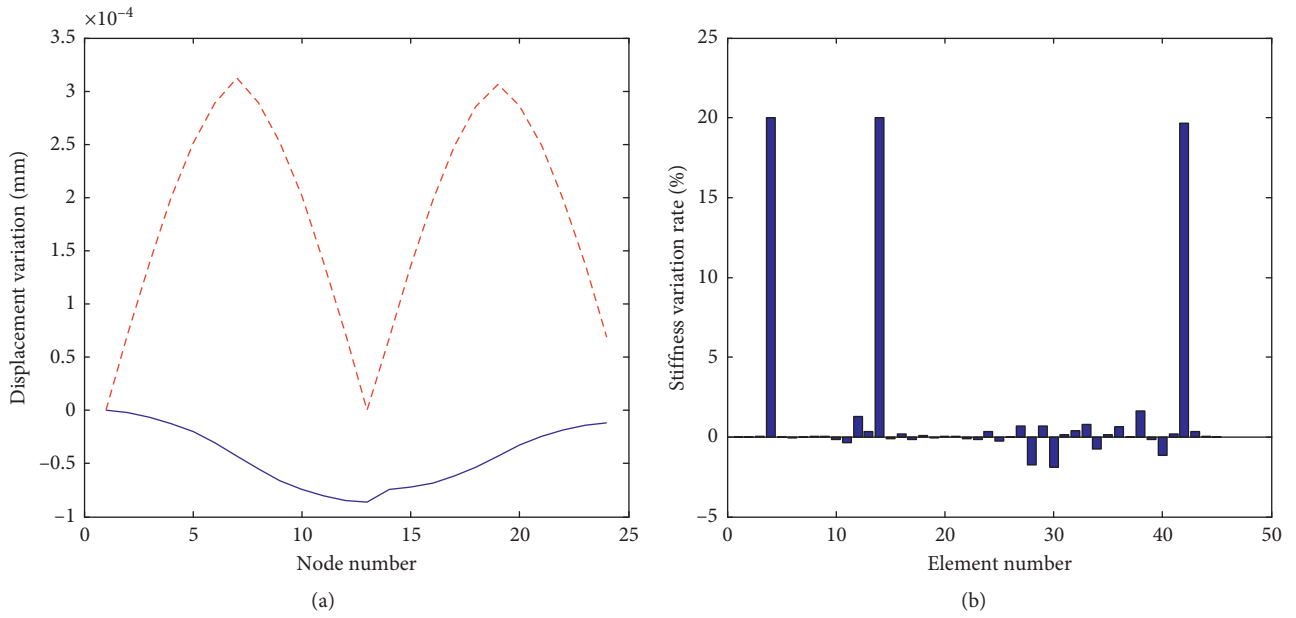


FIGURE 8: Numerical results using the complete measurement data contaminated by 1% noise level: (a) displacement variations; (b) stiffness variation rate. In (a), the solid line indicates the horizontal displacement and the dashed line indicates the vertical displacement.

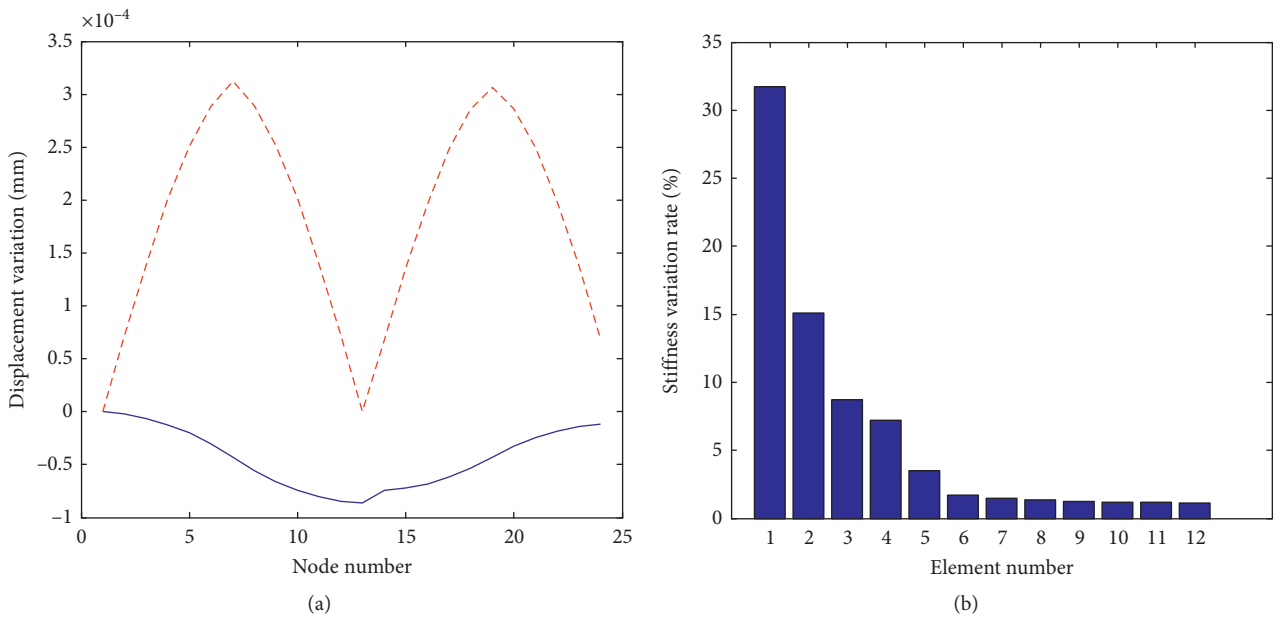


FIGURE 9: Continued.

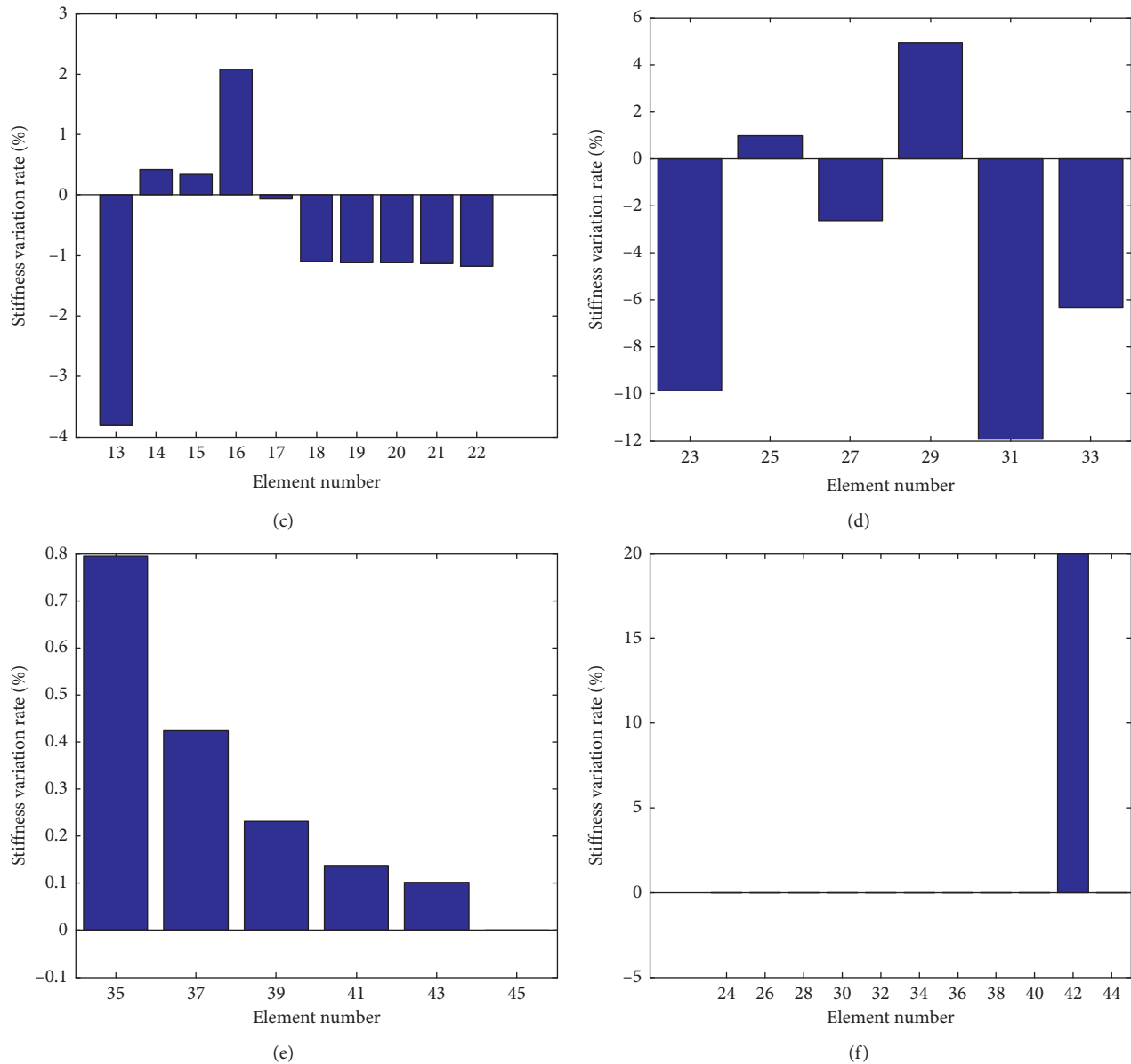


FIGURE 9: Damage detection using the expanded noise-free measurement data: (a) displacement variations; (b) stiffness variation rate at lower chords; (c) stiffness variation rate at upper chords; (d) stiffness variation rate at “ $P$ ”-type diagonal elements; (e) stiffness variation rate at “ $V$ ”-type diagonal elements; (f) stiffness variation rate at vertical elements. In (a), the solid line indicates the horizontal displacement and the dashed line indicates the vertical displacement.

are contaminated by 1% noise at the same DOFs as before and are expanded to the full set of DOFs. The numerical results are illustrated in Figure 11. The plots are very similar to those in Figure 9, and this method is not sensitive to external noise. Damage detection should be conducted by focusing on the region representing high stiffness variation rates. Thus, it is desirable to perform the analysis on the damage-expected element group with several measurement sensors, which constitutes the substructuring method.

**2.2.3. Substructuring Method.** We consider the damage detection of a substructure to be isolated from the truss structure

illustrated in Figure 12. The substructure in Figure 12 is composed of 13 elements and eight nodes. Multiple damages are located at elements 5, 17, and 29, with a 20% section loss. Measurements were taken at nine of 16 DOFs, as indicated in the figure. The number of sensors was significantly reduced, from 22 sensors in the previous test to nine in this test. The sensor locations are indicated in Figure 12. The mean values of the 10 repeated numerical experiments were taken for reducing the noise effect contained in the measurement data. The number of measurement locations is fewer than the substructure order, and data expansion is carried out.

Figure 13 displays the stiffness variation rate plots corresponding to the noise-free and 5% noise cases. Both

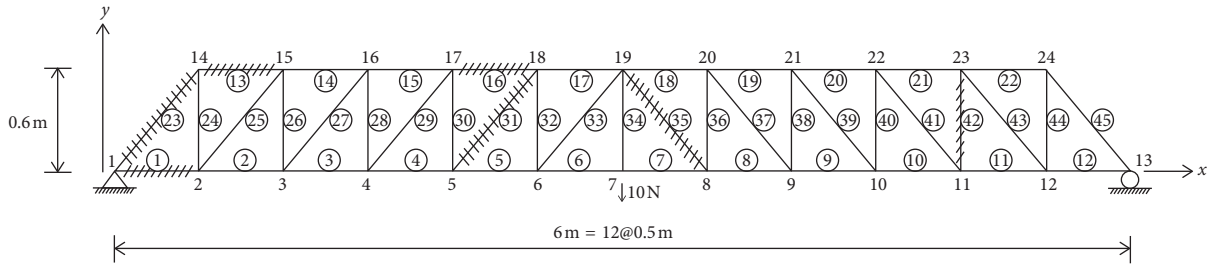
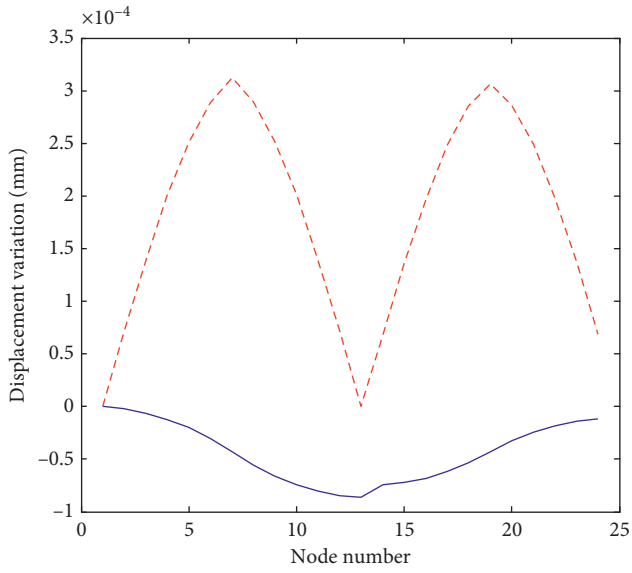
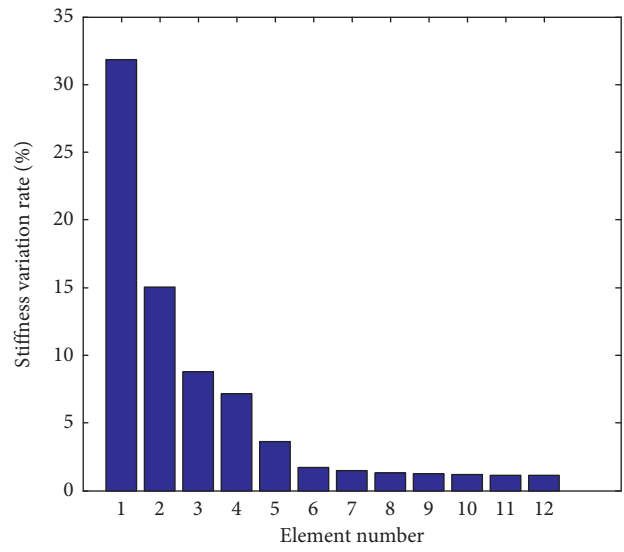


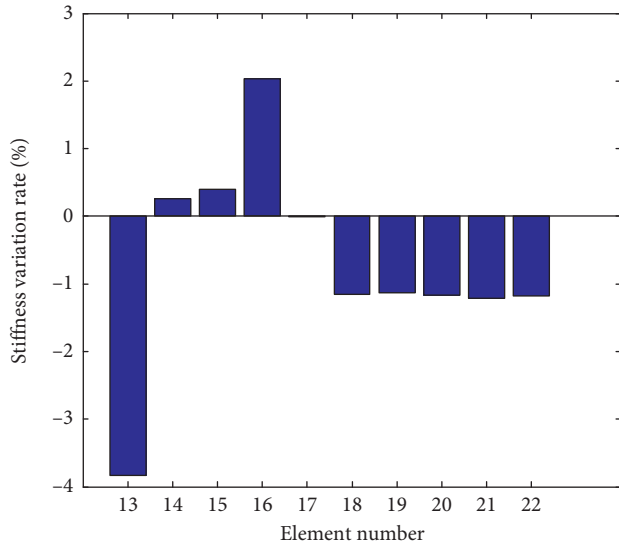
FIGURE 10: Truss members to represent high stress variation rates.



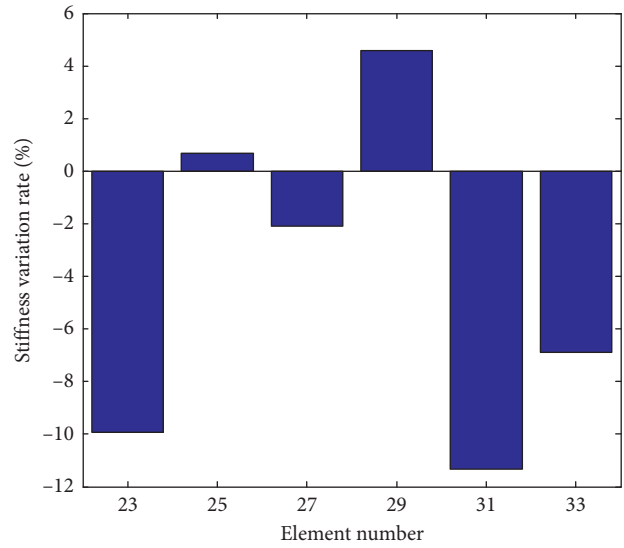
(a)



(b)



(c)



(d)

FIGURE 11: Continued.

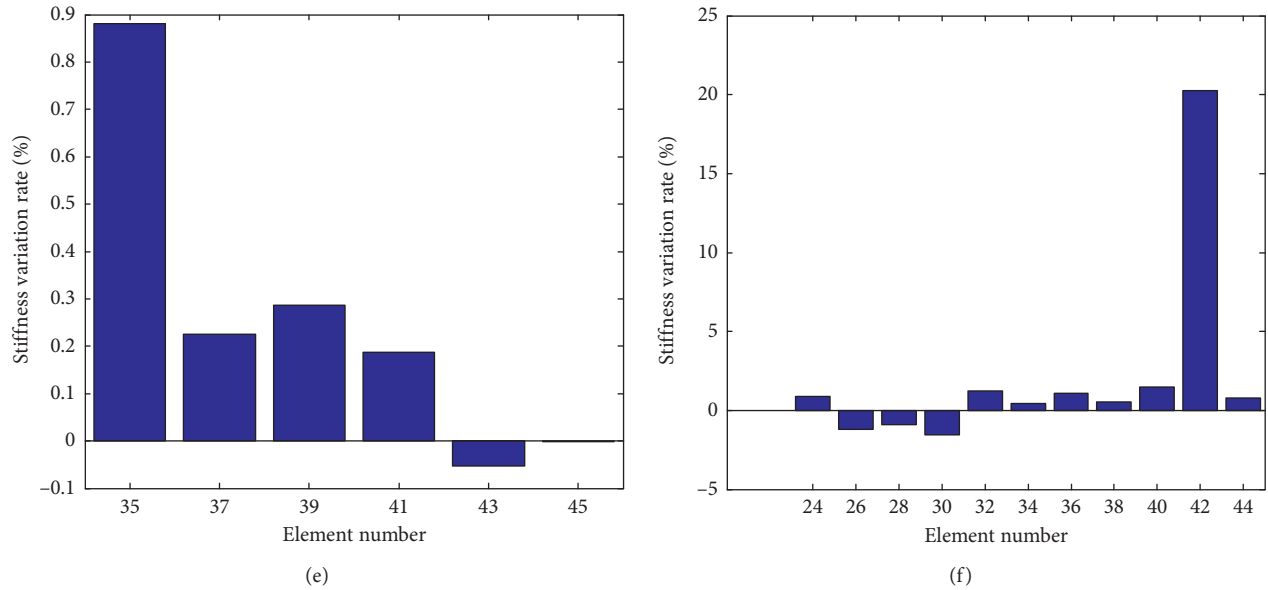


FIGURE 11: Damage detection using the expanded data contaminated by 1% noise: (a) displacement variations; (b) stiffness variation rate at lower chords; (c) stiffness variation rate at upper chords; (d) stiffness variation rate at diagonal elements; (e) stiffness variation rate at diagonal elements; (f) stiffness variation rate at vertical elements. In (a), the solid line indicates the horizontal displacement and the dashed line indicates the vertical displacement.

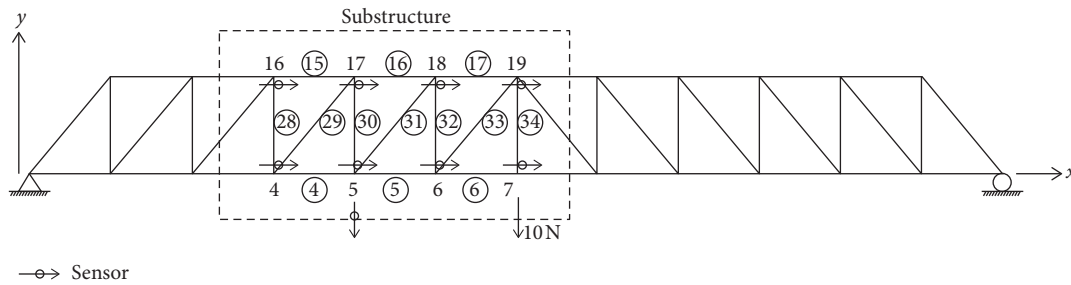


FIGURE 12: A substructure isolated from the entire truss structure.

cases demonstrate that the damage at elements 5 and 17 of the lower and upper chord members can be explicitly detected. Moreover, the diagonal and vertical elements 28, 29, and 30 display the same damage rate of 20%, and it is believed that the damage is located at one of these. The damage of the diagonal and vertical members can be estimated by the installation and measurement of additional sensors. It is observed that the method is not sensitive to noise from the plots. The large stiffness variation rate at elements 33 and 34 is owing to the external load because these are adjacent to the loading point.

**2.2.4. Dynamic Substructuring Approach.** The dynamic approach begins with the measured mode shape data, as with the displacements in the static approach. The stiffness variation rate is calculated by the mode shape data. This work uses the complete or incomplete mode shape data corresponding to the first natural frequency only. The incomplete mode shape data are expanded by equation (3)

with the stiffness matrix in the static approach. The damage detection on the truss structure in Figure 12 is performed by means of the substructuring method. The sensor locations are the same as in the previous example. In the noise-free case illustrated in Figure 14(a), the damage at the lower and upper chord members of 5 and 17 can be explicitly detected by the abrupt stiffness variation rate. The stiffness variation rates do not coincide with the damage rate because the analysis considers the first mode only and neglects the others. The damage at diagonal member 29 is not definitely detected because the adjacent members 28, 29, and 30 exhibit similar stiffness variations. The inadequacy of the numerical results arises from the neglect of the other modes. Similar results are indicated in the 5% noise case illustrated in Figure 14(b). It is observed that the damage at the vertical or diagonal members cannot be explicitly detected, but the damage-expected region can be predicted. The plots exhibit large variation rates at the members adjacent to the loading point. The variation rates near the loading point should be carefully investigated.

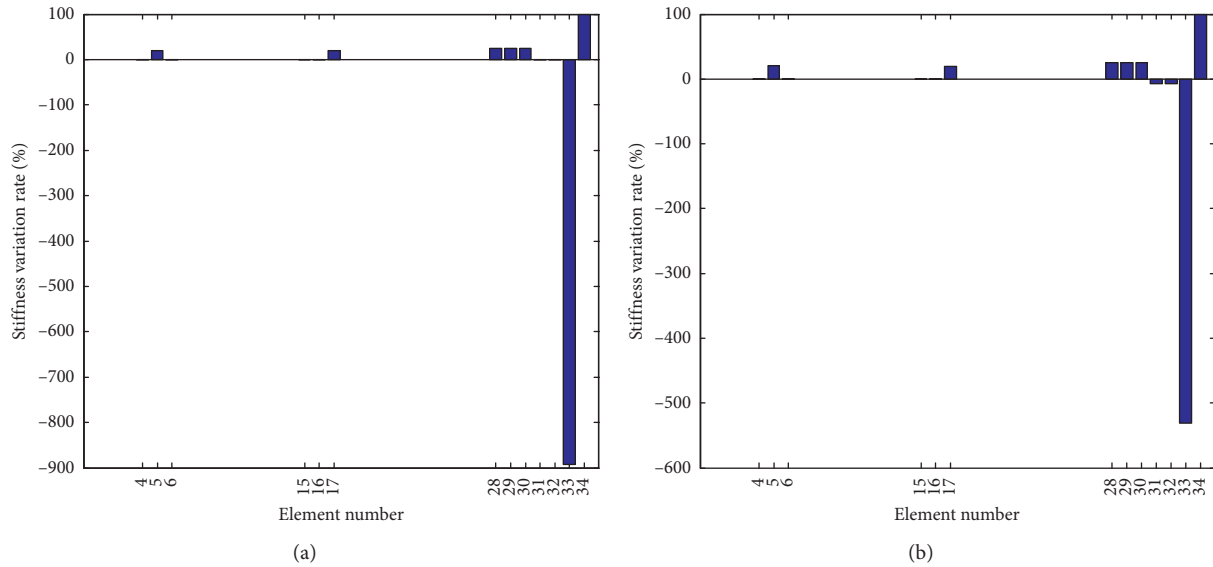


FIGURE 13: Damage detection by the substructuring method: (a) noise-free measurement data; (b) measurement data contaminated by 5% noise.

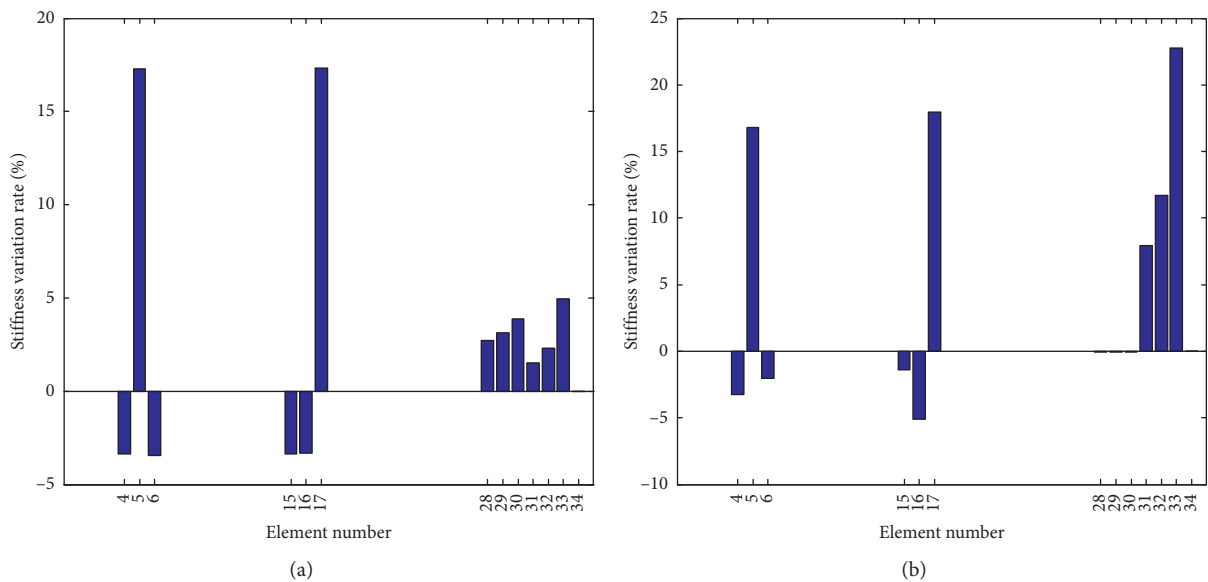


FIGURE 14: Dynamic substructuring approach: (a) noise-free measurement data; (b) measurement data contaminated by 5% noise.

According to the static-based and dynamic-based examples, it is demonstrated that the stiffness variation rate calculated by the complete and accurate displacement data indicates the accurate damage locations, despite external noise. In the case that the number of measurement sensors is fewer than the system order, the expanded dataset provides information for predicting the damage region, including the damage-expected elements. The static-based and dynamic-based damage identification approaches by means of substructuring can detect the damaged elements more clearly, despite few measurement sensors and external noise. However, the damage of the diagonal and vertical members can be predicted by the member group. The damage-

expected region should be investigated more thoroughly by means of the installation and measurement of additional sensors.

### 3. Conclusions

This work has investigated damage detection methods depending on the number of measurement locations to be causable in the evaluation of structural performance. This study has considered three different damage detection approaches utilizing complete and incomplete measurement data in an entire structure, and incomplete measurement data in substructures were compared. Furthermore, the

noise effect contained in the measurement data was investigated. The measured and expanded displacements were transformed into the internal stress of the elements, and the stiffness variation rate was used as a damage index for evaluating the damage. The complete measurement data method exhibits the drawback of requiring the same number of sensors as the system order. The incomplete measurement data method exhibits the disadvantage of unstable data expansion depending on the number and installation locations of sensors. The substructuring method offers merits in reducing the system order and number of measurement sensors and is insensitive to external noise. However, the substructuring method needs to investigate the damage-expected region more closely for accurate damage detection by means of the installation and measurement of additional sensors.

### Data Availability

The data used to support the findings of this study are available from the corresponding author upon request.

### Conflicts of Interest

The authors declare that they have no conflicts of interest.

### Acknowledgments

This research was supported by Basic Science Research Program through the National Research Foundation of Korea (NRF) funded by the Ministry of Education (NRF-2016R1D1A1A09918011).

### References

- [1] B. Blachowski, Y. An, and B. F. Spensor Jr., "Substructure-level based method for damage quantification in determinant trusses," in *Proceedings of ISMA2016 Conference: International Conference on Noise and Vibration Engineering*, Leuven, Belgium, September 2016.
- [2] K. C. Park and G. W. Reich, "Model-based health monitoring of structural systems: process, potential challenges," in *Proceedings of the 2nd International Workshop on Structural Health Monitoring*, Stanford, CA, USA, September 1999.
- [3] Z. Xing and A. Mita, "A substructure approach to local damage detection of shear structure," *Structural Control Health Monitoring*, vol. 19, pp. 309–318, 2012.
- [4] U. Ugalde, J. Anduaga, F. Martinez, and A. Iturrospe, "SHM method for damage localization based on substructuring and VARX models," 2015, <http://arxiv.org/abs/1501.01905>.
- [5] J. Hou, L. Jankowski, and J. Ou, "Substructure isolation and damage identification using free responses," *Science China Technological Sciences*, vol. 57, no. 9, pp. 1698–1706, 2014.
- [6] Y. Lei, C. Liu, Y. Q. Jiang, and Y. K. Mao, "Substructure based structural damage detection with limited input and output measurements," *Smart Structures and Systems*, vol. 12, no. 6, pp. 619–640, 2013.
- [7] E. T. Lee and H. C. Eun, "A model-based substructuring method for local damage detection of structure," *Shock and Vibration*, vol. 2014, Article ID 390769, 11 pages, 2014.
- [8] J. Li, S. S. Law, and Y. Ding, "Substructure damage identification based on response reconstruction in frequency domain and model updating," *Engineering Structures*, vol. 41, pp. 270–284, 2012.
- [9] Y. An, J. Ou, J. Li, and B. F. Spencer Jr., "Stochastic DLV method for steel truss structures: simulation and experiment," *Smart Structures and Systems*, vol. 14, no. 2, pp. 105–128, 2014.
- [10] Y. An, B. Li, and J. Ou, "An algorithm for damage localization in steel truss structures: numerical simulation and experimental validation," *Journal of Intelligent Material Systems and Structures*, vol. 24, no. 14, pp. 1683–1698, 2013.
- [11] Q. W. Yang and W. M. Jin, "Damage detection for truss structures using incomplete modes," in *Second International Workshop on Computer Science and Engineering*, Bertinoro, Italy, November 2009.
- [12] A. Kaveh and A. Zolghadr, "An improved CSS for damage detection of truss structures using changes in natural frequencies and mode shapes," *Advances in Engineering Software*, vol. 80, pp. 93–100, 2015.
- [13] Z. D. Xu and K. Y. Wu, "Damage detection for space truss structure based on strain mode under ambient excitation," *Journal of Engineering Mechanics ASCE*, vol. 138, no. 10, pp. 1215–1223, 2012.
- [14] M. Artar and A. Daloğlu, "Damage detection in simulated space frames using genetic algorithms," *Sigma Journal of Engineering And Natural Sciences*, vol. 33, no. 2, pp. 166–187, 2015.
- [15] H. C. Eun, E. T. Lee, and H. S. Chung, "On the static analysis of constrained structural systems," *Canadian Journal of Civil Engineering*, vol. 31, no. 6, pp. 1119–1122, 2004.

## Research Article

# Modeling of Energy Efficiency for Residential Buildings Using Artificial Neuronal Networks

José Antonio Álvarez,<sup>1</sup> Juan Ramón Rabuñal ,<sup>2</sup> Dolores García-Vidaurrázaga,<sup>1</sup> Alberto Alvarellos ,<sup>3,4</sup> and Alejandro Pazos<sup>4</sup>

<sup>1</sup>University of A Coruña, School of Technical Architecture, Zapateira Campus 15071, A Coruña, Spain

<sup>2</sup>University of A Coruña, Centre of Technological Innovation in Construction and Civil Engineering, Elviña Campus 15071, A Coruña, Spain

<sup>3</sup>University of A Coruña, CITIC-Research Center on Information and Communication, Elviña Campus 15071, A Coruña, Spain

<sup>4</sup>University of A Coruña, Computer Science Department, Elviña Campus 15071, A Coruña, Spain

Correspondence should be addressed to Juan Ramón Rabuñal; [juan.rabunal@udc.es](mailto:juan.rabunal@udc.es)

Received 3 August 2018; Revised 14 October 2018; Accepted 4 November 2018; Published 28 November 2018

Guest Editor: Murat Kankal

Copyright © 2018 José Antonio Álvarez et al. This is an open access article distributed under the Creative Commons Attribution License, which permits unrestricted use, distribution, and reproduction in any medium, provided the original work is properly cited.

Increasing the energy efficiency of buildings is a strategic objective in the European Union, and it is the main reason why numerous studies have been carried out to evaluate and reduce energy consumption in the residential sector. The process of evaluation and qualification of the energy efficiency in existing buildings should contain an analysis of the thermal behavior of the building envelope. To determine this thermal behavior and its representative parameters, we usually have to use destructive auscultation techniques in order to determine the composition of the different layers of the envelope. In this work, we present a nondestructive, fast, and cheap technique based on artificial neural network (ANN) models that predict the energy performance of a house, given some of its characteristics. The models were created using a dataset of buildings of different typologies and uses, located in the northern area of Spain. In this dataset, the models are able to predict the U-opaque value of a building with a correlation coefficient of 0.967 with the real U-opaque measured value for the same building.

## 1. Introduction

In the process of architectural design, the building needs to adapt its interior environment to the adequate comfort conditions. Therefore, the more adverse the weather conditions, the more effort that will have to be made by the passive and active systems of the building to maintain the level of interior comfort [1]. This circumstance generally entails an increase in energy consumption and consequently an increase in CO<sub>2</sub> emissions affecting the environment negatively [2].

According to the data provided by the Spanish Institute of Diversification and Energy Saving, the Spanish building sector destined for residential use consumes 17% of the total consumed energy and 25% of the demand for electrical energy [3]. This sector is subject to numerous initiatives of different administrations, all aimed at reducing CO<sub>2</sub> emissions and energy consumption, especially in the housing stock of buildings built

before 2006, the year when the Technical Building Code regulation in Spain started. The *Basic Document of Energy Saving* established the requirements that buildings and their thermal systems must comply with [4]. These regulations and requirements were the reason for the creation of a set of rules [5] to evaluate the energy efficiency of buildings.

In order to meet the requirements established by the regulation, we have to first evaluate the building energy efficiency and, if necessary, apply energy saving measures. Energy saving measures can be grouped into two categories:

- (i) Passive measures, which act on the constructive elements that make up the thermal envelope of the building. The intervention techniques in this category have the objective of decreasing the thermal transmittance value.
- (ii) Active measures, whose objective is to reduce the nonrenewable sources energy consumption,

increasing the performance of thermal equipment related to the conditioning of the indoor environment.

Any technique created to evaluate building energy efficiency has to include some criteria to facilitate the acquisition of knowledge about the enclosure thermal behavior and the thermal equipment [6]. It also needs to create a model, from datasets (databases) of evaluations in similar buildings [7], which provides a method for estimating the results of an evaluation. There are several approaches for creating the estimation method [8], all of which can be classified into three general categories [9]:

- (i) White box models: it is the conventional approach used in engineering
- (ii) Black box models: it is the approach used in machine learning
- (iii) Gray box models: it is a hybrid engineering/machine learning approach.

White box models range from simple statistical techniques, such as least squares or time series, to more complex numerical models that model physical systems simulating the physical laws that govern the system. These models do not achieve good results when working with large datasets [10], and the more complex the model is, the more time it takes to obtain an estimation for the energy efficiency of a building.

Black box models are created automatically from data that relate some system characteristics with the variable we want to estimate. This is called the training phase. Once the model is trained, it can give an output for the variable we want to estimate when given the system characteristics. This prediction is made quickly.

Black box models have been widely used for predicting the energy performance of buildings. Some of these uses are the prediction of heating [11], cooling [12], and electric power consumption [13–16] of buildings.

Artificial neural networks (ANNs) are one of the most widely used black box models, and they are achieving good results in a great variety of problems, including the prediction of energy consumption of a building. Some of the problems of energy estimation solved with ANN are energy test bench in buildings [17–20], electric power prediction [21–24], and heating/cooling consumption prediction [25–28].

The advantages ANNs provided with respect to more traditional engineering solutions are as follows:

- (i) They can easily create models with complex relationships between data, other than linear.
- (ii) They are fast making predictions: the process of training is slow, but once trained, the predictions are usually done in milliseconds.
- (iii) They can generalize better than traditional models if they have a class example for a region: they perform well when evaluating buildings that the model has never seen, given that we trained the model with an example fairly similar to the one never seen.
- (iv) They perform well with large datasets.

This work focuses on developing a technique for evaluating a building energy efficiency based on ANN. To achieve it, we created a dataset by evaluating the energy efficiency of a great number of buildings located in the north of Spain, focusing on residential buildings. Using this dataset, we trained and tested several different ANN architectures. The procedure is explained in the following sections.

## 2. Materials and Methods

ANNs need large datasets in order to function properly; thus, the first step for creating an ANN model for predicting the energy performance of a building is the generation of a reliable dataset [4]. The Spanish administration has not yet released the results of energy efficiency evaluations carried out since the end of 2013 in Spanish buildings [29]. There are other European Union countries where the energy certification process of existing buildings has been implemented for a longer period of time, such as Italy or Denmark. In these countries, there are web applications available that allow to query the results of the energy efficiency evaluation for all the evaluated buildings.

Due to this lack of data for Spanish buildings, in this work, we created the dataset that is used to train and evaluate ANN-based models. This dataset was generated from the evaluation of the energy efficiency of a number of buildings destined for different uses located in the north of Spain. The dataset is composed of data from 453 buildings, resulting in a total usable area of 570,438.30 m<sup>2</sup>. The classification of the buildings by destined use can be seen in Table 1. From those buildings, our work focuses on those with residential use.

A dataset is composed of individual examples. Each example consists of several input variables (features) and one or more outputs. The building energy efficiency evaluation procedure established by the current regulations generates two categories of data [30]:

- (i) Data regarding the thermal envelope: the thermal envelope affects the demand for heat energy, that is, the amount of energy needed to condition the interior environment in the building during the winter regime.
- (ii) Data regarding the thermal equipment: the thermal equipment affects the energy consumption, and it is related to the CO<sub>2</sub> emission level.

These data give us the input and output variables of our training set. One of the difficulties a certified technician faces when evaluating the energy efficiency of a building [31] is determining the real thermal transmittance of the building enclosure that is in contact with the air (U-opaque), information that allows to accurately estimate the losses of heat energy. The difficulty arises from the lack of information regarding the different inner layers of the opaque zone of the exterior enclosure. This difficulty could be overcome with the development of a model that allows the prediction of the thermal transmittance value U (measured in W/°K·m<sup>2</sup>) from other known building characteristics [32]. The objective of the ANN created in this work is to calculate this value using some easily obtained building characteristics.

TABLE 1: Buildings dataset by destined use.

Description	Quantity
Single family home	124
Block housing	292
Complete residential block (residential building)	4
Commercial building (shopping centers)	10
Public building (administrative and teaching buildings)	11
Residential group (hotels)	9
Hospital center (hospitals and health centers)	3
Total	453

One of the officially recognized tools for energy efficiency certification of existing buildings is named CE3X [33]. This tool consists of a user manual and a software that allows to simulate the behavior of a building regarding energy efficiency and calculate the impact of energy saving measures in the building energy efficiency. Using this tool with our ANN, we can obtain a value that indicates the building energy efficiency in terms of a variable that ranges from A+ to G.

*2.1. Training the ANN Model.* An ANN network consists of several elementary units, called neurons, organized in layers. There are three types of layers: input, hidden, and output layers. The input layer consists of the same number of neurons as the input variables we want to use. The output layer has as many neurons as output variables our dataset does. Between the input and output layers, we can place as many hidden layers as we desire with as many neurons per layer as we choose. Usually, all the neurons in a layer are connected to all the neurons of the following layer (feed forward and full connected), where each connection has an associated weight. This is the architecture we chose for our models.

The function of each neuron is to sum the results of multiplying each of its inputs with the associated weight for the input connection and apply a function to the result. This function is called the activation function.

The process of creating an ANN-based model is divided in the training and testing phases. The training phase consists in finding the best parameters that allow the model to infer the output(s) given the inputs, with the minimal overall error over the training set. This phase includes the selection of the architecture for the network. As said before, the problem we try to solve determines the input and output architectures of the network (as the input and output variables are determined by the problem). The selection of the number of hidden layers, elements per hidden layer, and the activation function of the elements is done manually. Usually, several architectures are selected and the training phase consists in training these different ANNs until we find the one that provides the best result for the problem at hand.

During the training phase, the connection weights are adjusted in an iterative manner in order to minimize the error between the real output of the dataset and the output the network provides. This adjustment is repeated many times (iterations or epochs) for all the training dataset until a

sufficient accuracy is achieved. In this work, we used the gradient descent-based backpropagation method for training the networks [34]. These types of algorithms try to minimize a value, usually the network error, propagating back the error to the hidden layer and updating the connections weights appropriately. The value the backpropagation method is trying to minimize is the error the network has over all the training set examples. As the network output variable is a real number, the error is set to be the mean square error (MSE). The backpropagation algorithm we chose is the Levenberg–Marquardt variation.

One of the problems ANNs has is variance (overtraining): if we train the network for a long time, with a converging algorithm, the network is going to have a low, even near zero, error over the training set but a much higher error over examples the network has never seen. There are several methods to minimize variance. We chose early stopping for training our ANN. This technique consists in further dividing the train set in a training and validation set. During the training process, the network error is calculated in the training set and the network weights are updated according to this error. Once updated, we calculate the error in the validation set. In the early iterations, both the training and validation errors decrease, up to a point where the training error continues to decrease but the validation error increases. This indicates that the network is overtraining. Early stopping consists in stopping when this point is reached.

### 3. Results and Discussion

As said before, the building dataset was created from a sample of buildings in the north of Spain. The thermal transmittance and the average values of several energy efficiency parameters for buildings in the dataset can be seen in Table 2.

As previously said, the objective of the ANN we created is to be able to calculate the U-opaque value for a building from a set of easily obtained variables. The variables we chose to create the dataset are the year of manufacture of the building, the area of the building, its two GPS coordinates, and the thermal transmittance of the opaque area of the envelope (U-opaque). Therefore, the ANN will have 4 inputs and one output (U-opaque prediction).

The northwest of Spain is made up of small and medium-sized towns, where there are few construction companies available. Using the GPS coordinates was thought to potentially capture this peculiarity: a company works in a close region using the same techniques and materials for a given period. The period is captured in the year of construction. The area of the building was thought to be related to the heat loss, so we also included this variable.

Although there may be other variables that could improve the prediction of the U-value, the values for the chosen variables are easily obtained and, almost always, publicly available (for instance, we could use the model for predicting the U-value for a house that is being advertised for sale).

For the design and training of ANN, we used the software MATLAB with artificial neural networks toolbox. Using this computer tool, we can train, validate, and test an ANN.

TABLE 2: Energy and environmental behavior summary for chosen building samples.

Description	Transmittance (W/°K·m <sup>2</sup> )		Energy efficiency average values		
	U-opaque	U-gap	CO <sub>2</sub> emissivity (CO <sub>2</sub> kg/m <sup>2</sup> ·y)	Heating demand (kWh/m <sup>2</sup> ·y)	Energy consumption (kWh/m <sup>2</sup> ·y)
Single family home	1.14	3.55	68.54	142.26	322.59
Block housing	1.21	3.64	62.22	114.22	270.8
Complete residential block	1.17	4.5	29.94	46.01	133.24
Commercial building	0.66	3.58	28.66	57.44	169.06
Public building	0.91	3.53	41.59	67.21	204.79
Residential group	0.76	3.24	34.14	31.77	178.28
Hospital	0.82	3.78	31.9	26.53	171.13

We used an iterative approach for creating the final ANN. In each iteration, we improve upon the results obtained in the previous iteration. We tested different ANN architectures with different hidden layers, different number of neurons in the hidden layer, and different activation functions in the neurons. The ANN was trained using 90% of the examples for training and 10% for validation.

### 3.1. First Training Iterations: Hyperparameters Selection.

In order to check if ANNs could provide a good solution for the problem at hand, the first tests were done using a small train set consisting of 138 buildings (named as “in blocks”). These tests were aimed at selecting the best hyperparameters for the ANN: number of layers and elements per layer, activation functions, and number of inputs.

The first iteration intended to choose the best activation function. We used two hidden layers, with 10 neurons and 5 neurons, respectively. With this configuration, after 10 training executions for the *TANSIG* function, the network achieved an average correlation of 0.746. Training the same initial ANN during 10 executions, changing the function to *LOGSIG*, made the ANN achieve an average correlation coefficient of 0.821. These results indicate that the *LOGSIG* is the best activation function for this problem, and it is the one that we used in the following iterations (Figure 1).

In the next iteration, we tested a configuration with a single hidden layer. We tested several architectures, ranging from 10 to 100 neurons in the hidden layer. Using 10 neurons, the ANN achieved a correlation of 0.56. A correlation of 0.82 resulted from using 50 neurons and a correlation of 0.96 using 100 neurons in the hidden layer. Although the best results were obtained using 100 neurons in the hidden layer, this configuration is not recommended, since we have almost the same neurons as training examples and this can easily produce an overtraining and limit the network generalization capacity.

In the next iteration, we carried out more tests using an architecture with 2 hidden layers. The number of elements in the first layer ranged from 5 to 30 and between 5 and 20 for the second layer (for a maximum of 50 neurons between both). We performed 10 equal executions for each resulting combination of elements in order to avoid the randomness of the training process. With an architecture of 5-5, the ANN

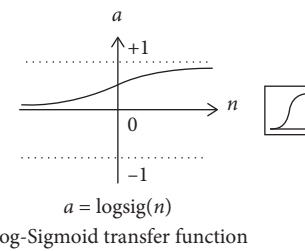


FIGURE 1: Activation function that produces the best results.

obtained an  $R = 0.656$  and  $R = 0.749$  for 10-5,  $R = 0.901$  for 10-10,  $R = 0.949$  for 15-1,  $R = 0.969$  for 15-15, and  $R = 0.987$  for 20-15.

Although the architectures with the highest number of elements in the hidden layers achieved similar values, the one with 20 elements in the first hidden layer and 15 in the second achieved the best results. This indicates that this architecture is the most suitable to solve the problem at hand. As previously explained, we chose the *LOGSIG* activation function for all neurons because it gave the best results in a previous iteration.

In Figure 2, we can see a comparison between the ANN predictions and the U-opaque real measured values as well as the correlation value obtained for the chosen 20-15 architecture.

In the next iteration, in order to analyze the ANN inputs sensitivity and to select the most representative ones, we trained several ANNs with the same architecture and different input combinations. In Figures 3–6 we can see the results obtained when using only a subset of all the inputs.

As we can see in the graphs 4 to 6, the *year of construction* and the *usable area* of a building are the variables that have more prediction power, the *usable area* of the building having a greater incidence in the prediction. In the next iteration, we use these two variables as inputs for the network.

**3.2. Training Process: Parameters Search.** Once these tests have been carried out and the viability of ANNs to solve the prediction of U-opaque has been confirmed, we created a dataset with a greater number of training and validation examples. We used this dataset to search for the best model

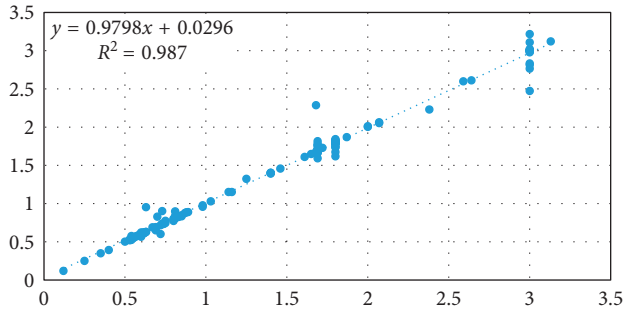


FIGURE 2: U-opaque prediction using 4 inputs: construction year, useful area, latitude, and longitude.

parameters (the network weights). The dataset is divided into 2 categories: *block buildings* (238 training examples) and *single-family buildings* (94 training examples). For this dataset, we used the same ANN architecture used in the initial test. We carried out two training tests, training two identical ANN, one in each category of the dataset, in order to check the training degree and generalization capacity of the ANN obtained in the initial test. For these tests, several errors (10 in total over the U-opaque value of the training file) were randomly introduced to verify the capacity of the ANN to isolate these anomalous behaviors.

In Figure 7, we show the comparison of the 2 ANNs, one of them using the data with errors (represented by the points in blue).

As we can see, the results are very similar and the behaviors with the most amplitude values are also very similar.

A comparison between the ANN trained in the new dataset and the real measured U-opaque values for the 238 block buildings of the dataset can be seen in Figure 8.

In Figure 9, we can see a case by case comparison between the same values in Figure 8 and the error the ANN has for these examples.

A comparison between the ANN trained in the new dataset and the real measured U-opaque values for the 94 single-family buildings of the dataset can be seen in Figure 10.

In Figure 11, we can see a case by case comparison between the same values in Figure 10 and the error the ANN has for these examples.

These results indicate that the ANNs created are capable of predicting the U-opaque with a high degree of correlation for both types of buildings.

**3.3. Training Process: Building a Single Model.** In the next iteration, we tried to obtain a single ANN that allowed the prediction of U-opaque for both types of buildings. In order to achieve this, we created a single training set combining both types of buildings (with a total of 334 training examples). A comparison between the ANN trained in this new dataset and the real measured U-opaque values for the 334 buildings of the dataset can be seen in Figure 12.

These results are not satisfactory. The ANN is not capable of differentiating the U-opaque behaviors from similar values due to the difference in the typology of the building, as

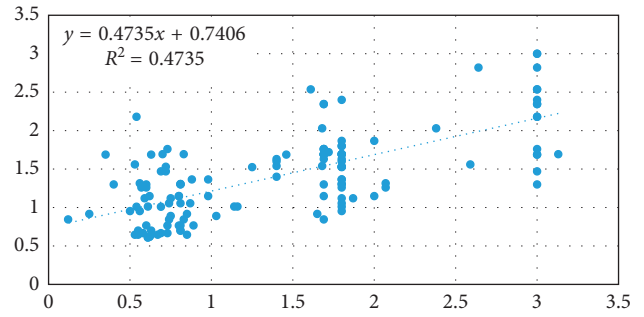


FIGURE 3: U-opaque prediction using only the year of construction of the building.

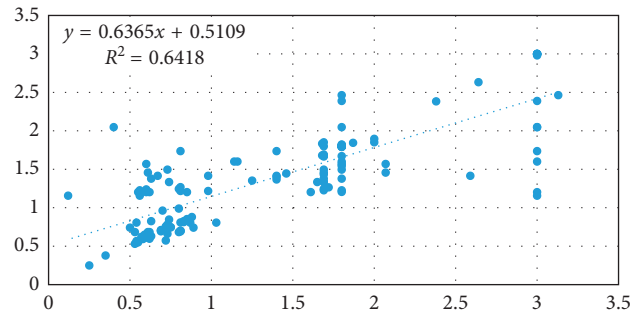


FIGURE 4: U-opaque prediction using only the usable area of the building.

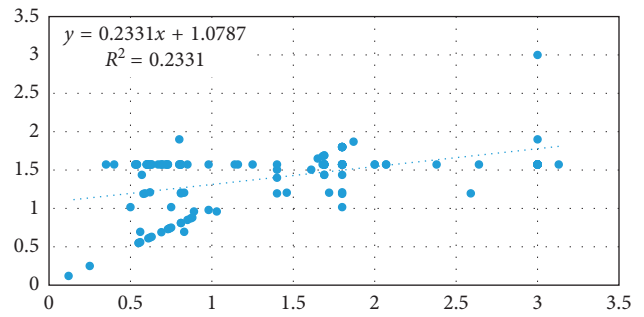


FIGURE 5: U-opaque prediction using the latitude and longitude of the building.

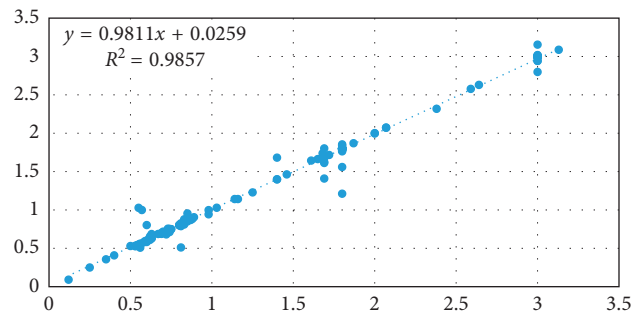


FIGURE 6: U-opaque prediction using the year of construction and the usable area of the building.

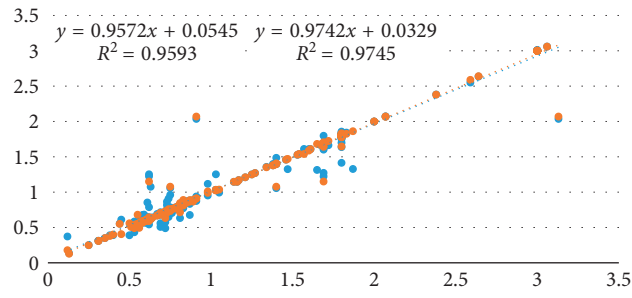


FIGURE 7: ANN training results for the prediction of the U-opaque of block buildings.

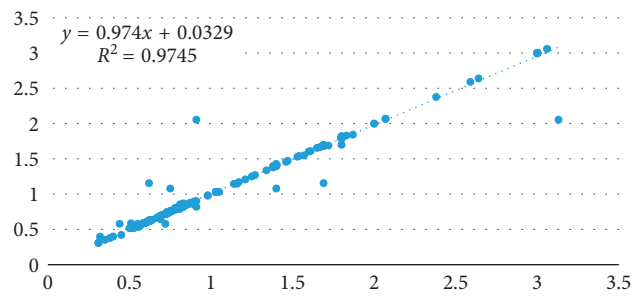


FIGURE 8: ANN training results for the prediction of the U-opaque in block buildings.

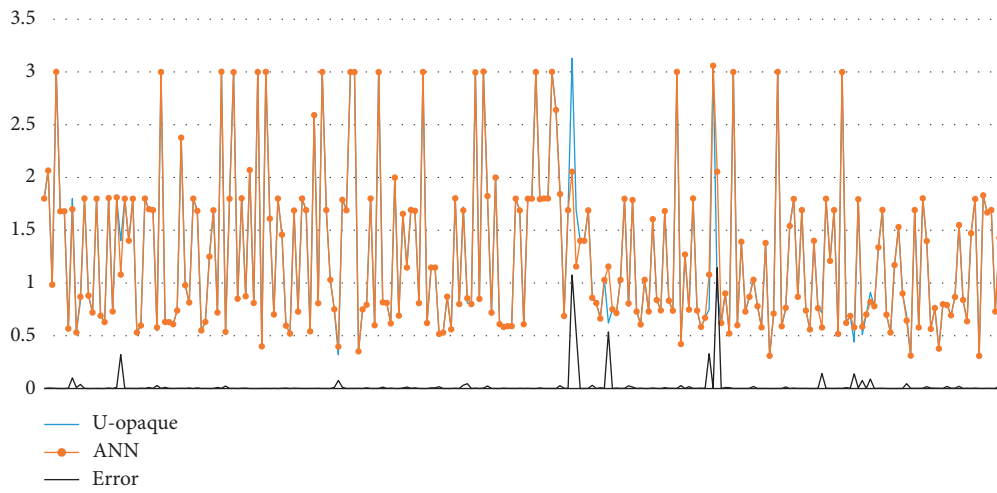


FIGURE 9: Comparison between measured and ANN predicted U-opaque values for block buildings.

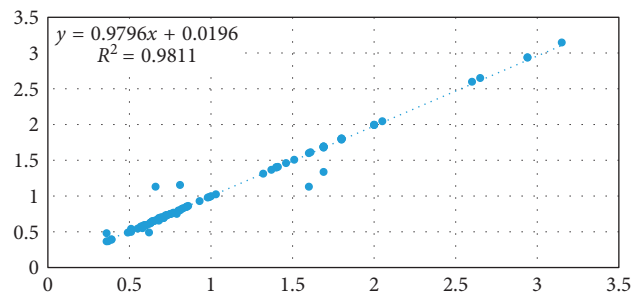


FIGURE 10: ANN training results for the prediction of the U-opaque in single-family buildings.

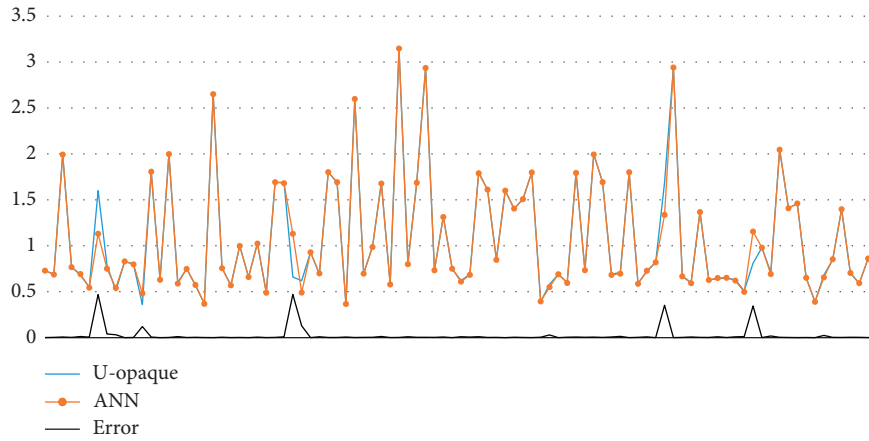


FIGURE 11: Comparison between measured and ANN predicted U-opaque values in single-family buildings.

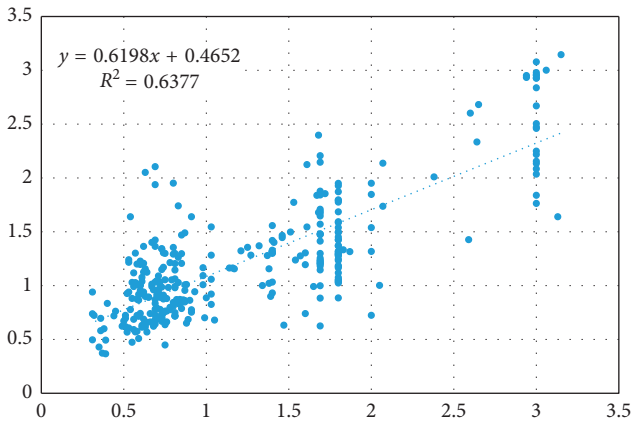


FIGURE 12: ANN training results for the prediction of the U-opaque in single-family and block buildings.

it can be observed, for example, around values of the 1.75 prediction of the U-Opaque.

To solve this lack of necessary information for the ANN, we created an additional input variable indicating the type of building, with value 0 for the single-family buildings and 1 for the block building. Therefore, the ANN will have 3 inputs and 1 output.

A comparison between the ANN trained in this new dataset and the real measured U-opaque values for the 334 buildings of the dataset can be seen in Figure 13, where we can see that the ANN has a good modeling capacity for the prediction of the U-opaque of both types of buildings.

In Figure 14, we can see a case by case comparison between the same values in Figure 13 and the error the ANN has for these examples.

Once the ANN for the different types of buildings was made, a sensitivity analysis of the ANN was carried out. To do so, we put some fictitious values in the dataset trying to simulate all the possible inputs that the ANN may have in the variable range and we evaluate the network in this variable grid. For this reason, all the buildings were analyzed. The years of construction of the building vary between 1900 and 2014, and the area of the building varies between 32.5 m<sup>2</sup> and 654 m<sup>2</sup>. With these characteristics, regular intervals were

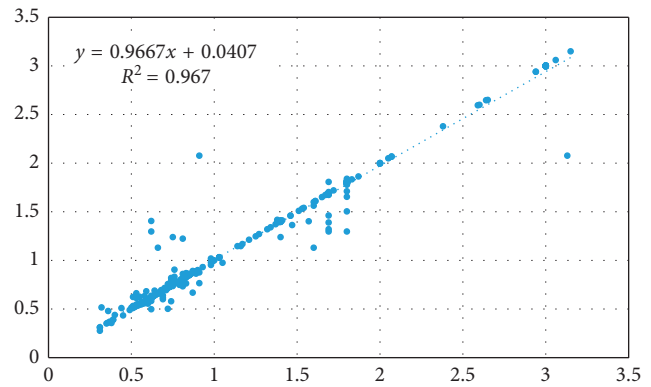


FIGURE 13: ANN U-opaque prediction results for all building types (ANN with additional building type input).

used for both inputs, for example, the values 1900, 1930, 1960, 1990, and 2015 have been used for the year, and the area varying linearly in 20 square meters increments (30, 50, 70, . . . , 650).

It should be noted that the ranges of the inputs for single-family buildings and block buildings are different (for example, in relation to the area, for single-family buildings the maximum is 654 m<sup>2</sup>, and for block buildings, the maximum area is 300 m<sup>2</sup>); however, the same configuration has been used to jointly analyze the results for both types of buildings.

The result of the ANN for both types of building can be seen in Figures 15–17.

We can see in Figure 15 a trend: newer buildings have lower U-opaque values. We corroborate this trend in Figure 16, where the ANN behavior for both types of buildings is similar: the older the building is, the higher the U-opaque average values are.

It should be noted that in block buildings, in the 2015 tests, zero values are produced when the usable areas are greater than 300 m<sup>2</sup>, which can be understood as situations in which ANN has not been trained, as the maximum values are below 300 m<sup>2</sup>.

We can see in Figure 17 that a downward trend in the value of the U-Opaque is verified as the area of the building

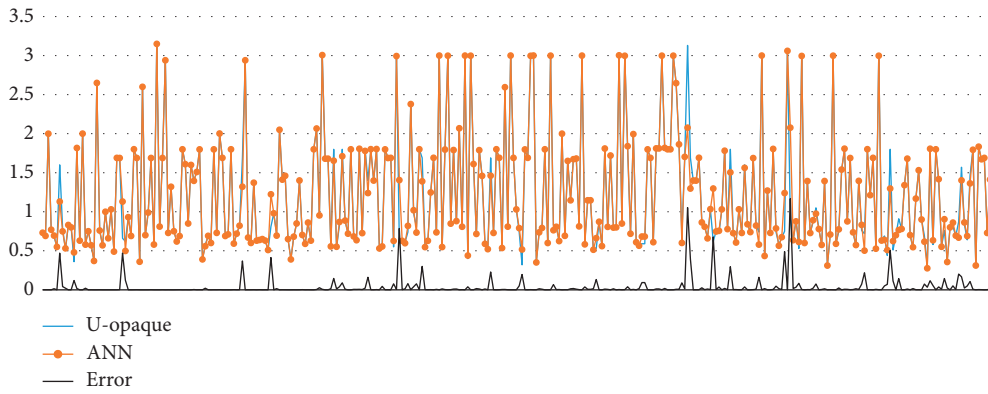


FIGURE 14: Comparison between measured and ANN predicted U-opaque values for all building types.

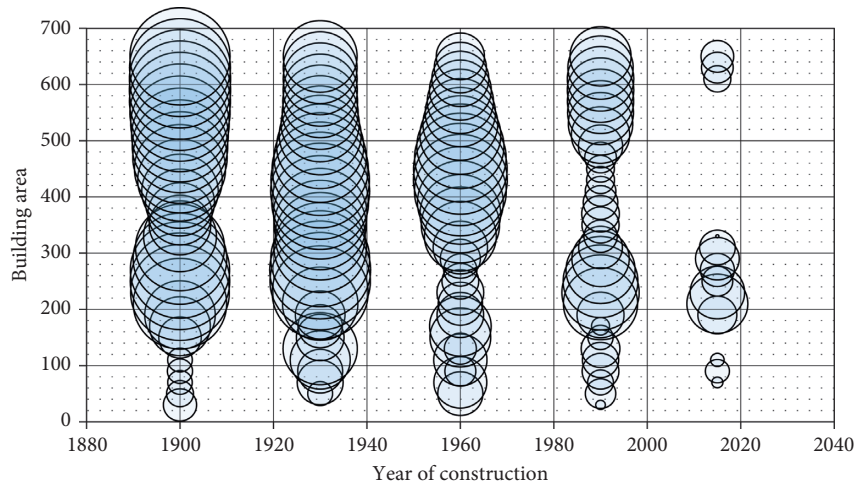


FIGURE 15: Sensitivity analysis results: U-opaque value for all variables. The relative bubble size is the U-opaque value.

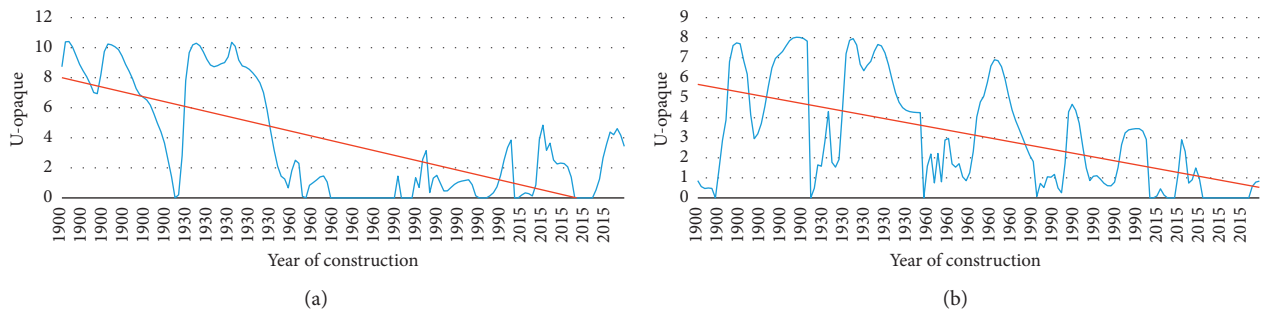


FIGURE 16: Sensitivity analysis results: U-opaque value versus year of construction. (a) Single-family buildings. (b) Block buildings.

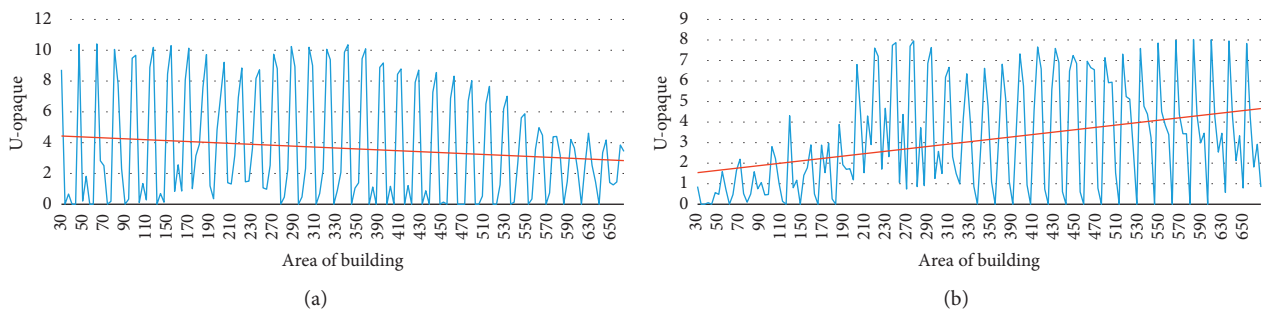


FIGURE 17: Sensitivity analysis results: U-opaque value versus area of the building. (a) Single-family buildings. (b) Block buildings.

increases for single-family buildings, while the opposite occurs in block buildings. This can be considered a coherent behavior, since the buildings with greater usable area usually correspond to a higher thermal quality standard in single-family buildings; therefore, the materials and constructive solutions used for the composition of the envelopment have a lower transmittance value. As we said, the opposite trend occurs in block buildings. A possible explanation of this behavior could be the fact that modern block buildings tend to be smaller, and thus more thermally efficient, but we need a detailed analysis to find the cause of this behavior.

We also observe in Figure 17 an oscillatory behavior, indicating that the network is not generalizing well for some ranges. This behavior could be mitigated by using a bigger dataset or trying a more suitable weight initialization.

#### 4. Conclusions and Future Developments

As the results indicate, ANNs are a good model for predicting the U-Opaque of a building using several of its characteristics. The outputs of the ANNs trained in our dataset have a high correlation coefficient with the real U-Opaque measured values for the same buildings.

We carried out several tests using different characteristics of a building as the ANN input variables. The building year of construction and the area of the building are the variables that have more prediction power for the U-opaque value, being the constructed area the one with the highest prediction power.

Using a single ANN for predicting the U-opaque value for both block buildings and single-family buildings and comparing its outputs with the real U-Opaque measured values for the same buildings, we obtained a correlation coefficient of 0.967 and a satisfactory generalization capacity as shown in the results.

The results of this work indicate that it is possible to estimate the energy efficiency of a building in a given geographic zone with a high degree of accuracy using some building characteristics, without doing an intervention in the building or using measurement devices. This supposes a great advance in the field of architecture, because the U-Opaque measurement is a costly and time-consuming task.

However, as explained before, ANNs are considered a black box system in the sense that we input some values to the network and the ANN produces an output without being able to know how these results are produced. But in the Civil Engineering and Architecture fields, it is important to be able to explain the processes that occur in a system or model, so in order to be able to have an explanation of how a model works for predicting the U-Opaque value of a building and be able to extract some formula that explains the model behavior, we plan to use another machine learning technique called evolutionary computation. Using the genetic expressions algorithm, we would be able to extract the model knowledge in the form of mathematical equations. This algorithm allows to obtain simple mathematical expressions, but with a low correlation value or predictive capacity. Using genetic programming algorithms and introducing trigonometric operators, we can obtain mathematical equations with a higher correlation coefficient, although the obtained equations can be more complex.

#### Data Availability

The energy efficiency dataset used to support the findings of this study has been deposited in the GitHub repository <https://github.com/mereshow/ann-energy-efficiency.git>.

#### Conflicts of Interest

The authors declare that there are no conflicts of interest regarding the publication of this paper.

#### References

- [1] M. P. Linares Alemparte, *CTE and Ventilation. Conference: "Ventilation in Buildings and their Consequences on Energy Demand, Acoustics and Air Quality"*, Laboratory of Quality Control in the Construction of the Basque Government, Vitoria-Gasteiz, Spain, 2011.
- [2] Ministry of Industry, Energy and Tourism-Secretary of State for Energy, *National Action Plan for Energy Efficiency 2014-2020*, Ministry of Industry, Energy and Tourism-Secretary of State for Energy, Madrid, Spain, 2014.
- [3] Institute of Diversification and Energy Saving (Department of Planning and Studies) IDAE, *Sech-Spahousec Project, Analysis of the Energy Consumption of the Residential Sector in Spain (FINAL REPORT)*, Institute of Diversification and Energy Saving, Madrid, Spain, 2011.
- [4] Government of Spain-Ministry of Housing, *Royal Decree 314/2006, of 17 March, Approving the Technical Building Code, BOE no. 74*, Government of Spain-Ministry of Housing, Madrid, Spain, 2006.
- [5] Government of Spain-Ministry of Development-General Directorate of Architecture, Housing and Land, *Observatory of Housing and Land. Annual Bulletin Year 2015*, General Directorate of Architecture, Housing and Land, Madrid, Spain, 2016.
- [6] European Parliament, *Directive 2012/27/EU of the European Parliament and of the Council of 25 October 2012 on Energy Efficiency, Amending Directives 2009/125/EC and 2010/30/EU, and the Repeal of Directives 2004/8/EC and 2006/32/EC*, OJEU, Brussels, Belgium, 2012.
- [7] Government of Spain-Head of State, *Law 38/1999, of November 05, on Building Ordination (LOE). BOE no. 266*, Government of Spain-Head of State, Madrid, Spain, 1999.
- [8] F. Khayatian and L. Sarto, "Application of neural networks for evaluating energy performance certificates of residential buildings," *Energy and Buildings*, vol. 125, pp. 45–54, 2016.
- [9] H.-X. Zhao and F. Magoulès, "A review on the prediction of building energy consumption," *Renewable and Sustainable Energy Reviews*, vol. 16, pp. 3586–3592, 2012.
- [10] Ministry of Energy, *Tourism and Digital Agenda-Secretary of State for Energy: Energy in Spain 2015*, Institute for Energy Diversification and Saving, Madrid Spain, 2016.
- [11] R. Ž. Jovanovic, A. A. Sretenovic, and B. D. Živkovic, "Ensemble of various neural networks for prediction of heating energy consumption," *Energy and Buildings*, vol. 94, pp. 189–199, 2015.
- [12] Q. Li, Q. Meng, J. Cai, H. Yoshino, and A. Mochida, "Predicting hourly cooling load in the building: a comparison of support vector machine and different artificial neural networks," *Energy Conversion and Management*, vol. 50, no. 1, pp. 90–96, 2009.
- [13] A. Azadeh, S. Ghaderi, S. Tarverdian, and M. Saberi, "Integration of artificial neural networks and genetic algorithm to

- predict electrical energy consumption,” *Applied Mathematics and Computation*, vol. 186, no. 2, pp. 1731–1741, 2007.
- [14] A. Ahmad, M. Hassan, M. Abdullah et al., “A review on applications of ANN and SVM for building electrical energy consumption forecasting,” *Renewable and Sustainable Energy Reviews*, vol. 33, pp. 102–109, 2014.
- [15] M. Aydinalp-Koksal and V. I. Ugursal, “Comparison of neural network, conditional demand analysis, and engineering approaches for modeling end-use energy consumption in the residential sector,” *Applied Energy*, vol. 85, no. 4, pp. 271–296, 2008.
- [16] P. A. González and J. M. Zamarrero, “Prediction of hourly energy consumption in buildings based on a feedback artificial neural network,” *Energy and Buildings*, vol. 37, no. 6, pp. 595–601, 2005.
- [17] S.-M. Hong, G. Paterson, D. Mumovic, and P. Steadman, “Improved benchmarking comparability for energy consumption in schools,” *Building Research and Information*, vol. 42, no. 1, pp. 47–61, 2014.
- [18] M. Yalcintas, “An energy benchmarking model based on artificial neural network method with a case example for tropical climates,” *International Journal of Energy Research*, vol. 30, no. 14, pp. 1158–1174, 2006.
- [19] M. Yalcintas and U. Aytun Ozturk, “An energy benchmarking model based on artificial neural network method utilizing us commercial buildings energy consumption survey (CBECS) database,” *International Journal of Energy Research*, vol. 31, no. 4, pp. 412–421, 2007.
- [20] R. Kumar, R. K. Aggarwal, and J. D. Sharma, “Energy analysis of a building using artificial neural network: a review,” *Energy and Buildings*, vol. 65, pp. 352–358, 2013.
- [21] R. Platon, V. R. Dehkordi, and J. Martel, “Hourly prediction of a building’s electricity consumption using case-based reasoning, artificial neural networks and principal component analysis,” *Energy and Buildings*, vol. 92, pp. 10–18, 2015.
- [22] M. Aydinalp, V. I. Ugursal, and A. S. Fung, “Modeling of the appliance, lighting, and space-cooling energy consumptions in the residential sector using neural networks,” *Applied Energy*, vol. 71, no. 2, pp. 87–110, 2002.
- [23] K. Li, C. Hu, G. Liu, and W. Xue, “Building’s electricity consumption prediction using optimized artificial neural networks and principal component analysis,” *Energy and Buildings*, vol. 108, pp. 106–113, 2015.
- [24] H. R. Khosravani, M. Castilla, M. Berenguel, A. Ruano, and P. Ferreira, “A comparison of energy consumption prediction models based on neural networks of a bioclimatic building,” *Energies*, vol. 9, no. 1, p. 57, 2016.
- [25] Z. Hou, Z. Lian, Y. Yao, and X. Yuan, “Cooling-load prediction by the combination of rough set theory and an artificial neural-network based on data-fusion technique,” *Applied Energy*, vol. 83, no. 93, pp. 1033–1046, 2006.
- [26] B. B. Ekici and U. T. Aksoy, “Prediction of building energy consumption by using artificial neural networks,” *Advances in Engineering Software*, vol. 40, no. 5, pp. 356–362, 2009.
- [27] S. Ferlito, M. Atrigna, G. Graditi et al., “Predictive models for building’s energy consumption: an Artificial Neural Network (ANN) approach,” in *Proceedings of AISEM Annual Conference*, pp. 1–4, Trento, Italy, February 2015.
- [28] J. Moon, S. Jung, Y. Lee, and S. Choi, “Prediction performance of an artificial neural network model for the amount of cooling energy consumption in hotel rooms,” *Energies*, vol. 8, no. 8, pp. 8226–8243, 2015.
- [29] Government of Spain - Ministry of the Presidency, *Royal Decree 235/2013, of April 5, Approving the Basic Procedure for the Certification of the Energy Efficiency of Buildings*, BOE, Madrid, Spain, 2013.
- [30] I. Zabalza, S. Diaz, and A. Aranda, *Analysis Methodologies for the Energy Rating of Buildings (Energy Efficiency Series)*, University of Zaragoza, Saragossa, Spain, 2010.
- [31] S. Pérez Cobos, *Energy Certification in Existing Buildings: Criteria for the Identification of the Thermal Envelope*, Editorial Marcombo, Barcelona, Spain, 2013.
- [32] Ecofys, *Ecofys VII - U-Values for Better Energy Performance of Buildings (U-VALUES for Better Energy Performance of Buildings)*, EURIMA, Brussels, Belgium, 2007.
- [33] Ministry of Industry, *Tourism and Commerce-IDAE: User Manual for Energy Qualification of Existing Buildings CE3x*, Institute for the Diversification and Saving of Energy, Madrid, Spain, 2013.
- [34] E. M. Johansson, F. U. Dowla, and D. M. Goodman, “Backpropagation learning for multi-layer feed-forward neural networks using the conjugate gradient method,” *International Journal of Neural Systems*, vol. 2, no. 4, pp. 291–301, 1991.

## Research Article

# Predicting Shear Capacity of FRP-Reinforced Concrete Beams without Stirrups by Artificial Neural Networks, Gene Expression Programming, and Regression Analysis

Ghazi Bahroz Jumaa <sup>1,2</sup> and Ali Ramadhan Yousif<sup>3</sup>

<sup>1</sup>Ph.D. Student, Department of Civil Engineering, Salahaddin University-Erbil, Erbil, Iraq

<sup>2</sup>Ass. Lecturer, University of Garmian, Kalar, Iraq

<sup>3</sup>Professor, Department of Civil Engineering, Salahaddin University-Erbil, Erbil, Iraq

Correspondence should be addressed to Ghazi Bahroz Jumaa; ghazijumaa@garmian.edu.krd

Received 29 July 2018; Accepted 18 October 2018; Published 15 November 2018

Guest Editor: Tayfun Dede

Copyright © 2018 Ghazi Bahroz Jumaa and Ali Ramadhan Yousif. This is an open access article distributed under the Creative Commons Attribution License, which permits unrestricted use, distribution, and reproduction in any medium, provided the original work is properly cited.

The shear strength prediction of fiber-reinforced polymer- (FRP-) reinforced concrete beams is one of the most complicated issues in structural engineering applications. Developing accurate and reliable prediction models is necessary and cost saving. This paper proposes three new prediction models, utilizing artificial neural networks (ANNs) and gene expression programming (GEP), as a recently developed artificial intelligent techniques, and nonlinear regression analysis (NLR) as a conventional technique. For this purpose, a large database including 269 shear test results of FRP-reinforced concrete members was collected from the literature. The performance of the proposed models is compared with a large number of available codes and previously proposed equations. The comparative statistical analysis confirmed that the ANNs, GEP, and NLR models, in sequence, showed excellent performance, great efficiency, and high level of accuracy over all other existing models. The ANNs model, and to a lower level the GEP model, showed the superiority in accuracy and efficiency, while the NLR model showed that it is simple, rational, and yet accurate. Additionally, the parametric study indicated that the ANNs model defines accurately the interaction of all parameters on shear capacity prediction and have a great ability to predict the actual response of each parameter in spite of its complexity and fluctuation nature.

## 1. Introduction

Although the behavior of steel-reinforced concrete (RC) members in shear has been extensively studied for more than one hundred years, and after numerous research challenges on shear behavior and on identification of the complex shear resistance mechanism of RC members, still there is an absence of comprehension and agreement on the mechanisms and behavior of shear resistance. While the behavior of steel-RC members in shear is an area of concern, the behavior of fiber-reinforced polymer-reinforced concrete (FRP-RC) members has additional complications due to their different mechanical properties [1]. Many important issues related to shear problems of FRP-RC members still remain without in-depth investigations and become open to discussion. Moreover, past investigations [2–4] inferred that the present shear design equations are exceptionally conservative in

predicting the shear capacity of FRP-RC beams. Consequently, the extra amount of FRP used to resist shear could be both costly and likely to create reinforcement congestion problems, and therefore, this study was motivated.

The shear strength of RC beams without web reinforcement was observed to be influenced by several variables, such as concrete strength ( $f'_c$ ), shear span-to-depth ratio ( $a/d$ ), beam depth ( $d$ ), longitudinal reinforcement ratio ( $\rho_f$ ), and beam width ( $b_w$ ) [5, 6]. Additionally, for FRP-RC members, the type of FRP rebar and their variable mechanical properties, like low elastic modulus ( $E_f$ ), high tensile strength, and low transverse shear strength, are other factors that should be taken into account.

Albeit many theoretical and empirical studies have been conducted to predict the shear strength of FRP-RC members, and to investigate the interaction between influencing parameters on shear strength mechanisms, up to date there is no

general agreement on a specific model. The vast majorities of the existing shear design equations have different forms and do not give a reliable factor of safety against shear failure; additionally, there is no general agreement between the existing codes and equations on the parameters affecting the shear capacity. This controversy in predicting models may be attributed to two main reasons; firstly, there is no comprehension theory on shear failure due to its complicated behavior and failure type which is sudden and catastrophic, and secondly, the existence wide variability in mechanical properties of FRP bars. Therefore, some existing predicting models were developed based on modifying the different theories which is originally proposed for steel-RC members and others are empirical or semiempirical models which were proposed based on a limited data; for instance, the ACI 440 algorithm was calibrated based on the test results from 326 steel-RC specimens and 44 FRP-RC specimens and the latter having a maximum effective depth of 360 mm. An alternative to classical and conventional methods for the prediction of complicated problems in various disciplines, such as the shear strength of FRP-RC members, is the utilization of artificial intelligence techniques like artificial neural networks (ANNs), fuzzy inference system (FIS), and genetic programming (GP). Throughout the most recent two decades, these methodologies have been prominent and effectively utilized as a part in an extensive variety of scientific applications particularly in civil engineering disciplines.

Recently, several studies have been performed on using different artificial intelligence techniques for predicting the shear capacity of FRP-RC members without stirrups. Kara [7] utilized gene expression programming (GEP) to obtain a simple model based on a set of 104 databases. Bashir and Ashour [8] suggested a model based on ANN using a set of 128 databases. Nasrollahzadeh and Basiri [9] developed an FIS to predict a model depending on a 128 database. Lee and Lee [10] used a database of 110 samples to propose a theoretical model utilizing ANN. Golafshani and Ashour [11] introduced a model using a new technique of biogeography-based programming based on an experimental database of 138 test specimens. Most of these studies proposed good models with a high level of accuracy; however, they used relatively a small size of a database. The size of the database used for training and testing the models plays a great role in the success of proposed models.

The present research aims to propose three new models to predict the shear strength,  $V_c$ , of FRP-RC slender beams without stirrups based on utilizing ANNs and GEP as artificial intelligence techniques and nonlinear regression analysis (NLR) as a conventional technique. These techniques were chosen due to the fact that the ANNs and GEP are powerful, accurate, and highly efficient tools in the model prediction of complicated problems, while the NLR is a classical tool which can be used to derive a simple, rational, and yet accurate model. The main affected parameters on shear strength are considered in modeling process which are  $f'_c$ ,  $d$ ,  $b_w$ ,  $a/d$ ,  $\rho_f$ , and  $E_f$ . The three models are derived using the largest collected database from the literature of (269) test specimens. The results of obtained models are compared to a large number of codes and proposed equations from the literature to examine their accuracy, validity, and efficiency. Additionally, a parametric study was conducted to indicate and compare the effect

of all parameters on shear capacity predicted by the proposed models and different well-known codes.

## 2. Reviews of Available Shear Design Equations

The last two decades witnessed development and rapid increase of using FRP-reinforcement for concrete structures; therefore, there are universal endeavors to create prediction models. These endeavors have brought about distributing a few codes and outline rules. However, there is no agreement in regards to shear configuration models among all available codes and guidelines. Table 1 provides a summary of the shear design equations for FRP-RC members without stirrups.

Most of the available shear design equations of FRP-RC members have been developed by modifying the existing equations adopted by design codes for steel-RC members. The methods of modification tried to cover the major changes in material properties by taking into account the effect of the lower elastic modulus, higher tensile strength, lower transverse shear strength, and no yielding criteria in the FRP rebar. Nevertheless, the relatively large variations in mechanical properties such as tensile strength, elastic modulus, bond properties, and transverse shear strength between the different FRP types have made it hard to precisely predict the shear capacity. Furthermore, the procedure that adopted by various codes, manuals, and guidelines to predict the shear strength are significantly different, and most of them are empirical and based on a limited set of test results. Consequently, some of the design models are quite conservative, whereas others sometimes yield unconservative results [3, 22]; as well as these equations are differing from each other in considered parameters. On the contrary, the design model that does not consider the effect of known parameters would lack generality, and its applicability to general design situations would be dubious [23]. Therefore, there is a need to develop shear design equations which will consider the effect of all parameters; as well as it will be accurate, consistent, and simple to use for the general application.

## 3. Collected Databases

For the purpose of this study, an extensive survey of the open literature was conducted and a large database containing the test results of a large number of 269 FRP-RC beams and one-way slabs were assembled. The database of the specimens were collected from 42 different references, reinforced with FRP rebars without transverse reinforcement, and only those that failed in the shear mode was compiled [1–3, 20, 22, 24–60]. Only slender beams and one way slabs with  $a/d \geq 2.5$  were considered in this study. The specimens included 230 beams and 39 one way slabs; all were simply supported and were tested either under three points or four bending points. The details of the specimens that were used as a database are shown in Table 2.

## 4. Artificial Neural Networks (ANNs)

*4.1. General Background.* In its most broad frame, a neural network is a machine that is intended to demonstrate the

TABLE 1: Shear design equations for FRP-RC beams without stirrups.

Reference	Provisions
[12]	$V_c = (2/5)\sqrt{f'_c}b_w c$ , $c = kd$ , $k = \sqrt{2\rho_f n_f + (\rho_f n_f)^2 - \rho_f n_f}$ , $\rho_f = A_f/(b_w d)$
[13]	$V_c = \beta_d \beta_p \beta_n f_{vcd} b_w d / \gamma_b$ ; $f_{vcd} = 0.2(f'_c)^{1/3} \leq 0.72$ N/mm <sup>2</sup> ; $\beta_d = (1000/d)^{1/4} \leq 1.5$ ; $\beta_p = ((100\rho_{f1} E_{f1})/E_s)^{1/3} \leq 1.5$ $\beta_n = 1.0$ for sections without the axial force, $\gamma_b =$ member safety factor, $\gamma_b = 1.3$
[14]	$V_c = 0.79(100\rho_w(E_f/E_s))^{1/3}(400/d)^{1/4}(f_{cu}/25)^{1/3}b_w d$ ( $100\rho_w(E_f/E_s)$ ) should not be taken greater than 3, and $(400/d)^{1/4}$ should not be taken if less than 1 for members with shear reinforcement
[15]	$V_c = 2.5\beta\varphi_c f_{cr} b_w d_v$ ; $\beta = (0.4/(1 + 1500\varepsilon_x))(1300/(1000 + S_{ze}))$ ; $\varepsilon_x = (M_f/d_{v+V_f+0.5N_f})/(2(E_f A_f)) \leq 0.003$ ; $S_{ze} = ((35S_z)/(15 + a_g)) \geq 0.85S_z$ , where $f_{cr} = 0.4\sqrt{f'_c}f_c \leq 69$ N/mm <sup>2</sup> $V_c = 0.2\lambda\varphi_c \sqrt{f'_c} b_w d \sqrt{E_{f1}/E_s}$
[16]	For sections with an effective depth greater than 300 mm, the concrete shear resistance, $V_c$ , is taken as $V_c = (260/(1000 + d))\lambda\varphi_c \sqrt{f'_c} b_w d \sqrt{(E_{f1}/E_s)} \geq 0.1\lambda\varphi_c \sqrt{f'_c} b_w d \sqrt{(E_{f1}/E_s)}$ ; $\sqrt{(E_{f1}/E_s)} \leq 1.0$ Where $\lambda =$ modification factor for density of concrete and $\varphi_c =$ resistance factor for concrete $V_{Rd,ct} = 1.3(E_f/E_s)^{1/2} \tau_{Rd} k (1.2 + 40\rho_1) b_w d$ Satisfying the limitation: $1.3(E_f/E_s)^{1/2} \leq 1$ $V_{Rd,max} = 0.5v f_c b_w 0.9dv = 0.7 - f_c/200 \geq 0.5$ Where $\tau_{Rd} =$ design shear stress, MPa, defined as $0.25f_{ct}$ ; $f_{ct} =$ characteristic tensile strength of concrete (5% fractile), MPa, $f_{ct} = 0.33\sqrt{f'_c}$ ; $\gamma_c =$ is the strength safety factor $f$ concrete, $\gamma_c = 1.6$ ; $k =$ factor taken equal to $ 1 $ in members where more than 50% of the bottom reinforcement is interrupted; if not, it will be $k =  (1.6 - d) \geq 1 $ ; $d =$ depth in meters; $\rho_1 = (A_f/b_w d)$ which cannot be taken less than 0.01 and greater than 0.02
[17]	$V_c = 0.05\lambda\varphi_c k_m k_r (f'_c)^{1/3} b_w d_v$ , $k_m = \sqrt{((V_f d)/M_f)} \leq 1.0$ , $k_r = 1 + (E_f \rho_{fw})^{1/3}$ Such that $0.11\lambda\varphi_c \sqrt{f'_c} b_w d_v \leq V_c \leq 0.22\lambda\varphi_c \sqrt{f'_c} b_w d_v$ , for $f'_c \leq 60$ MPa
[18]	In members with effective depth greater than 300 mm and with transverse reinforcement less than the minimum, $V_c$ should be multiplied by $k_s = (750/(450 + d)) \leq 1.0$
[4]	$V_c = 2.1(((f'_c \rho_f d)/a)(E_f/E_s))^{0.3} b_w d$
[7]	$V_c = c_0/c_2 (\sqrt[3]{d/a} 100\rho_f (E_f/E_s) f'_c (c_1^2/c_0))^{1/3} b_w d$ , $c_0 = 7.696$ , $c_1 = 7.254$ , $c_2 = 7.718$
[19]	$V_c = 0.045k_m k_r k_a k_s (f'_c)^{1/3} b_w d$ , $k_m = ((Vd)/M)^{1/2}$ , $k_r = 1 + (E_f \rho_f)^{1/3}$ , $k_a = \begin{cases} 1 & \text{for } (M/(Vd)) \geq 2.5 \\ 2.5/(M/(Vd)) & \text{for } (M/(Vd)) < 2.5 \end{cases}$ , $k_s = \begin{cases} 1 & \text{for } d \leq 300 \\ 750/(450 + d) & \text{for } d > 300 \end{cases}$
[1]	$V_c = ((0.2\lambda)/(a/d)^{2/3})((\rho_f E_f)/d)^{1/3} \sqrt{f'_c} b_w d$
[20]	$V_c = 2.76(\rho_{f1}(E_{f1}/E_s)(d/a)f'_c)^{1/3} b_w d$ $d \leq 300$ mm, $V_c = 2.76(\rho_{f1}(E_{f1}/E_s)(d/a)f'_c)^{1/3} (300/d)^{0.25} b_w d$ $d > 300$ mm
[21]	$V_c = v_c b_w d = ((0.134\sqrt{f'_c})/(\sqrt{1 + (d/(1.2d_c))})) b_w d$ , $d_c = (\rho_w E (d_a + 16))/(100(a/d)\sqrt{f'_c})$

manner by which the brain plays out a specific errand or function; the system is generally executed by utilizing electronic parts or is mimicked in programming on an advanced PC. The ANNs perform helpful calculations and simulate complex modeling through a procedure of learning similar to that of the human brain. ANNs do not represent the sophistication, complication, and multifaceted nature of the brain, as the simulated neurons are substantially more straightforward than natural neurons in the area of recognition, efficiency, control, and learning. Nonetheless, ANNs are similar to the brain in two main points; first, the building squares of the two systems are straightforward computational tools which are exceedingly interconnected; second, the connections between neurons decide the task of the networks [61, 62].

ANNs are made out of numerous interconnected processing units operating in parallel. Each processing unit keeps some data locally, can play out some basic calculations, can have numerous input data and, however, can send just a single output. The ANNs have the ability to react and create the relating response and to adjust to the changing condition by learning from experience [63].

Generally, ANNs are trained, with the goal that specific input data prompt a particular target output. The network is balanced, in view of an examination of the output and the target, until the networks yield the objective. Gradually training the network modifies the weights and biases required after the introduction of every individual input vector. ANNs have been prepared to perform complex functions in different fields of application including biological, engineering, business, financial, manufacturing, medical, and military. Today ANNs can be prepared to tackle issues that are troublesome for regular PCs or human beings [64]. The drawback of the ANNs modeling is that it is not as simple as ordinary design provision, where it is consist of regularly numerous small units; therefore, simple calculations of the ANNs models are excessively monotonous, and usually, computers are needed for calculations.

**4.2. Back Propagation ANNs.** The multilayer perceptron, trained through the back-propagation algorithm, is nowadays the most broadly utilized neural networks. The term back propagation neural networks (BPNNs) alludes to

TABLE 2: Details of database.

Reference	Number of members	$d$ (mm)	$a/d$	$b$ (mm)	$\rho_f$ (%)	$f'_c$ (MPa)	$E_f$ (GPa)	FRP type	$V_{exp}$ (kN)
[24]	4	250	3	150	0.55–2.2	27.5–35	94	C	38.3–59.1
[27]	2	250–500	2.5	150–300	1.04	29.5–34	100	C	38.4–142.8
[26]	2	150	4	300	1.34–1.8	22.7–28	29.4	G	33.7–37
[25]	3	250	3	150	1.51–3.0	34.3	105	C	41.2–47.6
[28]	1	260	2.69	200	1.36	34.7	130	C	62.9
[29]	2	210	3.65	150	1.36	32.9–38.1	45	G	22.8–27.3
[30]	1	222	3.15	154	1.36	39	34	G	39
[31]	2	104–154	8.44–12.5	1000	0.49–0.76	66	41.3	G	42.1–85.2
[32]	5	157.5	4.5–5.8	305	0.73	27–30.8	40	G	28–30.9
[33]	3	279–287	2.61–2.69	178	0.77–2.3	24.1	40	G	36.7–54
[2]	18	225	4.06	178–254	1.11–2.27	36.3	40.3	G	28.1–51.1
[34]	2	258	2.5	150	0.91	53.8–68.5	48	G	38.5–41.4
[35]	6	360	3.39	457	0.96–1.92	39.9–42.6	37.6–47.1	A, G	94.8–177
[36]	12	225	4.06	152–203	1.25–2.56	79.6	40.3	G	30.4–48.3
[37]	11	310–346	2.75–3.71	130–160	0.72–1.54	34.1–43.2	42–120	G, C	42.7–52.3
[38]	11	143	6.36	89–159	0.33–0.76	60.3–81.4	139	C	8.8–23.1
[3]	6	225	2.67–4.5	200	0.25–0.88	40.5	145	C	36.1–47.2
[39]	1	970	3.14	450	0.46	40	40	G	136
[40]	2	190	7.96	121	1.1–1.65	40–74.3	40	G	13.9–16.9
[41]	8	159–165	6.06–6.49	1000	0.39–2.63	40	40–114	G, C	118–195
[42]	11	78–83	3.61–6.41	420	0.61–2.61	61–93	42	G	22.1–55.6
[22]	6	326	3.07	250	0.87–1.72	43.6–50	39–134	G, C	63–127.5
[43]	4	326	3.07	250	1.71–2.2	63	42–135	G, C	90–177
[44]	6	163–263	2.54–4.09	150	0.45–1.39	28.9–50.2	32	G	13.1–30.9
[45]	1	150	3.35	224	1.28	43	45	G	27.9
[46]	9	75	6–6.16	420	0.68–1.16	48–92	42	G	24.6–34.3
[47]	3	404–441	3.02–3.71	300	3.25–3.98	43	44–63	G	118.4–154.3
[48]	2	262	6.68	600	0.77–1.53	68	48	G	91.2–118.2
[49]	4	170	4.12	150	0.92–1.54	20–26.6	46	G	12.7–15.4
[50]	4	170	5.88	150	1.33–2.22	20–26.6	113	C	19.3–27.7
[51]	6	194–937	3.26–3.93	450	0.51–2.54	35–46	37	G	74–232
[52]	6	200–500	3.5–6.5	300	0.28–0.35	52.3	114	C	54.1–71.2
[53]	6	291–594	2.5	250–300	0.42–1.37	65.3–74.2	46.3–144	G, C	71.6–155.2
[54]	13	146–883	3.13	114–457	0.6–1.17	29.5–59.7	41–43.2	G	17.9–264.8
[1]	8	305–744	2.5	250–300	0.42–0.91	34.5–44.7	47–144	G, C	61–138.5
[55]	9	140	6.2	1000	0.52–1.25	41.3–86.2	140–144	C	118.5–192
[56]	34	216	2.5–4.5	150–200	0.33–0.79	30	48–148	G, C	16.9–35.4
[57]	3	150	4–4.5	245–270	0.39–0.85	60	70	B	20.9–29.2
[20]	6	170–370	2.7–5.9	200	0.12–0.52	22.1–28.7	141.4	C	17.6–36.1
[58]	6	170	5.65–7	300	0.8–4.1	35.9	48–53	B	29.3–51.5
[59]	8	206–220	2.5–3.3	152	0.31–1.52	49	50	B	17–30
[60]	12	234–635	2.6	200	0.71–2.69	42.2–73.4	58	B	54–169.5
Mean		258.8	4.13	290.4	1.123	46.2	73.8		58.8
Standard deviation		157.2	1.51	220.5	0.7290	18.19	42.93		48.44
Minimum		73	2.5	89	0.12	20	29.4		8.8
Maximum		970	12.5	1000	4.121	93	147.9		232

the way in which the gradient is processed for nonlinear multilayer networks [64]. The BPNNs algorithm follows a technique to minimize the errors through the calibration of the weights in each cycle by a small amount for a specific training scheme.

BPNNs is one of the straightforward and most appropriate networks being utilized in the prediction of civil engineering problems [63, 65, 66], principally because of that it can modify the weights of each layer in view of the errors introduced at the output. A common structure of BPNNs display comprises of an input layer, at least one hidden layer and an output layer, and each layer comprises

of many neurons. Every neuron is a processing unit that gets at least one source of input and produces an output response through the transfer function. Related to every connection is a weighting that communicates the impact on the present procedure component of an information set or another procedure component in the past layer, as shown in Figure 1. The connection weighting and bias values are at first picked as arbitrary numbers and afterward settled by the consequences of the training procedure [67].

The calculations that carried out inside the BPNNs include summation process of weighted input values with the

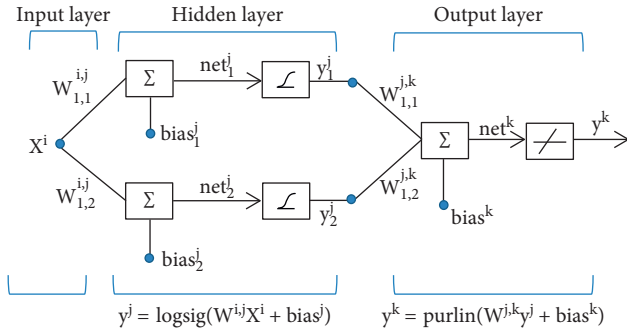


FIGURE 1: Typical architecture and log-sigmoid function of (1-2-1) BPNNs.

bias of the input layer, as in Equation (1), and then the results passed into the hidden layer neurons. Inside neurons, the process of sigmoid transformed function was performed by using one of the transformed functions such as that in Equation (2). Another linear process, using the purelin function, was carried out by summing the weighted output from the hidden layer neurons with the bias of the hidden layer as in Equation (3):

$$net_j = \sum_{i=1}^n w_{ij}x_i + bias_j, \quad (1)$$

$$y_j = f(net_j) = \frac{1}{(1 + \exp^{-(net_j)})}, \quad (2)$$

$$y_k = \text{purelin}\left(\sum_{j=1}^m w_{jk}y_j + bias_k\right), \quad (3)$$

where  $net_j$  is the weighted sum generated at the  $j$ th hidden neuron;  $x_i$  is the input value from the  $i$ th input neuron;  $w_{ij}$  and  $w_{jk}$  are the weights added to the hidden layer and the output layer neurons, respectively;  $bias_j$  and  $bias_k$  are the biases added to the hidden layer and the output layer neurons, respectively;  $y_j$  is the processed output from the  $j$ th hidden neuron;  $y_k$  is the processed output from the  $k$ th output neuron; and  $n$  is the number of input neurons, and  $m$  is the number of neurons in the hidden layer.

#### 4.3. BPNNs Model Used for the Prediction of Shear Capacity.

In this study, the BPNNs were utilized to produce a predictive model for shear strength of FRP-reinforced concrete members without stirrups. The key parameters affecting the shear strength which considered in this study are  $f'_c$ ,  $d$ ,  $b_w$ ,  $a/d$ ,  $\rho_f$ , and  $E_f$ . The most important issue in BPNNs modeling is selecting the number of hidden layers and the number of neurons in each hidden layer, which depend on several factors like type of problem of interest, the association of input parameters with the output pattern, size of instances, number of input parameters, and number of outputs. However, there is no basic acknowledged criteria to pick the number of hidden layers and the number of

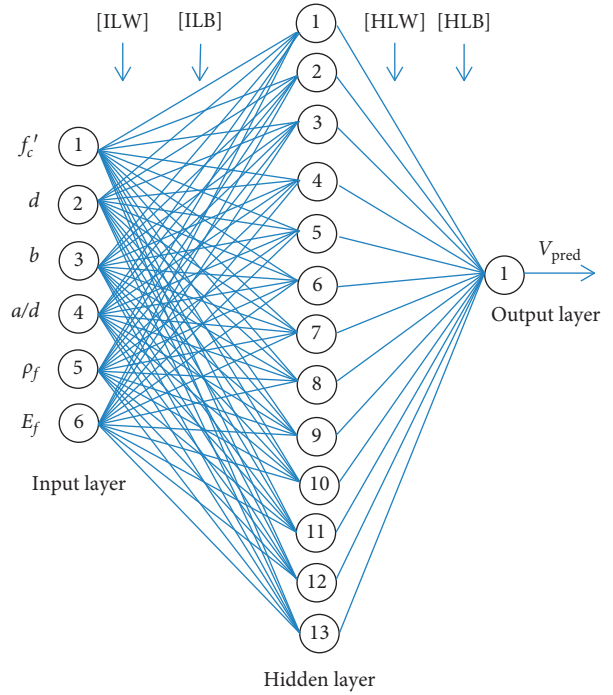


FIGURE 2: Architecture of BPNNs used for the prediction of the shear strength.

neurons; therefore, a trial and error method was achieved based on training and testing up to obtain a reasonable fit. Consequently, a BPNNs training algorithm was utilized in a feed-forward network trained using nonlinear hyperbolic log-sigmoid transfer function in the hidden layer and a linear purelin transfer function in the output layer, as in Equations (1)–(3).

The trial and error procedure resulted in that the best fitting model was that obtained using thirteen neurons in a single hidden layer (6-13-1), as demonstrated in Figure 2. The predictive model was trained through numerous iterations to find the best epoch value, momentum rate, and learning rate which give the optimum model for shear strength prediction. The data were divided arbitrarily into “training” 70%, “validating” 15%, and “testing” 15%, and the partitioning of data was chosen based on the results of model performance after numerous trials.

It is recommended by many authors [11, 63, 68, 69] to normalize the input and output data before using them to predict the model. In this study, the data of input and target were scaled by the linear normalization function in the range of (0 to 1), as shown in the following equation:

$$x_n = 0.6 \frac{x - x_{\min}}{x_{\min} - x_{\max}} + 0.2, \quad (4)$$

where  $x$  is the data sample,  $x_n$  is the normalized data sample,  $x_{\min}$  and  $x_{\max}$  is the minimum and maximum values of the data for the interested parameter.

The input layer weights (ILWs), the input layer biases (ILBs), the hidden layer weights (HLWs), and the hidden layer bias (HLB) of the (6-13-1) predictive BPNNs model are shown below:

$$\begin{aligned}
 \text{ILW} &= \left\{ \begin{array}{l} -2.3567 \quad 0.27166 \quad 1.4696 \quad -1.4038 \quad 0.99307 \quad 2.2234 \\ 2.3842 \quad -2.2831 \quad 0.83159 \quad 2.2855 \quad 1.4806 \quad -0.83455 \\ 2.8211 \quad 0.75441 \quad -4.086 \quad 1.4427 \quad 1.7982 \quad -1.0877 \\ 0.59955 \quad -0.74937 \quad 2.0882 \quad -2.6609 \quad 1.8418 \quad -1.5433 \\ 1.4527 \quad -1.7869 \quad -1.0477 \quad 1.6872 \quad -0.81981 \quad -2.5634 \\ 3.5416 \quad -1.9591 \quad -0.34353 \quad 1.0741 \quad -1.5276 \quad 2.2139 \\ 1.5643 \quad -2.8231 \quad 2.6211 \quad -1.6244 \quad 1.0879 \quad 1.7129 \\ 2.2825 \quad -0.40079 \quad 0.48425 \quad -2.312 \quad 0.07062 \quad 0.15858 \\ -1.749 \quad -0.25004 \quad -0.45657 \quad -2.2347 \quad -1.0796 \quad -1.0232 \\ -0.78404 \quad 2.66 \quad -2.8673 \quad -1.0803 \quad -0.86988 \quad -1.6247 \\ -0.25678 \quad -3.2562 \quad 2.2726 \quad 1.6206 \quad -1.2616 \quad 2.6619 \\ -1.2662 \quad -0.78168 \quad -0.52983 \quad -2.5791 \quad 1.0124 \quad 2.3284 \\ -2.3043 \quad 0.55942 \quad -1.2328 \quad -2.8413 \quad -1.3658 \quad 2.6415 \end{array} \right\}, \\
 \text{ILB} &= \left\{ \begin{array}{l} 5.1888 \\ -1.4396 \\ -2.1773 \\ -2.4823 \\ -1.6444 \\ -0.08813 \\ 0.12198 \\ 2.2041 \\ -2.362 \\ -1.9906 \\ -0.52466 \\ -3.7706 \\ -2.6641 \end{array} \right\}, \\
 \text{HLW} &= \left\{ -0.7663 \quad 1.2834 \quad -0.9729 \quad -0.66761 \quad -0.3835 \quad -0.87847 \quad 1.2312 \quad 1.3464 \quad -1.3058 \quad 1.206 \quad 1.169 \quad -0.9465 \quad -0.6511 \right\}, \\
 \text{HLB} &= \{-0.44036\}.
 \end{aligned}
 \tag{5}$$

## 5. Genetic Programming

*5.1. General Background.* Genetic programming (GP) is a naturally inspired machine learning (evolutionary) technique utilized for randomly reproducing a population of computer programs in light of Darwin's advancement hypothesis. GP, which was developed by Koza [70], can be regarded as a developed form of the genetic algorithm (GA), which is an evolutionary optimization tool that depends on the principles of genetics and normal determination. The systems of GA incorporate altering and changing the extent of chromosomes by genetic operators to solve function optimization problems. The fundamental contrast amongst

GA and GP is that the solution of GA is a binary string of fixed length utilized for parameters optimization of a specific arrangement of model parameters, while the solution of GP is a development program represented as a subset of parse trees which use input variables and corresponding outputs for generating optimized models [71–73].

The GP techniques for modeling incorporate production of an initial population of chromosomes (models) which include an arrangement of functions and an arrangement of terminals that selected and arranged randomly in the form of the parse tree (computer model). The models composed of a root node, functional nodes, and terminals, as shown in Figure 3.

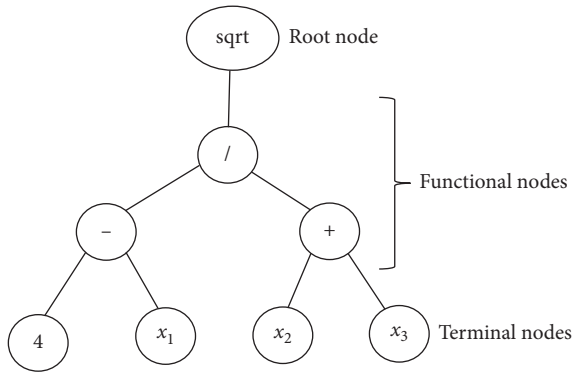


FIGURE 3: Typical example of a GP tree representation model  $((4 - x_1)/(x_2 + x_3))^{1/2}$  [74].

At that point, the produced population models are assessed and the fitness of the models is evaluated using the provided data of the particular problem. After that, other generations of models are produced by primary genetic operators: reproduction, crossover, and mutation, as shown in Figure 4. The evolutionary procedure of assessing the fitness of the present population and producing new population is continued until the point when an end termination criterion is approached, which can be either a particular acceptable error or a specified maximum number of generations. The model with the best solution which developed after each generation assigns the outcome of the GP program [76].

**5.2. Gene Expression Programming.** The most widely used GP in civil engineering problems is gene expression programming (GEP), which was developed by Ferreira [71]. GEP utilizes development of numerical conditions that is encoded linearly in chromosomes of a consistent length and considered nonlinearly as expression trees (ETs) with various shapes and sizes. The chromosomes are composed of several genes; each gene contains a smaller subprogram or subexpression trees (Sub-ETs). Every gene has a consistent length and comprises a head and a tail. The schematic of the GEP flowchart is shown in Figure 5. The implementation of GEP predictive modeling incorporates five main components including function set, terminal set, fitness function, control parameters, and termination condition [7, 75].

The preferred quality of GEP is that the genetic operators work at the chromosome level and the production of genetic diversity is to a great degree simplified. Another favorable position is credited to the remarkable multigenetic nature of GEP, which permits the advancement of all the more capable models made out of a few subprograms [71].

**5.3. GEP Model for Predicting Shear Capacity.** For predicting the shear strength of FRP-reinforced concrete beams without stirrups by GEP-based formulation, six influencing parameters were considered:  $f'_c$ ,  $d$ ,  $b$ ,  $a/d$ ,  $E_f$ , and  $\rho_f$ , through training and testing the experimental results. The data are evaluated on the GeneXproTools 5 [78] to develop the empirical model which is the most widely used software for

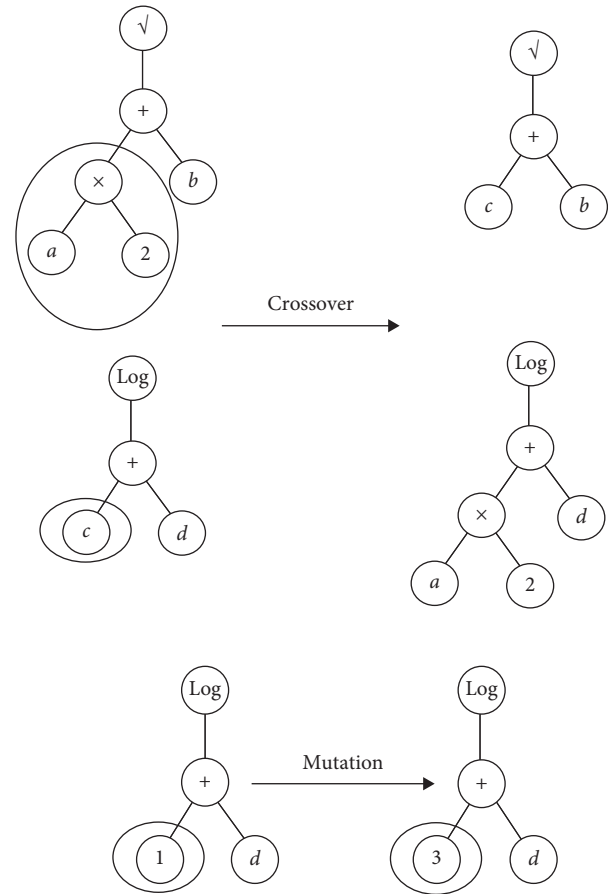


FIGURE 4: Typical operations of crossover and mutation in GP [75].

GEP model prediction. Similar to the ANNs model, the data are partitioned randomly to 70% for training and remaining 30% for testing such that both portions of data have balanced statistical parameters like mean, standard deviation, and max and min values.

To obtain the best GEP prediction model, many models with a different number of genes were evolved throughout a set of genetic operators (mutation, transposition, and crossover). Initially, a model composed of two genes with multiplication linking functions and head sizes of three was selected and evolved many times. Then, the model parameters were changed, step by step, through increasing the number of genes, head size, number of chromosomes, and weights of function sets. The program was evolved numerous times for various models, and the outcome models were monitored and compared to evaluate their performance. Other parameters like mutation rate, inversion, and points of recombination were chosen based on previous works [7, 79–82] and then evaluated to get their optimum effects. After many trials, the final mathematical model was chosen, for which the utilized parameters, fitness function, and function sets are given in Table 3. The final model was selected based on criteria of the best fitness and less complicity of mathematical formulation; the expression trees are shown in Figure 6 and the mathematical formulation is given in the following equation:

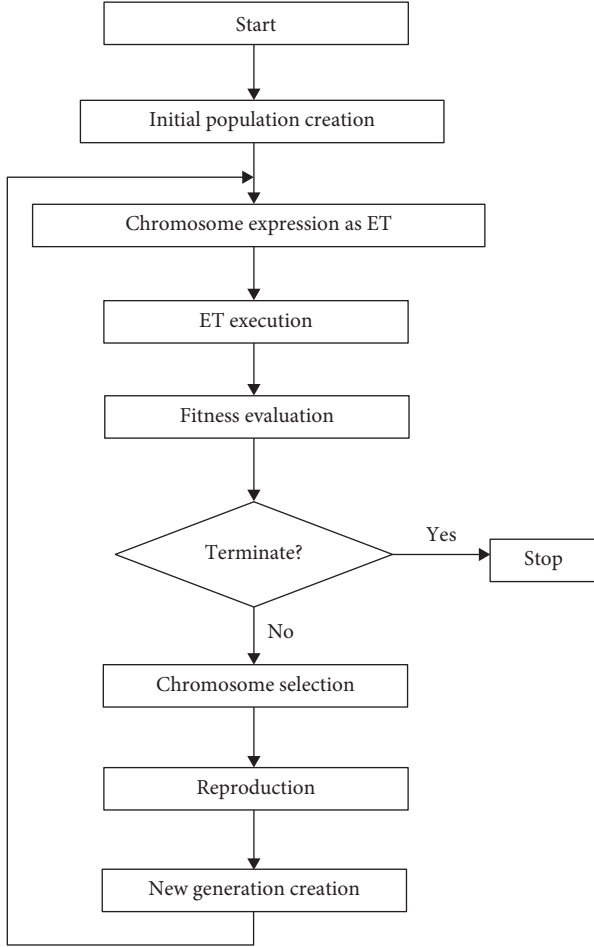


FIGURE 5: Flowchart of GEP [77].

$$\begin{aligned}
 V_c = & \left\{ \text{abs} \left( \left( \frac{c_3 + (d_5 * d_3)(d_2 + d_0)^2}{4} \right)^{1/3} \right) \right\} \\
 & * \left\{ \left( \tanh \left( \left( \frac{d_2}{d_1} \right)^{1/5} \right) - \tanh(d_2 * d_3^4) \right)^5 \right\} \\
 & * \left\{ d_2 + \left( \frac{d_3^{1/5}}{\max(d_1; c_6)} (c_8 + d_4) \right)^2 \right\} \\
 & * \left\{ \left( \tanh \left( \left( \frac{d_2}{d_1} \right)^{1/5} \right) - \left( \sqrt{\frac{d_1}{d_0}} \right)^3 \right)^5 \right\},
 \end{aligned} \quad (6)$$

where:  $d_0, d_1, d_2, d_3, d_4,$  and  $d_5$  refer to  $d, a/d, b, \rho_f, f'_c,$  and  $E_f$  respectively,  $c_2 = 6.56723946184092, c_3 = -241413.053630399, c_4 = -12.1479701959083, c_6 = 3.07014791103389,$  and  $c_8 = 22.0241396443835.$

## 6. Nonlinear Regression Model (NLR)

Regression analysis is considered as an important tool that can be used in the modeling process for solving complicated problems of various engineering disciplines.

TABLE 3: Parameters used in the GEP Model.

Parameters	Values
Number of chromosomes	30–500
Head size	3, 5, 8
Number of genes	2, 3, 4
Linking function	Multiplication
Function set	+, −, /, *, abs, tanh, $x^2, x^{1/2}, x^{1/3}, x^{1/5}, \dots$
Generation without changes	2000
Number of tries	12
Maximum complexity	10
Fitness function	RMSE
Mutation	0.044
Inversion	0.1
One-point recombination	0.3
Two-point recombination	0.3
Gene recombination	0.1
Gene transposition	0.1
IS transposition	0.1
RIS transposition	0.1
Data type	Floating point
Constants per gene	10

However, the proposed models based on nonlinear regression (NLR) are less accurate than the ANN and GEP; however, it is characterized by that it is simple and easy for application without the need of computers for calculations. A nonlinear regression model based on the experimental database collected from the literature was suggested. The proposed equation was derived based on developing a model similar to that proposed by Zsutty [83] which is the most accurate and simple empirical equation that was proposed for shear prediction of steel-RC members. In order to predict the shear strength of FRP-RC beams more accurately, considering the effect of all influencing parameters, the experimental shear strength was analyzed with most common influencing parameters:  $f'_c, d, b, a/d, E_f,$  and  $\rho_f.$  Based on data fitting analysis, and after some simplification, the following equation was proposed:

$$V_c = 0.32 \left( \frac{1}{d} \right)^{1/3} \left( \frac{E_f \rho_f}{a/d} \right)^{2/5} (f'_c)^{1/5} b_w d. \quad (7)$$

It can be observed that the equation is simple, rational, and more generalized than most codes and proposed equations from the literature as it considers the effect of all the influencing parameters on the shear strength of FRP-RC members without stirrups.

## 7. Results and Discussion

The shear strength results of FRP-reinforced concrete members for the three proposed models, the ANNs, GEP, and NLR, are evaluated and compared with the common design provisions (ACI 440-15, JSCE-97, CSA 806-12) and seven proposed equations [1, 4, 7, 10, 19–21]. The comparison was examined based on statistical terms such as

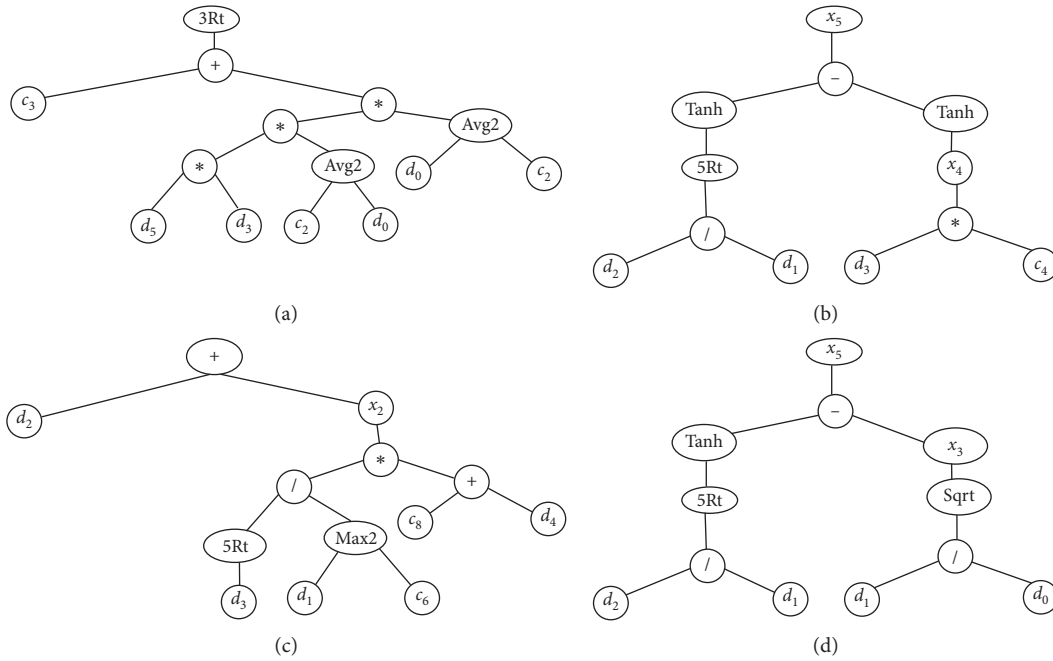


FIGURE 6: Expression trees ETs for the GEP model. (a) Sub-ET 1. (b) Sub-ET 2. (c) Sub-ET 3. (d) Sub-ET 4.

mean, standard deviation (SD), and coefficient of variation (COV) in addition to error values, such as mean absolute error (MAE), root mean square error (RMSE), and  $R^2$ , as shown below:

$$\text{RMSE} = \sqrt{\frac{\sum_{i=0}^N (e_i - p_i)^2}{N}},$$

$$\text{MAE} = \frac{1}{N} \sum_{i=0}^N |e_i - p_i|, \quad (8)$$

$$R^2 = 1 - \frac{\sum_{i=0}^N (e_i - p_i)^2}{\sum_{i=0}^N (e_i - \bar{e})^2},$$

where  $e_i$  and  $p_i$  are the experimental and predicted shear force in kN, respectively,  $\bar{e}$  is the average of the experimental values, and  $N$  is the total number of the considered samples. The model that minimized the error values (MAE and RMSE) and maximized  $R^2$  is selected as the optimum model.

Figure 7 presents the scatter of the experimental shear force,  $V_{\text{exp}}$ , versus the predicted shear strength,  $V_{\text{pred}}$ , for the proposed models, codes, and proposed equations from the literature. It is clear that the best models for predicting the shear strength are those suggested in this study, which in a sequence are ANNs, GEP, and NLR, as these models predict the shear strength very accurately with the optimum statistical performance of  $R^2$ , RMSE, and MAE. High correlation coefficients with low error rates indicate that the proposed three models are excellent models and exhibit generalization performance in predicting shear strength of FRP-reinforced concrete beams without stirrups. In contrast, the code design provisions and other proposed equations from the literature yielded dispersion results with

lower  $R^2$  and larger error rates as given in the scatter relationships.

Table 4 presents the statistical parameters (mean, standard deviation (SD), coefficient of variation (COV), minimum, maximum, range, RMSE, MAE, and  $R^2$ ) of the ratio of experimental shear strength to the predicted shear strength,  $V_{\text{exp}}/V_{\text{pred}}$ , for the proposed models in this study, seven well-known codes, and seven proposed equations from literature based on the (269) collected database. It is clear that the proposed equations yielded superior accuracy between all the codes and proposed equation from the literature because their optimum statistical parameters such as the mean, SD, range, RMSE, and  $R^2$  are 0.998, 0.113, 0.72, 5.3, and 0.9877, respectively, for ANNs; 1.007, 0.162, 0.88, 8.2, and 0.970, respectively, for GEP; and 1.003, 0.174, 0.99, 10.7, and 0.95, respectively, for NLR.

The ANNs and GEP models are artificial intelligent models derived based on soft computing; as verified above, these models are accurate, superior, and highly efficient in predicting the complicated problem such as shear strength. However, the drawback of artificial intelligent models is that it cannot be calculated manually and it needs computers for calculation. Besides, it is considered as a powerful and efficient tool which can be used in soft programs specialized for analysis and design of reinforced concrete structures. On the contrary, the NLR model is simply accurate and rational which can be used manually with sufficient accuracy more than the design codes and previously proposed equations. Nevertheless, the regression equations cannot properly define, with the same level of efficiency of artificial intelligent techniques, the interactions between the input and output parameters due to that the regression models usually are produced based only on a few predefined equations [79].

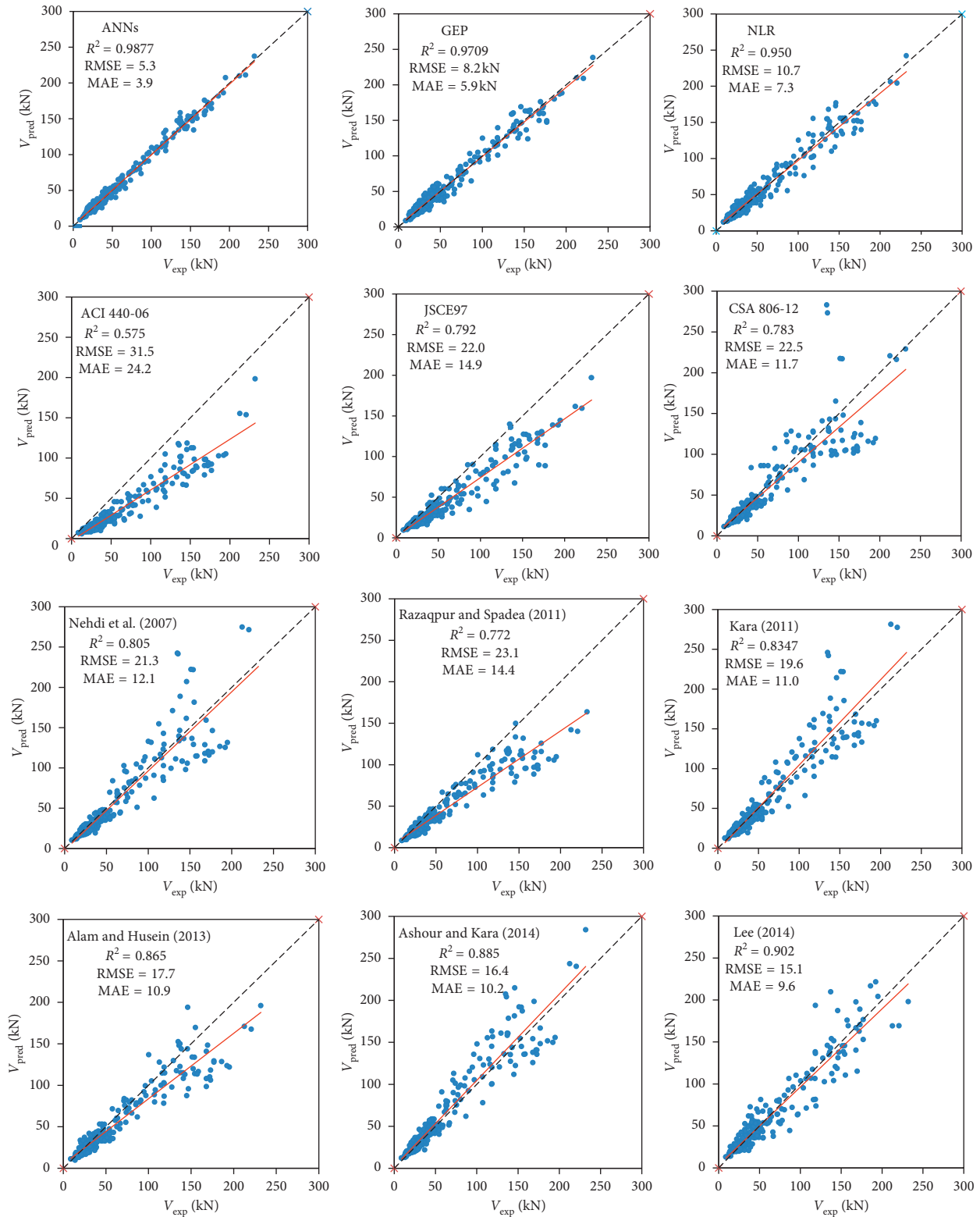


FIGURE 7: Scatter of  $V_{exp}$  versus  $V_{pred}$  for ANN, GEP, NLR, and different models from the literature.

Finally, it can be said that all the three proposed equations can be considered as accurate, efficient, and useful models, which were trained on a largest collected database, for predicting the shear strength of FRP-reinforced concrete members.

### 8. Parametric Analyses

For further verification of the proposed ANNs, GEP, and NLR prediction models, a parametric analysis was performed in this study. The main goal was to find the

TABLE 4: Statistical parameters of ( $V_{exp}/V_{pred}$ ) for the proposed models and different design equations.

Design equations	Mean ( $V_{exp}/V_{pred}$ )	SD	COV%	Minimum	Maximum	Range	RMSE	MAE	$R^2$
[12]	1.813	0.416	23.06	1.13	3.74	2.61	31.5	24.2	0.575
[13]	1.302	0.282	21.63	0.46	2.51	2.05	22.0	14.9	0.792
[18]	1.091	0.227	20.85	0.47	1.85	1.37	22.5	11.7	0.783
[16]	1.193	0.386	32.49	0.44	2.48	2.03	26.33	17.58	0.703
[17]	0.948	0.265	27.99	0.39	1.74	1.34	22.57	14.03	0.782
[14]	1.072	0.247	23.1	0.54	1.92	1.38	14.70	9.80	0.908
[15]	1.393	0.254	18.35	0.70	2.48	1.78	24.56	16.61	0.742
[4]	1.113	0.219	19.67	0.55	1.92	1.36	21.3	12.1	0.805
[19]	1.305	0.235	18.01	0.84	2.14	1.29	23.1	18.4	0.772
[7]	1.025	0.205	20.03	0.54	1.91	1.36	19.6	11.0	0.835
[1]	1.148	0.227	19.81	0.59	1.72	1.13	17.7	10.9	0.865
[20]	0.965	0.174	18.06	0.63	1.68	1.05	16.4	10.2	0.885
[10]	1.015	0.229	22.51	0.53	1.96	1.43	15.1	9.6	0.905
[21]	1.096	0.283	25.87	0.56	2.12	1.56	19.15	11.80	0.843
NLR	1.003	0.174	17.32	0.62	1.61	0.99	10.7	7.3	0.950
GEP	1.007	0.162	16.08	0.66	1.55	0.88	8.2	5.9	0.9709
ANNs	0.998	0.113	11.31	0.71	1.44	0.72	5.3	3.9	0.9877

response of the three proposed models to predict the shear strength for a set of input parameters which are selected taking into account the average value of each parameter in the collected database. For further showing the performance of the proposed models and for comparison purpose, the response of three well-known codes (ACI 440-15, JSCE-97, and CSA S806-12) was also considered. The approach depends on keeping all input parameters at their selected values, except that, in each time, a single parameter value was changed incrementally within the expected practical values. Consequently, an arrangement of manufactured data for the single considered parameter is produced; this procedure was repeated for all parameters so that all models are examined for the entire input parameters. The selected input parameters are  $f'_c = 46$  MPa,  $b_w = 200$  mm,  $d = 400$  mm,  $a/d = 4$ ,  $\rho_f = 0.011$ , and  $E_f = 74$  GPa. It is worthy to note that the ANNs model cannot properly predict the shear strength for input parameters outside the range of training data; therefore, it is only valid for prediction within the range of input parameters of the training data [8].

Figure 8 indicates the tendency of the predicted shear strength by different models to the varieties of the main design parameters ( $d$ ,  $f'_c$ ,  $\rho_f$ ,  $E_f$ ,  $a/d$ , and  $b_w$ ). Generally, it can be observed that the proposed models, particularly the ANNs model, yielded larger shear capacities for all parameters, while ACI 440-15 yielded the lowest shear capacities which indicate that the ACI 440-15 is very conservative.

The relationship of beam depth with the predicted shear strength showed that all the proposed models and codes increased with the increase in the beam depth throughout the range of 100–1000 mm. The ACI 440-15 considers the effect of beam depth linearly, while all other models represent the effect of depth nonlinearly; the ANNs, GEP, and NLR models consider the depth raised to a power of 0.83, 0.67, and 0.66 respectively. Also, it can be observed that the GEP and NLR yield almost the same results. All the proposed models and codes showed an increase in shear strength with the increase in the concrete compressive

strength but in different rates. It was found that  $f'_c$  is raised to a power of 0.66, 0.30, and 0.2 for ANNs, GEP, and NLR, respectively.

The effect of the flexure reinforcement ratio on shear strength indicates a similar trend of the NLR model and the design codes, but the ANNs and GEP models showed a slightly decreased trend for reinforcement ratios greater than 0.03; this is not in agreement with codes and previous studies because of that only few data were available with  $\rho_f$  larger than 0.03, and these data actually showed decreasing shear capacity. Additionally, these models were derived based only on the artificial technology of data training without manually choosing the general mathematical shape of the model, in contrary to the NLR model and design codes which was derived based on the theoretical or semiempirical criteria.

The shear strength also increased with the increase in the elastic modulus of the flexure reinforcement ratio. It can be observed that all models showed a similar trend line for the entire range of data, while the ANNs model showed an increased rate up to about 110 GPa, and then the increase rate reduced significantly; similar results also obtained by Bashir and Ashour [8]. On the contrary, the trend lines of the shear span to depth ratio are decreased for GEP and NLR models for the entire range of data; meanwhile for ANNs model, it decreases up to  $a/d$  of 5, and then it started to increase slightly. This behavior is in agreement with the few available experimental results [32, 52, 56] which were studied as  $a/d$  greater than 5. However, other codes do not consider the effect of  $a/d$  as the trend lines for ACI 440-15 and JSCE-97 are constant, while the CSA S806 trend line remains constant beyond the  $a/d$  value of 5. Finally, the effect of beam width on shear strength is linear as indicated by trend lines for all models except the ANNs model which showed a lower increase rate beyond 700 mm width.

To investigate how the proposed models consider the size effect on shear capacity, the same parametric data used for studying the beam depth are used. Figure 9 presents

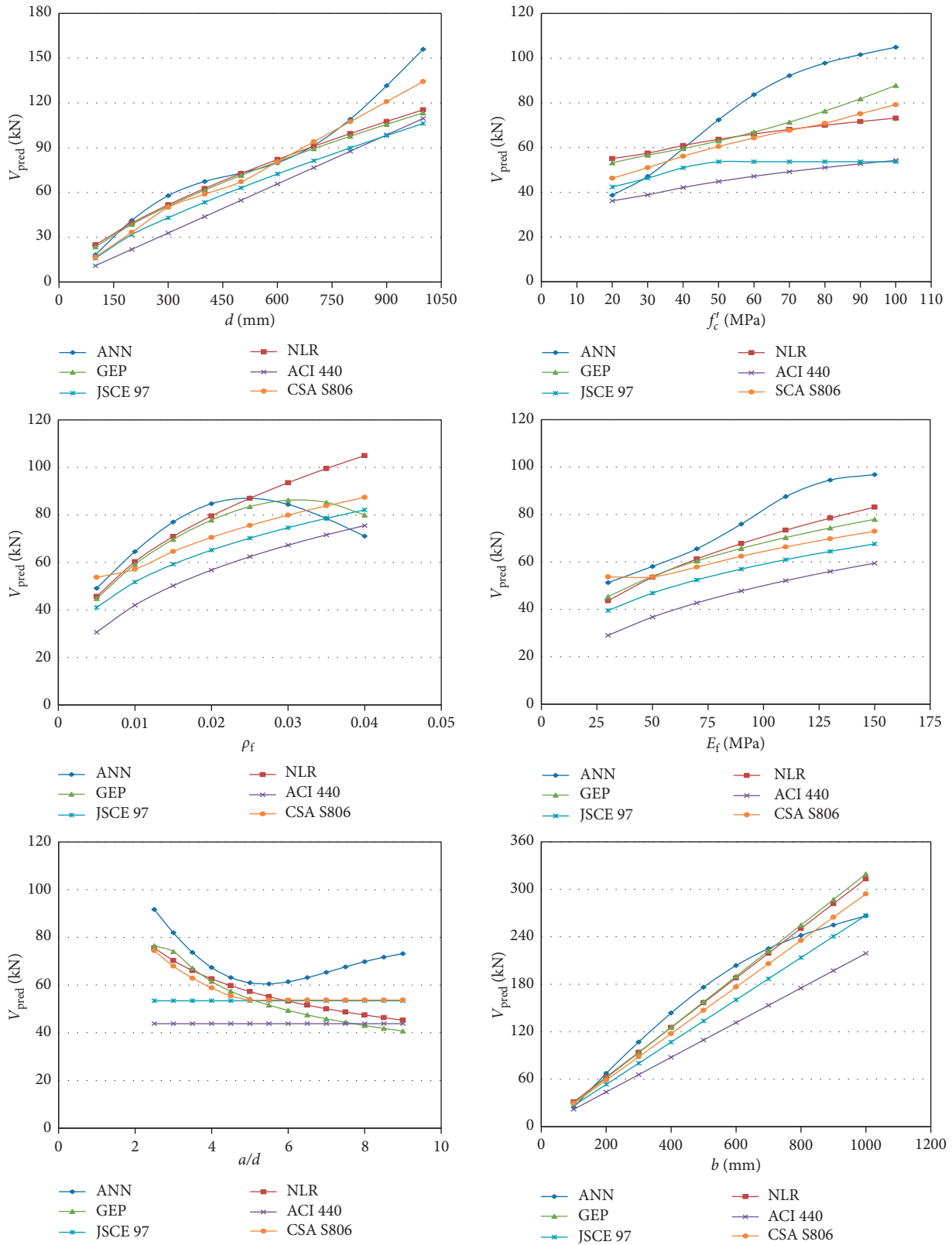


FIGURE 8: Effect of the parameters ( $d$ ,  $f'_c$ ,  $\rho_f$ ,  $E_f$ ,  $a/d$ , and  $b_w$ ) on shear capacity predicted by ANNs, GEP, NLR, and three design codes (ACI.1R 440-06, JSCE-97, and CSA S806-12).

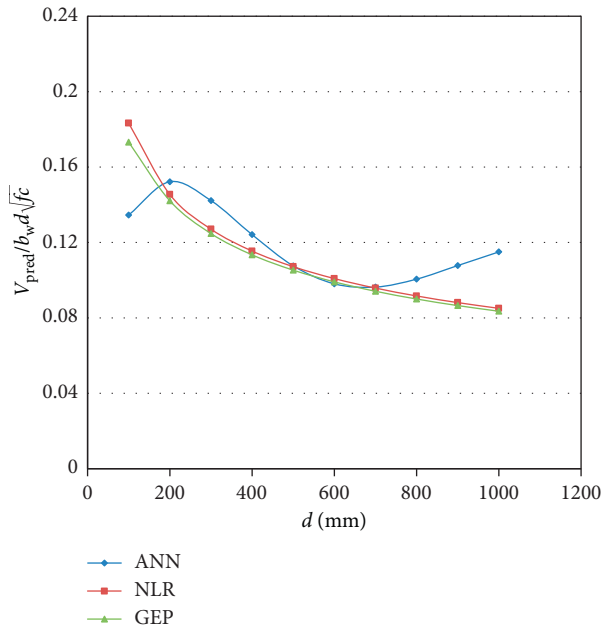


FIGURE 9: Normalized shear strength ( $V_{pred}/b_w d \sqrt{f'_c}$ ) versus beam depth.

the relationship between normalized shear strength as ( $V_{pred}/b_w d \sqrt{f'_c}$ ) and beam depth. It is clear that the normalized shear strength is decreased with the increase in the beam depth for ANNs, GEP, and NLR showing that the size effect is efficiently presented in these models. The trends of GEP and NLR are very close and compatible and decreased from a depth of 100 mm to 1000 mm, while the ANNs model seems to be more accurate as it shows an increase in the trend up to the depth of 200 mm, and then it decreased similarly to that of GEP and NLR; after that, the trend starts to increase slightly.

It can be summed up to that the artificial intelligent models, due to their efficiency and powerful ability in recognizing the parameters interaction, demonstrate various rates of change and fluctuation for the entire scope of input parameters. The ANNs and GEP models define accurately the interaction of each parameter on shear strength prediction and have a great ability to represent the actual response of each parameter in spite of its complexity and fluctuation nature. Furthermore, these models are evolved by training numerous preliminary linear and nonlinear models without any prior assumption regarding the shape and structure of the mathematical model.

## 9. Conclusions

An experimental database including 269 shear test results of FRP-reinforced concrete members without stirrups available in the literature was established to propose three prediction models to estimate the shear capacity of FRP-RC members using three powerful tools which are ANNs, GEP, and NLR. The following conclusions can be drawn from this study:

- (i) The proposed models for predicting the shear capacity of FRP-RC members based on ANNs and GEP techniques showed excellent performance, great efficiency, and high level of accuracy and yielded consistent results throughout a wide range of influencing parameters; moreover, the ANNs model is more superior than the GEP, as the SD and  $R^2$  for ANNs are 0.113 and 0.9877 and for GEP are 0.162 and 0.97, respectively.
- (ii) A simple, rational, and yet accurate empirical equation was proposed for predicting shear strength of FRP-RC members by NLR. The equation considers all the important influencing parameters and simplified to be easy for use. In addition, it gives consistent and accurate results with SD and  $R^2$  of 0.173 and 0.95, respectively.
- (iii) Through a comparative statistical analysis for the proposed models with seven shear design codes and six proposed equations from the literature, it has been found that the most accurate and efficient models are ANNs and GEP and to a lower degree NLR. Among the codes and available proposals, the CSA S806-12 and Ashour and Kara [20] equations were appearing to be more accurate than the others.
- (iv) From a parametric study considering all the influencing parameters on shear capacity, it was found that the ANNs model, and to a lower level GEP model, defines accurately the interaction of each parameter on shear capacity prediction and has a great ability to represent the actual response of each parameter in spite of its complexity and fluctuation nature.
- (v) The ANNs and GEP models demonstrate that the effect of flexure reinforcement ratio on shear capacity decreased beyond 0.03, as a real response to the available few data in this range; therefore, more studies are needed to confirm this case.
- (vi) The ANNs model demonstrated that the effect of  $a/d$  does not absolutely reduce the shear capacity, while beyond the  $a/d$  value of 5, its effect could become reverse and contribute to increase in the shear capacity as confirmed by few previous studies.
- (vii) The size effect is considered properly by the proposed models, particularly the ANNs model, which yields more accurate shear capacity prediction to the experimental results.

## Data Availability

The (database of shear strength of beams without stirrups) data used to support the findings of this study are included within the article.

## Conflicts of Interest

The authors declare that they have no conflicts of interest.

## References

- [1] M. S. Alam and A. Hussein, "Size effect on shear strength of FRP reinforced concrete beams without stirrups," *Journal of Composites for Construction*, vol. 17, no. 4, pp. 507–516, 2013.
- [2] J. R. Yost, S. P. Gross, and D. W. Dinehart, "Shear strength of normal strength concrete beams reinforced with deformed GFRP bars," *Journal of Composites for Construction*, vol. 5, no. 4, pp. 268–275, 2001.
- [3] A. G. Razaqpur, B. O. Isgor, S. Greenaway, and A. Selley, "Concrete contribution to the shear resistance of fiber reinforced polymer reinforced concrete members," *Journal of Composites for Construction*, vol. 8, no. 5, pp. 452–460, 2004.
- [4] M. Nehdi, H. El Chabib, and A. A. Saïd, "Proposed shear design equations for FRP-reinforced concrete beams based on genetic algorithms approach," *Journal of Materials in Civil Engineering*, vol. 19, no. 12, pp. 1033–1042, 2007.
- [5] ASCE-ACI.445, "Recent approaches to shear design of structural concrete," *Journal of Structural Engineering*, vol. 124, no. 12, pp. 1375–1417, 1998.
- [6] R. Park and T. Paulay, *Reinforced Concrete Structures*, John Wiley & Sons, Hoboken, NJ, USA, 1975.
- [7] I. F. Kara, "Prediction of shear strength of FRP-reinforced concrete beams without stirrups based on genetic programming," *Advances in Engineering Software*, vol. 42, no. 6, pp. 295–304, 2011.
- [8] R. Bashir and A. Ashour, "Neural network modelling for shear strength of concrete members reinforced with FRP bars," *Composites Part B: Engineering*, vol. 43, no. 8, pp. 3198–3207, 2012.
- [9] K. Nasrollahzadeh and M. M. Basiri, "Prediction of shear strength of FRP reinforced concrete beams using fuzzy inference system," *Expert Systems with Applications*, vol. 41, no. 4, pp. 1006–1020, 2014.
- [10] S. Lee and C. Lee, "Prediction of shear strength of FRP-reinforced concrete flexural members without stirrups using artificial neural networks," *Engineering Structures*, vol. 61, pp. 99–112, 2014.
- [11] E. M. Golafshani and A. Ashour, "A feasibility study of BBP for predicting shear capacity of FRP reinforced concrete beams without stirrups," *Advances in Engineering Software*, vol. 97, pp. 29–39, 2016.
- [12] ACI-440, *Guide for the Design and Construction of Structural Concrete Reinforced with Fiber-Reinforced Polymer (FRP)*, ACI 440. 1R-15, American Concrete Institute, Farmington Hills, MI, USA, 2015.
- [13] JSCE, "Recommendation for design and construction of concrete structures using continuous fiber reinforcing materials," in *Concrete Engineering Series 23*, A. Machida, Ed., Japan Society of Civil Engineers, Tokyo, Japan, 1997.
- [14] BISE, *Interim Guidance on the Design of Reinforced Concrete Structures Using Fiber Composite Reinforcement*, British Institution of Structural Engineers, Seto, Ltd., London, UK, 1999.
- [15] CSA, Canadian Highway Bridge, *Design Code. Supplement No. 1 to CAN/CSA S6-06 (S6.1S1-10)*, Canadian Standards Association (CSA), Mississauga, ON, Canada, 2010.
- [16] ISIS, *Reinforced Concrete Structures with Fibre Reinforced Polymers—Design Manual No. 3*, University of Manitoba, ISIS Canada Corporation, Winnipeg, MB, Canada, 2007.
- [17] CNR-DT.203, "Guide for the design and construction of concrete structures reinforced with fiber-reinforced polymer bars," in *Advisory Committee on Technical Recommendations for Construction*, CNR-DT 203/2006, CNR, Rome, Italy, 2007.
- [18] CSA, "Code for the design and construction of building structures with fibre-reinforced polymers," in *CAN/CSA/S806-12*, p. 198, Canadian Standard Association, Toronto, ON, Canada, 2012.
- [19] A. Razaqpur and S. Spadea, "Resistenza a taglio di elementi di calcestruzzo rinforzati e staffe di FRP," in *Proceedings of AIAS*, Maratea, Italy, September 2010.
- [20] A. F. Ashour and I. F. Kara, "Size effect on shear strength of FRP reinforced concrete beams," *Composites Part B: Engineering*, vol. 60, pp. 612–620, 2014.
- [21] A. R. Yousif, "Shear strength of large FRP-reinforced concrete beams without shear reinforcement," *Journal of Pure and Applied Sciences*, vol. 27, pp. 9–28, 2015.
- [22] A. K. El-Sayed, E. F. El-Salakawy, and B. Benmokrane, "Shear capacity of high-strength concrete beams reinforced with FRP bars," *ACI Structural Journal*, vol. 103, p. 383, 2006.
- [23] A. G. Razaqpur and O. B. Isgor, "Proposed shear design method for FRP-reinforced concrete members without stirrups," *ACI Structural Journal*, vol. 103, p. 93, 2006.
- [24] K. Maruyama and W. Zhao, "Flexural and shear behaviour of concrete beams reinforced with FRP rods," in *Proceedings of the International Conference on Corrosion and Corrosion Protection of Steel in Concrete*, pp. 24–28, Sheffield, UK, 1994.
- [25] W. Zhao, K. Maruyama, and H. Suzuki, "Shear behavior of concrete beams reinforced by FRP rods as longitudinal and shear reinforcement," in *Proceedings of the Second International RILEM Symposium on Non-Metallic (FRP) Reinforcement for Concrete Structures*, p. 352, Ghent, Belgium, August 1995.
- [26] H. Nakamura and T. Higai, "Evaluation of shear strength of the concrete beams reinforced with FRP," in *Proceedings of Japan Society of Civil Engineers*, p. 89, Ghent, Belgium, 1995.
- [27] K. Maruyama and W. Zhao, "Size effect in shear behavior of FRP reinforced concrete beam," in *Advanced Composite Materials in Bridges and Structures*, pp. 227–234, Canadian Society for Civil Engineering, Montreal, QC, Canada, 1996.
- [28] Y. Mizukawa, Y. Sato, T. Ueda, and Y. Kakuta, "A study on shear fatigue behavior of concrete beams with FRP rods," in *Proceedings of the Third International Symposium on Non-Metallic (FRP) Reinforcement for Concrete Structures (FRPRCS-3)*, pp. 309–316, Japan Concrete Institute, Sapporo, Japan, 1997.
- [29] N. Duranovic, K. Pilakoutas, and P. Waldron, "Tests on concrete beams reinforced with glass fibre reinforced plastic bars," in *Proceedings of the Third International Symposium on Non-Metallic (FRP) Reinforcement for Concrete Structures (FRPRCS-3)*, pp. 479–486, Sapporo, Japan, 1997.
- [30] N. Swamy and M. Aburawi, "Structural implications of using GFRP bars as concrete reinforcement," in *Proceedings of 3rd International Symposium, FRPRCS*, pp. 503–510, Sapporo, Japan, 1997.
- [31] C. R. Michaluk, S. H. Rizkalla, G. Tadros, and B. Benmokrane, "Flexural behavior of one-way concrete slabs reinforced by fiber reinforced plastic reinforcements," *ACI Structural Journal*, vol. 95, pp. 353–365, 1998.
- [32] D. Deitz, I. Harik, and H. Gesund, "One-way slabs reinforced with glass fiber reinforced polymer reinforcing bars," *Special Publication*, vol. 188, pp. 279–286, 1999.
- [33] T. Alkhrdaji, M. Wideman, A. Belarbi, and A. Nanni, "Shear strength of GFRP RC beams and slabs," in *Proceedings of the*

- International Conference, Composites in Construction-CCC*, pp. 409–414, Porto, Portugal, 2001.
- [34] G. S. Melo and J. A. Rayol, “Shear resistance of GFRP reinforced concrete beams,” in *Proceedings of the Rehabilitating and Repairing the Buildings and Bridges of Americas: Hemispheric Workshop on Future Directions*, Mayagüez, PR, USA, pp. 47–64, 2002.
- [35] A. K. Tureyen and R. J. Frosch, “Shear tests of FRP-reinforced concrete beams without stirrups,” *ACI Structural Journal*, vol. 99, pp. 427–434, 2002.
- [36] S. P. Gross, J. R. Yost, D. W. Dinehart, E. Svensen, and N. Liu, “Shear strength of normal and high strength concrete beams reinforced with GFRP bars,” in *Proceedings of International Conference on High Performance Materials in Bridges*, pp. 426–437, ASCE, Reston, VA, USA, 2003.
- [37] M. Tariq and J. Newhook, “Shear testing of FRP reinforced concrete without transverse reinforcement,” in *Proceedings of Annual Conference of the Canadian Society for Civil Engineering*, pp. 1330–1339, Moncton, NB, Canada, June 2003.
- [38] S. Gross, D. Dinehart, J. Yost, and P. Theisz, “Experimental tests of high-strength concrete beams reinforced with CFRP bars,” in *Proceedings of the 4th International Conference on Advanced Composite Materials in Bridges and Structures (ACMBS-4)*, Calgary, AB, Canada, 2004.
- [39] A. Lubell, T. Sherwood, E. Bentz, and M. P. Collins, “Safe shear design of large, wide beams: adding shear reinforcement is recommended,” *Concrete International*, vol. 26, pp. 66–78, 2004.
- [40] J. Yost, S. Gross, G. Masone, and P. Hamelin, “Sustained load effects on deflection and ultimate strength of concrete beams reinforced with GFRP,” in *Proceedings of the International Conference, Composites in Construction (CCC2005)*, Lyon, France, July 2005.
- [41] A. El-Sayed, E. El-Salakawy, and B. Benmokrane, “Shear strength of one-way concrete slabs reinforced with fiber-reinforced polymer composite bars,” *Journal of Composites for Construction*, vol. 9, no. 2, pp. 147–157, 2005.
- [42] A. E. Kilpatrick and L. Easden, “Shear capacity of GFRP reinforced high strength concrete slabs,” in *Proceedings of the 18th Australasian Conference on the Mechanics of Structures and Materials, Perth, Australia*, vol. 1, pp. 119–124, Taylor & Francis, London, UK, 2005.
- [43] A. K. El-Sayed, E. F. El-Salakawy, and B. Benmokrane, “Shear strength of FRP-reinforced concrete beams without transverse reinforcement,” *ACI Structural Journal*, vol. 103, p. 235, 2006.
- [44] A. Ashour, “Flexural and shear capacities of concrete beams reinforced with GFRP bars,” *Construction and Building Materials*, vol. 20, no. 10, pp. 1005–1015, 2006.
- [45] M. Guadagnini, K. Pilakoutas, and P. Waldron, “Shear resistance of FRP RC beams: experimental study,” *Journal of Composites for Construction*, vol. 10, no. 6, pp. 464–473, 2006.
- [46] R. Dawborn and A. Kilpatrick, *Flexural Shear Capacity of High Strength Concrete Slabs Reinforced with Longitudinal GFRP Bars*, 2006.
- [47] J. Niewels, “Zum Tragverhalten von Betonbauteilen mit Faserverbundkunststoffbewehrung,” Rheinisch-Westfälische Technische Hochschule Aachen, Lehrstuhl und Institut für Massivbau, Dissertation, 2008.
- [48] A. El-Sayed, K. Soudki, and E. Kling, “Flexural behaviour of self-consolidating concrete slabs reinforced with GFRP bars,” in *Proceedings of the 9th International Symposium on Fiber Reinforced Polymer Reinforcement for Reinforced Concrete Structures*, pp. 13–15, Sydney, NSW, Australia, 2009.
- [49] A. Caporale and R. Luciano, “Indagine sperimentale e numerica sulla resistenza a taglio di travi di calcestruzzo armate con barre di GFRP,” in *Proceedings of XXXVIII Convegno Nazionale AIAS*, Turin, Italy, September 2009.
- [50] R. Olivito and F. Zuccarello, “On the shear behaviour of concrete beams reinforced by carbon fibre-reinforced polymer bars: an experimental investigation by means of acoustic emission technique,” *Strain*, vol. 46, no. 5, pp. 470–481, 2010.
- [51] E. C. Bentz, L. Massam, and M. P. Collins, “Shear strength of large concrete members with FRP reinforcement,” *Journal of Composites for Construction*, vol. 14, no. 6, pp. 637–646, 2010.
- [52] A. G. Razaqpur, M. Shedid, and B. Isgor, “Shear strength of fiber-reinforced polymer reinforced concrete beams subject to unsymmetric loading,” *Journal of Composites for Construction*, vol. 15, no. 4, pp. 500–512, 2011.
- [53] M. Alam and A. Hussein, “Effect of member depth on shear strength of high-strength fiber-reinforced polymer-reinforced concrete beams,” *Journal of Composites for Construction*, vol. 16, no. 2, pp. 119–126, 2012.
- [54] F. Matta, A. K. El-Sayed, A. Nanni, and B. Benmokrane, “Size effect on concrete shear strength in beams reinforced with fiber-reinforced polymer bars,” *ACI Structural Journal*, vol. 110-S50, pp. 617–628, 2013.
- [55] B. Abdul-Salam, A. Farghaly, and B. Benmokrane, “Evaluation of shear behavior for one-way concrete slabs reinforced with carbon-FRP bars,” *GEN*, vol. 243, p. 1, 2013.
- [56] C. H. Kim and H. S. Jang, “Concrete shear strength of normal and lightweight concrete beams reinforced with FRP bars,” *Journal of Composites for Construction*, vol. 18, no. 2, article 04013038, 2014.
- [57] D. Tomlinson and A. Fam, “Performance of concrete beams reinforced with basalt FRP for flexure and shear,” *Journal of Composites for Construction*, vol. 19, no. 2, article 04014036, 2014.
- [58] M. A. Issa, T. Ovitigala, and M. Ibrahim, “Shear behavior of basalt fiber reinforced concrete beams with and without basalt FRP stirrups,” *Journal of Composites for Construction*, vol. 20, no. 4, article 04015083, 2015.
- [59] A. El Refai and F. Abed, “Concrete contribution to shear strength of beams reinforced with basalt fiber-reinforced bars,” *Journal of Composites for Construction*, vol. 20, no. 4, article 04015082, 2015.
- [60] G. B. Jumaa and A. R. Yuosif, “Size effect in shear failure of high strength concrete beams without stirrups reinforced with basalt FRP bars,” *KSCE Journal of Civil Engineering*, 2018, In press.
- [61] M. T. Hagan, H. B. Demuth, and M. H. Beale, *Neural Network Design (Electrical Engineering)*, Thomson Learning, Boston, MA, USA, 1995.
- [62] S. S. Haykin, S. S. Haykin, S. S. Haykin, and S. S. Haykin, *Neural Networks and Learning Machines*, Pearson, Vol. 3, Pearson, Upper Saddle River, NJ, USA, 2009.
- [63] M. Y. Mansour, M. Dicleli, J.-Y. Lee, and J. Zhang, “Predicting the shear strength of reinforced concrete beams using artificial neural networks,” *Engineering Structures*, vol. 26, no. 6, pp. 781–799, 2004.
- [64] H. Demuth, M. Beale, and M. Hagan, *Neural Network Toolbox™ 6, User’s Guide*, The MathWorks, Inc., vol. 10, p. 11, Natick, MA, USA, 2008.
- [65] A. W. Oreta and K. Kawashima, “Neural network modeling of confined compressive strength and strain of circular concrete columns,” *Journal of Structural Engineering*, vol. 129, no. 4, pp. 554–561, 2003.

- [66] S. Jung and K. S. Kim, "Knowledge-based prediction of shear strength of concrete beams without shear reinforcement," *Engineering Structures*, vol. 30, no. 6, pp. 1515–1525, 2008.
- [67] Z.-H. Duan, S.-C. Kou, and C.-S. Poon, "Prediction of compressive strength of recycled aggregate concrete using artificial neural networks," *Construction and Building Materials*, vol. 40, pp. 1200–1206, 2013.
- [68] H. El-Chabib, M. Nehdi, and A. Said, "Predicting shear capacity of NSC and HSC slender beams without stirrups using artificial intelligence," *Computers and Concrete*, vol. 2, no. 1, pp. 79–96, 2005.
- [69] F. Altun, Ö. Kişi, and K. Aydin, "Predicting the compressive strength of steel fiber added lightweight concrete using neural network," *Computational Materials Science*, vol. 42, no. 2, pp. 259–265, 2008.
- [70] J. R. Koza, "Genetic programming as a means for programming computers by natural selection," *Statistics and Computing*, vol. 4, no. 2, pp. 87–112, 1994.
- [71] C. Ferreira, "Gene expression programming in problem solving," in *Soft Computing and Industry*, pp. 635–653, Springer, Berlin, Germany, 2002.
- [72] C. Kayadelen, "Soil liquefaction modeling by genetic expression programming and neuro-fuzzy," *Expert Systems with Applications*, vol. 38, no. 4, pp. 4080–4087, 2011.
- [73] A. H. Gandomi, A. H. Alavi, and G. J. Yun, "Formulation of uplift capacity of suction caissons using multi expression programming," *KSCE Journal of Civil Engineering*, vol. 15, no. 2, pp. 363–373, 2011.
- [74] A. H. Gandomi, A. H. Alavi, and C. Ryan, *Handbook of Genetic Programming Applications*, Springer, Berlin, Germany, 2015.
- [75] A. H. Gandomi and A. H. Alavi, "A new multi-gene genetic programming approach to non-linear system modeling. Part II: geotechnical and earthquake engineering problems," *Neural Computing and Applications*, vol. 21, no. 1, pp. 189–201, 2012.
- [76] A. H. Alavi and A. H. Gandomi, "Energy-based numerical models for assessment of soil liquefaction," *Geoscience Frontiers*, vol. 3, no. 4, pp. 541–555, 2012.
- [77] L. Teodorescu and D. Sherwood, "High energy physics event selection with gene expression programming," *Computer Physics Communications*, vol. 178, no. 6, pp. 409–419, 2008.
- [78] GEPSOFT, *GeneXproTools, Version 5.0*, GEPSOFT, Bristol, UK, 2013, <http://www.gepsoft.com>.
- [79] S. M. Mousavi, P. Aminian, A. H. Gandomi, A. H. Alavi, and H. Bolandi, "A new predictive model for compressive strength of HPC using gene expression programming," *Advances in Engineering Software*, vol. 45, no. 1, pp. 105–114, 2012.
- [80] M. Saridemir, "Empirical modeling of splitting tensile strength from cylinder compressive strength of concrete by genetic programming," *Expert Systems with Applications*, vol. 38, no. 11, pp. 14257–14268, 2011.
- [81] M. Sonebi and A. Cevik, "Genetic programming based formulation for fresh and hardened properties of self-compacting concrete containing pulverised fuel ash," *Construction and Building Materials*, vol. 23, no. 7, pp. 2614–2622, 2009.
- [82] A. H. Alavi, P. Aminian, A. H. Gandomi, and M. A. Esmaili, "Genetic-based modeling of uplift capacity of suction caissons," *Expert Systems with Applications*, vol. 38, no. 10, pp. 12608–12618, 2011.
- [83] T. Zsutty, "Shear strength prediction for separate categories of simple beam tests," *ACI Journal Proceedings*, vol. 68, no. 2, pp. 138–143, 1971.

## Research Article

# Applicability of Artificial Neural Networks to Predict Mechanical and Permeability Properties of Volcanic Scoria-Based Concrete

Aref M. al-Swaidani <sup>1</sup> and Waed T. Khwies<sup>2</sup>

<sup>1</sup>Associate Professor, Faculty of Architectural Engineering, Arab International (Formerly European) University, Damascus, Syria

<sup>2</sup>Lecturer, Faculty of Information Technology, Arab International (Formerly European) University, Damascus, Syria

Correspondence should be addressed to Aref M. al-Swaidani; aydlswaidani@yahoo.fr

Received 30 July 2018; Accepted 26 September 2018; Published 25 October 2018

Guest Editor: Tayfun Dede

Copyright © 2018 Aref M. al-Swaidani and Waed T. Khwies. This is an open access article distributed under the Creative Commons Attribution License, which permits unrestricted use, distribution, and reproduction in any medium, provided the original work is properly cited.

Numerous volcanic scoria (VS) cones are found in many places worldwide. Many of them have not yet been investigated, although few of which have been used as a supplementary cementitious material (SCM) for a long time. The use of natural pozzolans as cement replacement could be considered as a common practice in the construction industry due to the related economic, ecologic, and performance benefits. In the current paper, the effect of VS on the properties of concrete was investigated. Twenty-one concrete mixes with three w/b ratios (0.5, 0.6, and 0.7) and seven replacement levels of VS (0%, 10%, 15%, 20%, 25%, 30%, and 35%) were produced. The investigated concrete properties were the compressive strength, the water permeability, and the concrete porosity. Artificial neural networks (ANNs) were used for prediction of the investigated properties. Feed-forward backpropagation neural networks have been used. The ANN models have been established by incorporation of the laboratory experimental data and by properly choosing the network architecture and training processes. This study shows that the use of ANN models provided a more accurate tool to capture the effects of five parameters (cement content, volcanic scoria content, water content, superplasticizer content, and curing time) on the investigated properties. This prediction makes it possible to design VS-based concretes for a desired strength, water impermeability, and porosity at any given age and replacement level. Some correlations between the investigated properties were derived from the analysed data. Furthermore, the sensitivity analysis showed that all studied parameters have a strong effect on the investigated properties. The modification of the microstructure of VS-based cement paste has been observed, as well.

## 1. Introduction

Concrete is the most widely used building material around the world because of the economic and widespread availability of its constituents, its versatility, its durability, and its adaptability [1]. Ordinary Portland Cement (OPC) concrete is a composite material, and its constituents are cement mixed with water, fine-grained aggregate (sand), and coarse-grained aggregate consisting of natural gravel or crushed stones [2]. The considerable amount of carbon dioxide (CO<sub>2</sub>) liberated during the production of Portland cement, the most commonly used hydraulic cement, is of a greater concern. On average, about 1 tonne of CO<sub>2</sub> is liberated per tonne of Portland cement produced [1].

The use of mineral admixtures such as pozzolans in concrete is now widespread due to many economic, ecological,

and performance-related benefits [3, 4]. The term “pozzolan” is originally from the town of Pozzuoli, northeast of Naples in Italy, where pozzolanic deposits from Vesuvius’ volcano were found [5].

Pozzolanic materials can be classified as natural and artificial pozzolans. Natural pozzolans could be considered the first cementitious materials used for the production of artificial stones, ancient mortars, and concretes, 3000 years ago [6]. Natural pozzolans may be further subdivided into two main groups: (i) those derived from volcanic rocks (volcanic scorias, pumices, etc.); (ii) others derived from rocks and earths [7]. An overview on the use of volcanic scoria as cement replacement can be found in the paper recently published by the author [8]. Although there are numerous works on using natural pozzolan as a substitute for cement, few studies investigating on volcanic scoria have been reported in the literature.

Many new prediction methods were developed in the last decades to investigate the compressive strength and durability of concrete containing supplementary cementitious materials (SCMs). However, there is no prediction model for concretes containing volcanic scoria as cement replacement. Some previous efforts to develop a predictive model for VS-based concrete used statistical methods that did not seem sufficient for different compositions of concrete. The objective of this work is to develop an empirical model to predict the compressive strength, porosity, and water permeability of concrete containing VS as cement replacement using ANNs. This prediction could be considered useful for concrete mix designers. For this purpose, twenty-one concrete mixes have been prepared with seven replacement levels and three different w/b ratios. Multiple linear regression (MLR) analysis has been used for comparison. In addition, some relationships among the investigated concrete properties have been established. Some estimation equations have been derived, as well.

The importance of this paper is to encourage countries having ample sources of scoria to investigate their potential use as cement replacement and thus making a greener concrete. The current paper focusses not only on one aspect but also it deals with both strength and durability of concrete containing VS as cement replacement. Moreover, technical information on the Syrian pozzolan is scarce, and this paper is part of the first comprehensive research that addresses the investigation of Syrian volcanic scoria. Furthermore, the paper might be particularly interesting for the regions where volcanic scoria is abundant, such as Harrat al-Shaam, which covers parts of Syria, Jordan, and KSA. Regions of similar geology may also get benefits from this study.

## 2. Background

*2.1. Artificial Neural Networks.* Artificial neural networks (ANNs) are algorithms simulating the human neurons. They are forms of artificial intelligence, which attempts to simulate the networks of the nerve cell (neurons) of the biological central nervous system [9]. An artificial neuron, also called a unit or a node, takes several input connections (dendrites in the biological neuron) which are assigned certain weights (analogous to synapses). The unit then computes the sum of the weighted inputs and applies an activation function (analogous to the cell body in the biological neuron). The result of the unit is then passed on using the output connection (axon function) [10].

In the recent year, such intelligent expert systems have been successfully applied in many fields of engineering, among which, they have been extensively used for predicting the compressive strength of blended cement-based concrete [11–27]. It was proved that the ANN-based strength prediction model could be successfully used to predict the strength of concrete for various mix ingredients and at different curing times. Bilim et al. [15] concluded in their study that ANNs can be an alternative approach for predicting compressive strength of ground-granulated blast furnace slag-(GGBFS-) based concrete. Saridemir [16] has established ANN models for predicting the compressive strength of concretes containing metakaolin and silica fume developed up to 180 days of curing. The results have shown that ANNs

have a great ability for predicting the compressive strength of metakaolin and silica fume-based concretes. Udhayakumar et al. [17] concluded also that a neural network-based strength model could be used successfully to find out the strength development of fly ash-based concrete with the curing time. Chithra et al. [18] have carried out a comparative study between ANN and MLR for predicting the compressive strength of concretes containing nanosilica and copper slag. The results have revealed that, in terms of the regression coefficient  $R^2$  and MSE, ANN models have provided better results than MLR. Other studies have used ANNs for predicting some durability-related properties of concrete [28–35]. They concluded that ANN models could be used effectively in predicting the concrete durability properties.

ANNs are able to model nonlinear relations between a set of inputs and corresponding outputs. The data set used to develop the ANN models are divided into subsets (i.e., training set, testing set, and validation set). The present paper deals with the prediction of the compressive strength, water permeability, and porosity of concrete using ANNs. MLR analysis has been used for comparison. The predicted concrete properties have been plotted versus the experimental results obtained in the laboratory.

The neural network uses the backpropagation (BP) procedure. The backpropagation learning algorithm, designed to train a feed-forward network, is an effective learning technique used to exploit the regularities and exceptions in the training sample [36, 37]. Backpropagation neural network (BPNN) which will be used in this research can be considered the most fundamental and widely used method among the ANN methods. It generally consists of multiple layers: an input layer, one or more hidden layers, and an output layer. Hidden layers may contain a large number of hidden neurons (processing units). Activation propagation is forwarded from the input layer toward the output layer, and then the algorithm compares the network outputs with known targets as it is a supervised learning algorithm and propagates the error backward. Weights and biases are updated based on calculated errors in order to meet the target.

The most common activation function is the sigmoid function, which is a continuously differentiable function that satisfies the relation, as follows [9]:

$$f(\alpha_i) = \frac{1}{1 + \exp(-\alpha_i)}, \quad (1)$$

where  $\alpha$  is a constant used to control the slope of the semilinear region [16].

The activation function is applied to bind the network input and output of the different layers to a specific range that the network can efficiently handle. The logistic sigmoid activation function with a scaling range between 0 and 1 was found to be the best settings for the present application.

By repeating the procedure described above until the error is acceptably small or no marked improvement is noted, the final output can be obtained [38].

*2.2. Multiple Linear Regression.* Multiple linear regression (MLR) is a statistical method whose general purpose is to

generate relationship between several independent variables and a dependent variable [39]. In MLR, the predicted value of a single dependent variable  $Y$  is a linear transformation of one or more independent variables  $X$  such that the sum of squared deviations of the observed and predicted  $Y$  is a minimum. With five independent variables, as in the present paper, the prediction of  $Y$  is expressed by the following formula:

$$Y = b_0 + b_1X_1 + b_2X_2 + b_3X_3 + b_4X_4 + b_5X_5, \quad (2)$$

where  $b_i$  values are called regression weights and are calculated in a way that minimizes the sum of squared deviations and  $X_i$  are the independent variables.

### 3. Materials and Methods

**3.1. Experimental Part.** Twenty-one concrete mixtures have been prepared using VS-based cements of seven replacement levels (0, 10, 15, 20, 25, 30, and 35%) and three w/b ratios of 0.5, 0.6, and 0.7. The volcanic scoria was quarried from southeast of Damascus (Figure 1). The investigated properties (i.e., compressive strength, water permeability, and concrete porosity) were obtained after five curing ages (i.e., 2, 7, 28, 90, and 180 days). The compression test was conducted on 150 mm cubic concrete specimens (Figures 2(a) and 2(b)) in accordance with ISO 4012. Water permeability measured in terms of depth of water penetration was carried out as per standard EN 12390-8 (Figure 2(c)). Porosity measurements were conducted using the vacuum saturation method in accordance with RILEM CPC 11.3 [40]. Table 1 and Figure 3 summarize the chemical composition of the materials used in the concrete mix and the aggregate grading with their physical properties. All of the experimental results were employed in the prediction process using ANNs.

**3.2. Network Architecture.** Artificial neural network is a powerful data-modeling tool that is able to capture and represent complex input and output relationships. The design of the ANN model requires identifying the network architecture (i.e., number of input neurons, output neurons, hidden layers, and neurons in each hidden layers) and the network settings (activation function and learning rate). Artificial neural networks consist of at least three layers, i.e., an input layer, one or more hidden layer/layers, and an output layer. Three ANN models have been established: ANN1 for predicting the concrete compressive strength, ANN2 for predicting the concrete water permeability, and ANN3 for predicting the concrete porosity. The adopted network architecture consists of the following:

- (i) Five neurons ( $N_i = 5$ ) in the input layer, which represent the variables of cement content (CC; kg), volcanic scoria content (VC; kg), water content (W; kg), superplasticizer content (SP; kg), and curing time ( $t$ ; day)
- (ii) One neuron in the output layer, which represents the value of the corresponding compressive strength (MPa), water permeability (mm), or concrete porosity (%).

- (iii) One hidden layer with 16 or 15 neurons in ANN1 and ANN3 models, respectively, and two hidden layers with 9 and 7 neurons in the ANN2 model.

Determining the optimum number of the hidden layer neurons is an important issue in order to predict accurately a characteristic using ANNs. The choice of one or two hidden layers is a common practice because of the ability of these networks to approximate any nonlinear function and map any unknown relationships between the input and output variables. Four-layer ANNs (i.e., two hidden layers) have superior fitting capabilities over three-layer ANNs (i.e., one hidden layer); however, three-layer ANNs are computationally faster and have better generalization capabilities [41, 42]. That is why three- or four-layer ANNs were selected for the present application.

No reasonable theory on how many hidden layer neurons need to be employed for a particular problem has been established. Thus, the best approach to find the optimum number of hidden neurons is to start with a fewer number of neurons and then slightly increase the number of neurons. In the current work, the network models were developed as follows:

- (i) ANN1 was built for predicting the compressive strength. The number of hidden neurons that was selected is 16 ( $\sim 3Ni$ ) [43] in one hidden layer. The learning rate and momentum were 0.6 and 0.3, respectively. This selection was made upon experimenting all the possibilities of increasing hidden neurons from 10 to 22, learning rate from 0.1 to 0.9, and momentum from 0.1 to 0.9 for each. The experimental data sets are 525, 314, and 316 samples for compressive strength, water permeability, and concrete porosity, respectively.
- (ii) ANN2 was built for predicting the concrete water permeability. The number of hidden neurons that was selected is 9 in the first hidden layer and 7 in the second layer. The learning rate and momentum were 0.5 and 0.9, respectively. This selection was made upon experimenting all the possibilities of increasing hidden neurons from 7 to 30 in one hidden layer, learning rate from 0.1 to 0.9, and momentum from 0.1 to 0.9 for each. The experimental data set is 314 samples.
- (iii) ANN3 was built for predicting the concrete porosity. The number of hidden neurons that was selected is 15 ( $=3Ni$ ) in one hidden layer. The learning rate and momentum were 0.3 and 0.4, respectively. This selection was made upon experimenting all the possibilities of increasing hidden neurons from 7 to 22, learning rate from 0.1 to 0.9, and momentum from 0.1 to 0.9 for each. The experimental data set is 316 samples.

The architecture of the ANN models is shown in Figures 4–6. Levenberg–Marquardt backpropagation was used as a training function and hyperbolic tangent sigmoid was used as a transfer function. The learning rate, which identifies the amount of adjustments to connection weights

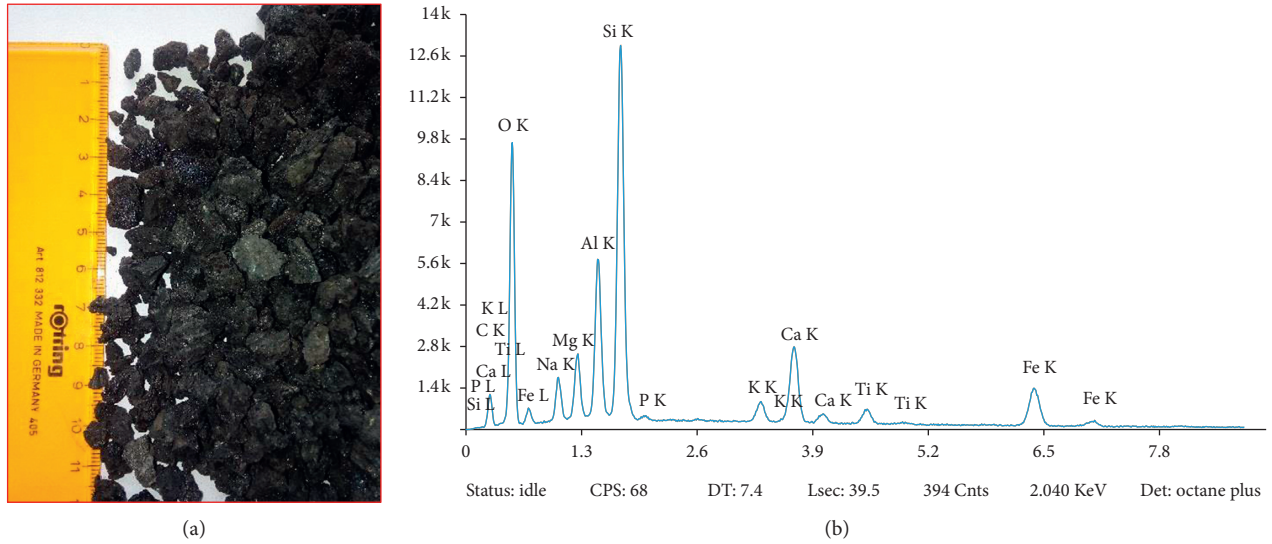


FIGURE 1: Macrograph of (a) the investigated volcanic scoria and (b) the EDX analysis.

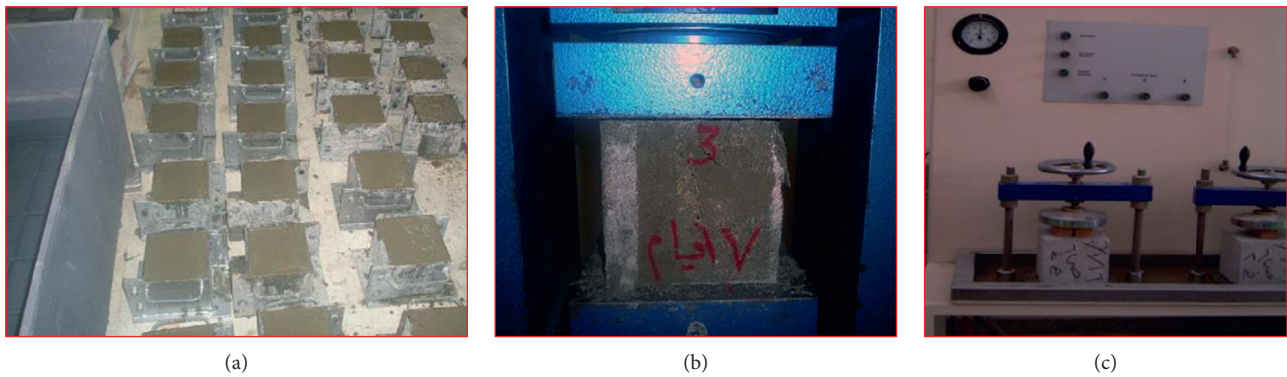


FIGURE 2: Photos of (a) the cubic concrete specimens, (b) the compression test, and (c) the water permeability set-up.

TABLE 1: Chemical composition of the ingredients used in the concrete mix.

Chemical composition (mass, %)	Materials				
	VS	Clinker	Gypsum	Dolomitic aggregate	Natural sand
SiO <sub>2</sub>	46.52	21.30	0.90	0.42	93.39
Al <sub>2</sub> O <sub>3</sub>	13.00	4.84	0.07	0.38	0.57
Fe <sub>2</sub> O <sub>3</sub>	11.40	3.99	0.10	0.10	0.24
CaO	10.10	65.05	32.23	31.40	1.70
CaO <sub>f</sub>	—	2.1	—	—	—
MgO	9.11	1.81	0.20	20.46	0.20
SO <sub>3</sub>	0.27	0.25	45.29	0.18	1.15
Loss on ignition	2.58	—	21.15	46.48	2.52
Na <sub>2</sub> O	2.14	0.60	—	0.06	0.06
K <sub>2</sub> O	0.77	0.28	—	0.30	0.05
Cl <sup>-</sup>	<0.1	0.05	—	0.021	0.017

during training, was determined based on the network performance. The learning rate and momentum were adjusted for each ANN to get the best performance. The data set was divided into three subsets as follows: 70% for training, 15% for testing, and 15% for validating. The

correlation coefficient ( $R$ ) obtained for training, testing, validating, and overall data for each ANN are shown in Table 2.

The artificial neural networks have been established using MATLAB software, Neural Network Toolbox. The

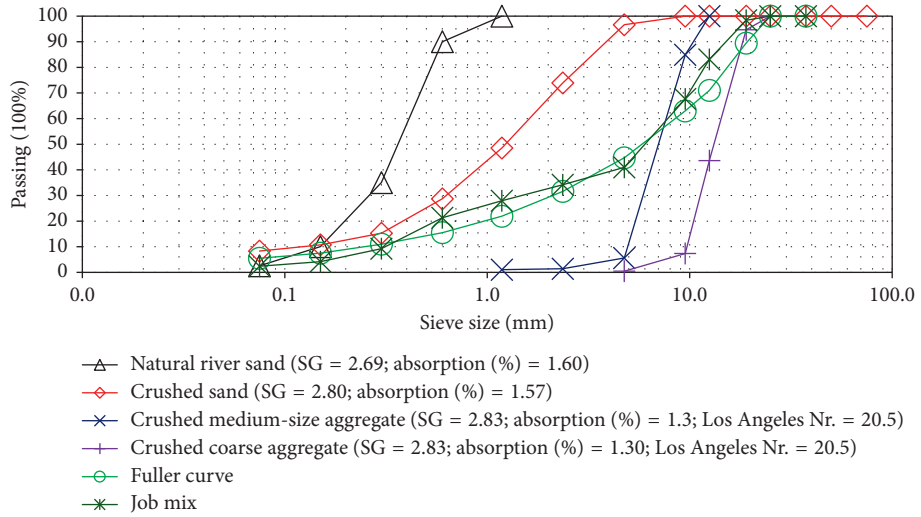


FIGURE 3: Particle-size distribution of the aggregates with some physical properties.

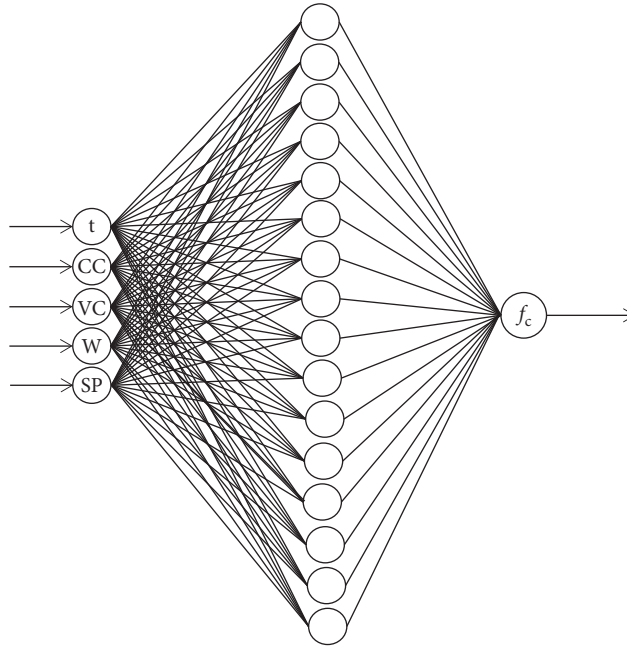


FIGURE 4: ANN1 model for predicting the compressive strength of VS-based concrete.

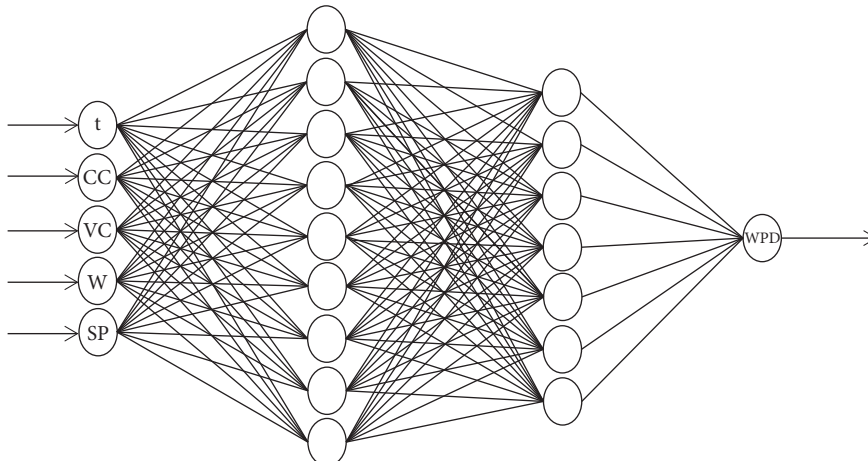


FIGURE 5: ANN2 model for predicting the water permeability of VS-based concrete.

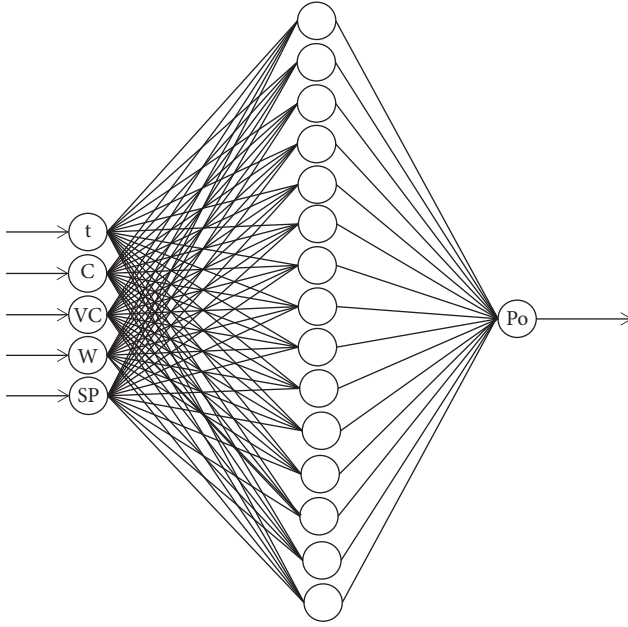


FIGURE 6: ANN3 model for predicting the porosity of VS-based concrete.

TABLE 2: Correlation coefficients ( $R$ ) of artificial neural network models.

ANN model	Correlation coefficient ( $R$ )			
	Training	Testing	Validating	Overall data
ANN1 (compressive strength)	0.99976	0.99937	0.99953	0.99968
ANN2 (water permeability)	0.99927	0.99732	0.99864	0.99891
ANN3 (porosity)	0.99972	0.99951	0.99873	0.99954

regression analysis has also been carried out using MATLAB software.

The validity of the constructed models was evaluated using the following criteria:

- (i) Root mean squared error (RMSE): the error that arose during the training, testing, and validating in ANN models can be evaluated by the RMSE, which can be calculated using the following function:

$$RMSE = \sqrt{\frac{1}{n} \sum_{i=1}^n (\text{experimental value} - \text{predicted value})^2}. \quad (3)$$

- (ii) The RMSE is used in evaluating the average vertical distance between the data points and the corresponding points on the fitting straight. When the RMSE value is smaller, the ANN model is better.
- (iii) Mean absolute percentage error (MAPE): the average of the absolute percentage error can be calculated using the following function:

$$MAPE = \left( \frac{1}{n} \sum_{i=1}^n \left| \frac{\text{experimental value} - \text{predicted value}}{\text{experimental value}} \right| \right) \times 100\%. \quad (4)$$

- (iv) R-square coefficient ( $R^2$ ): the R-square coefficient is the absolute fraction of variance of a model.  $R^2$  can be calculated using the following function:

$$R^2 = 1 - \frac{\text{sum of squares of residuals}}{\text{sum of squares of predicted values}}. \quad (5)$$

When  $R^2$  is closer to 1, this means, there is a closer relationship between output and targeted output.

- (v) Durbin-Watson statistic (DW): this statistic criterion is used to verify the existence of multicollinearity. It varies between 0 and 4. The acceptable range of 1.5 to 2.5 indicates that the established models are unaffected by problems related to multicollinearity.

## 4. Results and Discussion

**4.1. Compressive Strength Development.** Results of the compressive strength development test are plotted in Figures 7–9. As expected, all concretes showed an increase in strength with curing time. Concretes specimens containing VS0 had higher compressive strengths at any curing time compared to VS-based binder concretes. In addition, the compressive strength of VS-based concretes decreased with the volcanic scoria replacement level for all curing times. This could be explained by (i) the reduction of cement content in the mix with the increase of VS content; i.e., the dilution effect and (ii) the slowness of the pozzolanic reaction [40]. However, due to the continuation of this reaction and the formation of a secondary C-S-H, a greater degree of hydration was achieved resulting in strengths after 90 and 180 days which were comparable to those of VS0-based specimens [40]. Furthermore, the compressive strength decreased significantly with the increase in w/b ratio.

**4.2. Water Permeability and Concrete Porosity.** Results of water penetration depth and porosity tests are illustrated in Figures 10 and 11, respectively, for all binder types, curing age, and w/b ratios. Water penetration depth can be considered as an indication of permeable and impermeable concrete. A depth of less than 50 mm classifies the concrete as impermeable and a depth of less than 30 mm as impermeable under aggressive conditions [44]. None of concretes even with w/b = 0.5 was found to be impermeable before 28 days of curing. However, concretes containing VS20 to VS35 can be considered as impermeable after 28 days of curing and as impermeable under aggressive environments after 90 days of curing, according to Neville [44]. In addition, none of concretes with w/b = 0.7 was found to be impermeable under aggressive environments even after 180 days curing. Porosity of all mixes decreased with curing time. Furthermore, porosity of the concretes containing binders with high

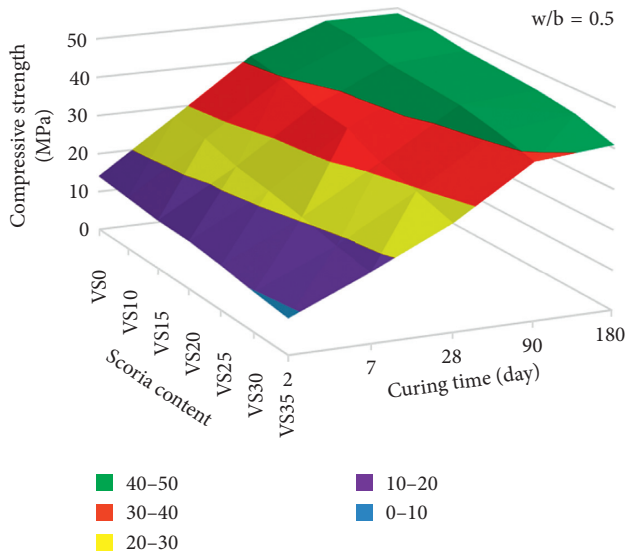


FIGURE 7: Development of compressive strength of VS-based binder concretes with curing ages at w/b = 0.5.

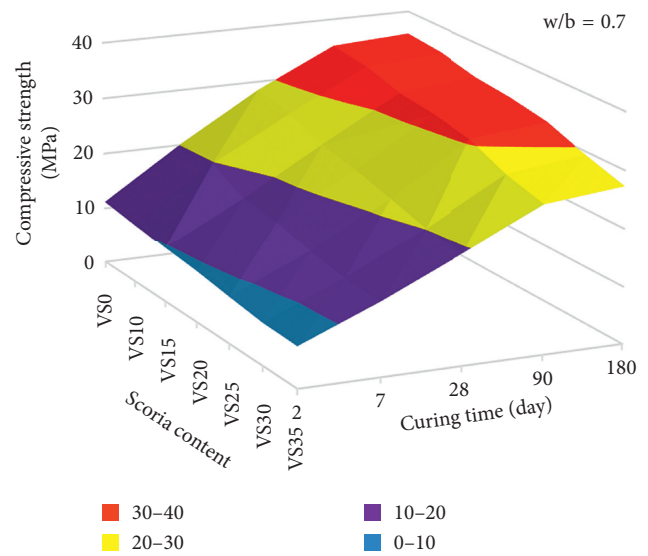


FIGURE 9: Development of compressive strength of VS-based binder concretes with curing ages at w/b = 0.7.

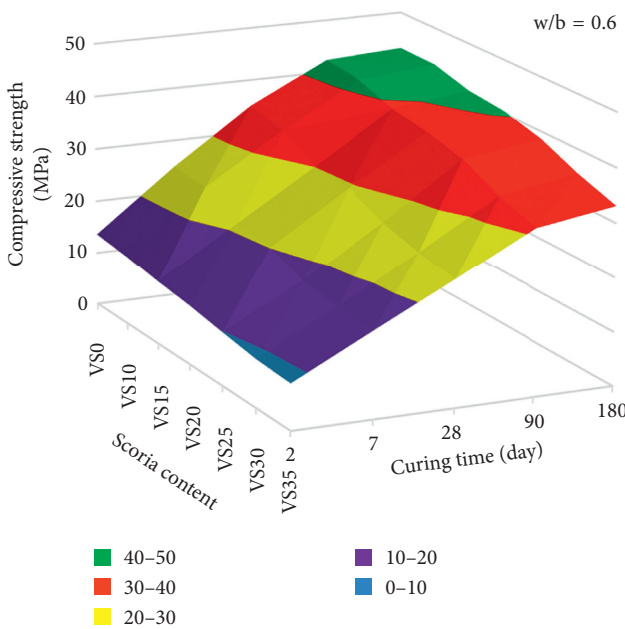


FIGURE 8: Development of compressive strength of VS-based binder concretes with curing ages at w/b = 0.6.

replacement levels of VS demonstrated much lower porosity as compared to the VS0-based concrete.

The reduction in the water permeability and porosity could be attributed to the pozzolanic reaction between the glassy phase in volcanic scoria and the CH liberated from hydration of C3S and C2S [40]. This was also confirmed by the SEM and EDX analysis.

4.3. *Correlations between Compressive Strength and Permeability-Related Properties.* Some correlations between compressive strength and each of water permeability and porosity of the investigated concretes are plotted in

Figures 12 and 13. These correlations were calculated for the entire population of test results. As shown in Figures 12 and 13, there are no reasonable relationships between the compressive strength and each of permeability-related properties of VS-based binder concrete. This supports the fact that strong concrete does not always ensure durable concrete. For instance, VS25-based binder concrete has lower compressive strengths, but higher water impermeability compared to VS0-based binder concrete at almost all curing times.

4.4. *Correlations between Water Permeability and Porosity.* The relationship between the water permeability and porosity is given in Figure 14. Definite correlations with a regression coefficient ( $R^2$ ) of 0.92 were observed between the water permeability and porosity, such that one can be predicted from the knowledge of the other. The correlation between the fitted parameters can be graded excellent when  $R^2 \geq 0.85$  [45]. Such similar relationship may need to be developed for other types of concrete aggregates, different volcanic scoria types, and other curing conditions.

4.5. *ANN and MLR Analysis.* Figures 4–6 show the structure of ANN models developed to predict the values of compressive strength, water permeability, and porosity of VS-based concrete. The calculated statistical values are tabulated in Table 3. The training has been carried out with 70% of the samples. RMSE values of 0.3066, 1.9783, and 0.3129, MAPE values of 1.2106, 2.6357, and 1.4998, and  $R^2$  values of 0.9999, 0.9995, and 0.9998 were obtained for prediction of the compressive strength, the water permeability, and the concrete porosity, respectively. The testing has been carried out with 15% of the samples. RMSE values of 0.3931, 2.4439, and 0.4050, MAPE values of 1.5470, 4.8220, and 2.0528, and  $R^2$  values of 0.9998, 0.9990, and 0.9997 were obtained for

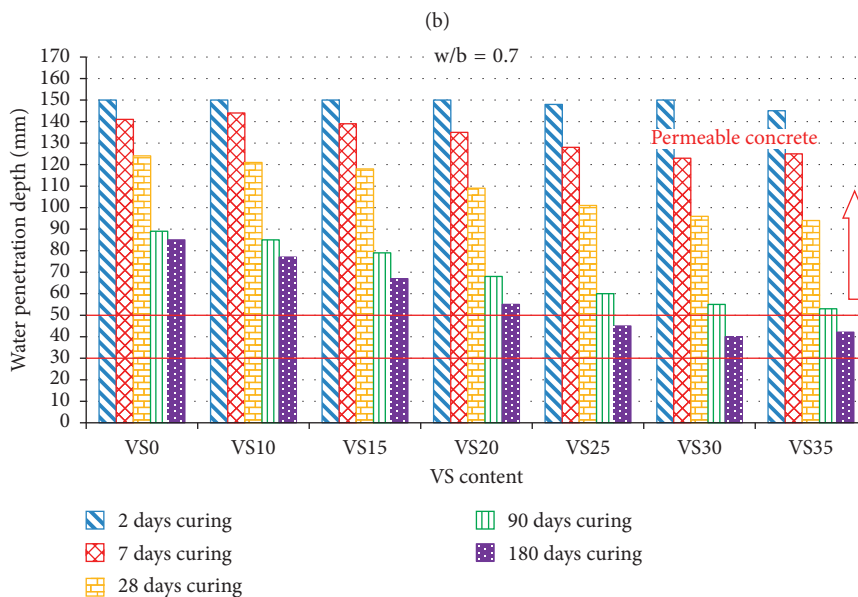
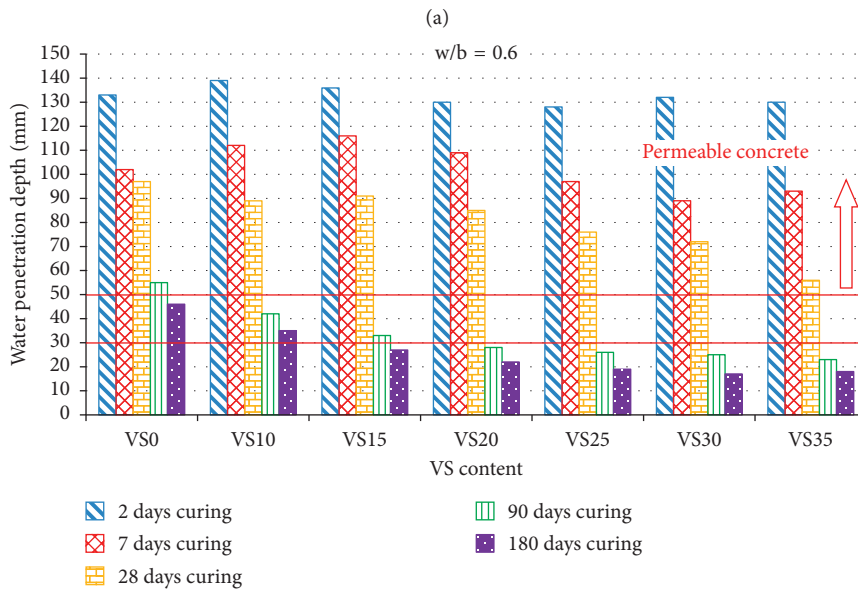
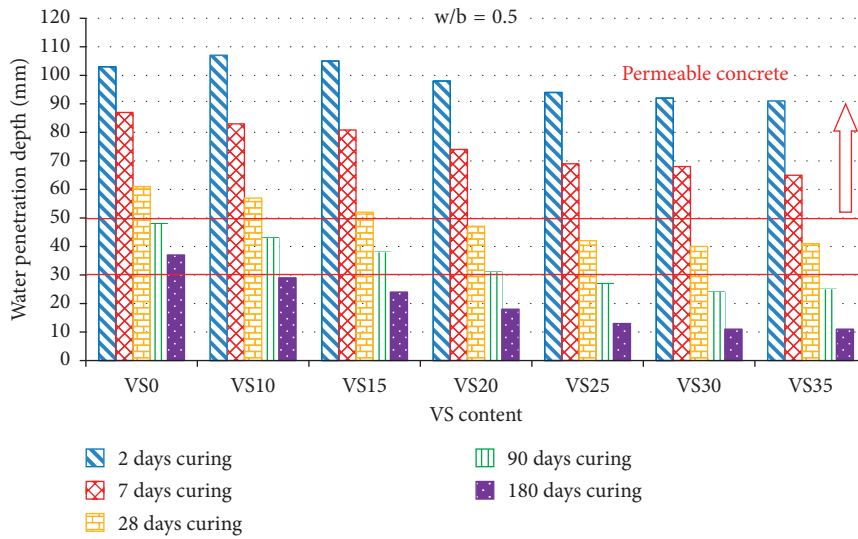


FIGURE 10: Water penetration depths of VS-based binder concretes of various w/b ratios cured for different times: (a)  $w/b = 0.5$ ; (b)  $w/b = 0.6$ ; (c)  $w/b = 0.7$ .

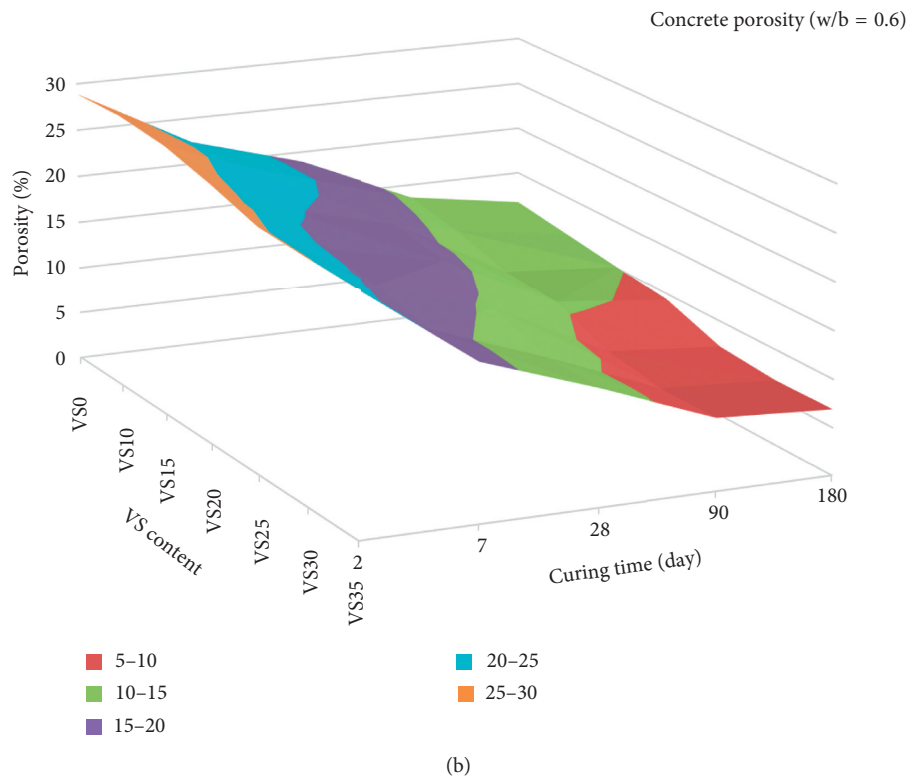
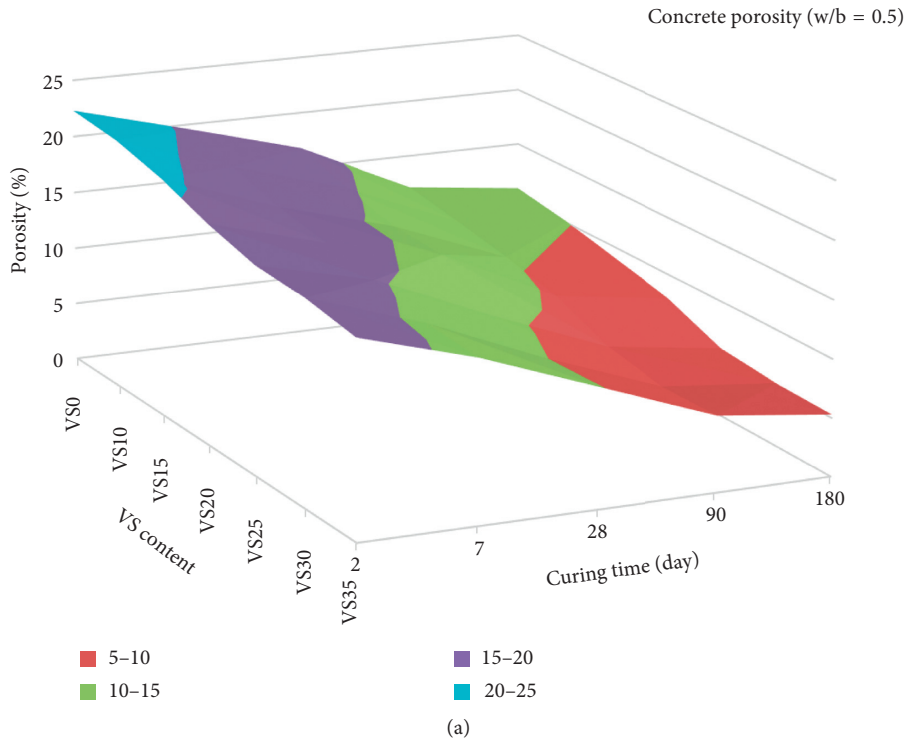


FIGURE 11: Continued.

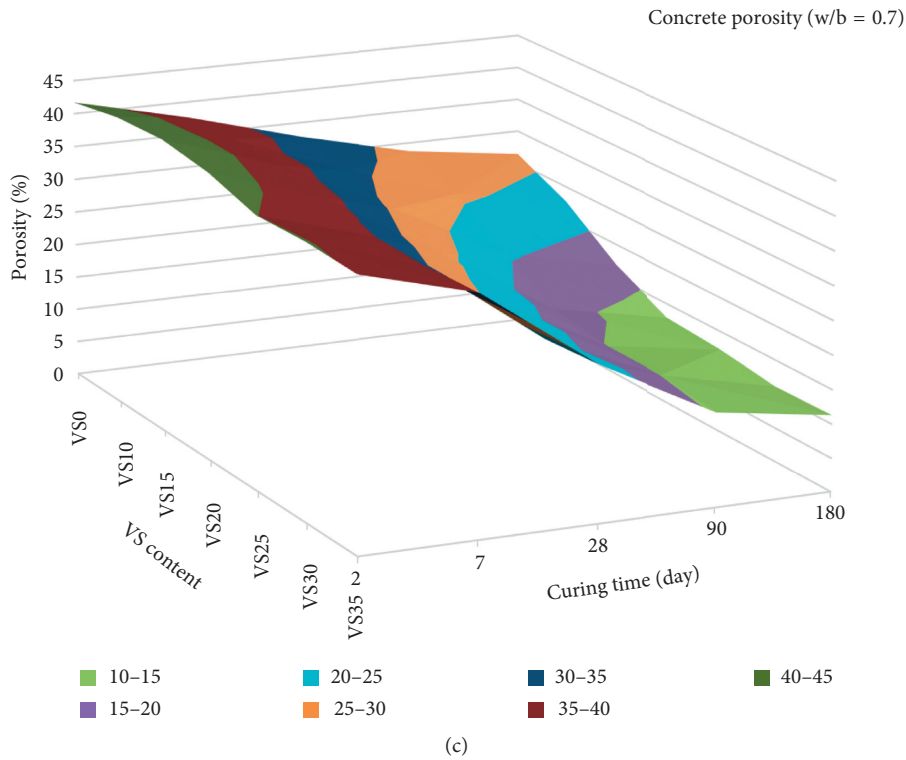


FIGURE 11: Porosity values of VS-based binder concretes of various w/b ratios cured for different times: (a) w/b = 0.5; (b) w/b = 0.6; (c) w/b = 0.7.

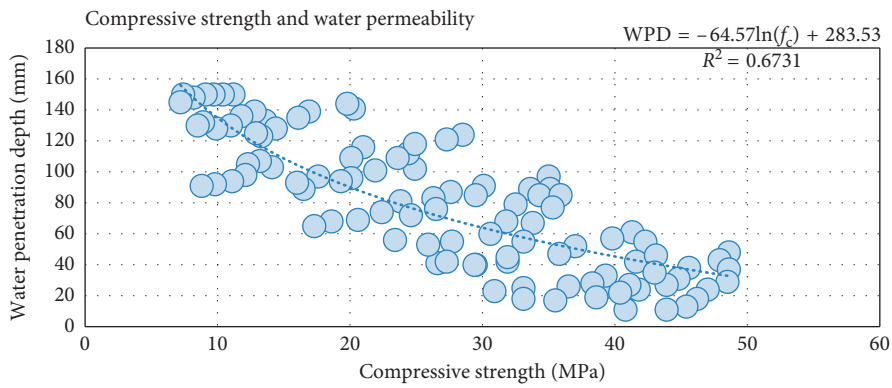


FIGURE 12: Correlation between water permeability and compressive strength of VS-based concretes.

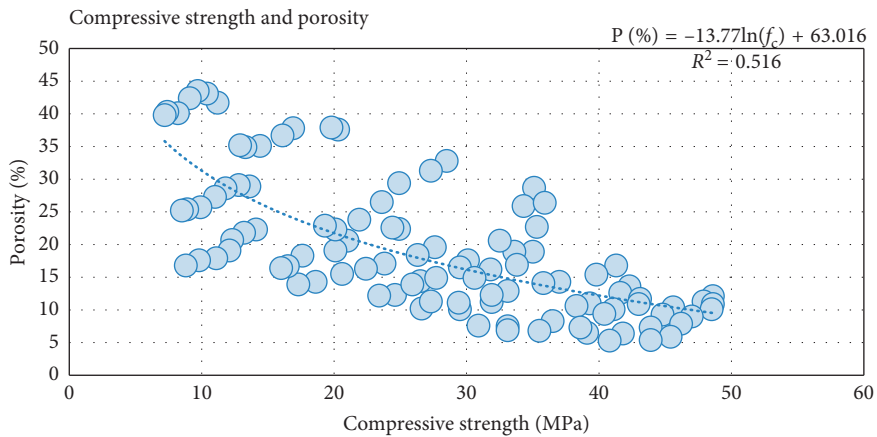


FIGURE 13: Correlation between porosity and compressive strength of VS-based concretes.

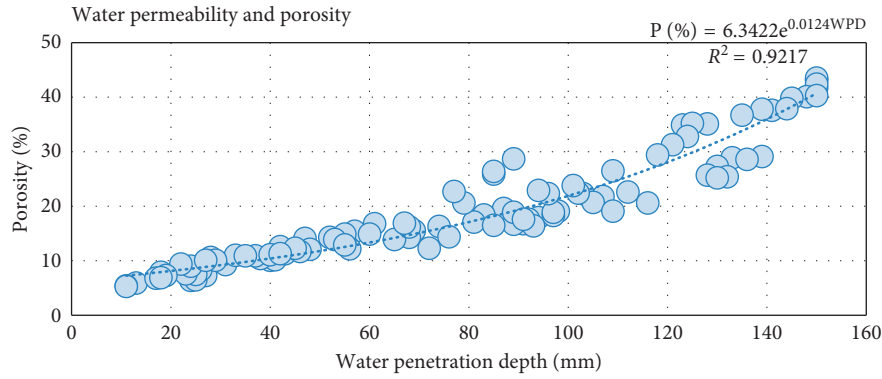


FIGURE 14: Correlation between water permeability and porosity of VS-based concretes.

TABLE 3: Results obtained for ANN models.

Model	Training				Testing				Validating			
	$R^2$	RMSE	MAPE	DW	$R^2$	RMSE	MAPE	DW	$R^2$	RMSE	MAPE	DW
ANN1	0.9999	0.3066	1.2106	1.7605	0.9998	0.3931	1.5470	1.9505	0.9998	0.3899	1.7307	1.6328
ANN2	0.9995	1.9783	2.6357	1.7003	0.9990	2.4439	4.8220	1.8094	0.9981	4.3322	4.7976	1.7467
ANN3	0.9998	0.3129	1.4998	1.5035	0.9997	0.4050	2.0528	1.9018	0.9995	0.4859	2.6921	1.6489

ANN1: compressive strength; ANN2: water permeability; ANN3: concrete porosity.

prediction of the compressive strength, the water permeability, and the concrete porosity, respectively. The validation has been carried out with also 15% of the samples. RMSE values of 0.3899, 4.3322, and 0.4859 and  $R^2$  values of 0.9998, 0.9981, and 0.9995 were obtained for prediction of the compressive strength, the water permeability, and the concrete porosity, respectively. The results mentioned above show that training has given the best performance by providing a very low MSE and  $R^2$  value very close to one. Furthermore, testing and validation have given an excellent performance by providing a very low RMSE and  $R^2$  value approximately equal to one. In contrast to the ANN results (Table 4), RMSE values of 6.11, 4.39, and 17.5, MAPE values of 20.922, 52.3229, and 59.212, and  $R^2$  values of 0.748, 0.82, and 0.829 were obtained by the MLR analysis for predicting the compressive strength, the water permeability, and concrete porosity, respectively. Furthermore, the obtained DW values for ANN models were between 1.5 and 2.5, consistent with the ideal range of values. However, the MLR models had very low DW values, which ranged from 0.026 to 0.157. The DW values signify the incidence of null and positive autocorrelation for ANN and MLR models, respectively.

Figures 15–17 clearly show that the goodness-of-fit of the ANN models is superior when compared to the MLR models. In addition, the statistical values shown above demonstrate that the prediction of the compressive strength, water permeability, and porosity of VS-based concrete with ANN models is highly accurate. The results related to compressive strength are in well agreement with those obtained by Chithra et al. [18], Ferhat Bingol et al. [46], and Saridemir [47]. However, as no or very little investigations on the prediction of water permeability and porosity of concretes containing natural pozzolans were found in the literature, the results could be comparable with other

TABLE 4: Results obtained for MLR models.

Models	Evaluation criteria				Number of data set samples
	$R^2$	DW	RMSE	MAPE	
MLR1	0.748	0.0259	6.11	20.922	367
MLR2	0.82	0.1566	4.39	52.3229	222
MLR3	0.829	0.1423	17.5	59.212	220

MLR1: compressive strength; MLR2: water permeability; MLR3: concrete porosity.

concrete durability-related properties, such as chloride ion permeability [31] and sulfate attack [30].

Furthermore, it is worth mentioning that the accuracy of ANN models in terms of RMSE, MAPE,  $R^2$ , and DW can be arranged in the following order: compressive strength  $\rightarrow$  concrete porosity  $\rightarrow$  water permeability. The sequence in MLR models is different from that in ANNs and can be written as follows when  $R^2$  is taken into account: concrete porosity  $\rightarrow$  water permeability  $\rightarrow$  compressive strength and can be written as follows when RMSE and MAPE are taken into account: compressive strength  $\rightarrow$  water permeability  $\rightarrow$  concrete porosity.

The equations obtained by MLR analysis are as follows:

$$\begin{aligned}
 f_c \text{ (MPa)} &= 0.1311 \times t + 0.1631 \times CC + 0.0768 \\
 &\quad \times VC - 0.1509 \times W - 0.0164 \times SP, \\
 \text{WPD (mm)} &= -0.4772 \times t - 0.2582 \times CC - 0.4815 \\
 &\quad \times VC + 0.9757 \times W + 4.7588 \times SP, \\
 \text{Po (\%)} &= -0.0884 \times t - 0.292 \times CC - 0.359 \\
 &\quad \times VC + 0.5724 \times W + 5.9841 \times SP,
 \end{aligned} \tag{6}$$

where  $f_c$  is the compressive strength (MPa), WPD is the water penetration depth (mm), Po is the concrete porosity (%),  $t$  is the curing time (day), CC is the cement content (kg),

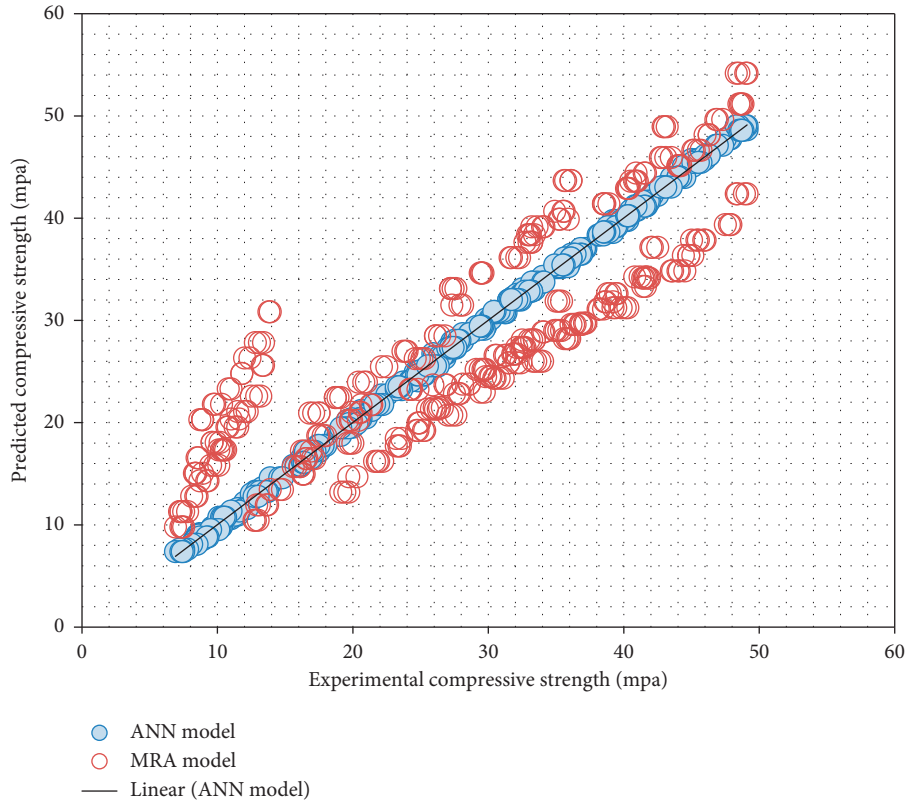


FIGURE 15: Predicted compressive strength versus experimental compressive strength for models ANN1 and MLR1.

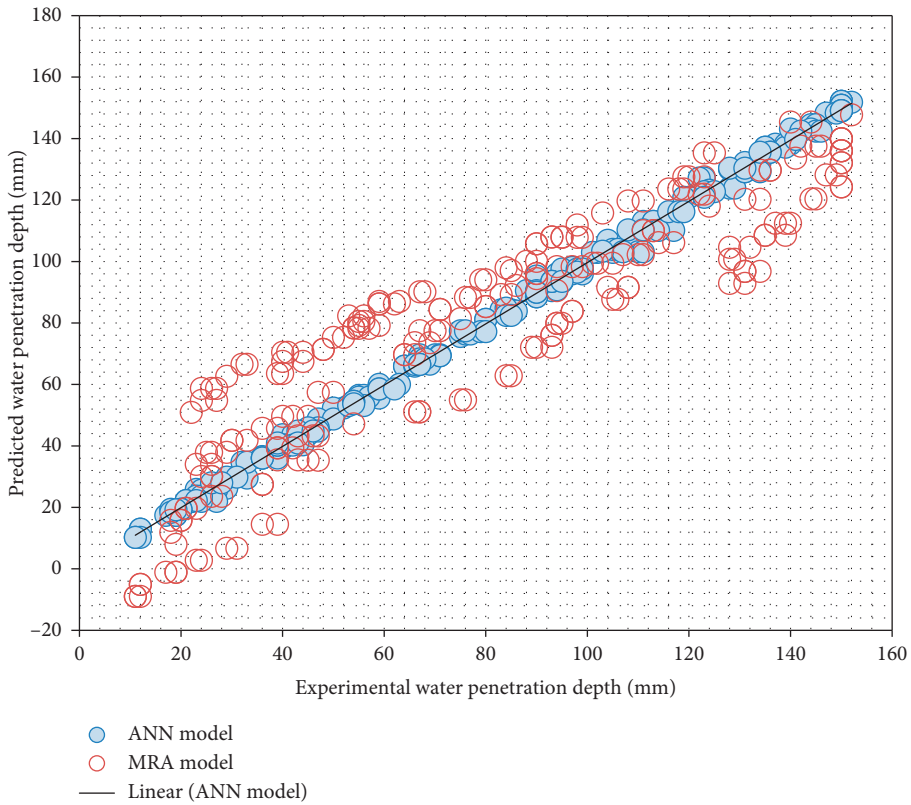


FIGURE 16: Predicted water permeability versus experimental water permeability for models ANN1 and MLR1.

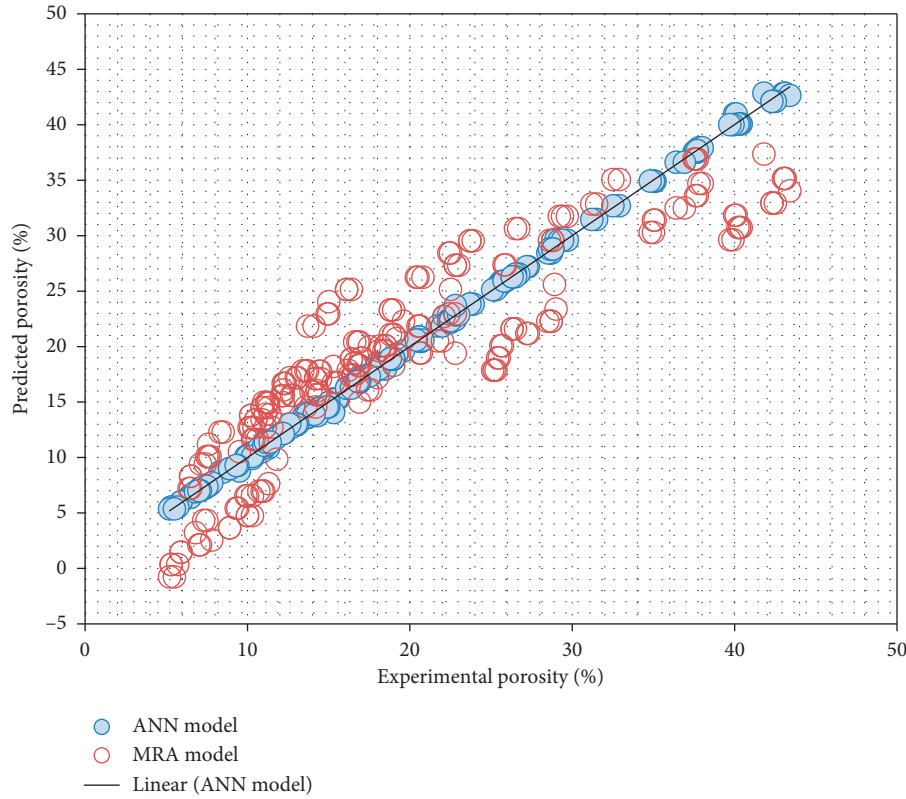


FIGURE 17: Predicted concrete porosity versus experimental concrete porosity for models ANN1 and MLR1.

VC is the volcanic scoria content (kg), W is the water content, and SP is the superplasticizer content.

**4.6. Sensitivity Analysis of ANN Models.** In order to assess the relative importance of the input variables, sensitivity analysis was conducted based on the Garson equation [48]. Garson [48] proposed an equation based on the partitioning of connection weights:

$$I_j = \frac{\sum_{m=1}^{m=Nh} \left( \left( |w_{jm}^{ih}| / \sum_{k=1}^{Ni} |w_{km}^{ih}| \right) \times |w_{mn}^{ho}| \right)}{\sum_{k=1}^{k=Ni} \left\{ \sum_{m=1}^{m=Nh} \left( \left( |w_{km}^{ih}| / \sum_{k=1}^{Ni} |w_{km}^{ih}| \right) \times |w_{mn}^{ho}| \right) \right\}} \quad (7)$$

where  $I_j$  is the relative importance of the  $j$ th input parameter on the output;  $Ni$  and  $Nh$  are the numbers of input and hidden neurons, respectively;  $w$  is connection weights; the superscripts  $i$ ,  $h$ , and  $o$  refer to input, hidden, and output layers, respectively; and the subscripts  $k$ ,  $m$ , and  $n$  refer to input, hidden, and output neurons, respectively.

Table 5 shows the weights between input and hidden layers (W1) and weights between hidden and output layers (W2). Table 6 shows the relative importance of the input parameters (curing time, cement content, VS content, water content, and superplasticizer content). It can be noted that all parameters have a strong effect on the investigated properties.

As clearly seen in Table 5, curing time was found to be the most influential parameter with a relative importance of 32.2%, 33.52%, and 51.80% for compressive strength, concrete

porosity, and water permeability, respectively. The higher relative importance of curing time can be attributed to the significant effect of this parameter on the permeability-related properties of concretes containing volcanic scoria as cement replacement. As mentioned earlier, a significant gradual improvement in permeability-related properties can be obtained with an increase in curing time, particularly at ages  $\geq 28$  days [38]. In addition, it is to be noted that other parameters have also considerable effects on the output values, particularly those forming the “w/b” ratio, i.e., cement content, VS content, and water content.

**4.7. Microstructural Investigation.** Scanning electron micrographs (SEM) of 7 day-, 28 day-, and 90 day-cured VS30-based pastes are shown in Figure 18. Figure 18(a) clearly shows a porous and noncompacted structure in seven day-cured VS30-based paste. However, a denser structure can be clearly observed after 28 and 90 days of curing (Figures 18(b) and 18(c)). This can be attributed to the continuation of the cement hydration, and formation of cementitious phases, such as (C-S-H) and (C-A-S-H) through the pozzolanic reaction between the glassy phase in volcanic scoria and CH released during the hydration of calcium silicates ( $C_3S$  and  $C_2S$ ) [49].

## 5. Conclusion

In this study, artificial neural networks were used for the prediction of 2, 7, 28, 90, and 180 days compressive strength,

TABLE 5: Weight matrix and weights between input and hidden layers (W1) and between hidden and output layers (W2) for the ANNI model.

Neuron	W1				W2	
	Time (day)	Cement content (kg)	VS content (kg)	Water content (kg)	SP	Output
1	-2.105944022	1.075228351	1.255199036	0.438755839	-0.030683697	1.279718465
2	0.144053427	-0.972020695	0.742996724	1.753640631	-1.340918263	-1.208902522
3	1.732934016	0.61985474	-1.155641212	-1.283690471	3.243864115	0.460723363
4	0.903445767	0.372764295	1.572839487	-0.87906307	1.904073089	0.705296001
5	0.938501968	-1.091473696	-2.116933639	-0.459056052	1.573936415	1.53887134
6	0.344253977	-0.597794971	0.779210827	1.235683476	2.059459437	0.961634634
7	-1.024890536	-1.466697926	-1.591821924	-1.081779779	1.829483202	0.698867474
8	-0.064928174	-1.591852569	1.716382139	1.62579402	-2.437814145	-0.331804241
9	-1.498209432	0.875620108	-0.423664145	-1.895854904	2.039710262	0.545700344
10	-0.233072918	-1.362387421	1.333842112	-1.465558	1.098041189	-0.562090401
11	-0.936088182	2.726784678	-1.120598625	-2.150579249	-0.530783246	0.108067552
12	-11.888422	0.182734218	0.268691589	0.167278196	0.141190095	-4.372180414
13	-0.214986128	-1.611586142	1.972556139	-1.4704395	1.201024837	-0.399869245
14	1.564288124	0.63694431	1.050612614	-0.532653652	0.778724302	0.192780767
15	0.430315807	-0.418860675	0.04929488	-0.345348435	-1.723849754	2.899735928
16	-0.007106844	-1.904352783	-1.119167674	1.319502798	0.223633621	2.309346307

TABLE 6: The relative importance of input parameters.

Concrete property	Relative importance of the input parameters				
	Time (day)	Cement content (kg)	VS content (kg)	Water content (kg)	SP
Compressive strength	32.2%	16.2%	14.8%	14.9%	21.9%
Water permeability	33.52%	18.97%	20.74%	12.86%	13.92%
Porosity	51.80%	8.59%	11.64%	12.16%	15.81%

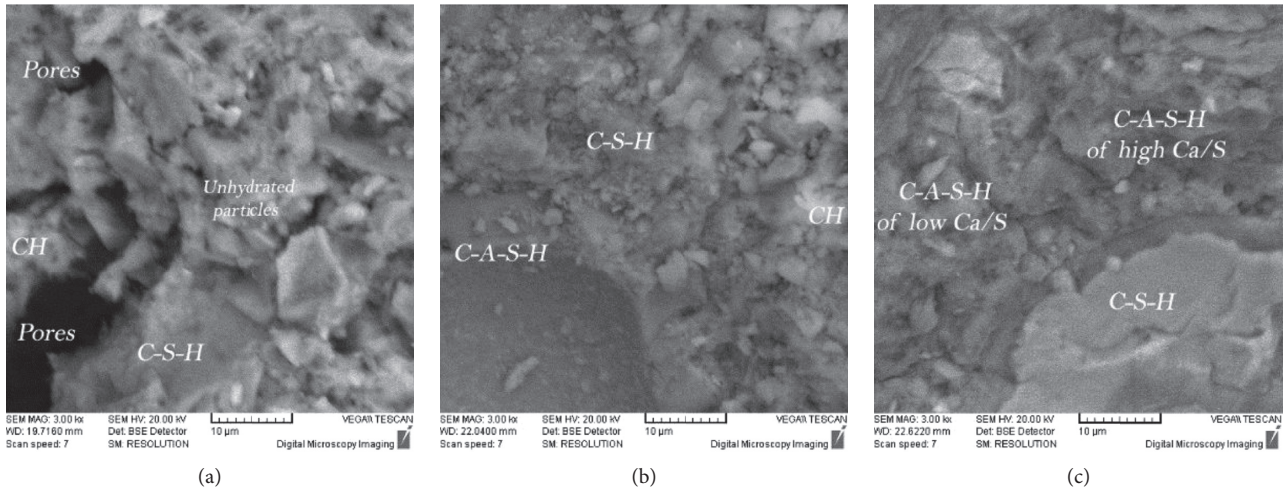


FIGURE 18: SEM of (a) 7 day-cured VS30-based paste, (b) 28 day-cured VS30-based paste, and (c) 90 day-cured VS30-based paste.

water permeability, and porosity of concretes containing volcanic scoria as cement replacement. MLR was also used for comparison. Based on the results obtained, the following conclusions can be drawn:

- (1) Volcanic scoria may be more efficient in terms of its contribution to one property rather than another one. For example, volcanic scoria makes a significant

contribution to reducing permeability of concrete despite the lower compressive strength.

- (2) In terms of concrete durability, the binders containing  $\geq 25\%$  VS were better than the control binder and globally gave the best performance among all the replacement levels. Consequently, a significant reduction in OPC consumption and greenhouse gas

emissions can be obtained. Therefore, incorporation of more than 25% VS can be adopted in the design of ecoconcrete.

- (3) Incorporation of volcanic scoria in concrete has significant effects on the properties of concrete, particularly durability-related properties. The water penetration depth and the porosity of VS-based cement concrete demonstrated better performance as compared to plain concrete, especially at curing age of 28 days and longer.
- (4) A comparison between ANN and MLR methods depicts that ANNs can be used to predict the investigated concrete properties, effectively.
- (5) The values predicted by ANN models are close to the experimental results. Statistical values, such as RMSE, MAPE,  $R^2$ , and DW which are used to evaluate the feasibility of the ANN and MLR models, have demonstrated that ANN models are all accurate methods for predicting the compressive strength, water permeability, and porosity of VS-based concrete. Their higher accuracy and applicability have made them a desirable substitute for the conventional regression methods. MLR models are less accurate than the ANN ones. Therefore, by adopting ANN models, there is no need to go through time-consuming and costly laboratory tests to obtain the investigated properties of VS-based concrete.
- (6) Results have indicated that ANN models are not only practical for predicting the compressive strength but also highly efficient for predicting the water permeability and porosity of VS-based concrete. Comparison between ANN models and MLR models in terms of RMSE, MAPE,  $R^2$ , and DW statistics showed that ANNs provide better results than those of MLR in prediction of all investigated properties. For instance,  $R^2$  values of 0.748, 0.82, and 0.829 were obtained by the MLR analysis for predicting the compressive strength, the water permeability, and concrete porosity, respectively, while these values, by contrast, were close to one in all ANNs models.
- (7) Sensitivity analysis showed that all studied parameters in this work (curing time, cement content, VS content, water content, and superplasticizer content) have considerable effects on the properties of concrete containing VS as cement replacement. However, curing time was found to be the most influential parameter with relative importance of more than 30%.
- (8) Investigating the volcanic scoria cones that have not been exploited yet is highly recommended. In addition, making more sustainable and durable concrete using volcanic scoria is highly encouraged.

## Data Availability

The data used to support the findings of this study are available from the corresponding author upon request.

## Conflicts of Interest

The authors declare that there are no conflicts of interest regarding the publication of this paper.

## References

- [1] P. C. Aitcin and S. Mindess, *Sustainability of Concrete*, SponPress, London, UK, 1st edition, 2011.
- [2] A. M. Brandt, *Cement-Based Composites: Materials, mechanical Properties and Performance*, Taylor & Francis, Abingdon, UK, 2nd edition, 2009.
- [3] P. K. Mehta and P. J. M. Monteiro, *Concrete: Microstructure, Properties and Materials*, McGraw-Hill, New York City, NY, USA, 3rd edition, 2006.
- [4] A. M. al-Swaidani and S. D. Aliyan, "Effect of adding scoria as cement replacement on durability-related properties," *International Journal of Concrete Structures and Materials*, vol. 9, no. 2, pp. 241–254, 2015.
- [5] P. Jahren and T. Sui, *Concrete and Sustainability*, CRC Press, Boca Raton, FL, USA, 2014.
- [6] C. Dedeloudis, M. Zervaki, K. Sideris et al., "Natural pozzolans," in *Properties of Fresh and Hardened Concrete Containing Supplementary Cementitious Materials*, N. De Belie et al., Ed., RILEM State-of-the-Art Reports 25, 2018.
- [7] A. A. Hammond, *Pozzolana Cements for Low Cost Housing*, Building and Road Research Institute, Japan, 1983.
- [8] A. Al-Swaidani, "Volcanic scoria as cement replacement," in *Volcanoes*, G. Aeillo, Ed., Intechopen, UK, 2018.
- [9] D. Graupe, *Principles of Artificial Neural Networks*, World Scientific, Singapore, 2nd edition, 2007.
- [10] S. Khan, H. Rahmani, S. A. A. Shah, and M. Bennamoun, *A Guide to Convolutional Neural Networks for Computer Vision*, Morgan and Claypool, CA, USA, 2018.
- [11] J. I. Kim, D. K. Kim, M. Q. Feng, and F. Yazdani, "Application of neural networks for estimation of concrete strength," *Journal of Materials in Civil Engineering*, vol. 16, no. 3, pp. 257–264, 2004.
- [12] F. Khademi, S. M. Jamal, N. Deshpande, and S. Londhe, "Predicting strength of recycled aggregate concrete using artificial neural network, adaptive neuro-fuzzy inference system and multiple linear regression," *International Journal of Sustainable Built Environment*, vol. 5, no. 2, pp. 355–369, 2016.
- [13] M. Sebastia, I. Fernandez Olmo, and A. Irabien, "Neural network prediction of unconfined compressive strength of coal fly-ash cement mixtures," *Cement and Concrete Research*, vol. 33, no. 8, pp. 1137–1146, 2003.
- [14] F. Ozcan, C. D. Atis, D. Karahan, E. Uncuoglu, and H. Tanyildizi, "Comparison of artificial neural network and fuzzy logic models for prediction of long-term compressive strength of silica fume concrete," *Advances in Engineering Software*, vol. 40, no. 9, pp. 856–863, 2009.
- [15] C. Bilim, C. D. Atis, H. Tanyildizi, and O. Karahan, "Predicting the compressive strength of ground granulated blast furnace slag concrete using artificial neural network," *Advances in Engineering Software*, vol. 40, no. 5, pp. 334–340, 2009.
- [16] M. Saridemir, I. B. Topcu, F. Ozcan et al., "Prediction of long term effects of GGBFS on compressive strength of concrete by artificial neural networks and fuzzy logic," *Construction and Building Materials*, vol. 23, no. 3, pp. 1279–1286, 2009.
- [17] V. Udhaya Kumar, B. H. Bharat Kumar, K. Balasubramanian, and T. S. Krishna Moorthy, "Applications of neural networks for concrete strength prediction," *Indian Concrete Journal*, vol. 2007, pp. 13–17, 2007.

- [18] S. Chithra, S. R. R. Senthil Kumar, K. Chimaraju, and F. Alfin Ashmita, "A comparative study on the compressive strength prediction models for high performance concrete containing nano silica and copper slag using regression analysis and artificial neural networks," *Construction and Building Materials*, vol. 114, pp. 528–535, 2016.
- [19] P. Chopra, R. K. Sharma, and M. Kumar, "Prediction of compressive strength of concrete using artificial neural network and genetic programming," *Advances in Materials Science and Engineering*, vol. 2016, Article ID 7648467, 10 pages, 2016.
- [20] M. I. Khan, "Predicting properties of high performance concrete containing composite cementitious materials using artificial neural networks," *Automation in Construction*, vol. 22, pp. 516–524, 2012.
- [21] M. Pala, E. Ozbay, A. Oztas, and M. I. Yuce, "Appraisal of long-term effects of fly ash and silica fume on compressive strength of concrete by neural networks," *Construction and Building Materials*, vol. 21, no. 2, pp. 384–394, 2007.
- [22] U. Atici, "Prediction of the strength of mineral admixture concrete using multivariable regression analysis and an artificial neural network," *Expert Systems with Applications*, vol. 38, no. 8, pp. 9609–9618, 2011.
- [23] I. B. Topcu and M. Saridemir, "Prediction of compressive strength of concrete containing fly ash using artificial neural networks and fuzzy logic," *Computational Materials Science*, vol. 41, no. 3, pp. 305–311, 2008.
- [24] B. Boukhatem, M. Ghrici, S. Kenai, and A. Tagnit-Hamou, "Prediction of efficiency factor of ground-granulated blast furnace slag of concrete using artificial neural network," *ACI Materials Journal*, vol. 108, no. 1, pp. 55–63, 2011.
- [25] S. Subasi, "Prediction of mechanical properties of cement containing class C fly ash by using artificial neural network and regression technique," *Scientific Research and Essay*, vol. 4, no. 4, pp. 289–297, 2009.
- [26] S. J. S. Hakim, J. Noorzaei, M. S. Jaafar, M. Jameel, and M. Mohammadhassani, "Application of artificial neural networks to predict compressive strength of high strength concrete," *International Journal of the Physical Sciences*, vol. 6, no. 5, pp. 975–981, 2011.
- [27] J. Noorzaei, S. J. S. Hakim, M. S. Jaafar, and W. A. M. Thanoon, "Development of artificial neural networks for predicting concrete compressive strength," *International Journal of Engineering and Technology*, vol. 4, no. 2, pp. 141–153, 2007.
- [28] O. A. Hodhod and H. I. Ahmed, "Modelling the corrosion initiation time of slag concrete using the artificial neural network," *HBRC Journal*, vol. 10, no. 3, pp. 231–234, 2014.
- [29] O. A. Hodhod and H. I. Ahmed, "Developing an artificial neural network model to evaluate the chloride diffusivity in high performance concrete," *HBRC Journal*, vol. 9, no. 1, pp. 15–21, 2014.
- [30] A. B. Goktepe, G. Inan, K. Ramyar, and A. Sezer, "Estimation of sulphate expansion level of PC mortar using statistical and neural approaches," *Construction and Building Materials*, vol. 20, no. 7, pp. 441–449, 2006.
- [31] E. Guneyisi, M. Gesoglu, T. Ozturan, and E. Ozbay, "Estimation of chloride permeability of concretes by empirical modelling: considering effects of cement type, curing condition and age," *Construction and Building Materials*, vol. 23, no. 1, pp. 469–481, 2009.
- [32] L. Sadowski and M. Nikoo, "Corrosion current density prediction in reinforced concrete by imperialist competitive algorithm," *Neural Computing and Applications*, vol. 25, no. 7–8, pp. 1627–1638, 2014.
- [33] R. Parichatprecha and P. Nimityongskul, "Analysis of durability of high performance concrete using artificial neural networks," *Construction and Building Materials*, vol. 23, no. 2, pp. 910–917, 2009.
- [34] H. Li and C. Lu, "Artificial neural network analysis of concrete carbonation under sustained loads," in *Proceedings of International Conference on Computer Application and System Modeling*, pp. 160–164, IEEE, Taiyuan, China, October 2010.
- [35] H. Yasarer and Y. Najjar, "Development of a mix-design based rapid chloride permeability assessment model using neuro-nets," in *Proceedings of International Joint Conference on neural networks*, pp. 2756–2760, IEEE, CA, USA, July–August 2011.
- [36] L. Yu, S. Wang, and K. K. Lai, *Foreign-Exchange-Rate Forecasting with Artificial Neural Networks*, Springer, Berlin, Germany, 2007.
- [37] A. Togholi, M. Mohammadhassani, M. Shariati, M. Suhartil, Z. Ibrahim, and N. H. Ramli Sulong, "Prediction of shear capacity of channel shear connectors using ANFIS," *Steel and Composite Structures*, vol. 17, no. 5, pp. 623–639, 2014.
- [38] T. Masters, *Practical neural network recipes C++*, Academic Press, Cambridge, MA, USA, 1993.
- [39] J. W. Johnson, "A heuristic method for estimating the relative weight of predictor variables in multiple regression," *Multivariate Behavioral Research*, vol. 35, no. 1, pp. 1–19, 2000.
- [40] A. M. Al-Swaidani, "Prediction of compressive strength and some permeability-related properties of concretes containing volcanic scoria as cement replacement," *Romanian Journal of Materials*, vol. 46, no. 4, pp. 505–514, 2016.
- [41] S. Tamura and M. Tateishi, "Capabilities of four-layered feed-forward neural networks: four layers versus three," *IEEE Transactions on Neural Networks*, vol. 8, no. 2, pp. 251–255, 1997.
- [42] P. Simpson, *Neural Networks Theory, Technology and Applications*, IEEE, New York, NY, USA, 1996.
- [43] T. Kavazoglu and P. M. Mather, "The use of backpropagating artificial neural networks in land cover classification," *International Journal of Remote Sensing*, vol. 24, no. 23, pp. 4907–4938, 2003.
- [44] A. M. Neville, *Properties of Concrete*, Pearson Education, London, UK, 5th edition, 2011.
- [45] D. C. Montgomery and E. A. Peck, *Introduction to Linear Regression Analysis*, Wiley, New York, NY, USA, 1982.
- [46] A. Ferhat Bingol, A. Tortun, and R. Gul, "Neural networks analysis of compressive strength of lightweight concrete after high temperatures," *Materials and Design*, vol. 52, pp. 258–264, 2013.
- [47] M. Saridemir, "Predicting the compressive strength of mortars containing metakaolin by artificial neural networks and fuzzy logic," *Advances in Engineering Software*, vol. 40, no. 9, pp. 920–927, 2009.
- [48] G. D. Garson, "Interpreting neural-network connection weights," *AI Expert*, vol. 6, pp. 47–51, 1991.
- [49] A. M. al-Swaidani, "Production of more durable and sustainable concretes using volcanic scoria as cement replacement," *Materiales De Construccion*, vol. 67, no. 326, p. 118, 2017.

## Research Article

# A Novel Dynamic Multicriteria Decision-Making Approach for Low-Carbon Supplier Selection of Low-Carbon Buildings Based on Interval-Valued Triangular Fuzzy Numbers

Xia Cao, Zeyu Xing , Yuqi Sun, and Shi Yin 

*School of Economics and Management, Harbin Engineering University, Harbin, Heilongjiang 150001, China*

Correspondence should be addressed to Zeyu Xing; [hrq962@163.com](mailto:hrq962@163.com)

Received 27 April 2018; Accepted 5 September 2018; Published 24 October 2018

Guest Editor: Tayfun Dede

Copyright © 2018 Xia Cao et al. This is an open access article distributed under the Creative Commons Attribution License, which permits unrestricted use, distribution, and reproduction in any medium, provided the original work is properly cited.

Due to the lack of natural resources and environmental problems which have been appearing increasingly, low-carbon buildings are more and more involved in the construction industry. The selection of low-carbon supplier is a significant part in the process of low-carbon building construction projects. In this paper, we propose a novel dynamic multicriteria decision-making approach for low-carbon supplier selection in the process of low-carbon building construction projects to deal with these problems. First, the paper establishes 5 main criteria and 17 subcriteria for low-carbon supplier selection in the process of low-carbon building construction projects. Then, a method considering interaction between criteria and the influence of constructors subjective preference and objective criteria information is proposed. It uses the basic concept and properties of the interval-valued triangular fuzzy number intuitionistic fuzzy weighted Bonferroni means (IVTFNIFWBM) operators and the objective information entropy and TOPSIS-based Euclidean distance to calculate the comprehensive evaluation results of potential low-carbon suppliers. The proposed method is much easier for constructors to select low-carbon supplier and make the localization of low-carbon supplier more practical and accurate in the process of building construction projects. Finally, a case study about a low-carbon building project is given to verify practicality and effectiveness of the proposed approach.

## 1. Introduction

Low-carbon building has been a popular research topic from academic and industrial sectors in recent years. Buildings play a central part in causing greenhouse gas (GHG) emissions and account for nearly 70% of GHG emissions in Hong Kong and up to 40% of total energy consumption [1]. These facts show that low-carbon building plays an important role in reducing the amount of GHG emissions. Many countries have launched a series of measures to reduce GHG emissions in the construction industry [2]. To cope with pressure, it is a vital factor to select their suitable low-carbon suppliers. Many factors should be taken into account in the process of low-carbon supplier selection as a complex multicriteria decision-making (MCDM) problem [3]. Therefore, it is critically important and necessary to study low-carbon supplier selection in the process of low-carbon building construction projects.

Many scholars have stressed the importance of selecting suitable criteria in the process of low-carbon supplier selection. Lee et al. [4] proposed 5 main criteria for supplier selection, such as quality, technology capability, pollution control, green products, and green competencies. Hsu et al. [5] established 13 criteria of supplier selection with three main criteria, such as planning, implementation, and management. Kannan et al. [6] and Tsui and Wen [7] thought low-carbon supplier selection should consider low-carbon criteria in environmental aspects, such as waste reduction, green technologies, and the usage of ecodesign. Gurel et al. [8] established 8 main criteria that include cost, delivery, quality, service, strategic alliance, and pollution control. Chen et al. [9] proposed 20 criteria for supplier selection and evaluation criteria with two dimensions (economic criteria and environmental criteria). Yu et al. [10] took the economic criteria and environmental criteria into consideration during low-carbon supplier selection.

Govindan and Sivakumar [11] took economics, operational factors, and environmental criteria into consideration. Pang et al. [12] proposed 4 main criteria including production and service. However, most of them focus on low-carbon supply chain management, and the research on the low-carbon supplier selection in the process of low-carbon building construction projects is fairly rare. Moreover, comparing with the traditional low-carbon supplier selection criteria, constructors must pay special attention to the environmental capabilities, low-carbon building technologies, and social factors for low-carbon supplier selection criteria in the process of low-carbon building construction projects [13]. This research takes these aspects into consideration, which have been ignored in many studies such as an evaluation criterion.

In recent years, extensive MADM methods have been proposed for supplier selection. Govindan et al. [14] concluded that the most frequently used method is AHP (27.78%), followed by ANP (16.6%), DEA (11.1%), LP (8.76%), TOPSIS (5.56%), and multiobjective optimization (2.77%). In addition, many methods have been developed to select suitable low-carbon supplier based on specific methods that include fuzzy set theory [9, 12, 15, 16, 19], genetic algorithm [17–19], structural equation modeling and fuzzy logic [20], and artificial neural network [21, 22]. Hu et al. [23] proposed a multicriteria group decision-making method with 2-tuple linguistic assessments for low-carbon supplier selection under a fuzzy uncertain information environment. Qin et al. [24] developed a new TODIM technique to select low-carbon supplier within the context of interval type-2 fuzzy sets. Bakeshlou et al. [25] presented a multiobjective hybrid fuzzy linear programming model for low-carbon supplier selection problem.

However, most of these methods, which do not consider interaction between criteria, can lead to irrational decision-making of low-carbon supplier selection in the process of low-carbon building construction projects. In fact, there is always an interactive relationship between criteria of low-carbon supplier selection, such as complementarity between criteria, the redundancy of criteria, and preference relation of criteria.

The Bonferroni mean (BM) is a mean type aggregation technique, which considers interaction between attributes that makes it very useful in decision-making [26, 27]. Then, many scholars proposed BM operator [26, 27], IFBM operator [27, 28], IFGBM operator [26, 29, 30], and WIFBM operator [31, 32]. Unfortunately, there still is a lack of further theory and method research on the TFNIFN based on BM operator. Therefore, this paper focuses on a dynamic multiattribute decision-making method with interval-valued triangular fuzzy number intuitionistic fuzzy that considers interaction between attributes.

In real life, past and current information should also be considered when conducting dynamic decision-making, and how to solve the problem of time sequences weight has become the key to solving the dynamic decision-making problem. Scholars, such as Wei [33], Park et al. [34], and Yin et al. [35], have designed dynamic intuitionistic fuzzy decision models of time dimension. At present, some of the

commonly used time sequence weights are as follows: the arithmetic progression and geometric progression method [36], the binomial distribution method [37], the normal distribution method [38], the exponential distribution method [39], and the time sequence ideal solution method [40, 41]. These methods provide a reference for solving the time sequence weights in dynamic multiattribute decision-making problems, but their weights fully based on objective assignment methods or decision maker's subjective preference, and did not consider to combine objective assignment methods with decision maker's subjective preference. In our paper, we construct a comprehensive time weight while considering the objective assignment information as well as subjective preference. In addition, dynamic stochastic multiattribute decision-making problems possess a time dimension and an attribute dimension, so determining attribute weights is a prerequisite for assembling the attribute information required for the final decision-making result. Relevant scholars have developed a variety of methods for successfully determining attribute weight, Wei [42] has designed a new method based on maximizing deviation and two-tuple, Chen et al. [43] have obtained attribute weights by solving the grey relation function of attribute information per the grey correlation model, and Wang et al. [44] have proposed a method by using hesitant fuzzy entropy. Finally, we provide a new method of calculating the attribute weight by objective information entropy and TOPSIS-based Euclidean distance.

The main contribution of this paper is developing a new dynamic MADM that considers interaction between criteria under time sequence for low-carbon supplier selection in the process of low-carbon building construction projects. The new dynamic multiattribute decision-making method is proposed with the interval-valued triangular fuzzy number intuitionistic fuzzy weighted Bonferroni means (IVTFNIFWBM) operator that considers interaction between attributes under time-sequence. This method puts forward some concepts of IVTFNIFWBM operator and proves that. To calculate attribute weights, we introduce the objective information entropy and TOPSIS-based Euclidean distance and present a new weight calculation method of IVTFNIFWBM. Also, the method constructs a comprehensive time weight while considering the objective assignment information as well as subjective preference and can reflect the process of dynamic decision-making more comprehensively and reasonable. The proposed method has been successfully implemented in case construction projects to select the best low-carbon supplier. Besides, the developed method can be widely used as a structural model for low-carbon supplier selection in other industries.

The structure of this paper is organized as follows. The proposed methodological framework for low-carbon supplier evaluation and selection is presented in Section 2. Section 3 establishes the criteria for low-carbon supplier selection in the process of low-carbon building construction projects. Section 4 draws some related concepts of the proposed approach for low-carbon supplier selection. Section 5 proposes a method that considers interaction between criteria under time sequence based on IVTFNIFWBM operator and comprehensive time sequence weighted

calculation model and a new method of attribute weighted based on the objective information entropy and TOPSIS-based Euclidean distance for low-carbon supplier selection. Section 6 provides a real case study that concerns low-carbon supplier selection in the process of low-carbon building construction projects. In Section 7, we end the paper by summarizing the conclusions.

## 2. Methodological Framework for Low-Carbon Supplier Evaluation and Selection

The proposed framework for low-carbon supplier evaluation and selection of low-carbon buildings is illustrated in Figure 1, and it mainly consists of three stages. First, the low-carbon supplier selection criteria in the process of low-carbon building construction projects are identified from the comprehensive literature review, on-site investigation, and the policy analysis according to the triple bottom line principle. Various realistic features in supplier selection of low-carbon building construction projects are considered. Second, the validity of low-carbon supplier selection criteria is assessed by senior purchasing experts and project managers with rich civil industry experience, and then, we further modify the low-carbon supplier selection criteria until the validity of criteria is satisfactory according to the feedbacks of experts and project managers. Then the experts and project managers evaluate alternative low-carbon supplier. The best alternative is selected via the interval-valued triangular fuzzy multicriteria decision-making model, which is mainly made up of four procedures, including calculating attribute weight based on Entropy-TOPSIS, calculating time weight based on time degree and ideal solution, calculating information contents by IVTFIFWBM operator, and evaluating and selecting the best low-carbon supplier. These procedures of the fuzzy multicriteria decision-making model will be introduced in Section 5 in detail.

## 3. Low-Carbon Supplier Evaluation Criteria

For most projects, in the process of low-carbon building construction, the successful implementation of a project requires selecting low-carbon supplier that contributes to the project objective. Low-carbon supply chain in the construction industry is a functional network structure model, which consists of main parts of construction industry, with building units as the core and logistics, capital flow, information flow, and knowledge flow as the support in the whole life cycle of building projects. In this section, we will introduce the proposed criteria for low-carbon supplier selection based on above reviews and the identified criteria. We establish 5 main criteria and 17 subcriteria for low-carbon supplier selection in the process of low-carbon building construction projects (Table 1).

Low-carbon materials information is the basic point for low-carbon supplier selection in the process of low-carbon building construction projects. In building's construction process, projects demand different product types, such as different types of concrete, steel, and template, and product structure to guarantee the successful completion of

construction projects. Therefore, low-carbon supplier selection in the process of low-carbon building construction projects should focus on materials flexibility, efficiency, information, and other aspects of building materials. It is particularly important to provide constructors with high quality and inexpensive building materials or service, such as payment terms, to meet the needs of constructor. In addition, the low-carbon degree of building materials reflects its ability of saving resources and reducing energy consumption, and the higher the low-carbon degree is, the more application potential the building materials will have in the future. Meanwhile, it also needs to improve service quality and user experience and strengthens after sales service support. Therefore, building materials information is mainly reflected from four aspects: materials cost, low-carbon degree of materials, materials quality, and materials flexibility.

In the complex and changing market environment, the competitiveness of low-carbon supply chain in the construction industry depends on rapid response to the needs of different product types and product structure in building's construction process. High level of low-carbon business operation can contribute to reducing carbon emissions which can be reflected by the level of low-carbon information sharing, the cost control of transportation, and the supply chain management of construction industry. In addition, constructors need to consider the financial capability to reduce the risk of cooperation between constructors and its suppliers' protection for the successful completion of construction projects. Here, we use level of low-carbon information sharing, low-carbon logistics, financial capability, and emergency response capability to measure the supplier's low-carbon business operation.

In the construction industry, the main purpose of establishing low-carbon supply chain is to establish cooperative alliance of construction industry, which can reduce building materials' cost and obtain more income in projects. Cooperation potential is the premise of establishing strategic alliance, and strong cooperation intention and long-time cooperation are the foundation of establishing strategic alliance. If constructors want to maintain the long-term stability of low-carbon supply chain cooperation, they should choose those suppliers who have advanced management and desire of low-carbon cooperation for development. We can measure potential for sustainable cooperation from these four aspects: compatibility of low-carbon culture, desire of low-carbon cooperation, enterprise reputation, and low-carbon image.

Low-carbon culture can promote the implementation of enterprise strategic objectives of sustainable development virtually. If the low-carbon culture between partners cannot be integrated, it means that it will lead to different values between constructors and suppliers. Then, it may lead to dispute on both sides of the fierce confrontation and even relationship broken. Ecodesign of building materials can reduce environmental pollution in the production process and reduce carbon emissions. In addition, low-carbon certifications reflect the environmental management capability of low-carbon supplier.

Low-carbon technology capability, which is used to evaluate whether the low-carbon supplier meets the

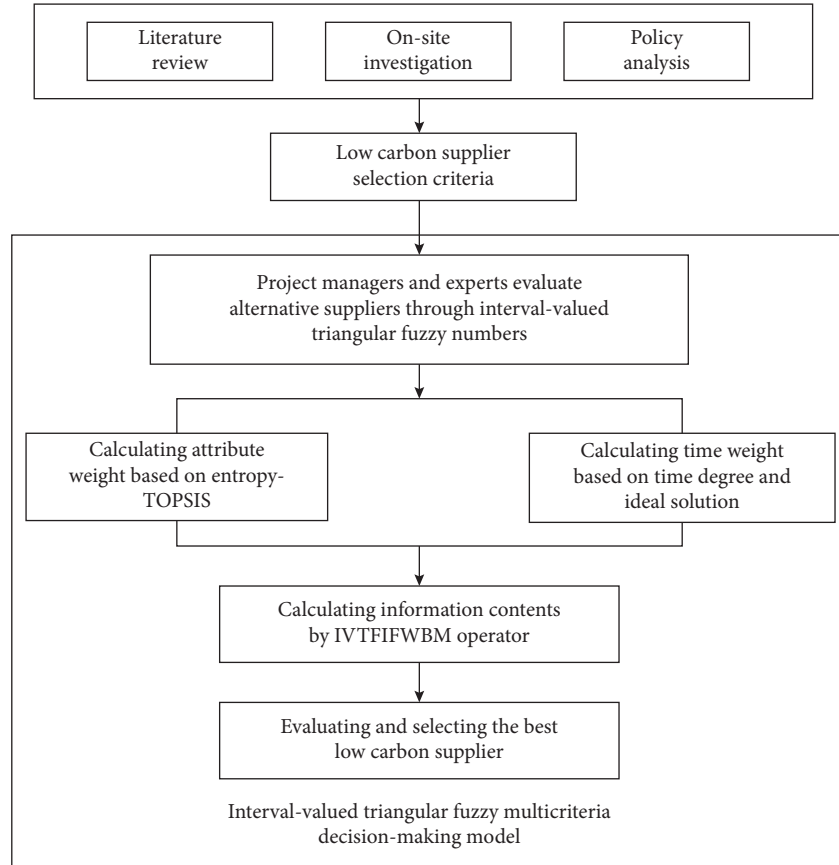


FIGURE 1: Methodological framework for low-carbon supplier evaluation and selection.

TABLE 1: Criteria for low-carbon supplier selection in the process of low-carbon building construction projects.

Criteria	Main criteria	Subcriteria
Low-carbon supplier selection in the process of low-carbon building construction projects	$C_1$ : low-carbon materials information	$C_{11}$ : materials cost $C_{12}$ : low-carbon degree of materials $C_{13}$ : materials quality $C_{14}$ : materials flexibility
	$C_2$ : low-carbon business operation	$C_{21}$ : level of low-carbon information sharing $C_{22}$ : low-carbon logistics $C_{23}$ : financial capability
	$C_3$ : potential for sustainable cooperation	$C_{24}$ : emergency response capability $C_{31}$ : desire of low-carbon cooperation $C_{32}$ : enterprise reputation $C_{33}$ : low-carbon image
	$C_4$ : low-carbon potential	$C_{41}$ : low-carbon certifications $C_{42}$ : ecodesign of materials
	$C_5$ : low-carbon technology capability	$C_{43}$ : compatibility of low-carbon culture $C_{51}$ : low-carbon production $C_{52}$ : waste materials reclamation $C_{53}$ : low-carbon R&D innovation

requirements of low-carbon building, is increasingly crucial to successfully implement low-carbon building and attain sustainability goals. Low-carbon building technologies are incorporated into building design and construction to make the end product sustainable. Low-carbon R&D innovation include new launch of building materials and low-carbon building technologies, and there are many different

low-carbon building technologies applicable in the whole process of delivering building projects.

#### 4. Preliminaries

Here, we introduce some basic concepts and terminologies of intuitionistic fuzzy set (IFS), which will be used in the proposed method. Its definition is introduced as follows:

*Definition 1.* Let  $A$  as an intuitionistic fuzzy set (IFS), and  $A = \{\langle x, u_A(x), v_A(x) \rangle | x \in X\}$  with the condition that [45]

$$\begin{aligned} u_A : X &\longrightarrow [0, 1], x \in X \longrightarrow u_A(x) \in [0, 1], \\ v_A : X &\longrightarrow [0, 1], x \in X \longrightarrow v_A(x) \in [0, 1], \\ 0 \leq u_A(x) + v_A(x) &\leq 1, x \in X. \end{aligned} \quad (1)$$

We can find that an IFS is constructed by two information functions, which not only describe the membership degree  $u_A(x)$ , but also describe the non-membership degree  $v_A(x)$ . Moreover, the hesitancy information of  $x \in X$  can be denoted by  $\pi_A(x) = 1 - u_A(x) - v_A(x)$  which is called the hesitant index, and therefore IFS can describe the uncertainty and fuzziness more objectively than the usual fuzzy set.

*Definition 2.* Zadeh first proposed the concept of triangular fuzzy number [43]. Let  $X$  as a nonempty finite set. A triangular fuzzy number intuitionistic fuzzy set (TFNIFS)  $A$  in  $X$  is defined as  $X = \{\langle x, \hat{u}_A(x), \hat{v}_A(x) \rangle | x \in X\}$ , where  $\hat{u}_A = [\hat{u}_A^l(x), \hat{u}_A^m(x), \hat{u}_A^u(x)]$  and  $\hat{v}_A = [\hat{v}_A^l(x), \hat{v}_A^m(x), \hat{v}_A^u(x)]$  denote, respectively, membership and nonmembership of the element  $x$  in  $X$  to  $A$ , and

$$0 \leq \hat{u}_A^u(x) + \hat{v}_A^u(x) \leq 1, \hat{u}_A^l(x) \geq 0, \hat{v}_A^l(x) \geq 0. \quad (2)$$

Then, we call  $([\hat{u}_A^l(x), \hat{u}_A^m(x), \hat{u}_A^u(x)], [\hat{v}_A^l(x), \hat{v}_A^m(x), \hat{v}_A^u(x)])$  as an IVTFNIFN, and it is also called as  $([a, b, c], [d, e, f])$  [46].

*Definition 3.* Let  $\tilde{\alpha}_1 = ([a_1, b_1, c_1], [d_1, e_1, f_1])$  and  $\tilde{\alpha}_2 = ([a_2, b_2, c_2], [d_2, e_2, f_2])$  are two random IVTFNIFN, then

$$\begin{aligned} \tilde{\alpha}_1 \oplus \tilde{\alpha}_2 = & ([a_1 + a_2 - a_1a_2, b_1 + b_2 - b_1b_2, c_1 + c_2 - c_1c_2], \\ & [d_1d_2, e_1e_2, f_1f_2]), \end{aligned} \quad (3)$$

$$\begin{aligned} \tilde{\alpha}_1 \otimes \tilde{\alpha}_2 = & ([a_1a_2, b_1b_2, c_1c_2], [d_1 + d_2 - d_1d_2, e_1 + e_2 - e_1e_2, \\ & f_1 + f_2 - f_1f_2]), \end{aligned} \quad (4)$$

$$\begin{aligned} \lambda \tilde{\alpha}_1 = & ([1 - (1 - a_1)^\lambda, 1 - (1 - b_1)^\lambda, 1 - (1 - c_1)^\lambda], \\ & [d_1^\lambda, e_1^\lambda, f_1^\lambda]), \end{aligned} \quad (5)$$

$$\begin{aligned} \tilde{\alpha}_1^\lambda = & ([a_1^\lambda, b_1^\lambda, c_1^\lambda], [1 - (1 - d_1)^\lambda, 1 - (1 - e_1)^\lambda, \\ & 1 - (1 - f_1)^\lambda]). \end{aligned} \quad (6)$$

*Definition 4.* For any IVTFNIFN  $\tilde{\alpha} = ([a, b, c], [d, e, f])$ , the score of  $\tilde{\alpha}$  can be evaluated by the score function  $S$  as follows [47]:

$$S(\tilde{\alpha}) = \frac{a + 2b + c}{4} - \frac{d + 2e + f}{4}, \quad (7)$$

where  $S(\tilde{\alpha}) \in [-1, 1]$ .

And, an accuracy function is shown below:

$$H(\tilde{\alpha}) = \frac{a + 2b + c}{4} \left( 2 - \frac{a + 2b + c}{4} - \frac{d + 2e + f}{4} \right). \quad (8)$$

*Definition 5.* Suppose  $\tilde{\alpha}_1$  and  $\tilde{\alpha}_2$  are two IVTFNIFN [48], where

- (1) If  $S(\tilde{\alpha}_1) < S(\tilde{\alpha}_2)$ , then  $\tilde{\alpha}_1 < \tilde{\alpha}_2$
- (2) If  $S(\tilde{\alpha}_1) = S(\tilde{\alpha}_2)$ , and when  $H(\tilde{\alpha}_1) < H(\tilde{\alpha}_2)$ , then  $\tilde{\alpha}_1 < \tilde{\alpha}_2$ ; when  $H(\tilde{\alpha}_1) = H(\tilde{\alpha}_2)$ , then  $\tilde{\alpha}_1 = \tilde{\alpha}_2$

## 5. The Proposed Approach for Low-Carbon Suppliers Selection

*5.1. Low-Carbon Suppliers Problem Description.* To the low-carbon supplier selection problem in the process of low-carbon building construction projects, for which  $S_i = \{S_1, S_2, \dots, S_m\}$  ( $m \geq 2$ ) is a discrete and feasible alternative solution set of low-carbon suppliers,  $C_j = \{C_1, C_2, \dots, C_n\}$  ( $n \geq 2$ ) is the finite set of criteria for low-carbon supplier selection in the process of low-carbon building construction projects;  $w = (w_1, w_2, \dots, w_n)^T$  is a weight vector, which satisfies  $0 \leq w_j \leq 1, \sum_{j=1}^n w_j = 1$ ; and  $\eta(t_k) = (\eta(t_1), \eta(t_2), \dots, \eta(t_\psi))^T$  is the time weight vector, where  $0 \leq \eta(t_k) \leq 1$  and  $\sum_{k=1}^\psi \eta(t_k) = 1$ . The value of criteria  $C_j$ , to which solution  $S_i$  is subject at moment  $t_k$ , is denoted as  $X_{ij}(t_k)$ , which is subject to an interval-valued triangular intuitionistic fuzzy, denoted as  $X_{ij}(t_k) \sim \eta_{ij}(t_k) = ([a_{ij}(t_k), b_{ij}(t_k), c_{ij}(t_k)], [d_{ij}(t_k), e_{ij}(t_k), f_{ij}(t_k)])$ , forming a matrix  $D_{X_{ij}(t_k)} = ([a_{ij}(t_k), b_{ij}(t_k), c_{ij}(t_k)], [d_{ij}(t_k), e_{ij}(t_k), f_{ij}(t_k)])_{m \times n}$  based on  $\psi$  moment of criteria for low-carbon supplier selection in the process of low-carbon building construction projects. Low-carbon supplier selection problems consist of multiple dimensions, such as supplier, criteria, and time. Integration operator and determining time sequence weight are important technologies to reduce dimensionality and solve low-carbon supplier selection problem under interval-valued intuitionistic fuzzy environment.

### 5.2. Interval-Valued Triangular Fuzzy Number Intuitionistic Fuzzy Bonferroni Means Operator

*Definition 6.* Let  $p, q \geq 0$ , and  $a_i$  ( $i = 1, 2, \dots, n$ ) be a collection of nonnegative numbers [48]. If

$$B^{p,q}(a_1, a_2, \dots, a_n) = \left( \frac{1}{n(n-1)} \sum_{\substack{i,j=1 \\ i \neq j}}^n a_i^p a_j^q \right)^{1/p+q}, \quad (9)$$

then,  $B^{p,q}$  is called the Bonferroni mean (BM).

*Definition 7.* Let  $\tilde{\alpha}_i = ([a_i, b_i, c_i], [d_i, e_i, f_i])$  as a collection of IVTFNIFNs. For any  $p, q > 0$ , if

$$IVTFNIFBM^{p,q}(\tilde{\alpha}_1, \tilde{\alpha}_2, \dots, \tilde{\alpha}_n) = \left( \frac{1}{n(n-1)} \left( \bigoplus_{\substack{i,j=1 \\ i \neq j}}^n (\tilde{\alpha}_i^p \otimes \tilde{\alpha}_j^q) \right) \right)^{1/p+q} \quad (10)$$

**Theorem 1.** Let  $p, q > 0$ , and  $\tilde{\alpha}_i = ([a_i, b_i, c_i], [d_i, e_i, f_i])$  as a collection of positive IVTFNIFN. Then, by using the IVTFNIFBM, is also an IVTFNIFN, and

$$IVTFNIFBM^{p,q}(\tilde{\alpha}_1, \tilde{\alpha}_2, \dots, \tilde{\alpha}_n) = ([a, b, c], [d, e, f]),$$

$$a = \left( 1 - \prod_{\substack{i,j=1 \\ i \neq j}}^n (1 - a_i^p a_j^q)^{1/n(n-1)} \right)^{1/p+q},$$

$$b = \left( 1 - \prod_{\substack{i,j=1 \\ i \neq j}}^n (1 - b_i^p b_j^q)^{1/n(n-1)} \right)^{1/p+q},$$

$$c = \left( 1 - \prod_{\substack{i,j=1 \\ i \neq j}}^n (1 - c_i^p c_j^q)^{1/n(n-1)} \right)^{1/p+q},$$

$$d = 1 - \left( 1 - \prod_{\substack{i,j=1 \\ i \neq j}}^n (1 - (1 - d_i)^p (1 - d_j)^q)^{1/n(n-1)} \right)^{1/p+q},$$

$$e = 1 - \left( 1 - \prod_{\substack{i,j=1 \\ i \neq j}}^n (1 - (1 - e_i)^p (1 - e_j)^q)^{1/n(n-1)} \right)^{1/p+q},$$

$$f = 1 - \left( 1 - \prod_{\substack{i,j=1 \\ i \neq j}}^n (1 - (1 - f_i)^p (1 - f_j)^q)^{1/n(n-1)} \right)^{1/p+q}. \quad (11)$$

*Proof.* By operations (4) and (6), we have

$$\alpha_i^p = ([a_i^p, b_i^p, c_i^p], [1 - (1 - d_i)^p, 1 - (1 - e_i)^p, 1 - (1 - f_i)^p]),$$

$$\alpha_j^q = ([a_j^q, b_j^q, c_j^q], [1 - (1 - d_j)^q, 1 - (1 - e_j)^q, 1 - (1 - f_j)^q]), \quad (12)$$

$$\alpha_i^p \otimes \alpha_j^q = \left( [a_i^p a_j^q, b_i^p b_j^q, c_i^p c_j^q], [1 - (1 - d_i)^p (1 - d_j)^q, 1 - (1 - e_i)^p (1 - e_j)^q, 1 - (1 - f_i)^p (1 - f_j)^q] \right). \quad (13)$$

and then

As following, we first prove that

$$\bigoplus_{\substack{i,j=1 \\ i \neq j}}^n (\alpha_i^p \otimes \alpha_j^q) = \left( \left[ \left( 1 - \prod_{\substack{i,j=1 \\ i \neq j}}^n (1 - a_i^p a_j^q) \right), \left( 1 - \prod_{\substack{i,j=1 \\ i \neq j}}^n (1 - b_i^p b_j^q) \right), \left( 1 - \prod_{\substack{i,j=1 \\ i \neq j}}^n (1 - c_i^p c_j^q) \right) \right], \left[ \prod_{\substack{i,j=1 \\ i \neq j}}^n (1 - (1 - d_i)^p (1 - d_j)^q), \prod_{\substack{i,j=1 \\ i \neq j}}^n (1 - (1 - e_i)^p (1 - e_j)^q), \prod_{\substack{i,j=1 \\ i \neq j}}^n (1 - (1 - f_i)^p (1 - f_j)^q) \right] \right), \quad (14)$$

by using mathematical induction on  $n$  as follows:

(1) For  $n = 2$ , we have

$$\begin{aligned} \bigoplus_{\substack{i,j=1 \\ i \neq j}}^2 (\tilde{\alpha}_i^p \otimes \tilde{\alpha}_j^q) &= (\tilde{\alpha}_1^p \otimes \tilde{\alpha}_2^q) \oplus (\tilde{\alpha}_2^p \otimes \tilde{\alpha}_1^q) \\ &= \left( \left[ 1 - (1 - a_1^p a_2^q)(1 - a_2^p a_1^q), 1 - (1 - b_1^p b_2^q)(1 - b_2^p b_1^q), 1 - (1 - c_1^p c_2^q)(1 - c_2^p c_1^q) \right], \right. \\ &\quad \left[ (1 - (1 - d_1)^p (1 - d_2)^q)(1 - (1 - d_2)^p (1 - d_1)^q), (1 - (1 - e_1)^p (1 - e_2)^q)(1 - (1 - e_2)^p (1 - e_1)^q), \right. \\ &\quad \left. \left. (1 - (1 - f_1)^p (1 - f_2)^q)(1 - (1 - f_2)^p (1 - f_1)^q) \right] \right). \end{aligned} \quad (15)$$

(2) If (14) holds for  $n = k$ , *i.e.*, then, when  $n = k + 1$ , we have

$$\bigoplus_{\substack{i,j=1 \\ i \neq j}}^{k+1} (\tilde{\alpha}_i^p \otimes \tilde{\alpha}_j^q) = \left( \bigoplus_{\substack{i,j=1 \\ i \neq j}}^k (\tilde{\alpha}_i^p \otimes \tilde{\alpha}_j^q) \right) \oplus \left( \bigoplus_{i=1}^k (\tilde{\alpha}_i^p \otimes \tilde{\alpha}_{k+1}^q) \right) \oplus \left( \bigoplus_{j=1}^k (\tilde{\alpha}_{k+1}^p \otimes \tilde{\alpha}_j^q) \right). \quad (16)$$

Now, we prove that

$$\begin{aligned} \bigoplus_{i=1}^k (\tilde{\alpha}_i^p \otimes \tilde{\alpha}_{k+1}^q) &= \left( \left[ 1 - \prod_{i=1}^k (1 - a_i^p a_{k+1}^q), 1 - \prod_{i=1}^k (1 - b_i^p b_{k+1}^q), 1 - \prod_{i=1}^k (1 - c_i^p c_{k+1}^q) \right], \right. \\ &\quad \left. \left[ \prod_{i=1}^k (1 - (1 - d_i)^p (1 - d_{k+1})^q), \prod_{i=1}^k (1 - (1 - e_i)^p (1 - e_{k+1})^q), \prod_{i=1}^k (1 - (1 - f_i)^p (1 - f_{k+1})^q) \right] \right), \end{aligned} \quad (17)$$

by using mathematical induction on  $k$  as follows.

(1) For  $k = 2$ , then by (17), we have

$$\tilde{\alpha}_i^p \otimes \tilde{\alpha}_{2+1}^q = \left[ [a_i^p a_{2+1}^q, b_i^p b_{2+1}^q, c_i^p c_{2+1}^q], [1 - (1 - d_i)^p (1 - d_{2+1})^q, 1 - (1 - e_i)^p (1 - e_{2+1})^q, 1 - (1 - f_i)^p (1 - f_{2+1})^q] \right] \quad i = 1, 2, \quad (18)$$

and thus

$$\begin{aligned} \bigoplus_{i=1}^2 (\tilde{\alpha}_i^p \otimes \tilde{\alpha}_{2+1}^q) &= (\tilde{\alpha}_1^p \otimes \tilde{\alpha}_{2+1}^q) \oplus (\tilde{\alpha}_2^p \otimes \tilde{\alpha}_{2+1}^q) \\ &= \left( \left[ 1 - (1 - a_1^p a_{2+1}^q)(1 - a_2^p a_{2+1}^q), 1 - (1 - b_1^p b_{2+1}^q)(1 - b_2^p b_{2+1}^q), 1 - (1 - c_1^p c_{2+1}^q)(1 - c_2^p c_{2+1}^q) \right], \right. \\ &\quad \left[ (1 - (1 - d_1)^p (1 - d_{2+1})^q)(1 - (1 - d_2)^p (1 - d_{2+1})^q), (1 - (1 - e_1)^p (1 - e_{2+1})^q)(1 - (1 - e_2)^p (1 - e_{2+1})^q), \right. \\ &\quad \left. \left. (1 - (1 - f_1)^p (1 - f_{2+1})^q)(1 - (1 - f_2)^p (1 - f_{2+1})^q) \right] \right). \end{aligned} \quad (19)$$

(2) If (17) holds for  $k = k_0$ , *i.e.*, then, when  $k = k_0 + 1$ , we have

$$\begin{aligned}
\bigoplus_{i=1}^{k_0+1} (\tilde{\alpha}_i^p \otimes \tilde{\alpha}_{k_0+2}^q) &= \bigoplus_{i=1}^{k_0} (\tilde{\alpha}_i^p \otimes \tilde{\alpha}_{k_0+1}^q) \oplus (\tilde{\alpha}_{k_0+1}^p \otimes \tilde{\alpha}_{k_0+2}^q) \\
&= \left[ \left( 1 - \left( \prod_{i=1}^{k_0} (1 - a_i^p a_{k_0+1}^q) \right) (1 - a_{k_0+1}^p a_{k_0+2}^q), 1 - \left( \prod_{i=1}^{k_0} (1 - b_i^p b_{k_0+1}^q) \right) (1 - b_{k_0+1}^p b_{k_0+2}^q), 1 - \left( \prod_{i=1}^{k_0} (1 - c_i^p c_{k_0+1}^q) \right) (1 - c_{k_0+1}^p c_{k_0+2}^q) \right) \right], \\
&\quad \left[ \prod_{i=1}^{k_0} (1 - (1 - d_i)^p (1 - d_{k_0+1})^q) (1 - (1 - d_{k_0+1})^p (1 - d_{k_0+2})^q), \right. \\
&\quad \left. \prod_{i=1}^{k_0} (1 - (1 - e_i)^p (1 - e_{k_0+1})^q) (1 - (1 - e_{k_0+1})^p (1 - e_{k_0+2})^q), \right. \\
&\quad \left. \prod_{i=1}^{k_0} (1 - (1 - f_i)^p (1 - f_{k_0+1})^q) (1 - (1 - f_{k_0+1})^p (1 - f_{k_0+2})^q) \right] \\
&= \left[ \left( 1 - \prod_{i=1}^{k_0+1} (1 - a_i^p a_{k+1}^q), 1 - \prod_{i=1}^{k_0+1} (1 - b_i^p b_{k+1}^q), 1 - \prod_{i=1}^{k_0+1} (1 - c_i^p c_{k+1}^q) \right) \right], \\
&\quad \left[ \prod_{i=1}^{k_0+1} (1 - (1 - d_i)^p (1 - d_{k+1})^q), \prod_{i=1}^{k_0+1} (1 - (1 - e_i)^p (1 - e_{k+1})^q), \prod_{i=1}^{k_0+1} (1 - (1 - f_i)^p (1 - f_{k+1})^q) \right] \Big],
\end{aligned} \tag{20}$$

i.e., (17) holds for  $k = k_0 + 1$ ; thus, (17) holds for all  $k$ .

Similarly, we can Prove that

$$\begin{aligned}
\bigoplus_{j=1}^k (\tilde{\alpha}_{k+1}^p \otimes \tilde{\alpha}_j^q) &= \left( \left[ 1 - \prod_{j=1}^k (1 - a_{k+1}^p a_j^q), 1 - \prod_{j=1}^k (1 - b_{k+1}^p b_j^q), 1 - \prod_{j=1}^k (1 - c_{k+1}^p c_j^q) \right] \right. \\
&\quad \left. \left[ \prod_{j=1}^k (1 - (1 - d_{k+1})^p (1 - d_j)^q), \prod_{j=1}^k (1 - (1 - e_{k+1})^p (1 - e_j)^q), \prod_{j=1}^k (1 - (1 - f_{k+1})^p (1 - f_j)^q) \right] \right).
\end{aligned} \tag{21}$$

Thus, by (16), (17), and (21), we further transform (16) as

$$\begin{aligned}
\bigoplus_{\substack{i,j=1 \\ i \neq j}}^{k+1} (\tilde{\alpha}_i^p \otimes \tilde{\alpha}_j^q) &= \left( \bigoplus_{\substack{i,j=1 \\ i \neq j}}^k (\tilde{\alpha}_i^p \otimes \tilde{\alpha}_j^q) \right) \oplus \left( \bigoplus_{i=1}^k (\tilde{\alpha}_i^p \otimes \tilde{\alpha}_{k+1}^q) \right) \oplus \left( \bigoplus_{j=1}^k (\tilde{\alpha}_{k+1}^p \otimes \tilde{\alpha}_j^q) \right) \\
&= \left( \left[ 1 - \prod_{\substack{i,j=1 \\ i \neq j}}^k (1 - a_i^p a_j^q), 1 - \prod_{\substack{i,j=1 \\ i \neq j}}^k (1 - b_i^p b_j^q), 1 - \prod_{\substack{i,j=1 \\ i \neq j}}^k (1 - c_i^p c_j^q) \right] \right. \\
&\quad \left[ \prod_{\substack{i,j=1 \\ i \neq j}}^k (1 - (1 - d_i)^p (1 - d_j)^q), \prod_{\substack{i,j=1 \\ i \neq j}}^k (1 - (1 - e_i)^p (1 - e_j)^q), \prod_{\substack{i,j=1 \\ i \neq j}}^k (1 - (1 - f_i)^p (1 - f_j)^q) \right] \Big) \\
&\quad \oplus \left( \left[ 1 - \left( \prod_{i=1}^{k_0+1} (1 - a_i^p a_{k+1}^q) \right), 1 - \left( \prod_{i=1}^{k_0+1} (1 - b_i^p b_{k+1}^q) \right), 1 - \left( \prod_{i=1}^{k_0+1} (1 - c_i^p c_{k+1}^q) \right) \right] \right. \\
&\quad \left[ \prod_{i=1}^{k_0+1} (1 - (1 - d_i)^p (1 - d_{k+1})^q), \prod_{i=1}^{k_0+1} (1 - (1 - e_i)^p (1 - e_{k+1})^q), \right. \\
&\quad \left. \prod_{i=1}^{k_0+1} (1 - (1 - f_i)^p (1 - f_{k+1})^q) \right] \Big) \oplus \left( \left[ 1 - \prod_{j=1}^k (1 - a_{k+1}^p a_j^q), 1 - \prod_{j=1}^k (1 - b_{k+1}^p b_j^q), 1 - \prod_{j=1}^k (1 - c_{k+1}^p c_j^q) \right] \right. \\
&\quad \left[ \prod_{j=1}^k (1 - (1 - d_{k+1})^p (1 - d_j)^q), \prod_{j=1}^k (1 - (1 - e_{k+1})^p (1 - e_j)^q), \prod_{j=1}^k (1 - (1 - f_{k+1})^p (1 - f_j)^q) \right] \Big) \\
&= \left( \left[ 1 - \left( \prod_{\substack{i,j=1 \\ i \neq j}}^{k+1} (1 - a_i^p a_j^q) \right), 1 - \left( \prod_{\substack{i,j=1 \\ i \neq j}}^{k+1} (1 - b_i^p b_j^q) \right), 1 - \left( \prod_{\substack{i,j=1 \\ i \neq j}}^{k+1} (1 - c_i^p c_j^q) \right) \right] \right. \\
&\quad \left[ \prod_{\substack{i,j=1 \\ i \neq j}}^{k+1} (1 - (1 - d_i)^p (1 - d_j)^q), \prod_{\substack{i,j=1 \\ i \neq j}}^{k+1} (1 - (1 - e_i)^p (1 - e_j)^q), \prod_{\substack{i,j=1 \\ i \neq j}}^{k+1} (1 - (1 - f_i)^p (1 - f_j)^q) \right] \Big),
\end{aligned} \tag{22}$$

i.e., (14) holds for  $n = k + 1$ . Thus, (14) holds for all  $n$ .

Then, by operations (5) and (6), we get

$$\frac{1}{n(n-1)} \left( \bigoplus_{\substack{i,j=1 \\ i \neq j}}^n (\alpha_i^p \otimes \alpha_j^q) \right)^{1/p+q} = ([a, b, c], [d, e, f]),$$

$$a = \left( 1 - \prod_{\substack{i,j=1 \\ i \neq j}}^n (1 - a_i^p a_j^q)^{1/n(n-1)} \right)^{1/p+q},$$

$$b = \left( 1 - \prod_{\substack{i,j=1 \\ i \neq j}}^n (1 - b_i^p b_j^q)^{1/n(n-1)} \right)^{1/p+q},$$

$$c = \left( 1 - \prod_{\substack{i,j=1 \\ i \neq j}}^n (1 - c_i^p c_j^q)^{1/n(n-1)} \right)^{1/p+q},$$

$$d = 1 - \left( 1 - \prod_{\substack{i,j=1 \\ i \neq j}}^n (1 - (1 - d_i)^p (1 - d_j)^q)^{1/n(n-1)} \right)^{1/p+q},$$

$$e = 1 - \left( 1 - \prod_{\substack{i,j=1 \\ i \neq j}}^n (1 - (1 - e_i)^p (1 - e_j)^q)^{1/n(n-1)} \right)^{1/p+q},$$

$$f = 1 - \left( 1 - \prod_{\substack{i,j=1 \\ i \neq j}}^n (1 - (1 - f_i)^p (1 - f_j)^q)^{1/n(n-1)} \right)^{1/p+q},$$
(23)

which completes the proof of Theorem 1.

Based on the studies above, we can look at some properties of IVTFNIFBM as below:

- (1) Idempotency: if  $\tilde{\alpha}_i = ([a_i, b_i, c_i], [d_i, e_i, f_i]) = \tilde{\alpha} = ([a, b, c], [d, e, f])$ , for all  $i$ , then

$$\text{IVTFNIFN}^{p,q}(\tilde{\alpha}_1, \tilde{\alpha}_2, \dots, \tilde{\alpha}_n) = \text{IVTFNIFN}^{p,q}(\tilde{\alpha}, \tilde{\alpha}, \dots, \tilde{\alpha}) = \tilde{\alpha}. \tag{24}$$

- (2) Commutativity: let  $(\tilde{\alpha}_1, \tilde{\alpha}_2, \dots, \tilde{\alpha}_n)$  as a positive collection of IVTFNIFN, then

$$\text{IVTFNIFN}^{p,q}(\tilde{\alpha}_1, \tilde{\alpha}_2, \dots, \tilde{\alpha}_n) = \text{IVTFNIFN}^{p,q}(\tilde{\alpha}_1, \tilde{\alpha}_2, \dots, \tilde{\alpha}_n), \tag{25}$$

where  $(\tilde{\alpha}_1, \tilde{\alpha}_2, \dots, \tilde{\alpha}_n)$  is any permutation of  $(\tilde{\alpha}_1, \tilde{\alpha}_2, \dots, \tilde{\alpha}_n)$ .

- (3) Monotonicity: let  $\tilde{\alpha}_i = ([a_i, b_i, c_i], [d_i, e_i, f_i]) (i = 1, 2, \dots, n)$  and  $\tilde{\alpha}_i^\Delta = ([\hat{a}_i, \hat{b}_i, \hat{c}_i], [\hat{d}_i, \hat{e}_i, \hat{f}_i])$  are two positive collections of IVTFNIFN; if,  $a_i \geq \hat{a}_i, b_i \geq \hat{b}_i, c_i \geq \hat{c}_i, d_i \leq \hat{d}_i, e_i \leq \hat{e}_i, f_i \leq \hat{f}_i$ , for all  $i$ , then

$$\text{IVTFNIFN}^{p,q}(\tilde{\alpha}_1, \tilde{\alpha}_2, \dots, \tilde{\alpha}_n) \geq \text{IVTFNIFN}^{p,q}(\tilde{\alpha}_1^\Delta, \tilde{\alpha}_2^\Delta, \dots, \tilde{\alpha}_n^\Delta). \tag{26}$$

- (4) Boundedness: let  $\tilde{\alpha}_i = ([a_i, b_i, c_i], [d_i, e_i, f_i]) (i = 1, 2, \dots, n)$  as a positive collection of IVTFNIFN, then

$$\tilde{\alpha}^- \leq \text{IVTFNIFBM}^{p,q}(\tilde{\alpha}_1, \tilde{\alpha}_2, \dots, \tilde{\alpha}_n) \leq \tilde{\alpha}^+,$$

$$\tilde{\alpha}^- = \left( \left[ \min_i a_i, \min_i b_i, \min_i c_i \right], \left[ \min_i d_i, \min_i e_i, \min_i f_i \right] \right),$$

$$\tilde{\alpha}^+ = \left( \left[ \max_i a_i, \max_i b_i, \max_i c_i \right], \left[ \max_i d_i, \max_i e_i, \max_i f_i \right] \right). \tag{27}$$

The TFNIFWBM considers the interaction between criteria for low-carbon supplier selection in the process of low-carbon building construction projects, but they have different levels of importance in low-carbon supplier selection. Therefore, we first propose IVTFNIFBM operator.

In the aforementioned analysis, we consider the attribute interrelationships, which are important. However, in many practical situations, we should take into account the weights of the data. So, we first define an IVTFNIFBM operator.

*Definition 8.* Let  $\tilde{\alpha}_i = ([a_i, b_i, c_i], [d_i, e_i, f_i])$  as a positive collection of IVTFNIFN.  $w = (w_1, w_2, \dots, w_n)^T$  is the weight vector of  $\tilde{\alpha}_i (i = 1, 2, \dots, n)$ , where  $w_i \geq 0$  and  $\sum_{i=1}^n w_i = 1$ . If

$$\text{IVTFNIFBM}_w^{p,q}(\tilde{\alpha}_1, \tilde{\alpha}_2, \dots, \tilde{\alpha}_n) = \left( \frac{1}{n(n-1)} \left( \bigoplus_{\substack{i,j=1 \\ i \neq j}}^n ((w_i \tilde{\alpha}_i^p) \otimes (w_j \tilde{\alpha}_j^q)) \right) \right)^{1/p+q}. \quad (28)$$

Then  $\text{IVTFNIFBM}_w^{p,q}$  is called the interval-valued triangular fuzzy number intuitionistic fuzzy weighted Bonferroni mean (IVTFNIFWBM).

Similar to Theorem 1, we have Theorem 2.

**Theorem 2.** Let  $\tilde{\alpha}_i = ([a_i, b_i, c_i], [d_i, e_i, f_i]) (i = 1, 2, \dots, n)$  be a positive collection of IVTFNIFN.  $w = (w_1, w_2, \dots, w_n)^T$  is the weight vector of  $\tilde{\alpha}_i (i = 1, 2, \dots, n)$ , where  $w_i \geq 0$  and  $\sum_{i=1}^n w_i = 1$ . Then, the aggregated value, by using the IVTFNIFWBM, is also an IVTFNIFN, and

$$\text{IVTFNIFWBM}^{p,q}(\tilde{\alpha}_1, \tilde{\alpha}_2, \dots, \tilde{\alpha}_n) = ([\hat{a}, \hat{b}, \hat{c}], [\hat{d}, \hat{e}, \hat{f}]). \quad (29)$$

Then

$$\begin{aligned} \hat{a} &= \left( 1 - \prod_{\substack{i,j=1 \\ i \neq j}}^n (1 - (w_i a_i)^p (w_j a_j)^q)^{1/n(n-1)} \right)^{1/p+q}, \\ \hat{b} &= \left( 1 - \prod_{\substack{i,j=1 \\ i \neq j}}^n (1 - (w_i b_i)^p (w_j b_j)^q)^{1/n(n-1)} \right)^{1/p+q}, \\ \hat{c} &= \left( 1 - \prod_{\substack{i,j=1 \\ i \neq j}}^n (1 - (w_i c_i)^p (w_j c_j)^q)^{1/n(n-1)} \right)^{1/p+q}, \\ \hat{d} &= 1 - \left( 1 - \prod_{\substack{i,j=1 \\ i \neq j}}^n (1 - (1 - w_i d_i)^p (1 - w_j d_j)^q)^{1/n(n-1)} \right)^{1/p+q}, \\ \hat{e} &= 1 - \left( 1 - \prod_{\substack{i,j=1 \\ i \neq j}}^n (1 - (1 - w_i e_i)^p (1 - w_j e_j)^q)^{1/n(n-1)} \right)^{1/p+q}, \\ \hat{f} &= 1 - \left( 1 - \prod_{\substack{i,j=1 \\ i \neq j}}^n (1 - (1 - w_i f_i)^p (1 - w_j f_j)^q)^{1/n(n-1)} \right)^{1/p+q}. \end{aligned} \quad (30)$$

Theorem 2 can be proved by mathematical induction; in a similar way, we can prove that IVTFNIFWBM operator also has idempotency, commutativity, monotonicity, and boundedness features, and the detailed proof procedures are omitted here.

### 5.3. Time Weight Based on Time Degree and Ideal Solution

*Definition 9.* Supposing  $\eta(t_k) = (\eta(t_1), \eta(t_2), \dots, \eta(t_k))^T$  represents time sequence weight vector, where  $\eta(t_k)$  represents the weight of  $k$ th time period, and  $\eta(t_k) \in [0, 1]$ ,  $\sum_{k=1}^{\psi} \eta(t_k) = 1$ , time sequence weight indicates the attention-attaching degree on different time periods in decision-making process.

Information entropy can reflect the uptake degree of time weight vector against information quantity; the greater the entropy is, the less the information quantity it contains. Therefore, based on maximum entropy principle, we solve the time weight of time degree and information entropy and set up a nonlinear programming model as follows:

$$\begin{cases} \max & I = - \sum_{k=1}^{\psi} \eta(t_k) \ln \eta(t_k), \\ \text{s.t.} & \lambda = \sum_{k=1}^{\psi} \frac{\psi - k}{\psi - 1} \eta(t_k), \sum_{k=1}^{\psi} \eta(t_k) = 1, \eta(t_k) \in [0, 1]. \end{cases} \quad (31)$$

When  $\lambda$  gets closer to 0, indicating decision-maker attaches more preference to recent information of time series; when  $\lambda$  gets closer to 1, indicating decision-maker attaches more preference to forward information of time series. We solve this model by Lingo.11 software and acquire the time sequence weight vector.

*Definition 10.* Based on the Definition 8, when we consider the equilibrium of time preference of decision makers in different time periods, we can determine time weight based on an objective function of maximization closeness degree to ideal solution with subjective time preference. We denote  $\eta(t_k)^+$  as positive ideal time weight, and negative ideal time weight is denoted by  $\eta(t_k)^-$ .

Let the distance between the two time weight vectors  $\eta(\hat{t}_k) = (\eta(\hat{t}_1), \eta(\hat{t}_2), \dots, \eta(\hat{t}_{\psi}))^T$  and  $\eta(\tilde{t}_k) = (\eta(\tilde{t}_1), \eta(\tilde{t}_2), \dots, \eta(\tilde{t}_{\psi}))^T$  be

$$d(\eta(\tilde{t}_k), \eta(\hat{t}_k)) = \sqrt{\sum_{k=1}^{\psi} (\eta(\tilde{t}_k) - \eta(\hat{t}_k))^2}. \quad (32)$$

Then the distances between a time weight vector  $\eta(t_k) = (\eta(t_1), \eta(t_2), \dots, \eta(t_k))^T$  and positive and negative ideal time weight vectors respectively are

$$d(\eta(t_k), \eta(t_k)^+) = \sqrt{\sum_{k=1}^{\psi-1} \eta(t_k)^2 + (1 - \eta(t_\psi))^2},$$

$$d(\eta(t_k), \eta(t_k)^-) = \sqrt{(1 - \eta(t_1))^2 + \sum_{k=2}^{\psi} \eta(t_k)^2}. \tag{33}$$

The relative closeness degree between time weight vector  $\eta(t_k)$  and ideal time weight vector  $\eta(t_k)^+$  can be obtained:

$$c(\eta(t_k), \eta(t_k)^+) = \frac{d(\eta(t_k), \eta(t_k)^-)}{d(\eta(t_k), \eta(t_k)^+) + d(\eta(t_k), \eta(t_k)^-)}. \tag{34}$$

Then, based on time degree and ideal solution, constructing a nonlinear programming model is as follows:

$$\begin{cases} \max & c(\eta(t_k), \eta(t_k)^+) = \frac{\sqrt{(1 - \eta(t_1))^2 + \sum_{k=2}^{\psi} \eta(t_k)^2}}{\sqrt{(1 - \eta(t_1))^2 + \sum_{k=2}^{\psi} \eta(t_k)^2} + \sqrt{\sum_{k=1}^{\psi-1} \eta(t_k)^2 + (1 - \eta(t_\psi))^2}}, \\ \text{s.t.} & \lambda = \sum_{k=1}^{\psi} \frac{\psi - k}{\psi - 1} \eta(t_k), \sum_{k=1}^{\psi} \eta(t_k) = 1, \eta(t_k) \in [0, 1], \quad k = 1, 2, \dots, \psi. \end{cases} \tag{35}$$

Based on the thought of “stress the present rather than the past”, the more recent information can fully reflect the characteristics of decision-making attributes, and it would be more effective for decision-making evaluation results. We solve this model by Lingo.11 software and acquire the time sequence weight vector.

Based on (31) and (35), this paper constructs a comprehensive time weight while considering the uptake ability of time weight against information as well as the effectiveness of recent decision-making information, as follows:

$$\begin{cases} \max & R = l \frac{\sqrt{(1 - \eta(t_1))^2 + \sum_{k=2}^{\psi} \eta(t_k)^2}}{\sqrt{(1 - \eta(t_1))^2 + \sum_{k=2}^{\psi} \eta(t_k)^2} + \sqrt{\sum_{k=1}^{\psi-1} \eta(t_k)^2 + (1 - \eta(t_\psi))^2}} + (1 - l) \left( - \sum_{k=1}^{\psi} \eta(t_k) \ln \eta(t_k) \right), \\ \text{s.t.} & \lambda = \sum_{k=1}^{\psi} \frac{\psi - k}{\psi - 1} \eta(t_k), \sum_{k=1}^{\psi} \eta(t_k) = 1, \eta(t_k) \in [0, 1], \quad k = 1, 2, \dots, \psi, \end{cases} \tag{36}$$

where  $l$  is an adjustable coefficient,  $l \in [0, 1]$ , if  $l$  is close to 0, it is the sign that decision makers are more inclined to the time weight based on objective information-driven, and when the  $l$  is close to 1, the decision makers are more emphasized on time weight based on subjective preference information. We also solve this model by Lingo.11 software and acquire the time sequence weight vector.

#### 5.4. The Weight of Attribute Based on Entropy-TOPSIS

*Definition 11.* Let  $\tilde{\alpha} = (a_i, b_i, c_i)$  and  $\tilde{\beta} = (\hat{a}_i, \hat{b}_i, \hat{c}_i)$  are two collections of IVTFNIFNs, then the distances between  $\tilde{\alpha}$  and  $\tilde{\beta}$  is

$$D(\tilde{\alpha}, \tilde{\beta}) = \sqrt{\frac{1}{3} \left[ (a_i - \hat{a}_i)^2 + (b_i - \hat{b}_i)^2 + (c_i - \hat{c}_i)^2 \right]}. \tag{37}$$

Based on the decision-making situations of uncertainty, multicriteria, and finite case, we let  $\tilde{A} = (A_1, A_2, \dots, A_n)$  as  $n$  alternatives,  $\tilde{C} = (C_1, C_2, \dots, C_n)$  as a collection of attributes.  $w = (w_1, w_2, \dots, w_n)^T$  is the weight vector of  $\tilde{C}$ , where  $w_i \geq 0$  and  $\sum_{i=1}^n w_i = 1$ .

If the performance of the alternative  $A_i$  with respect to the attributes  $C_j$  is measured by an IVTFNIFNs, all IVTFNIFNs are contained in an intuitionistic fuzzy decision  $D = (\tilde{d}_{ij})_{n \times m}$ .

*Definition 12.* If  $d_j^* = (\tilde{d}_j, \hat{d}_j, \bar{d}_j)$  is an ideal performance values of attributes, there are, generally, benefit criteria and cost criteria.

When the performance values of the benefit type, then  $\tilde{d}_j = \max \tilde{d}_{ij}$ ,  $\hat{d}_j = \max \hat{d}_{ij}$ ,  $\bar{d}_j = \max \bar{d}_{ij}$ .

When the performance values of the cost type, then  $\tilde{d}_j = \min \tilde{d}_{ij}$ ,  $\hat{d}_j = \min \hat{d}_{ij}$ ,  $\bar{d}_j = \min \bar{d}_{ij}$ .

In general, the alternatives have a small difference in the performance value of attributes, namely, the attributes have a small influence on a multiple attribute decision-making problem. Conversely, the more the difference, the more the effect. Therefore, the larger the performance value of attributes deviation, the larger the attributes weight. We can learn from the entropy that the lower the entropy is, the more the information quantity it contains.

Due to the limit of entropy, we need to acquire standardized decision-making matrix by (37) and get a distance between the attributes and the ideal attributes.

Steps of the weight of attribute are provided as follows:

First, constructing the ideal performance values of attributes by Definition 11 based on the IVTFNIFN. Next, calculating the distance from each attributes and ideal attributes via Formula (37). Then, we can construct a distance matrix  $R_1 = (\tilde{r}_{ij})_{n \times m}$ ,  $R_2 = (\hat{r}_{ij})_{n \times m}$  where we use  $r_{ij}^* = r_{ij} / \sum_{i=1}^m r_{ij}$ , then conduct standardization on IVTFNIFN distance matrix  $R_1^* = (\tilde{r}_{ij}^*)_{n \times m}$  and  $R_2^* = (\hat{r}_{ij}^*)_{n \times m}$ . Finally, calculating the weight of attributes  $\bar{C} = (C_1, C_2, \dots, C_n)$ .

$$e_j = - \sum_{i=1}^n (r_{ij}^* \times \ln r_{ij}^*) / \ln n,$$

$$w_j^1 = \frac{1 - e_j^1}{\sum_{j=1}^m (1 - e_j^1)} \quad (j = 1, 2, \dots, m),$$

$$w_j^2 = \frac{1 - e_j^2}{\sum_{j=1}^m (1 - e_j^2)} \quad (j = 1, 2, \dots, m),$$

$$w_j = \sqrt{w_j^1 w_j^2} \quad (j = 1, 2, \dots, m).$$

We can know the final comprehensive weight,  $w_j$  ( $j = 1, 2, 3, \dots, m$ ).

**5.5. Steps of Low-Carbon Supplier Selection in the Process of Low-Carbon Building Construction Projects.** According to the calculation process of the above model for low-carbon supplier selection in the process of low-carbon building construction projects, the calculation steps are as follows.

**Step 1.** The original information matrix  $D_{X_{ij}(t_k)} = ([a_{ij}(t_k), b_{ij}(t_k), c_{ij}(t_k)], [d_{ij}(t_k), e_{ij}(t_k), f_{ij}(t_k)])_{m \times n}$  of low-carbon supplier selection is given by our project collaborators who are construction project managers, practitioners, and industry experts, based on the different  $\psi$  moments.

**Step 2.** Based on the main criteria of low-carbon supplier selection for constructor in Table 1, we form information matrix for criteria and calculate the criteria weight set  $w = (w_1, w_2, \dots, w_n)^T$  according to Formulas (37) and (38). Then, we calculate the time sequence weight set  $\eta(t_k) = (\eta(t_1), \eta(t_2), \dots, \eta(t_\psi))^T$  according to Formula (36) by solving the model via Lingo 11.0 software.

**Step 3.** Utilizing the IVTFIFWBM operator to aggregate the criteria information of low-carbon supplier selection based on the criteria weight which is calculated in Step 2. Then, we need to aggregate all individual criteria information  $C_j$  potential low-carbon suppliers into a collective criteria information matrix  $D'_{X_{ij}(t_k)} = ([a'_{ij}(t_k), b'_{ij}(t_k), c'_{ij}(t_k)], [d'_{ij}(t_k), e'_{ij}(t_k), f'_{ij}(t_k)])_{m \times n}$  according to Formula (23).

**Step 4.** Gathering the information of time dimension of low-carbon supplier selection based on the time sequence weight

set  $\eta(t_k) = (\eta(t_1), \eta(t_2), \dots, \eta(t_\psi))^T$ . Then, we create the comprehensive decision information matrix  $D''_{X_i} = ([a''_i, b''_i, c''_i], [d''_i, e''_i, f''_i])_{m \times 1}$  via Formula (29) for the single dimension to potential low-carbon suppliers  $S_i$ .

**Step 5.** Finally, selecting the best low-carbon supplier in the process of low-carbon building construction projects based on ranking value  $L_i = (L_1, L_2, \dots, L_i)$  and further determining the priority sequence of low-carbon supplier  $S_i$  ( $i = 1, 2, \dots, m$ ).

## 6. Case Study

**6.1. Case Company Background.** According to the above analysis, the proposed method is applied on the case of the housing construction project entity in the construction industry to solve low-carbon supplier selection problem.

Company *HFG*, founded in 1986, is a builder enterprise, which has special qualifications for construction, located in Tai Yuan, a city of Shan Xi Province in China. *HFG*'s business scope involves housing construction general contracting, infrastructure construction, real estate investment, engineering design, and other fields in the major cities. *HFG* will be committed to green housing technology development and practice, with product innovation and the provision of low-carbon building products as the development goal. For builder *HFG*, one of the important issues is how to reduce carbon emissions of construction projects to enhance low-carbon competitiveness and profit. In this circumstances, *HFG* needs to select its low-carbon supplier from a large number of suppliers in the process of low-carbon building construction projects.

As builder *HFG* has some experience accumulation in the supplier selection, it is still a difficult problem for *HFG* to select its best low-carbon supplier from these potential suppliers in the process of low-carbon building construction projects. On the one hand, builder *H* has established a criterion, which is not appropriate to use it to select low-carbon supplier. It did not establish the criteria for the low-carbon supplier selection in the process of low-carbon building construction projects. On the other hand, builder *HFG* not only has to nondimensionalize the criteria to previous supplier selection, but also more focus on the single period of decision criteria information, and even if *HFG* considers multiple timings during supplier selection, it may still lead to subjectivity and objectivity in the time weight. Moreover, the selection method is very difficult for builder *HFG* to deal with qualitative criteria in the process of low-carbon supplier selection.

**6.2. Application of the Proposed Criteria and Method.** To builder *HFG*, the proposed criteria and method is suitable to be used to select low-carbon supplier in the process of low-carbon building construction projects, because the managers and practitioner's understanding of the weights of criteria for low-carbon supplier selection is in the fuzzy state in builder *HFG*. In addition, expert scoring method which is usually used to select traditional supplier in their

TABLE 2: Original evaluation criteria information matrix at the moment  $t_1$ .

	$C_1$	$C_2$	$C_3$	$C_4$	$C_5$
$S_1$	([0.6,0.7,0.8], [0.1,0.2,0.3])	([0.5,0.6,0.6], [0.2,0.2,0.2])	([0.1,0.1,0.4], [0.2,0.2,0.5])	([0.6,0.7,0.7], [0.1,0.2,0.3])	([0.7,0.8,0.9], [0.1,0.1,0.1])
$S_2$	([0.2,0.3,0.4], [0.4,0.5,0.5])	([0.4,0.4,0.5], [0.4,0.4,0.5])	([0.1,0.2,0.2], [0.6,0.7,0.8])	([0.3,0.4,0.5], [0.2,0.2,0.3])	([0.5,0.6,0.7], [0.2,0.2,0.3])
$S_3$	([0.4,0.5,0.6], [0.1,0.2,0.2])	([0.3,0.4,0.5], [0.3,0.4,0.4])	([0.2,0.3,0.4], [0.5,0.6,0.6])	([0.6,0.7,0.8], [0.1,0.2,0.2])	([0.7,0.7,0.7], [0.1,0.2,0.2])
$S_4$	([0.6,0.6,0.7], [0.2,0.2,0.2])	([0.4,0.5,0.6], [0.2,0.2,0.3])	([0.6,0.6,0.7], [0.1,0.1,0.1])	([0.4,0.5,0.5], [0.1,0.2,0.3])	([0.2,0.3,0.4], [0.5,0.6,0.6])

construction projects makes the proposed criteria and method more realistic and practical.

For the moment, builder *HFG* is required to purchase a batch of rebar for a low-carbon building in Tai Yuan. After the primary selection of steel production enterprises, there are four enterprises  $S_i = \{S_1, S_2, S_3, S_4\}$  to enter the final selection. Builder *H* needs to select its steel supplier from 4 main low-carbon suppliers by the proposed criteria and method. Therefore, *H*'s 15 managers, practitioners, and experts are asked to determine the criteria of low-carbon supplier selection to construction projects based on the preliminary list of criteria compiled including literature review about low-carbon supplier selection and the builder *H*'s actual situation. It can be seen in Table 1 including 5 main criteria and 17 subcriteria. Moreover, they select the time sequence set of different historical periods for nearly three years,  $t_k = (t_1, t_2, t_3)$ , for the previously mentioned potential low-carbon suppliers. For the sake of simplicity, we only give out the calculation for the 5 main criteria. The evaluated values of 4 main suppliers which are given by 15 managers, practitioners, and experts are listed in Tables 2–4.

Based on the original evaluation criteria information matrix of low-carbon supplier selection which only includes supplier  $S_1$ , supplier  $S_2$ , supplier  $S_3$ , and supplier  $S_4$  in the process of low-carbon building construction projects, per Step 2, according to Formulas (37) and (38), the criteria weight is shown in Table 5. The time degree parameter  $\lambda = 0.3$ , and the discrete time weight vector is solved via Step 2 and Lingo 11.0 software.  $\eta(t_k) = (\eta(t_1), \eta(t_2), \eta(t_3))^T = (0.582, 0.236, 0.182)$ .

Based on the criteria weight vector  $w = (w_1, w_2, w_3, w_4, w_5)$ , per Step 3, the five criteria were assembled into a collective the criteria information of low-carbon supplier selection matrix from 3 periods of time. Comprehensive criteria making information of each potential low-carbon suppliers were assembled from different moment, per Step 4, forming comprehensive selection information matrix for the target single dimension; in the end, the value of each potential low-carbon suppliers for the construction project was determined based on Step 5 and is shown in Tables 6–8.

Thus, the low-carbon supplier, who will provide the batch of rebar for the low-carbon building in Tai Yuan, is determined to  $S_1$ . Based on the evaluation and selection above, supplier  $S_1$  is recommended as builder *HFG*'s best low-carbon supplier. In fact, builder *HFG* has given priority to supplier  $S_1$ , who provides the batch of rebar for the low-carbon building in Tai Yuan, according to the results. In

addition, supplier  $S_3$  is recommended as the reserved low-carbon supplier. *HFG*'s low-carbon housing technology development and practice will improve its competitiveness and profitability in the construction industry based on the concept of continuous improvement.

## 7. Conclusions

There has been broad consensus on carbon emissions reduction around the world. Low-carbon building not only can bring a healthier and more comfortable living environment, but also can reduce carbon emissions in the construction industry. For constructors, using low-carbon building materials for construction and sustainable development of the environment is particularly important. In addition, GSCM has become an inevitable choice for constructors to cope with the pressure from the government and the market. Therefore, it is one of the most important factors to select low-carbon supplier in the process of low-carbon building construction projects.

In this paper, we propose a dynamic multiattribute decision-making approach with interval-valued triangular fuzzy numbers intuitionistic fuzzy for low-carbon supplier selection in the process of low-carbon building construction projects. According to the demand of constructors in the process of low-carbon building construction projects, 5 main criteria and 17 subcriteria are established for low-carbon supplier selection in the construction industry. The proposed method considers interaction between criteria of low-carbon supplier selection and the influence of constructors' subjective preference and objective criteria information. The evaluated values of potential low-carbon suppliers are given by managers, practitioners, and experts. The proposed criteria and method are suitable to use to select low-carbon supplier in the process of low-carbon building construction projects because the managers and practitioner's understanding of the weights of criteria for low-carbon supplier selection are in the intuitionistic fuzzy due to the nature of unquantifiable and incomplete information in low-carbon supplier selection. In addition, expert scoring method, which is usually used to select traditional supplier in their construction projects, makes the proposed criteria and method more realistic and practical. The proposed criteria and method have been successfully implemented in a case construction project to select the best low-carbon supplier. It not only is much easier for constructors to select low-carbon supplier, but also can make the localization of low-carbon

TABLE 3: Original evaluation criteria information matrix at the moment  $t_2$ .

	$C_1$	$C_2$	$C_3$	$C_4$	$C_5$
$S_1$	[[0.2,0.3,0.4], [0.3,0.4,0.4]]	[[0.5,0.6,0.7], [0.2,0.2,0.2]]	[[0.5,0.5,0.6], [0.1,0.2,0.5]]	[[0.6,0.7,0.7], [0.1,0.2,0.3]]	[[0.4,0.5,0.6], [0.1,0.1,0.1]]
$S_2$	[[0.3,0.4,0.5], [0.1,0.2,0.3]]	[[0.4,0.5,0.5], [0.1,0.2,0.2]]	[[0.3,0.4,0.5], [0.1,0.2,0.3]]	[[0.4,0.5,0.6], [0.2,0.2,0.3]]	[[0.6,0.6,0.7], [0.1,0.2,0.2]]
$S_3$	[[0.4,0.5,0.6], [0.1,0.2,0.2]]	[[0.7,0.7,0.7], [0.1,0.1,0.1]]	[[0.4,0.5,0.5], [0.1,0.2,0.3]]	[[0.6,0.7,0.8], [0.1,0.2,0.2]]	[[0.3,0.4,0.5], [0.2,0.3,0.3]]
$S_4$	[[0.6,0.6,0.7], [0.1,0.1,0.1]]	[[0.4,0.5,0.6], [0.2,0.2,0.3]]	[[0.6,0.6,0.7], [0.1,0.1,0.1]]	[[0.2,0.3,0.3], [0.3,0.4,0.5]]	[[0.2,0.3,0.4], [0.5,0.6,0.6]]

TABLE 4: Original evaluation criteria information matrix at the moment  $t_3$ .

	$C_1$	$C_2$	$C_3$	$C_4$	$C_5$
$S_1$	[[0.6,0.7,0.8], [0.1,0.2,0.2]]	[[0.8,0.9,0.9], [0.1,0.1,0.1]]	[[0.2,0.3,0.4], [0.3,0.4,0.5]]	[[0.7,0.8,0.9], [0.1,0.1,0.1]]	[[0.4,0.5,0.6], [0.2,0.3,0.4]]
$S_2$	[[0.8,0.8,0.9], [0.1,0.1,0.1]]	[[0.7,0.7,0.8], [0.2,0.2,0.2]]	[[0.7,0.7,0.8], [0.1,0.2,0.2]]	[[0.4,0.5,0.6], [0.2,0.2,0.3]]	[[0.5,0.6,0.7], [0.1,0.2,0.2]]
$S_3$	[[0.4,0.5,0.6], [0.1,0.2,0.2]]	[[0.4,0.5,0.5], [0.2,0.3,0.4]]	[[0.4,0.5,0.5], [0.1,0.2,0.3]]	[[0.7,0.7,0.8], [0.1,0.1,0.1]]	[[0.4,0.6,0.7], [0.2,0.3,0.3]]
$S_4$	[[0.3,0.4,0.5], [0.1,0.1,0.3]]	[[0.4,0.5,0.6], [0.2,0.2,0.3]]	[[0.6,0.6,0.7], [0.1,0.1,0.1]]	[[0.4,0.5,0.7], [0.1,0.2,0.3]]	[[0.1,0.2,0.3], [0.5,0.6,0.6]]

TABLE 5: The criteria weight.

	$C_1$	$C_2$	$C_3$	$C_4$	$C_5$
$t_1$	0.199	0.192	0.208	0.201	0.200
$t_2$	0.217	0.225	0.162	0.185	0.211
$t_3$	0.086	0.288	0.107	0.183	0.336

TABLE 6: The comprehensive evaluation value under the different  $l$ .

	Comprehensive evaluation value	
$l=0.2$		
$S_1$	[[0.008,0.185,0.213], [0.439,0.452,0.469]]	
$S_2$	[[0.007,0.154,0.180], [0.458,0.471,0.482]]	
$S_3$	[[0.008,0.177,0.199], [0.444,0.466,0.469]]	
$S_4$	[[0.007,0.152,0.180], [0.457,0.465,0.475]]	
$l=0.5$		
$S_1$	[[0.008,0.185,0.213], [0.438,0.451,0.468]]	
$S_2$	[[0.007,0.153,0.179], [0.458,0.471,0.482]]	
$S_3$	[[0.008,0.176,0.197], [0.444,0.466,0.469]]	
$S_4$	[[0.007,0.150,0.179], [0.456,0.464,0.475]]	
$l=0.8$		
$S_1$	[[0.008,0.181,0.208], [0.436,0.449,0.465]]	
$S_2$	[[0.006,0.150,0.175], [0.458,0.470,0.480]]	
$S_3$	[[0.007,0.170,0.190], [0.443,0.465,0.468]]	
$S_4$	[[0.006,0.144,0.172], [0.453,0.462,0.473]]	

supplier more practical and more accurate in the construction industry. Finally, low-carbon supplier selection of builder *HFG* for a low-carbon building in Tai Yuan is studied to verify the scientificity and feasibility of the proposed criteria and method. The result shows that this criteria and method are of effectiveness and practicality of low-carbon supplier selection in the process of low-carbon building construction projects. Also, it can be mentioned that the

TABLE 7: The comprehensive evaluation value under the fully objective/subjective information.

	Comprehensive evaluation value
$l=0$	
$S_1$	[[0.008,0.189,0.215], [0.440,0.453,0.466]]
$S_2$	[[0.007,0.169,0.196], [0.444,0.459,0.468]]
$S_3$	[[0.008,0.180,0.200], [0.439,0.461,0.466]]
$S_4$	[[0.006,0.146,0.177], [0.456,0.465,0.477]]
$l=1$	
$S_1$	[[0.008,0.174,0.197], [0.436,0.449,0.461]]
$S_2$	[[0.007,0.158,0.183], [0.437,0.453,0.461]]
$S_3$	[[0.007,0.166,0.184], [0.434,0.455,0.461]]
$S_4$	[[0.006,0.132,0.161], [0.452,0.461,0.473]]

TABLE 8: The value of each potential low-carbon suppliers and the rank results comparison for the construction project.

	$S_i$	Ranking result
$l=0$	(-0.303, -0.322, -0.315, -0.347)	$S_1 > S_3 > S_2 > S_4$
$l=1$	(-0.311, -0.325, -0.321, -0.354)	$S_1 > S_3 > S_2 > S_4$
$l=0.2$	(-0.305, -0.347, -0.321, -0.343)	$S_1 > S_3 > S_4 > S_2$
$l=0.5$	(-0.304, -0.348, -0.322, -0.343)	$S_1 > S_3 > S_4 > S_2$
$l=0.8$	(-0.305, -0.349, -0.326, -0.346)	$S_1 > S_3 > S_4 > S_2$

proposed model can be easily extended to analyze other management decision problems as a structural model.

This study has some limitations that warrant future research attention. The attribute weight method based on the Entropy-TOPSIS model in this paper is only an objective assignment method. A comprehensive attribute weight method considering the objective assignment information and subjective preferences of decision makers should be studied in the future. Moreover, evaluation criteria information cannot be

effectively reflected by using IVTFNs under uncertain linguistic environment. For further study, we will extend the proposed method in this paper with linguistic intuitionistic fuzzy number and prospect theory in other civil engineering fields.

## Data Availability

All data generated or analyzed to support the findings of this study are included within the article.

## Conflicts of Interest

The authors declare that they have no conflicts of interest.

## Acknowledgments

The authors would like to thank Min Yan. This research was supported by the National Natural Science Foundation of China (71473055), the Fundamental Research Special Funds for the Central Universities (HEUCFW170912, HEUCFP201824), the Humanities and Social Sciences Foundation of Ministry of Education of China (14YJA630002), the National Natural Science Foundation of China (71804084), the Humanities and Social Sciences Foundation of Ministry of Education of China (15YJC630162), the Humanities and Social Sciences Foundation of Ministry of Education of China (18YJC630245), the China Postdoctoral Science Foundation Funded Project (2017M620814), and the National Social Science Foundation of China (17BGL238).

## References

- [1] J. Yudelson, *Green Building A to Z: Understanding the Language of Green Building*, New Society Publishers, Gabriola Island, BC, Canada, 2007.
- [2] IPOC, *Climate Change 2014 Synthesis Report, Environmental Policy Collection*, vol. 27, no. 2, p. 408, 2014.
- [3] B. Kang, Y. Hu, Y. Deng, and D. Zhou, "A new methodology of multicriteria decision-making in supplier selection based on Z-numbers," *Mathematical Problems in Engineering*, vol. 2016, no. 1, pp. 1–17, 2016.
- [4] A. H. I. Lee, H. Y. Kang, C. F. Hsu, and H. C. Hung, "A green supplier selection model for high-tech industry," *Expert Systems with Applications*, vol. 36, no. 4, pp. 7917–7927, 2009.
- [5] C. W. Hsu, T. C. Kuo, S. H. Chen, and A. H. Hu, "Using DEMATEL to develop a carbon management model of supplier selection in green supply chain management," *Journal of Cleaner Production*, vol. 56, no. 10, pp. 164–172, 2013.
- [6] D. Kannan and C. J. C. Jabbour, "Selecting green suppliers based on GSCM practices: Using fuzzy TOPSIS applied to a Brazilian electronics company," *European Journal of Operational Research*, vol. 233, no. 2, pp. 432–447, 2014.
- [7] C. W. Tsui and U. P. Wen, "A hybrid multiple criteria group decision-making approach for green supplier selection in the TFT-LCD industry," *Mathematical Problems in Engineering*, vol. 2014, Article ID 709872, 13 pages, 2014.
- [8] O. Gurel, A. Z. Acar, I. Onden, and I. Gumus, "Determinants of the green supplier selection," *Procedia-Social and Behavioral Sciences*, vol. 181, no. 4, pp. 131–139, 2015.
- [9] H. M. W. Chen, S. Y. Chou, Q. D. Luu, and H. K. Yu, "A fuzzy MCDM approach for green supplier selection from the economic and environmental aspects," *Mathematical Problems in Engineering*, vol. 2016, Article ID 8097386, 10 pages, 2016.
- [10] F. Yu, Y. Yang, D. Chang, F. Yu, and Y. Yang, "Carbon footprint based green supplier selection under dynamic environment," *Journal of Cleaner Production*, vol. 170, no. 8, pp. 880–889, 2017.
- [11] K. Govindan and R. Sivakumar, "Green supplier selection and order allocation in a low-carbon paper industry: integrated multi-criteria heterogeneous decision-making and multi-objective linear programming approaches," *Annals of Operations Research*, vol. 238, no. 3, pp. 243–276, 2016.
- [12] Q. Pang, T. Yang, M. Li, and Y. Shen, "A fuzzy-grey multicriteria decision making approach for green supplier selection in low-carbon supply chain," *Mathematical Problems in Engineering*, vol. 1, pp. 1–9, 2017.
- [13] A. P. C. Chan, A. Darko, and E. A. Effah, "Strategies for promoting green building technologies adoption in the construction industry—An international study," *Sustainability*, vol. 9, no. 6, p. 969, 2017.
- [14] K. Govindan, R. Khodaverdi, and A. Jafarian, "A fuzzy multi criteria approach for measuring sustainability performance of a supplier based on triple bottom line approach," *Journal of Cleaner Production*, vol. 47, no. 47, pp. 345–354, 2013.
- [15] S. Yin, B. Li, H. Dong, and Z. Xing, "A new dynamic multicriteria decision-making approach for green supplier selection in construction projects under time sequence," *Mathematical Problems in Engineering*, vol. 2017, Article ID 7954784, 13 pages, 2017.
- [16] S. Darabi and J. Heydari, "An interval-valued hesitant fuzzy ranking method based on group decision analysis for green supplier selection," *IFAC-Papers On Line*, vol. 49, no. 2, pp. 12–14, 2016.
- [17] W. C. Yeh and M. C. Chuang, "Using multi-objective genetic algorithm for partner selection in green supply chain problems," *Expert Systems with Applications*, vol. 38, no. 4, pp. 4244–4253, 2011.
- [18] A. Kumar, V. Jain, S. Kumar, and C. Chandra, "Green supplier selection: a new genetic/immune strategy with industrial application," *Enterprise Information Systems*, vol. 10, no. 8, pp. 911–943, 2015.
- [19] M. Gupta, "Supplier selection using artificial neural network and genetic algorithm," *International Journal of Indian Culture and Business Management*, vol. 11, no. 4, pp. 457–472, 2015.
- [20] M. Punniyamoorthy, P. Mathiyalagan, and P. Parthiban, "A strategic model using structural equation modeling and fuzzy logic in supplier selection," *Expert Systems with Applications*, vol. 38, no. 1, pp. 458–474, 2011.
- [21] A. Fallahpour, E. U. Olugu, S. N. Musa, D. Khezrimotlagh, and K. Y. Wong, "An integrated model for green supplier selection under fuzzy environment: application of data envelopment analysis and genetic programming approach," *Neural Computing and Applications*, vol. 27, no. 3, pp. 707–725, 2016.
- [22] L. H. Li, J. C. Hang, Y. Gao, and C. Y. Mu, "Using an integrated group decision method Based on SVM, TFN-RS-AHP, and TOPSIS-CD for cloud service supplier selection," *Mathematical Problems in Engineering*, vol. 3, pp. 1–14, 2017.
- [23] Z. Hu, C. Rao, Y. Zheng, and D. Huang, "Optimization decision of supplier selection in green procurement under the mode of low carbon economy," *International Journal of Computational Intelligence Systems*, vol. 8, no. 3, pp. 407–421, 2015.

- [24] J. Qin, X. Liu, and W. Pedrycz, "An extended TODIM multi-criteria group decision making method for green supplier selection in interval type-2 fuzzy environment," *European Journal of Operational Research*, vol. 258, no. 4, pp. 626–638, 2017.
- [25] P. Ghadimi, A. Dargi, and C. Heavey, "Sustainable supplier performance scoring using audition check-list based fuzzy inference system: a case application in automotive spare part industry," *Computers and Industrial Engineering*, vol. 105, no. 2, pp. 12–27, 2017.
- [26] R. R. Yager, "On generalized Bonferroni mean operators for multi-criteria aggregation," *International Journal of Approximate Reasoning*, vol. 50, no. 8, pp. 1279–1286, 2009.
- [27] Z. S. Xu, "Intuitionistic fuzzy Bonferroni means," *IEEE Transactions on Systems, Man, and Cybernetics-Part B: Cybernetics*, vol. 41, no. 2, pp. 568–578, 2011.
- [28] M. Xia, Z. Xu, and B. Zhu, "Generalized intuitionistic fuzzy Bonferroni means," *International Journal of Intelligent Systems*, vol. 27, no. 1, pp. 23–47, 2011.
- [29] W. Zhou and J. M. He, "Intuitionistic fuzzy geometric Bonferroni means and their application in multicriteria decision making," *International Journal of Intelligent Systems*, vol. 27, no. 12, pp. 995–1019, 2012.
- [30] B. Zhu, "Hesitant fuzzy geometric Bonferroni means," *Information Science*, vol. 205, no. 1, pp. 72–85, 2012.
- [31] P. D. Liu, L. L. Zhang, X. Liu, and P. Wang, "Multi-valued neutrosophic number Bonferroni mean operators with their applications in multiple attribute group decision making," *International Journal of Information Technology & Decision Making*, vol. 15, no. 5, pp. 1181–1210, 2016.
- [32] X. Liu, Z. Tao, H. Chen, and L. Zhou, "A new interval-valued 2-tuple linguistic bonferroni mean operator and its application to multi-attribute group decision making," *International Journal of Fuzzy Systems*, vol. 19, no. 1, pp. 86–108, 2017.
- [33] G. W. Wei, "Some geometric aggregation functions and their application to dynamic multiple attribute decision making in the intuitionistic fuzzy setting," *International Journal of Uncertainty, Fuzziness and Knowledge-Based Systems*, vol. 17, no. 2, pp. 179–196, 2011.
- [34] J. H. Park, H. J. Cho, and Y. C. Kwun, "Extension of the VIKOR method to dynamic intuitionistic fuzzy multiple attribute decision making," *Computers and Mathematics with Applications*, vol. 65, no. 4, pp. 731–744, 2013.
- [35] S. Yin, B. Li, H. Dong, and Z. Xing, "A new dynamic multicriteria decision making approach for green supplier selection in construction projects under time sequence," *Mathematical problems in Engineering*, vol. 2, pp. 1–13, 2017.
- [36] Z. S. Xu, "On multi-period multi-attribute decision making," *Knowledge-Based Systems*, vol. 21, no. 2, pp. 164–171, 2008.
- [37] Z. S. Xu and J. Chen, "Binomial distribution based approach to deriving time series weights," in *IEEE International Conference on Industrial Engineering and Engineering Management*, pp. 154–158, Bangkok, Thailand, 2007.
- [38] P. Liu and F. Teng, "Multiple criteria decision making method based on normal interval-valued intuitionistic fuzzy generalized aggregation operator," *Complexity*, vol. 21, no. 5, pp. 277–290, 2016.
- [39] R. Sadiq and S. Tesfamariam, "Probability density functions based weights for ordered weighted averaging (OWA) operators: an example of water quality indices," *European Journal of Operational Research*, vol. 183, no. 3, pp. 1350–1365, 2007.
- [40] X. Z. Zhang and C. X. Zhu, "Generalized precedence order method with ranking preference for multi-attribute decision making," *Systems Engineering-Theory and Practice*, vol. 33, no. 11, pp. 2852–2858, 2013.
- [41] B. Sun and X. F. Xu, "A dynamic stochastic decision-making method based on discrete time sequences," *Knowledge-Based Systems*, vol. 105, no. 4, pp. 23–28, 2016.
- [42] G. W. Wei, "Two-tuple linguistic multiple attribute group decision making with incomplete attribute weight information," *Systems Engineering and Electronics*, vol. 30, no. 2, pp. 273–277, 2008.
- [43] Z. S. Chen and Y. S. Li, "Approach for normal triangular fuzzy stochastic multiple attribute decision making based on prospect mean-variance rule," *Control and Decision*, vol. 29, no. 7, pp. 1239–1249, 2014.
- [44] Y. M. Wang, C. P. Que, and Y. X. Lan, "Hesitant fuzzy TOPSIS multi-attribute decision method based on prospect theory," *Control and Decision*, vol. 32, no. 5, pp. 864–870, 2017.
- [45] K. T. Atanassov, "Intuitionistic fuzzy sets," *Fuzzy Sets and Systems*, vol. 20, pp. 87–96, 1986.
- [46] Z. S. Xu and Q. Chen, "A multi-attribute decision-making process based on interval-valued intuitionistic fuzzy Bonferroni mean," *Journal of Systems Engineering and Electronics*, vol. 20, no. 2, pp. 217–228, 2011.
- [47] X. F. Wang, "Fuzzy number intuitionistic fuzzy geometric aggregation operators and their application to decision making," *Control and Decision*, vol. 23, no. 6, pp. 607–612, 2008.
- [48] C. Bonferroni, "Sulle medie multiple di potenze," *Bolletino Matematica Italiana*, vol. 5, pp. 267–270, 1950.

## Research Article

# A Computer-Aided Approach to Pozzolan Concrete Mix Design

Ching-Yun Kao <sup>1</sup>, Chin-Hung Shen,<sup>2</sup> Jing-Chi Jan,<sup>3</sup> and Shih-Lin Hung <sup>4</sup>

<sup>1</sup>Associate Professor, Department of Applied Geoinformatics, Chia Nan University of Pharmacy & Science, No. 60, Sec. 1, Erh-Jen Rd., Tainan 71710, Taiwan

<sup>2</sup>Graduate Student, Department of Civil Engineering, National Chiao Tung University, No. 1001, University Rd., Hsinchu 300, Taiwan

<sup>3</sup>Associate Professor, Department of Computer Science and Information Engineering, Chien Hsin University of Science and Technology, No. 229, Jianxing Rd., Zhongli Dist., Taoyuan City 32097, Taiwan

<sup>4</sup>Professor, Department of Civil Engineering, National Chiao Tung University, No. 1001, University Rd., Hsinchu 300, Taiwan

Correspondence should be addressed to Shih-Lin Hung; slhung@mail.nctu.edu.tw

Received 30 May 2018; Accepted 2 September 2018; Published 10 October 2018

Guest Editor: Maksym Grzywinski

Copyright © 2018 Ching-Yun Kao et al. This is an open access article distributed under the Creative Commons Attribution License, which permits unrestricted use, distribution, and reproduction in any medium, provided the original work is properly cited.

Pozzolan concrete has superior properties, such as high strength and workability. The precise proportioning and modeling of the concrete mixture are important when considering its applications. There have been many efforts to develop computer-aided approaches for pozzolan concrete mix design, such as artificial neural network- (ANN-) based approaches, but these approaches have proven to be somewhat difficult in practical engineering applications. This study develops a two-step computer-aided approach for pozzolan concrete mix design. The first step is establishing a dataset of pozzolan concrete mixture proportioning which conforms to American Concrete Institute code, consisting of experimental data collected from the literature as well as numerical data generated by computer program. In this step, ANNs are employed to establish the prediction models of compressive strength and the slump of the concrete. Sensitivity analysis of the ANN is used to evaluate the effect of inputs on the output of the ANN. The two ANN models are tested using data of experimental specimens made in laboratory for twelve different mixtures. The second step is classifying the dataset of pozzolan concrete mixture proportioning. A classification method is utilized to categorize the dataset into 360 classes based on compressive strength, pozzolan admixture replacement rate, and material cost. Thus, one can easily obtain mix solutions based on these factors. The results show that the proposed computer-aided approach is convenient for pozzolan concrete mix design and practical for engineering applications.

## 1. Introduction

Concrete plays an important role in the growing construction industry. Presently, various types of by-product materials, such as fly ash, silica fume, rice husk ash, and others have been widely used as pozzolan materials in concrete. Studies [1–4] have shown that utilization of pozzolan material not only improves concrete properties (such as strength and durability) but also helps to preserve the environment. Moreover, superplasticizers play a crucial role in the development of high strength and high-performance concrete. Superplasticizers are admixtures which are added to concrete mixture in very small dosages. Their addition results in a significant increase in the

workability of the mixture, as well as a reduction of water/cement ratio and of cement quantity [5].

Several researchers have looked into the characteristic parameters that affect the compressive strength and slump of conventional and high-strength concrete [6–8]. These parameters typically include water, cement, coarse aggregate, and fine aggregate. Conventional methods initially involve constructing a mathematical model, which is followed by a regression analysis using experimental data to determine unknown coefficients in that model and establish correlations between these parameters and compressive strength and slump. Conventional methods generally include complex modeling and are inappropriate where experimental data are imprecise and parameters

affecting compressive strength and slump are incomplete in the experimental data.

Artificial neural networks (ANNs) were originally developed to simulate the function of the human brain or neural system. Subsequently, they have been widely applied to diverse fields, ranging from biology to many engineering fields. ANNs exhibit a number of desirable properties not found in conventional symbolic computation systems, including robust performance when dealing with noisy or incomplete input patterns, a high degree of fault tolerance, high parallel computation rates, the ability to generalize, and adaptive learning [9–11]. ANNs are capable of modeling input-output functional relations, even when mathematically explicit formulas are unavailable. Therefore, ANNs are suitable for prediction of compressive strength and slump of concrete. Accordingly, the feasibility of applying ANNs to predict compressive strength and slump of concrete has received considerable attention. Yeh [12] investigated the potential of using design of experiments and ANNs to determine the effect of fly ash replacements on early and late compressive strength of low- and high-strength concrete. Yeh [13] further demonstrated the possibilities of adapting ANNs to predict the compressive strength of high-performance concrete. Kasperkiewics et al. [14] applied ANNs to predict the 28-day compressive strength of high-performance concrete composed of six components (cement, silica, superplasticizer, water, fine aggregate, and coarse aggregate). Lee [15] used ANNs to predict the compressive strength development of concrete. Bai et al. [16] developed neural network models to predict the workability of concrete incorporating metakaolin and fly ash. Duan et al. [17] applied ANNs to predict the compressive strength of recycled aggregate concrete. Ni and Wang [18] developed a method to predict 28-day compressive strength of concrete by using ANNs based on the inadequacy of methods dealing with multiple variable and nonlinear problems.

In light of the above developments, this study develops a two-step computer-aided approach for pozzolanic concrete mix design. The first step is establishing the dataset of pozzolanic concrete mixture proportioning which conform to American Concrete Institute (ACI) code. The dataset consists of experimental data collected from the literature and numerical data generated by computer program. In this step, ANNs are employed to establish the prediction models of compressive strength and slump of concrete. Sensitivity analysis of the ANN is used to evaluate the effect of inputs on the output of the ANN. The two ANN models are tested using data of experimental specimens made in laboratory for twelve different mixtures. The second step is classifying the dataset of pozzolanic concrete mixture proportioning. A classification method is utilized to categorize the dataset into 360 classes based on compressive strength of concrete, pozzolanic admixture replacement rate, and cost of the concrete.

## 2. Artificial Neural Networks

ANNs form a class of systems that are inspired by biological neural networks. The topology of an ANN model consists of

a number of simple processing elements, called nodes, which are interconnected to each other. Interconnection weights that represent the information stored in the system are used to quantify the strength of the interconnections; these weights hold the key to the functioning of an ANN.

**2.1. Back-Propagation Neural Networks.** Among the many different types of ANN, by far the most commonly applied neural network learning model, due to its simplicity, is the feedforward, multilayered, supervised neural network with error back-propagation algorithm, the so-called back-propagation (BP) network [11]. Before an ANN can be used in an application, it must either learn or be trained from an existing database consisting of pairs of input-output patterns. The topology of BP networks consists of an input layer, one or more hidden layers, and an output layer. The training of a supervised neural network usually involves three stages. The first stage is the data feedforward. The output of each node is defined as follows:

$$\begin{aligned} \text{net}_j &= \sum_{i=1}^n W_{ij} O_i + \theta_j, \\ O_j &= f(\text{net}_j), \end{aligned} \quad (1)$$

where  $W_{ij}$  is the weight associated with the  $i$ th node in the preceding layer to the  $j$ th node in the current layer;  $O_i$  is the output of  $i$ th node in the preceding layer;  $\theta_j$  is the threshold value of node  $j$  in the current layer;  $O_j$  is the output of node  $j$  in the current layer; and function  $f$  is the activation function, which has to be differentiable. Herein, the hyperbolic tangent function is used as the activation function and is defined as follows:

$$f(x) = \frac{e^x - e^{-x}}{e^x + e^{-x}}. \quad (2)$$

The second stage is error back-propagation and adjustment of the network weights. The training process applies mean square error ( $E$ ), the absolute fraction of variance ( $R^2$ ), and sum of the squares error (SSE), to monitor the learning performance of the network.  $E$ ,  $R^2$ , and SSE are defined, respectively, as

$$\begin{aligned} E &= \frac{1}{P} \sum_{p=1}^P \sum_{k=1}^K (d_{pk} - o_{pk})^2, \\ R^2 &= 1 - \frac{\sum_{p=1}^P \sum_{k=1}^K (d_{pk} - o_{pk})^2}{\sum_{p=1}^P \sum_{k=1}^K (o_{pk})^2}, \\ \text{SSE} &= \sum_{p=1}^P \sum_{k=1}^K (d_{pk} - o_{pk})^2, \end{aligned} \quad (3)$$

where  $P$  denotes the number of instances in the training set, while  $d_{pk}$  and  $o_{pk}$  represent the desired and calculated output of the  $k$ th output node for the  $p$ th instance, respectively. The standard BP algorithm employs a gradient descent approach with a constant step length (learning ratio) to train the network.

$$W_{ij,k+1} = W_{ij,k} + \Delta W_{ij}, \quad (4)$$

$$\Delta W_{ij} = -\eta \frac{\partial E}{\partial W_{ij}},$$

where  $\eta$  is the learning ratio, which is a constant in the range of  $[0, 1]$ . The suffix index  $k$  denotes the  $k$ th learning iteration. Unfortunately, BP supervised neural network learning models require a significant amount of time to learn. Moreover, the convergence of a BP neural network is highly dependent upon the use of a learning rate ( $\eta$ ). Consequently, several different approaches are developed here to enhance the learning performance of the BP learning algorithm [10].

Hung and Lin [19] developed a more effective adaptive limited memory Broyden–Fletcher–Goldfarb–Shanno (L-BFGS) learning algorithm based on the approach of a L-BFGS quasi-Newton second-order method [20, 21] with an inexact line search algorithm. This algorithm achieved a superior convergence rate to the BP learning algorithm by using second-order derivatives of the system error function with respect to the network weights. In the conventional BFGS method, the approximation  $\mathbf{H}_{k+1}$  to the inverse Hessian matrix of function  $E(\mathbf{W})$  is updated by

$$\mathbf{H}_{k+1} = (\mathbf{I} - \boldsymbol{\rho}_k \mathbf{s}_k \mathbf{y}_k^T) \mathbf{H}_k (\mathbf{I} - \boldsymbol{\rho}_k \mathbf{y}_k \mathbf{s}_k^T) + \boldsymbol{\rho}_k \mathbf{s}_k \mathbf{s}_k^T \quad (5)$$

$$\equiv \mathbf{V}_k^T \mathbf{H}_k \mathbf{V}_k + \boldsymbol{\rho}_k \mathbf{s}_k \mathbf{s}_k^T,$$

where

$$\boldsymbol{\rho}_k = \frac{1}{\mathbf{y}_k^T \mathbf{s}_k},$$

$$\mathbf{V}_k = \mathbf{I} - \boldsymbol{\rho}_k \mathbf{y}_k \mathbf{s}_k^T,$$

$$\mathbf{s}_k = \mathbf{W}_{k+1} - \mathbf{W}_k, \quad (6)$$

$$\mathbf{y}_k = \mathbf{g}_{k+1} - \mathbf{g}_k,$$

$$\mathbf{g}_k = \frac{\partial E}{\partial \mathbf{W}}$$

Instead of forming the matrix  $\mathbf{H}_k$  with the BFGS method, the vectors  $\mathbf{s}_k$  and  $\mathbf{y}_k$  are saved. These vectors first define and then implicitly and dynamically update the Hessian approximation using information from the last few iterations, referred to here as  $m$ . Therefore, the final stage of the adjustment of the weights in a BP-based ANN is modified as follows:

$$\mathbf{W}_{k+1} = \mathbf{W}_k + \alpha_k \mathbf{d}_k. \quad (7)$$

The search direction is given by

$$\mathbf{d}_k = -\mathbf{H}_k \mathbf{g}_k + \beta_k \mathbf{d}_{k-1}, \quad (8)$$

where

$$\beta_k = \frac{\mathbf{y}_{(k-1)}^T \mathbf{H}_{(k-1)} \mathbf{g}_{(k-1)}}{\mathbf{y}_{(k-1)}^T \mathbf{d}_{(k-1)}}. \quad (9)$$

The step length,  $\alpha_k$ , is adapted during the learning process through a mathematical approach: the inexact line search algorithm. This approach is used in the L-BFGS learning algorithm instead of a constant learning ratio [19]. The inexact line search algorithm is based on three sequential approaches: bracketing, sectioning, and interpolation. The bracketing approach brackets the potential step length,  $\alpha$ , between two points, through a series of function evaluations. The sectioning approach then uses the two points of the bracket as the initial points, reducing the step size, and locating the minimum between points, such as,  $\alpha_1$  and  $\alpha_2$ , to a specified degree of accuracy. Finally, the quadratic interpolation approach uses the three points,  $\alpha_1$ ,  $\alpha_2$ , and  $(\alpha_1 + \alpha_2)/2$ , to fit a parabola to determine the step length,  $\alpha_k$ . Consequently, the step length  $\alpha_k$  must satisfy the following conditions in each iteration [19]:

$$E(\mathbf{W}_k + \alpha_k \mathbf{d}_k) \leq E(\mathbf{W}_k) + \beta \alpha_k (\nabla E(\mathbf{W}_k))^T \mathbf{d}_k$$

$$\beta \in (0, 1) \text{ and } \alpha_k > 0,$$

$$\nabla E(\mathbf{W}_k + \alpha_k \mathbf{d}_k)^T \mathbf{d}_k \geq \theta (\nabla E(\mathbf{W}_k))^T \mathbf{d}_k$$

$$\theta \in (\beta, 1) \text{ and } \alpha_k > 0,$$

$$\nabla E(\mathbf{W}_k + \alpha_k \mathbf{d}_k)^T \mathbf{d}_{(k+1)} < 0. \quad (10)$$

The problem of selecting a learning ratio through trial and error in the BP algorithm is thus circumvented in the adaptive L-BFGS learning algorithm.

**2.2. Architectures of ANN Models.** The ANN models, compressive strength prediction neural network (CSPNN) and slump prediction neural network (SPNN), are used in this study for prediction of the 28-day compressive strength (abbreviated below as compressive strength) and slump of pozzolanic concrete, respectively. The architectures of the CSPNN and SPNN are illustrated in Figure 1. Both CSPNN and SPNN developed in this study have seven neurons in the input layer and one neuron in the output layer. The inputs of both CSPNN and SPNN are water, cement, ground granulated blast furnace slag (GGBFS), fly ash, coarse aggregate (CA), fine aggregate (FA), and superplasticizer (SP). The outputs of CSPNN and SPNN are compressive strength ( $f'_c$ ) and slump ( $S$ ), respectively. Table 1 shows the minimum and maximum values of the seven input parameters used in CSPNN and SPNN.

**2.3. Sensitivity Analysis.** Cybenko [22] and Funahashi [23] rigorously demonstrated that even with only one hidden layer, neural networks can uniformly approximate any continuous function. Although neural networks can find a relationship between the input and output values internally, it is not always easy to interpret the resulting weight state. Thus, the effect of one input parameter on the output is difficult to analyze. Alternatively, it is possible to compute the sensitivity of the output value with respect to one of its inputs by taking the first-order partial derivative [24, 25].

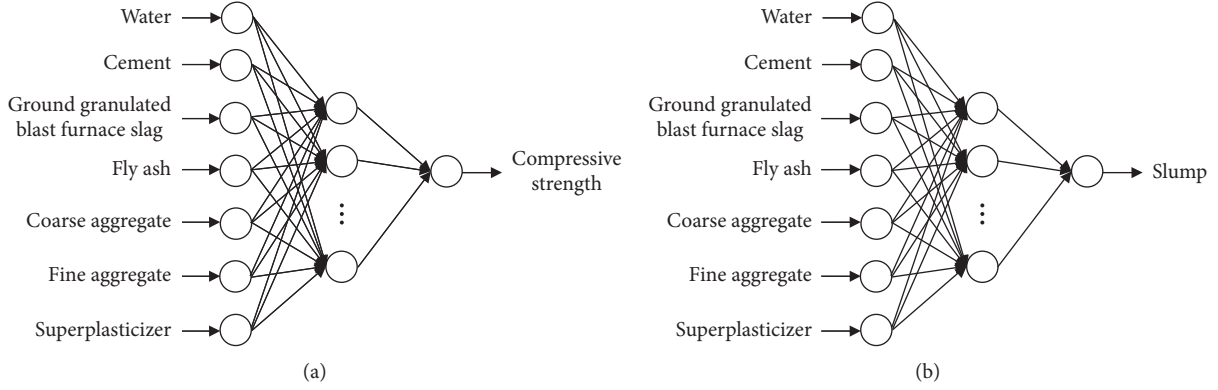


FIGURE 1: The architectures of (a) CSPNN and (b) SPNN.

TABLE 1: Range of input parameters of CSPNN and SPNN in dataset.

Input parameters	Range (kg/m <sup>3</sup> )
Water	125 ≤ Water ≤ 240
Cement	110 ≤ Cement ≤ 500
GGBFS	0 ≤ GGBFS ≤ 300
Fly ash	0 ≤ fly ash ≤ 300
CA	CA ≥ 450
FA	FA ≥ 450
SP	SP < 2% (cement + pozzolanic admixtures)

If there is a network with  $n$  hidden layers, the output of the  $k$ th node in the output layer is defined as follows:

$$\begin{aligned} O_k &= f(\text{net}_{ok}), \\ \text{net}_{ok} &= \sum_j W_{mj,ok} H_{nj} + \theta_{ok}, \end{aligned} \quad (11)$$

where  $H_{nj}$  is the output of the  $j$ th node in the  $n$ th hidden layer,  $\theta_{ok}$  is the threshold value of the  $k$ th node in the output layer,  $W_{mj,ok}$  is the weight associated with the  $j$ th node in the  $n$ th hidden layer to the  $k$ th node in the output layer, and function  $f$  is the activation function.

The first-order partial derivative of the  $k$ th output with respect to  $i$ th input  $D_{ki}^1$  can be derived as follows:

$$\begin{aligned} D_{ki}^1 &= \frac{\partial O_k}{\partial X_i} \\ &= \sum_{jn} \dots \sum_{j1} W_{mjn,ok} f'(\text{net}_{ok}), \dots, W_{xi,h1j1} f'(\text{net}_{h1j1}), \end{aligned} \quad (12)$$

where  $W_{xi,h1j1}$  is the weight associated with the  $i$ th node in the input layer to the  $j1$ th node in the first hidden layer and  $W_{mjn,ok}$  is the weight associated with the  $j$ th node in the  $n$ th hidden layer to the  $k$ th node in the output layer. Equation (12) indicates that  $D_{ki}^1$  is a function of weights, threshold value, and the first-order derivative of the activation function (or a function of weights, threshold values, and training instances). Since  $D_{ki}^1$  is a function of training instances, generally, the mean of  $D_{ki}^1$  for the entire training instances can be used to describe the nominal value of the

sensitivity of the  $k$ th output parameter with respect to the  $i$ th input parameter. The mean of  $D_{ki}^1$  for the entire training instances is

$$\bar{D}_{ki}^1 = \frac{1}{P} \sum_{p=1}^P D_{ki,p}^1, \quad (13)$$

where  $D_{ki,p}^1$  is the value of  $D_{ki}^1$  of the  $p$ th training instance, and  $P$  is the total number of training instances. In fact,  $\bar{D}_{ki}^1$  can represent the correlation between the  $k$ th output parameter and the  $i$ th input parameter. A positive (negative) value of  $\bar{D}_{ki}^1$  represents a positive (negative) correlation. The absolute value of  $\bar{D}_{ki}^1$  represents the strength of the correlation. A larger absolute value of  $\bar{D}_{ki}^1$  represents a stronger correlation. Absolute values of  $\bar{D}_{ki}^1$  near zero indicate little or no correlation.

### 3. Proposed Approach for Pozzolanic Concrete Mix Design

This study develops a computer-aided approach for pozzolanic concrete mix design. This approach is suitable for designing a mix of pozzolanic concrete with compressive strength,  $f'_c$ , from 210 kgf/cm<sup>2</sup> to 980 kgf/cm<sup>2</sup> and slump,  $S$ , equal to 20 cm. As shown in Figure 2, this approach involves two steps. The first step is establishing the dataset of pozzolanic concrete mixture proportioning that conform to ACI code, consisting of experimental data collected from literature and numerical data generated by computer program. The second step is classifying the dataset of pozzolanic concrete mixture proportioning. A classification method is utilized to categorize data into 360 clusters according to compressive strength of concrete, pozzolanic admixtures replacement rate, and material cost. The following presents the details of the proposed approach.

*3.1. Establishing the Dataset of Pozzolanic Concrete Mixture Proportioning.* As shown in Figure 2, the process of establishing the dataset of pozzolanic concrete mixture proportioning is listed as follows:

- (1) Collecting experimental data of pozzolanic concrete mixture proportioning from the literature [3, 26–38].

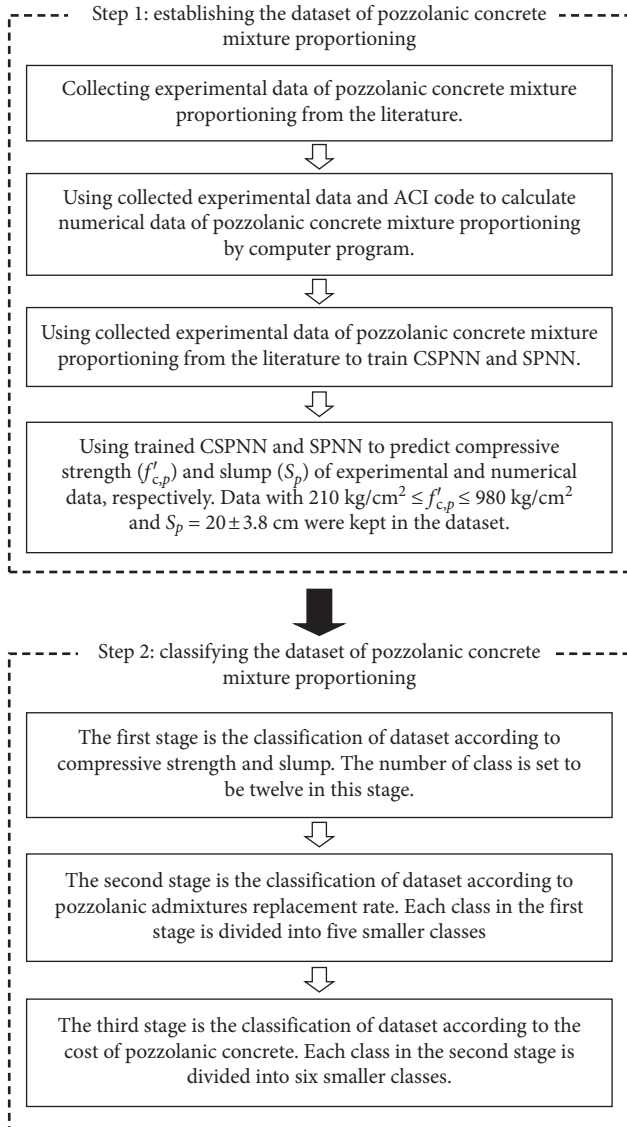


FIGURE 2: Schematic diagram of the proposed approach for pozzolanic concrete mix design.

- (2) Generating numerical data of pozzolanic concrete mixture proportioning since the collected experimental data may be insufficient. Before generating numerical data, the ranges of material contents (as listed in Table 1) are set based on collected experimental data of pozzolanic concrete mixture proportioning and ACI code for pozzolanic concrete mix design (as listed in Tables 2–8) [39]. Numerical data of pozzolanic concrete mixture proportioning are then generated randomly using the ACI mix design method for pozzolanic concrete (as shown in Figure 3).
- (3) Using a portion of collected experimental data of pozzolanic concrete mixture proportioning to train CSPNN and SPNN. The effect of input parameters on the output is evaluated by sensitivity analysis. The prediction accuracy of CSPNN and SPNN is tested using the remainder of the collected experimental

data and data from experimental specimens made in our laboratory for twelve different mixtures.

- (4) Using trained CSPNN and SPNN to predict compressive strength and slump of experimental and numerical data, respectively. Data that satisfy the following conditions are kept in the dataset.

$$\begin{aligned} 210 \text{ kgf/cm}^2 &\leq f'_{c,\text{CSPNN}} \leq 980 \text{ kgf/cm}^2, \\ 20 + 3.8 \text{ cm} &\leq S_{\text{SPNN}} \leq 20 - 3.8 \text{ cm}, \end{aligned} \quad (14)$$

where  $f'_{c,\text{CSPNN}}$  and  $S_{\text{SPNN}}$  are compressive strength and slump predicted by CSPNN and SPNN, respectively. The reasons for this are (1) this approach is suitable for mixing design of pozzolanic concrete with compressive strength,  $f'_c$ , from 210 kgf/cm<sup>2</sup> to 980 kgf/cm<sup>2</sup> and slump,  $S$ , equal to 20 cm, and (2) the allowable data range width of slump in Taiwan is set to be 3.8 cm when slump is larger than 10 cm [40].

**3.2. Classifying the Dataset of Pozzolanic Concrete Mixture Proportioning.** To produce a dataset of pozzolanic concrete mixture proportioning which is more feasible and convenient for engineering applications, it is classified further.

In classification, a sampling unit (subject or object) whose class membership is unknown is assigned to a class on the basis of the vector,  $\mathbf{y}$ , associated with the unit. To classify the unit, we must have available a previously obtained sample of observation vectors from each class. One approach is to then compare  $\mathbf{y}$  with the mean vectors  $\bar{\mathbf{y}}_1, \bar{\mathbf{y}}_2, \dots, \bar{\mathbf{y}}_k$  of the  $k$  classes and assign the unit to the class whose  $\bar{\mathbf{y}}_i$  is closest to  $\mathbf{y}$  [41]. Many techniques use an index of similarity or proximity between  $\mathbf{y}$  and  $\bar{\mathbf{y}}_i$ . A convenient measure of proximity is the distance. The distances used in classification algorithms include Euclidean distance, Manhattan distance, Chebyshev distance, Minkowski distance, and Mahalanobis distance. Since Euclidean distance is the most well-known distance, it is applied in this study. The Euclidean distance between two vectors (points)  $\mathbf{a}$  and  $\mathbf{b}$  is defined as

$$\text{dis}(\mathbf{a}, \mathbf{b}) = \sqrt{\sum_j (a_j - b_j)^2}, \quad (15)$$

where  $a_j$  and  $b_j$  are the  $j$ th element of  $\mathbf{a}$  and  $\mathbf{b}$ , respectively.

The proposed classification of the dataset of pozzolanic concrete mixture proportioning is according to compressive strength, pozzolanic admixture replacement rate, and cost. As shown in Figure 2, the classification method used in this study involves three stages. The first stage is the classification of dataset according to compressive strength and slump. The number of classes is set as twelve in this stage. The mean (designed) values of compressive strength of the twelve classes are increased from 210 kgf/cm<sup>2</sup> (20.6 MPa) to 980 kgf/cm<sup>2</sup> (96.1 MPa) every 70 kgf/cm<sup>2</sup> (6.8 MPa). The mean (designed) values of slump of all twelve classes are the same and are equal to 20 cm. According to the related code in Taiwan, the allowable data range width of compressive strength and slump is 3.4 MPa and 3.8 cm, respectively. Thus, the classification rule can be written as

TABLE 2: Cementitious materials requirements for concrete exposed to deicing chemicals “Table 2 is reproduced from Kosmatka et al. [39] (under the creative commons attribution license/public domain).”

Cementitious materials	Maximum percent of total cementitious materials by mass
Fly ash and natural pozzolans	25
Slag	50
Silica fume	10
Total of fly ash, slag, silica fume, and natural pozzolans	50
Total of natural pozzolans and silica fume	35

TABLE 3: Approximate mixing water and target air content requirements for different slumps and nominal maximum sizes of aggregate “Table 3 is reproduced from Kosmatka et al. [39] (under the creative commons attribution license/public domain).”

Slump (mm) or air content	Water, kilograms per cubic meter of concrete, for indicated sizes of aggregate (kg/m <sup>3</sup> )							
	9.5 mm	12.5 mm	19 mm	25 mm	37.5 mm	50 mm	75 mm	150 mm
	Non-air-entrained concrete							
25 to 50	207	199	190	179	166	154	130	113
75 to 100	228	216	205	193	181	169	145	124
150 to 175	243	228	216	202	190	178	160	–
Approximate amount of entrapped air in non-air-entrained concrete (%)	3	2.5	2	1.5	1	0.5	0.3	0.2
	Air-entrained concrete							
25 to 50	181	175	168	160	150	142	122	107
75 to 100	202	193	184	175	165	157	133	119
150 to 175	216	205	197	184	174	166	154	–
Recommended average total air content, percent, for level of exposure:								
Mild exposure	4.5	4.0	3.5	3.0	2.5	2.0	1.5	1.0
Moderate exposure	6.0	5.5	5.0	4.5	4.5	4.0	3.5	3.0
Severe exposure	7.5	7.0	6.0	6.0	5.5	5.0	4.5	4.0

TABLE 4: Bulk volume of coarse aggregate per unit volume of concrete “Table 4 is reproduced from Kosmatka et al. [39] (under the creative commons attribution license/public domain).”

Nominal maximum size of aggregate (mm)	Bulk volume of dry-rodded coarse aggregate per unit volume of concrete for different fineness moduli of fine aggregate			
	2.40	2.60	2.80	3.00
9.5	0.50	0.48	0.46	0.44
12.5	0.59	0.57	0.55	0.53
19	0.66	0.64	0.62	0.60
25	0.71	0.69	0.67	0.65
37.5	0.75	0.73	0.71	0.69
50	0.78	0.76	0.74	0.72
75	0.82	0.80	0.78	0.76
150	0.87	0.80	0.83	0.81

TABLE 5: Relationship between water to cementitious material ratio and compressive strength of concrete “Table 5 is reproduced from Kosmatka et al. [39] (under the creative commons attribution license/public domain).”

Compressive strength at 28 days (MPa)	Water-cementitious materials ratio (by mass)	
	Non-air-entrained concrete	Air-entrained concrete
45	0.38	0.30
40	0.42	0.34
35	0.47	0.39
30	0.54	0.45
25	0.61	0.52
20	0.69	0.60
15	0.79	0.70

TABLE 6: Maximum water-cementitious material ratios and minimum design strengths for various exposure conditions “Table 6 is reproduced from Kosmatka et al. [39] (under the creative commons attribution license/public domain).”

Exposure condition	Maximum water-cementitious material ratio by mass for concrete	Minimum design compressive strength, $f'_c$ (Mpa)
Concrete protected from exposure to freezing and thawing, application of deicing chemicals, or aggressive substances	Select water-cementitious material ratio on basis of strength, workability, and finishing needs	Select strength based on structural requirements
Concrete intended to have low permeability when exposed to water	0.50	28
Concrete exposed to freezing and thawing in a moist condition or deicers	0.45	31
For corrosion protection for reinforced concrete exposed to chlorides from deicing salts, salt water, brackish water, sea water, or spray from these sources	0.40	35

TABLE 7: Recommended slumps for various types of construction “Table 7 is reproduced from Kosmatka et al. [39] (under the creative commons attribution license/public domain).”

Concrete construction	Slump (mm)	
	Maximum	Minimum
Reinforced foundation walls and footings	75	25
Plain footings, caissons, and substructure walls	75	25
Beams and reinforced walls	100	25
Building columns	100	25
Pavements and slabs	75	25
Mass concrete	75	25

TABLE 8: Requirements for concrete exposed to sulfates in soil or water “Table 8 is reproduced from Kosmatka et al. [39] (under the creative commons attribution license/public domain).”

Sulfate exposure	Water-soluble sulfate ( $\text{SO}_4$ ) in soil, percent by mass	Sulfate ( $\text{SO}_4$ ) in water, ppm	Cement type	Maximum water-cementitious material ratio, by mass	Minimum design compressive strength, $f'_c$ (MPa)
Negligible	Less than 0.10	Less than 150	No special type required	–	–
Moderate	0.10 to 0.20	150 to 1500	II, MS, IP(MS), IS(MS), P (MS), I(PM) (MS), I(SM) (MS)	0.50	28
Severe	0.20 to 2.00	1500 to 10,000	V, HS	0.45	31
Very severe	Over 2.00	Over 10,000	V, HS	0.40	35

$$\text{if } \text{dis}_{p,i} = \sqrt{(f'_{c,p} - \bar{f}'_{c,i})^2 + (S_p - \bar{S}_i)^2} \leq 5.10$$

$$\text{then class}_p = i (i = 1, 2, \dots, 12), \quad (16)$$

$$\text{else class}_p = \text{null},$$

where  $f'_{c,p}$  and  $S_p$  are the compressive strength and slump of the  $p$ th instance in the dataset, respectively;  $\bar{f}'_{c,i}$  and  $\bar{S}_i$  are the mean (designed) compressive strength and mean (designed) slump of the  $i$ th class, respectively;  $d_{p,i}$  is the Euclidean distance between the vector associate to the  $p$ th instance in the dataset,  $\mathbf{y}_p = (f'_{c,p}, S_p)$ , and mean vector of class  $i$ ,  $\bar{\mathbf{y}}_i = (\bar{f}'_{c,i}, \bar{S}_i)$ ; and  $\text{class}_p$  is the class the  $p$ th instance in the database belongs to.

The second stage is the classification of dataset according to pozzolanic admixtures replacement rate. Pozzolanic admixtures can be used as a partial replacement of cement in

concrete. The pozzolanic admixtures used in this study are fly ash and ground granulated blast furnace slag. Pozzolanic admixture replacement rate,  $R_{PA}$ , is expressed as follows:

$$R_{PA} = \frac{PA}{PA + \text{cement}} \times 100\%, \quad (17)$$

where PA is pozzolanic admixtures. Each class in the first stage is divided into five smaller classes. The class intervals of  $R_{PA}$  are 0–≤10%, >10%–≤20%, >20%–≤30%, >30%–≤40%, and >40%–≤50%.

The third stage is the classification of dataset according to the cost of pozzolanic concrete. Each class in the second stage is divided into six smaller classes. The class intervals of the cost of pozzolanic concrete are 0 (NTD/m<sup>3</sup>)–≤2000 (NTD/m<sup>3</sup>), >2000 (NTD/m<sup>3</sup>)–≤2250 (NTD/m<sup>3</sup>), >2250 (NTD/m<sup>3</sup>)–≤2500 (NTD/m<sup>3</sup>), >2500 (NTD/m<sup>3</sup>)–≤2750 (NTD/m<sup>3</sup>), >2750 (NTD/m<sup>3</sup>)–≤3000 (NTD/m<sup>3</sup>), and >3000

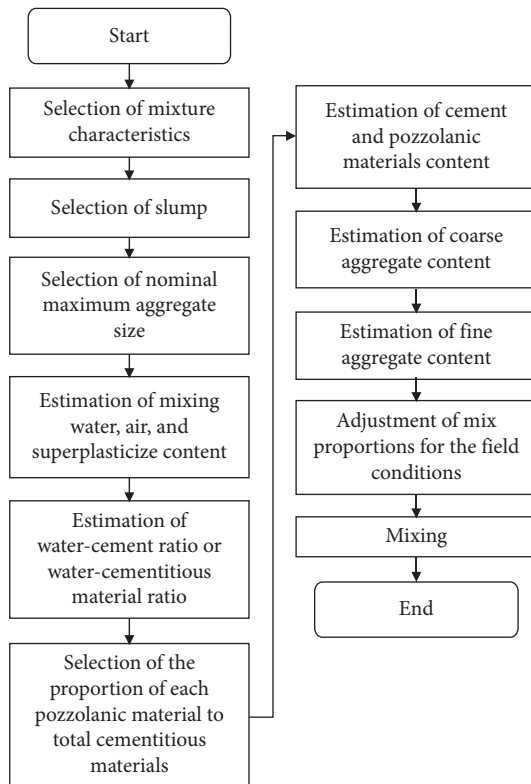


FIGURE 3: The flow chart of ACI mix design method.

(NTD/m<sup>3</sup>). There are 360 classes overall in the dataset of pozzolanic concrete mixture proportioning.

## 4. Results and Discussion

### 4.1. ANN-Based Compressive Strength Prediction

Model: CSPNN

**4.1.1. Training and Testing of the CSPNN Using Collected Experimental Data.** All 482 samples collected were used to train and test the CSPNN. Among the 482 samples, 462 and 20 samples were used to train and test CSPNN, respectively. Here, the CSPNN is constructed with seven, fourteen, and one nodes in input layer, hidden layer, and output layer, respectively, and denoted as CSPNN(7-14-1). The complete offline training process took 47 cycles. The  $E$  and  $R^2$  were 0.005988 and 0.92556, respectively. After the CSPNN was trained on the 462 training samples, it was tested to observe how accurately it would predict compression strength of other samples. Table 9 and Figure 4 summarize the results of these tests, indicating that the CSPNN can satisfactorily predict the compression strength in all 20 testing samples.

**4.1.2. Sensitivity Analysis of the CSPNN.** Figure 5 shows the distribution of compressive strength and water for the training samples of the CSPNN. It shows that compressive strength decreases with increasing amounts of water in the concrete mixture. Compressive strength is inversely proportional to water content, and the slope of the fitted simple

TABLE 9: Comparison of exact compressive strength with CSPNN-predicted compressive strength for the 20 testing samples.

No. of sample	Exact compressive strength ( $f'_{c,e}$ ) (MPa)	Predicted compressive strength ( $f'_{c,CSPNN}$ ) (MPa)	$f'_{c,e} - f'_{c,CSPNN}$ (MPa)
1	57.67	54.93	2.74
2	67.06	58.74	8.32
3	54.90	51.92	2.98
4	41.67	41.12	0.54
5	57.45	58.72	-1.27
6	51.08	52.51	-1.43
7	60.70	62.97	-2.27
8	44.70	38.17	6.53
9	24.20	16.85	7.35
10	46.14	54.93	-8.79
11	44.62	40.39	4.23
12	40.80	44.19	-3.39
13	25.00	30.28	-5.28
14	57.00	59.32	-2.32
15	77.00	70.62	6.38
16	69.00	65.30	3.70
17	64.00	57.01	6.99
18	84.30	85.01	-0.71
19	78.10	75.91	2.19
20	59.00	59.52	-0.52

regression line is  $-0.123$ . Figure 6 shows the distribution of water and the first-order partial derivative of compressive strength with respect to water for the training samples of the CSPNN, and its mean is  $-0.092$ . The negative mean value of the first-order partial derivative of compressive strength with respect to water indicates a negative correlation between compressive strength and water, which is consistent with the negative slope value of the fitted simple regression line in Figure 5.

Figure 7 shows the distribution of compressive strength and cement for the CSPNN training samples. It shows that compressive strength increases with an increase in the amount of cement in the concrete mixture. Compressive strength is proportional to cement, and the slope of the fitted simple regression line is 0.0764. Figure 8 shows the distribution of cement and the first-order partial derivative of compressive strength with respect to cement for the CSPNN training samples, where the mean is found to be 0.037. The positive mean value of the first-order partial derivative of compressive strength with respect to cement indicates a positive correlation between compressive strength and cement, which is consistent with the positive slope value of the fitted simple regression line in Figure 7.

Figure 9 shows a similar distribution of compressive strength and SP for the CSPNN training samples. Compressive strength increases with an increase in the amount of SP in the concrete mixture. Compressive strength is proportional to SP, and the slope of the fitted simple regression line is 1.6298. Figure 10 shows the distribution of SP and the first-order partial derivative of compressive strength with respect to SP for the CSPNN training samples. The mean of the first-order partial derivative of compressive strength

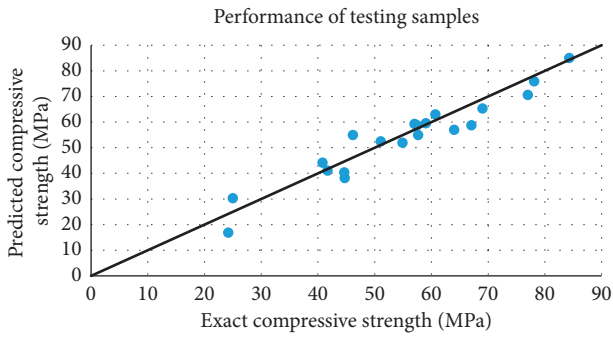


FIGURE 4: Performance of the 20 testing compressive strength samples.

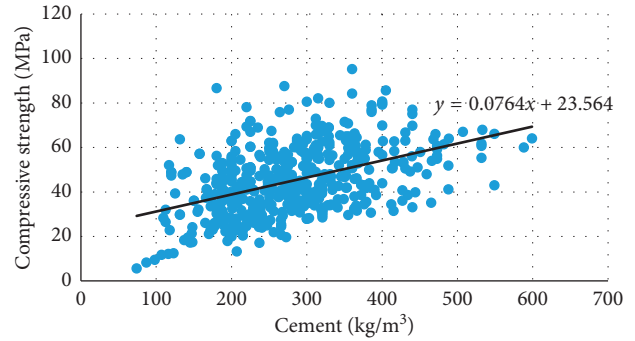


FIGURE 7: Distribution of compressive strength and cement for the training samples of the CSPNN.

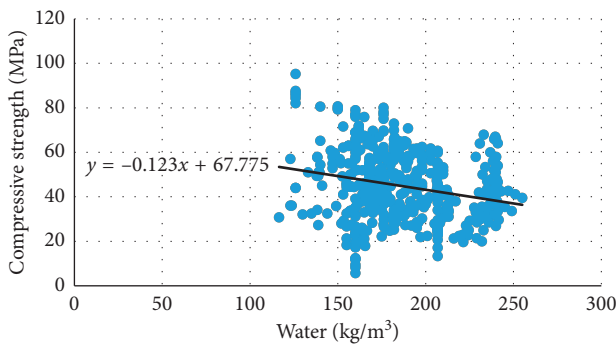


FIGURE 5: Distribution of compressive strength and water for the training samples of the CSPNN.

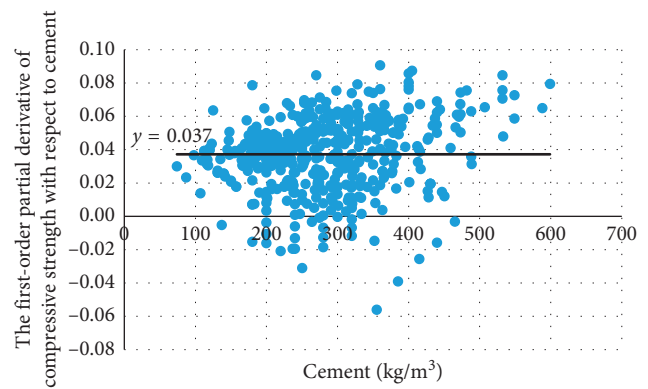


FIGURE 8: Distribution of cement and the first-order partial derivative of compressive strength with respect to cement for the training samples of the CSPNN.

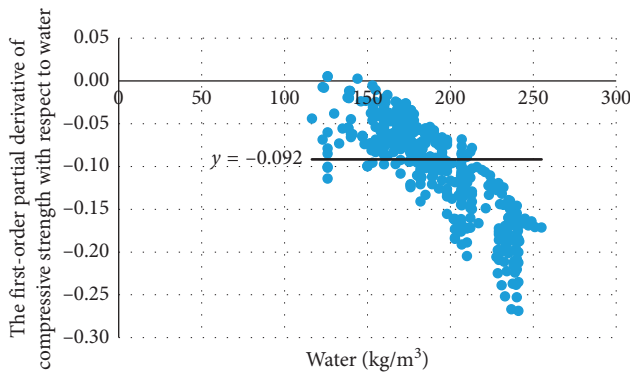


FIGURE 6: Distribution of water and the first-order partial derivative of compressive strength with respect to water for the training samples of the CSPNN.

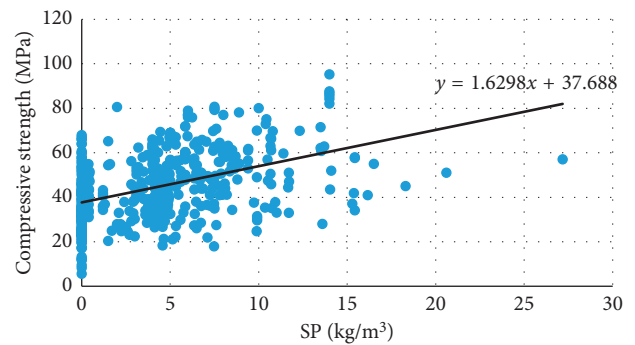


FIGURE 9: Distribution of compressive strength and SP for the training samples of the CSPNN.

with respect to SP for the training samples of the CSPNN is 0.087. The positive mean value of the first-order partial derivative of compressive strength with respect to SP indicates positive correlation between compressive strength and SP, which is again consistent with the positive slope value of the fitted simple regression line in Figure 9. Sensitivity analysis results of the CSPNN therefore indicate that the CSPNN is a reasonable model representing the relationship between the 7 input parameters and compressive strength.

#### 4.2. ANN-Based Slump Prediction Model: SPNN

4.2.1. *Training and Testing of the SPNN Using Collected Experimental Data.* As mentioned, only 295 samples have slump data among the total of 482 collected samples. Therefore, 295 samples were used to train and test the SPNN. Among the 295 samples, 285 and 10 samples were used to train and test SPNN, respectively. Here, the SPNN is constructed with seven, six, and one nodes in the input layer,

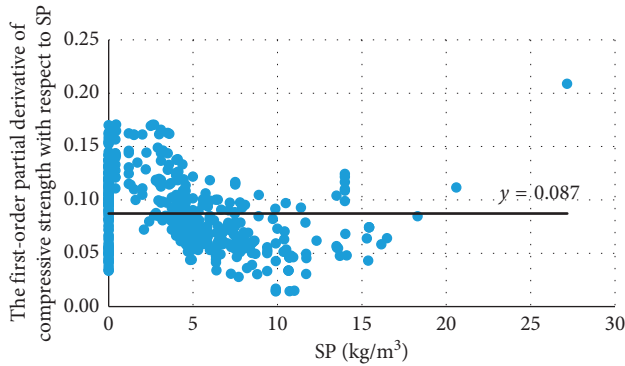


FIGURE 10: Distribution of SP and the first-order partial derivative of compressive strength with respect to SP for the training samples of the CSPNN.

hidden layer, and output layer, respectively, and is denoted as

TABLE 10: Comparison of exact slump with SPNN-predicted slump for the 10 testing samples.

No. of sample	Exact slump ( $S_e$ ) (cm)	Predicted slump ( $S_p$ ) (cm)	$S_e - S_p$ (cm)
1	23.0	19.9	3.1
2	20.0	17.6	2.4
3	23.5	24.6	-1.1
4	27.0	27.2	-0.2
5	13.5	16.1	-2.6
6	11.5	11.5	0.0
7	22.0	22.4	-0.4
8	26.5	25.9	0.6
9	26.0	22.8	3.2
10	19.0	21.1	-2.1

SPNN(7-6-1). The complete offline training process took 31 cycles. The  $E$  and  $R^2$  were 0.0079527 and 0.93996, respectively. After the SPNN was trained on the 285 training samples, it was tested to observe how accurately it would predict slump of other samples. Table 10 and Figure 11 summarize the results of these tests, indicating that the SPNN can satisfactorily predict the slump in all 10 testing samples.

4.2.2. *Sensitivity Analysis of the SPNN.* Figure 12 shows the distribution of slump and SP for the training samples of the SPNN. It shows that slump increases with an increase in the amount of SP in the concrete mixture. Slump is proportional to SP, and the slope of the fitted simple regression line is 0.6246. Figure 13 shows the distribution of SP and the first-order partial derivative of slump with respect to SP for the SPNN training samples. The mean of the first-order partial derivative of slump with respect to SP for the training samples of the SPNN is  $-0.146$ . The negative mean value of the first-order partial derivative of slump with respect to SP indicates negative correlation between slump and SP, which is inconsistent with the positive slope value of the fitted simple regression line in Figure 12. The reason may be that SP is a material with larger variance, and the properties of different brands of SP are different.

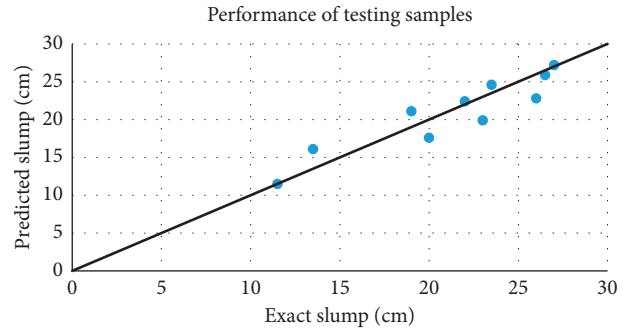


FIGURE 11: Performance of the 10 testing slump samples.

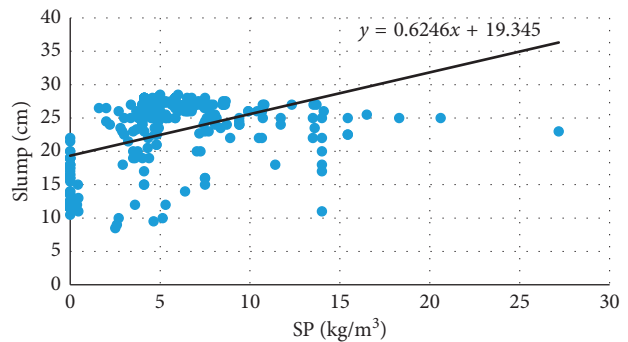


FIGURE 12: Distribution of slump and SP for the training samples of the SPNN.

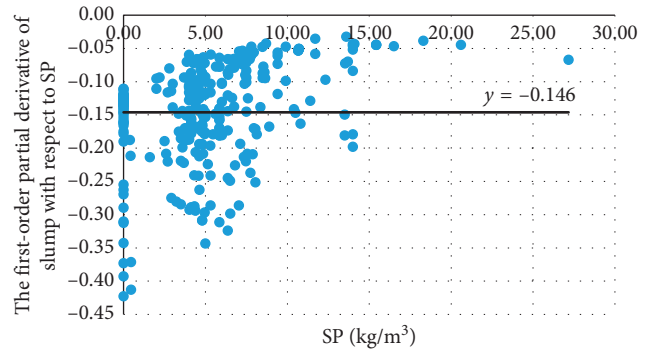


FIGURE 13: Distribution of SP and the first-order partial derivative of slump with respect to SP for the training samples of the SPNN.

4.3. *Experimental Program.* Experimental specimens were also made in the laboratory to study the prediction accuracy of the CSPNN and SPNN in terms of pozzolanic concrete conforming to the ACI concrete mixture code. Twelve concrete mixtures (listed in Table 11) were generated randomly by computer program according to the concrete mixture in ACI code. Four experimental specimens were made for each concrete mixture.

4.3.1. *Prediction of Compressive Strength.* Figure 14 shows a comparison of exact compressive strength to CSPNN-

TABLE 11: Twelve experimental concrete mixtures and their exact and predicted compressive strength and slump.

No. of concrete mix	Water (kg/m <sup>3</sup> )	Cement (kg/m <sup>3</sup> )	Fly ash (kg/m <sup>3</sup> )	GGBFS (kg/m <sup>3</sup> )	CA (kg/m <sup>3</sup> )	FA (kg/m <sup>3</sup> )	SP (kg/m <sup>3</sup> )	Exact compressive strength ( $f'_{c,e}$ ) (MPa)	Predicted compressive strength ( $f'_{c,CSPNN}$ ) (MPa)	$f'_{c,e} - f'_{c,CSPNN}$ (MPa)	Exact slump ( $S_e$ ) (cm)	Predicted slump ( $S_{SPNN}$ ) (cm)	$S_e - S_{SPNN}$ (cm)
1	194	223	72	76	1040	669	0.74	44.10	34.32	9.77	19.0	19.0	0.0
2	184	244	19	105	1104	649	0.79	47.99	32.26	15.73	20.0	18.5	1.5
3	187	194	22	171	1072	650	0.81	49.75	34.85	14.90	20.0	19.0	1.0
4	189	272	14	121	1040	670	0.70	52.87	35.60	17.27	20.0	19.2	0.8
5	191	346	41	38	1136	549	0.73	46.70	45.96	0.74	20.0	16.9	3.1
6	189	261	57	93	1072	619	0.88	47.06	39.04	8.02	20.0	18.7	1.3
7	204	331	54	99	1136	457	0.77	54.52	54.55	-0.03	18.0	14.1	3.9
8	191	280	46	121	1104	555	0.68	47.61	50.16	-2.55	19.5	17.2	2.3
9	210	300	51	131	1040	535	0.54	46.06	52.05	-5.99	20.5	16.7	3.8
10	207	430	61	20	960	604	0.76	54.30	40.08	14.22	21.0	19.1	1.9
11	190	329	52	112	1104	516	0.87	54.98	55.07	-0.09	19.0	17.2	1.8
12	208	351	121	52	960	554	0.72	55.13	40.91	14.22	21.5	14.1	7.4

predicted compressive strength for the 12 experimental concrete mixtures. The compressive strength of each concrete mixture is the average compressive strength of the four specimens for each concrete mixture. Most exact compressive strength values are larger than the CSPNN-predicted compressive strength values. Possible reasons may be that (1) coarse aggregates were crushed by machine; thus, the edges of coarse aggregates are sharp, producing a good interlocking effect which increases compressive strength or that (2) experimental specimens were kept submerged in lime water, and the fine weather and relative humidity was sufficient during the curing period to cause the concrete hydration to occur more quickly such that the late compressive strength was reached early. Although some predicted errors of compressive strength are large, it is still acceptable.

**4.3.2. Prediction of Slump.** Figure 15 shows a comparison of exact slump to SPNN-predicted slump for the 12 experimental concrete mixtures. The slump of each concrete mix is the average slump of the four specimens for each concrete mixture. Most predicted errors for slump are within the allowable data range for width of slump (3.8 cm), with only one being extreme (7.4 cm). The predicted error of slump may be mainly caused by SP, since SP is a material with larger variance and the properties of different brands of SP are different. Notably, CSPNN and SPNN were trained using experimental data of pozzolanic concrete mixture proportioning collected from the literature. It is believed that predicted error of compressive strength and slump can be largely decreased if a sufficient number of experimental specimens could be made and used for training of CSPNN and SPNN.

The trained and tested CSPNN and SPNN represent accurate models for compressive strength and slump, respectively, and they were used to predict compressive strength and slump of experimental and numerical data. Among 1500 experimental and numerical data, 278 data satisfy Equation (14) and they were kept in the dataset.

**4.4. Classification of Pozzolanic Concrete Mixture Proportioning.** After establishing the dataset of pozzolanic concrete mixture proportioning, it was classified further according to compressive strength, pozzolanic admixture replacement rate, and cost of concrete. Tables 12 and 13 give some of the results. Table 12 lists concrete mixture proportioning samples for compressive strength = 210 kgf/cm<sup>2</sup> and cost ≤ 2000 NTD/m<sup>3</sup>. Table 13 lists concrete mixture proportioning samples for compressive strength = 700 kgf/cm<sup>2</sup> and 2000 NTD/m<sup>3</sup> ≤ cost ≤ 2250 NTD/m<sup>3</sup>. Engineers can utilize the classified dataset to easily predict mix proportioning (solution) from required compressive strength of concrete, pozzolanic admixture replacement rate, and cost of concrete.

## 5. Conclusions

This study develops a two-step computer-aided approach for pozzolanic concrete mix design. The first step is to establish a dataset of pozzolanic concrete mixture proportioning that conforms to ACI code. In this step, ANNs are employed to

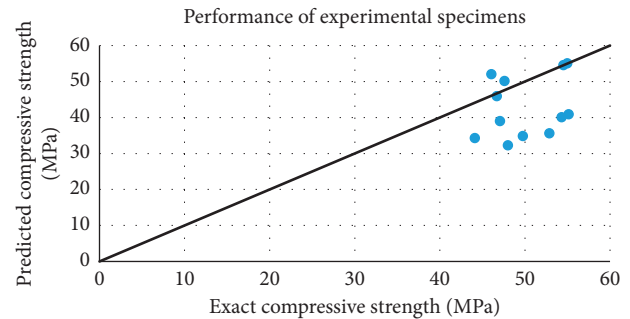


FIGURE 14: Comparison of exact compressive strength with CSPNN-predicted compressive strength for the 12 experimental concrete mixtures.

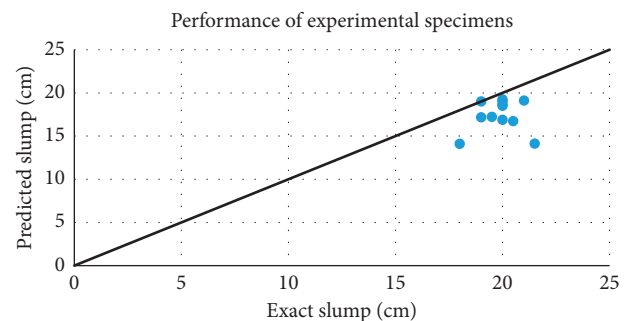


FIGURE 15: Comparison of exact slump with SPNN-predicted slump for the 12 experimental concrete mixtures.

establish the prediction models of compressive strength and slump of concrete. The second step is to classify the dataset of pozzolanic concrete mixture proportioning. A classification method is utilized to categorize the dataset into 360 classes based on compressive strength of concrete, pozzolanic admixture replacement rate, and material cost. The following important conclusions are drawn from the results:

- (1) The CSPNN and SPNN were trained using a portion of collected experimental data. After training, the CSPNN and SPNN were tested using the rest of collected experimental data and data of experimental specimens made in our laboratory for twelve different mixtures. Results prove that CSPNN and SPNN can satisfactorily predict compressive strength and slump, respectively, from respective amounts of water, cement, ground granulated blast furnace slag, fly ash, coarse aggregate, fine aggregate, and superplasticizer.
- (2) Sensitivity analysis of the ANN can be used to explore the cause and effect relationship between network input and output. Therefore, sensitivity analysis of the CSPNN and SPNN, respectively, can be used to evaluate the effect of various concrete mix constituents (water, cement, ground granulated blast furnace slag, fly ash, coarse aggregate, fine aggregate, and superplasticizer) on the compressive strength and slump of concrete.

TABLE 12: Concrete mixture proportioning samples for compressive strength = 210 kg/cm<sup>2</sup> and cost ≤ 2000 NTD/m<sup>3</sup>.

Water-binder ratio	Water (kg/m <sup>3</sup> )	Cement (kg/m <sup>3</sup> )	Fly ash (kg/m <sup>3</sup> )	GGBFS (kg/m <sup>3</sup> )	CA (kg/m <sup>3</sup> )	FA (kg/m <sup>3</sup> )	SP (kg/m <sup>3</sup> )	$f'_{c,CSPNN}$ (MPa)	$S_{SPNN}$ (cm)	Cost (NTD/m <sup>3</sup> )	$R_{PA}$ (%)
0.55	199	337	20	6	704	991	0.74	23.80	20.4	1952	7.16
0.55	192	244	65	41	1024	703	2.26	23.45	23.0	1858	30.29
0.48	177	221	39	106	1136	629	3.58	21.55	22.9	1971	39.62
0.52	186	195	72	92	1056	671	2.67	23.87	23.3	1826	45.68

TABLE 13: Concrete mixture proportioning samples for compressive strength = 700 kg/cm<sup>2</sup> and 2000 NTD/m<sup>3</sup> < cost ≤ 2250 NTD/m<sup>3</sup>.

Water-binder ratio	Water (kg/m <sup>3</sup> )	Cement (kg/m <sup>3</sup> )	Fly ash (kg/m <sup>3</sup> )	GGBFS (kg/m <sup>3</sup> )	CA (kg/m <sup>3</sup> )	FA (kg/m <sup>3</sup> )	SP (kg/m <sup>3</sup> )	$f'_{c,CSPNN}$ (MPa)	$S_{SPNN}$ (cm)	Cost (NTD/m <sup>3</sup> )	$R_{PA}$ (%)
0.34	134	292	3	103	1104	763	2.43	71.16	22.2	2137	26.63
0.30	145	281	97	101	1056	673	0.90	71.17	22.5	2013	41.34
0.33	144	232	36	173	736	1009	3.56	68.25	23.4	2127	47.39
0.32	157	253	3	239	1056	648	0.73	65.67	21.5	2065	48.89
0.28	175	322	131	183	944	542	1.46	69.62	18.0	2213	49.37

- (3) The distribution of slump and SP for the training samples of the SPNN shows that slump increases with an increase in the amount of SP in the concrete mixture. Slump is proportional to SP, and the slope of the fitted simple regression line is a positive value (0.6246). However, the mean of the first-order partial derivative of slump with respect to SP for the training samples of the SPNN is a negative value (−0.146). The negative mean value of the first-order partial derivative of slump with respect to SP indicates negative correlation between slump and SP, which is inconsistent with the positive slope value of the fitted simple regression line. The reason for this may be that SP is a material with larger variance and the properties of different brands of SP are different.
- (4) To construct a dataset of pozzolanic concrete mixture proportioning which is practical and convenient for engineering applications, it is classified further. Engineers can utilize the classified dataset to easily predict mix proportioning from required compressive strength of concrete, pozzolanic admixture replacement rate, and the necessary cost of concrete.

## Abbreviations

AAN:	Artificial neural network
ACI:	American Concrete Institute
BFGS method:	Broyden–Fletcher–Goldfarb–Shanno method
BP network:	Back-propagation network
CA:	Coarse aggregate
class <sub><i>p</i></sub> :	The class the <i>p</i> th instance in the database belongs to
CSPNN:	Compressive strength prediction neural network
<i>d</i> :	Search direction
$D_{ki}^1$ :	The first-order partial derivative of the <i>k</i> th output with respect to <i>i</i> th input
$\bar{D}_{ki}^1$ :	The mean of $D_{ki}^1$

$d_{pk}$ :	The desired output of the <i>k</i> th output node for the <i>p</i> th instance
dis( <b>a</b> , <b>b</b> ):	The Euclidean distance between two vectors (points) <b>a</b> and <b>b</b>
dis <sub><i>p,i</i></sub> :	The Euclidean distance between the vector associate to the <i>p</i> th instance in the dataset
<i>E</i> :	Mean square error
<i>f</i> :	The activation function
FA:	Fine aggregate
$f'_i$ :	Compressive strength
$f'_{c,CSPNN}$ :	Compressive strength predicted by CSPNN
$\bar{f}'_{c,i}$ :	Mean (designed) compressive strength of the <i>i</i> th class
$f'_{c,p}$ :	Compressive strength of the <i>p</i> th instance in the dataset
GGBFS:	Ground granulated blast furnace slag
<b>H</b> :	The inverse Hessian matrix
$H_{nj}$ :	The output of the <i>j</i> th node in the <i>n</i> th hidden layer
L-BFGS learning algorithm:	Limited memory Broyden–Fletcher–Goldfarb–Shanno
$O_i$ :	The output of <i>i</i> th node
$o_{pk}$ :	The calculated output of the <i>k</i> th output node for the <i>p</i> th instance
<i>P</i> :	The number of instances in the training set
PA:	Pozzolanic admixtures
$R^2$ :	The absolute fraction of variance
$R_{PA}$ :	Admixture replacement rate
<i>S</i> :	Slump
$\bar{S}_i$ :	The mean (designed) slump of the <i>i</i> th class
$S_p$ :	The slump of the <i>p</i> th instance in the dataset
$S_{SPNN}$ :	Slump predicted by SPNN
SP:	Superplasticizer
SPNN:	Slump prediction neural network

SSE:	Sum of the squares error
$W_{hmj,ok}$ :	The weight associated with the $j$ th node in the $n$ th hidden layer to the $k$ th node in the output layer
$W_{hmjn,ok}$ :	The weight associated with the $j$ th node in the $n$ th hidden layer to the $k$ th node in the output layer
$W_{ij}$ :	The weight associated with the $i$ th node in the preceding layer to the $j$ th node in the current layer
$W_{xi,h1,j1}$ :	The weight associated with the $i$ th node in the input layer to the $j$ th node in the first hidden layer
$\theta_j$ :	The threshold value of node $j$ in the current layer
$\theta_{ok}$ :	The threshold value of the $k$ th node in the output layer
$\eta$ :	Learning ratio
$\alpha$ :	Step length.

## Data Availability

The data used to support the findings of this study are available from the corresponding author upon request.

## Conflicts of Interest

The authors declare that they have no conflicts of interest.

## References

- [1] N. Bouzoubaa, B. Fournier, V. M. Malhotra, and D. Golden, "Mechanical properties and durability of concrete made with high volume fly ash blended cement produced in cement plant," *ACI Materials Journal*, vol. 99, no. 6, pp. 560–567, 2002.
- [2] M. Mazloom, A. A. Ramezani-pour, and J. J. Brooks, "Effect of silica fume on mechanical properties of high strength concrete," *Cement and Concrete Composites*, vol. 26, no. 4, pp. 347–357, 2004.
- [3] K. Tan and X. Pu, "Strengthening effects of finely ground fly ash, granulated blast furnace slag, and their combination," *Cement and Concrete Research*, vol. 28, no. 12, pp. 1819–1825, 1998.
- [4] C. Ozyildirim and W. J. Halstead, "Improved concrete quality with combination of silica fume and fly ash," *ACI Materials Journal*, vol. 91, no. 6, pp. 587–594, 1994.
- [5] I. Papayianni, G. Tsohos, N. Oikonomou, and P. Mavria, "Influence of superplasticizer type and mix design parameters on the performance of them in concrete mixtures," *Cement and Concrete Composites*, vol. 27, no. 2, pp. 217–222, 2005.
- [6] D. A. Abrams, *Design of concrete mixtures. Bulletin No. 1*, Structural Materials Laboratory, Lewis Institute, Chicago, IL, USA, 1918.
- [7] S. Popovics, "Analysis of concrete strength versus water-cement ratio relationship," *ACI Materials Journal*, vol. 87, no. 5, pp. 517–529, 1990.
- [8] F. De Larrard and M. Buil, "Granularité et compacité dans les matériaux de génie civil," *Materials and Structures*, vol. 20, no. 2, pp. 117–126, 1987.
- [9] H. Adeli and S. L. Hung, *Machine Learning: Neural Networks, Genetic Algorithms, and Fuzzy Systems*, Wiley, New York, NY, USA, 1995.
- [10] J. Suykens, J. Vandewalle, and J. De Moor, *Artificial Neural Networks for Modeling and Control of Non-Linear Systems*, Kluwer Academic Publishers, Boston, MA, USA, 1996.
- [11] D. E. Rumelhart, G. E. Hinton, and R. J. Williams, "Learning international representation by error propagation," in *Parallel Distributed Processing*, D. E. Rumelhart, J. L. McClelland, and The PDP Research Group, Eds., pp. 318–362, The MIT Press, Cambridge, MA, USA, 1986.
- [12] I. C. Yeh, "Analysis of strength of concrete using design of experiments and neural networks," *Journal of Materials in Civil Engineering*, vol. 18, no. 4, pp. 597–604, 2006.
- [13] I. C. Yeh, "Modeling of strength of high-performance concrete using artificial neural networks," *Cement and Concrete Research*, vol. 28, no. 12, pp. 1797–1808, 1998.
- [14] J. Kasperkiewicz, J. Racz, and A. Dubrawski, "HPC strength prediction using ANN," *Journal of Computing in Civil Engineering*, vol. 9, no. 4, pp. 279–284, 1995.
- [15] S. C. Lee, "Prediction of concrete strength using artificial neural networks," *Engineering Structures*, vol. 25, no. 7, pp. 849–857, 2003.
- [16] J. Bai, S. Wild, J. A. Ware, and B. B. Sabir, "Using neural networks to predict workability of concrete incorporating metakaolin and fly ash," *Advances in Engineering Software*, vol. 34, no. 11–12, pp. 663–669, 2003.
- [17] Z. H. Duan, S. C. Kou, and C. S. Poon, "Prediction of compressive strength of recycled aggregate concrete using artificial neural networks," *Construction and Building Materials*, vol. 40, pp. 1200–1206, 2013.
- [18] G. H. Ni and J. Z. Wang, "Prediction of compressive strength of concrete by neural networks," *Cement and Concrete Research*, vol. 30, no. 8, pp. 1245–1250, 2000.
- [19] S. L. Hung and Y. L. Lin, "Application of an L-BFGS neural network learning algorithm in engineering analysis and design," in *Second National Conference on Structural Engineering*, pp. 221–230, Chinese Society of Structural Engineering, Nantou, Taiwan, 1994.
- [20] J. Nocedal, "Updating quasi-Newton matrix with limited storage," *Mathematics of Computation*, vol. 35, no. 151, p. 773, 1980.
- [21] T. F. Coleman and Y. Li, *Large-Scale Numerical Optimization*, Society for Industrial and Applied Mathematics, Philadelphia, PA, USA, 1990.
- [22] G. Cybenko, "Approximations by superpositions of a sigmoidal function," *Mathematics of Control, Signals, and Systems*, vol. 2, no. 4, pp. 303–314, 1989.
- [23] K. Funahashi, "On the approximate realization of continuous mappings by neural networks," *Neural Networks*, vol. 2, no. 3, pp. 183–192, 1989.
- [24] S. L. Hung and C. Y. Kao, "Structural damage detection using the optimal weights of the approximating artificial neural networks," *Earthquake Engineering and Structural Dynamics*, vol. 31, no. 2, pp. 217–234, 2002.
- [25] C. Y. Kao and S. L. Hung, "Detection of structural damage via free vibration responses generated by approximating artificial neural networks," *Computers and Structures*, vol. 81, no. 29, pp. 2631–2644, 2003.
- [26] I. C. Yeh and H. B. Zhang, "Comparisons of mixture design of experiments for high performance concrete," *Journal of Technology*, vol. 22, pp. 179–185, 2007.

- [27] A. S. Cheng, "Research on the microstructure and strength prediction of pozzolanic concrete," Dissertation, National Chung Hsing University, 2011.
- [28] M. Nehdi, M. Pardhan, and S. Koshowski, "Durability of self-consolidating concrete incorporating high-volume replacement composite cements," *Cement and Concrete Research*, vol. 34, no. 11, pp. 2103–2112, 2004.
- [29] M. A. Megat Johari, J. J. Brooks, S. Kabir, and P. Rivard, "Influence of supplementary cementitious materials on engineering properties of high strength concrete," *Construction and Building Materials*, vol. 25, no. 5, pp. 2639–2648, 2011.
- [30] N. Su, K. C. Hsu, and H. W. Chai, "A simple mix design method for self-compacting concrete," *Cement and Concrete Research*, vol. 31, no. 12, pp. 1799–1807, 2001.
- [31] E. Güneysi, M. Gesoglu, and E. Özbay, "Evaluating and forecasting the initial and final setting times of self-compacting concretes containing mineral admixtures by neural network," *Materials and Structures*, vol. 42, no. 4, pp. 469–484, 2009.
- [32] R. Siddique, "Properties of self-compacting concrete containing class F fly ash," *Materials and Design*, vol. 32, no. 3, pp. 1501–1507, 2011.
- [33] A. Oner, S. Akyuz, and R. Yildiz, "An experimental study on strength development of concrete containing fly ash and optimum usage of fly ash in concrete," *Cement and Concrete Research*, vol. 35, no. 6, pp. 1165–1171, 2005.
- [34] R. Siddique, "Performance characteristics of high-volume class F fly ash concrete," *Cement and Concrete Research*, vol. 34, no. 3, pp. 487–493, 2004.
- [35] G. Li and X. Zhao, "Properties of concrete incorporating fly ash and ground granulated blast-furnace slag," *Cement and Concrete Composites*, vol. 25, no. 3, pp. 293–299, 2003.
- [36] G. Li, "Properties of high-volume fly ash concrete incorporating nano-SiO<sub>2</sub>," *Cement and Concrete Research*, vol. 34, no. 6, pp. 1043–1049, 2004.
- [37] A. A. Ramezani-pour and V. M. Malhotra, "Effect of curing on the compressive strength, resistance to chloride ion penetration and porosity of concretes incorporating slag, fly ash or silica fume," *Cement and Concrete Composites*, vol. 17, no. 2, pp. 125–133, 1995.
- [38] M. C. Li, "A study on rational mix proportion and vibration characteristics of high flowing concrete," Dissertation, National Taiwan University, 2010.
- [39] S. H. Kosmatka, B. Kerkhoff, and W. C. Panarese, *Design and Control of Concrete Mixtures, Engineering Bulletin; 001*, Portland Cement Association, Skokie, IL, USA, 14th edition, 2002.
- [40] Public Construction Commission, "Chapter 03050: general requirements of concrete basic materials and construction," in *Construction Outline Code for Public Construction*, Public Construction Commission, Taipei, Taiwan, 2010.
- [41] A. C. Rencher, *Methods of Multivariate Analysis*, Wiley, New York, NY, USA, 2003.

## Research Article

# Fast Local Laplacian-Based Steerable and Sobel Filters Integrated with Adaptive Boosting Classification Tree for Automatic Recognition of Asphalt Pavement Cracks

Nhat-Duc Hoang  and Quoc-Lam Nguyen

*Faculty of Civil Engineering, Institute of Research and Development, Duy Tan University, R. 809–No. 03 Quang Trung, Da Nang 550000, Vietnam*

Correspondence should be addressed to Nhat-Duc Hoang; [hoangnhatduc@dtu.edu.vn](mailto:hoangnhatduc@dtu.edu.vn)

Received 15 June 2018; Revised 21 August 2018; Accepted 30 August 2018; Published 24 September 2018

Academic Editor: Moacir Kripka

Copyright © 2018 Nhat-Duc Hoang and Quoc-Lam Nguyen. This is an open access article distributed under the Creative Commons Attribution License, which permits unrestricted use, distribution, and reproduction in any medium, provided the original work is properly cited.

Effective road maintenance requires adequate periodic surveys of asphalt pavement condition. The manual process of pavement assessment is labor intensive and time-consuming. This study proposes an alternative for automating the periodic surveys of pavement condition by means of image processing and machine learning. Advanced image processing techniques including fast local Laplacian filter, Sobel filter, steerable filter, and projection integral are employed for image enhancement and analysis to extract useful features from digital images. Based on the features produced by these image processing techniques, adaptive boosting classification tree is used to perform pavement crack recognition tasks. A dataset of image samples consisting of five classes (alligator crack, diagonal crack, longitudinal crack, noncrack, and transverse crack) has been collected to construct and verify the performance of the adaptive boosting classification tree. The experimental results show that the proposed approach has achieved a high crack classification accuracy which is roughly 90%. Therefore, the newly developed model is a promising alternative to help transportation agencies in pavement condition evaluation.

## 1. Introduction

To ensure the safety and the serviceability of the road network, periodic survey and assessment of the pavement condition is a crucial task done by transportation agencies around the world [1]. Based on such periodic surveys, various pavement distresses can be identified and documented. This information serves as important input information used in the task of determining pavement rehabilitation methods and allocating resources for concurrently demanding pavement maintenance projects.

Based on a recent statistics done by the Central Intelligence Agency, the total length of road networks in the world has amounted to 64,285,009 km; such length of roads demands an enormous cost for maintenance and upgrading tasks [2]. In Vietnam, according to the report of the General Statistics Office of Vietnam in 2010, the total length of

asphalted roads has reached 93,535 km [3]. Due to a large number of existing and road sections and the rapid extension of road networks per year, management and maintenance of asphalt pavements become challenging tasks.

The aging and deterioration of pavements are mainly caused by surface fatigue and shear development in the subgrade, subbase, base, or surface layers [4]. The most easily observable form of pavement deterioration is cracks. Cracks are widely considered to be the most important indicator of pavement condition because this type of distress directly affects in pavement serviceability and structural integrity [5, 6]. Therefore, timely detection of pavement cracks is necessary to evaluate the pavement surface condition and to develop appropriate mitigation measures in order to restore the acceptable quality of roads. It is noted that besides cracks, there are other forms of pavement deteriorations including

potholes (small or medium bowl-shaped depressions), depressions (depressed areas in the pavement surface), ruts (channelized depressed areas), upheaval areas, and raveling (disintegration of aggregate particles in the pavement surface). However, the detection of these forms of pavement damages is not within the scope of the current study.

In developing countries like Vietnam, the common approach of the road surface condition is visual inspection performed by human. This method is only effective for surveying a small quantity of road lengths. Nevertheless, the manual process of road inspection is notorious for its low productivity and variations in surveying outcomes due to human subjectivity [7]. Therefore, a robust method for automatic recognition of pavement cracks can help us to expedite the pavement assessment process, enhance the evaluation accuracy, and guarantee the consistency in the assessment result. Such method is currently a pressing need of transportation agencies in many countries.

Since images of pavements can provide a direct presentation of pavement defects related to cracks, two-dimensional digital images have been the subject of interest for many researchers and practitioners. It is because the pavement cracks can be identified via the image pixel intensities and the shape of the crack objects. However, recognizing cracks from digital images is by no means an easy task. This fact is due to the noisy and complex background texture of the asphalt pavement, the heterogeneous pixel intensity, and the inconsistency of the illumination condition [7].

To overcome the aforementioned challenges, a large proportion of the research works have been dedicated in developing automatic pavement crack detection models using image filtering methods. In image processing and computer vision, filtering is a popular approach specifically used to alter the presentation of images and enhance certain features of images. Mahler et al. [8], Kirschke and Velinsky [9], and Cheng et al. [10] proposed algorithms based on intensity thresholding for crack detection; these models rely on the assumption that cracks have a lower intensity value than those of the pavement background. Lee and Kim [11] proposed a simplified method for crack category realization based on the concept of crack-type index; this method relies on the image thresholding technique and information obtained from neighboring pixels to determine the state of crack and noncrack.

An improved Canny edge detection algorithm and an edge preservation filtering algorithm for pavement edge recognition had been proposed by Zhao et al. [12]. Zou et al. [13] put forward a function to measure the difference of image intensity and used this function to enhance the image thresholding outcome. Zhang et al. [14] employed a set of predesigned filters to extract cracks from the background. Salman et al. [15] and Eduardo et al. [16] have proposed automatic crack detection models based on the Gabor filter. Li et al. [17] employed two techniques of steerable matched filtering and active contour model for the task of crack detection and segmentation.

It is noted that besides image filtering methods, there are many other potential algorithms used for crack detection

investigated by various scholars; these algorithms include wavelet transform [18], beamlet transform [19], wavelet-morphology-based detection [20], weighted neighborhood segmentation [21], deep learning [2, 22–24], fuzzy Hough transform [25], probabilistic generative model [7], and optimized minimal path selection [5]. However, these aforementioned algorithms are not within the focus of the current study.

In addition, recent literature reviews show an increasing trend of combining image filtering and machine learning to develop an intelligent model capable of not only detecting cracks but also categorizing the types of cracks. Rababaah [26] carried out a comparative work which investigated the performance of multilayer perceptron neural network, genetic algorithms, and self-organizing maps in pavement crack classification. Mokhtari et al. [27] recently employed neural network models to tackle the problem of interest; this study concluded that neural network models are more capable than other learning strategies of decision tree and  $k$ -nearest neighbor. Banharnsakun [28] combined the advantage of metaheuristic and neural network for pavement surface distress detection and classification; the metaheuristic of artificial bee colony was used in the phase of image segmentation, and the subsequent classification task was performed by neural network.

Recently, an efficient approach which can perform both detection and classification of pavement cracks was proposed by Cubero-Fernandez et al. [29]; this study incorporated various image processing techniques of logarithmic transformation, bilateral filter, Canny algorithm, and a morphological filter in the feature extraction phase; a classification tree is utilized to construct the crack categorization model using the extracted features. Fujita et al. [30] and Wang et al. [31] proposed crack classification models that employed the support vector machine. Hoang and Nguyen [32] relied on the steerable filter to extract useful features from pavement images and employed machine learning algorithms including support vector machine, neural network, and random forest to classify the images into categories of longitudinal, transverse, and alligator cracks, as well as the status of the intact pavement.

Based on recent review works [33, 34], there is an increasing trend of applying image filtering and machine learning approaches in pavement crack classification. However, due to the aforementioned challenges of crack detection from noisy and complex background texture of asphalt pavements, other advanced image processing techniques should be investigated to improve the accuracy of the automatic crack recognition process. This study constructs and compares the performances of four feature extraction methods that rely on image filtering techniques of fast local Laplacian filter (FLLF), Sobel filter (SBF) for edge detection, and steerable filter (STF) as well as projection integral (PI). The fast local Laplacian filter (FLLF) is applied as a pre-processing step to better smooth the image and highlight edges in the image. SBF and STF are employed to create crack prominent maps. PI finally utilizes these prominent maps to produce a vector of features. The adaptive boosting classification tree (Adaboost CTree) is selected to use the

feature vectors extracted from the image for categorizing the pavement crack status. The aforementioned hybrid filtering approaches (FLLF-based SBF and FLLF-based STF) have demonstrated positive effects on the classification performance of Adaboost CTree.

The rest of the study is organized as follows: Section 2 reviews the research methodology, followed by the section that describes the collected dataset of asphalt pavement images (Section 3). Section 4 describes the proposed approach of automatic pavement crack detection, followed by the experimental results (Section 5). Section 6 summarizes the current study with several remarks.

## 2. Research Methodology

### 2.1. Image Filtering Approaches

**2.1.1. Fast Local Laplacian Filter (FLLF).** FLLF is an edge-preserving image filtering technique [35]. This image processing technique is an improved version of the standard local Laplacian filter (LLF) which was developed by Paris et al. [36]. LLF is the algorithm based on the Laplacian pyramid which is widely employed in the tasks of decomposing images into multiple scales and image analysis. In image processing field, pyramid representation is a form of multiscale signal representation in which a digital image is processed by repeated smoothing and subsampling. In FLLF, the output image is obtained by collapsing the output pyramid. To implement FLLF, one first needs to specify a remapping function  $r$  and intensity threshold  $S_r$ . Accordingly, the process of FLLF can be divided into three major steps [37]:

- (i) First, FLLF uses point-wise nonlinearity function  $r(\cdot)$  which depends on the Gaussian pyramid coefficient  $g = G_l[I](x, y)$  where  $l$  denotes the level of the Gaussian pyramid and  $(x, y)$  represents the position of the pixel to process input image  $I$ . For various values of  $g$ , this approach obtains a large number of intermediate images.
- (ii) Second, FLLF integrates all of these intermediate images, and computes each output coefficient  $L_l[O](x, y)$  of the Laplacian pyramid of the transformed image.
- (iii) Third, the method collapsed the output pyramid  $L(O)$  to obtain the output image  $O$ .

Paris et al. [36] proposed the remapping functions in the following formula:

$$\tilde{r}(i) = \begin{cases} \frac{g + \text{sign}(i-g)S_r(|i-g|)^\alpha}{S_r} & \text{if } i \leq S_r, \\ g + \text{sign}(i-g)(\beta|i-g| - S_r) + S_r & \text{if } i > S_r, \end{cases} \quad (1)$$

where  $g$  denotes the coefficient of the Gaussian pyramid.  $\alpha$  determines the amount of detail increase ( $0 \leq \alpha < 1$ ) or decrease ( $\alpha > 1$ ),  $\beta$  governs the dynamic range compression ( $0 \leq \beta < 1$ ) or expansion ( $\beta > 1$ ), and  $S_r$  represents the intensity threshold to separate details in the image from edges.

Aubry et al. [35] stated a general form of the function  $r(\cdot)$  as follows:

$$r(i) = i - (i-g)f(i-g), \quad (2)$$

where  $f$  denotes a continuous function. In fact, Equation (1) is a special case of Equation (2) in which  $f(i) = (i - \tilde{r}(i))/(i-g)$ .

For the purpose of image enhancement and image smoothing, Aubry et al. [35] defines the function  $f$  as

$$f(i-g) = -m_f G_{S_r}(i-g), \quad (3)$$

where  $G_{S_r}(i-g)$  denotes the Gaussian function expressed in the following form:

$$G_{S_r}(i-g) = \exp\left(\frac{-(i-g)^2}{2S_r^2}\right), \quad (4)$$

where  $m_f$  is a parameter denoting the amplitude magnification factor.

In essence,  $m_f$  affects the smoothing of details, and  $S_r$  characterizes the amplitude of edges in  $I$  [38]. The effects of FLLF on asphalt pavement images with different scenarios of the amplitude magnification factor  $m_f$  and the intensity threshold  $S_r$  are illustrated in Figure 1. It is noted that before being analyzed by FLLF, the images are preprocessed by the median filter to remove the dot noise. In this study, based on several trial and error experiments, the median filter with a window size of  $5 \times 5$  pixels has been selected for noise suppression.

**2.1.2. Steerable Filter.** The steerable filter (STF), proposed in the previous work of Freeman and Adelson [39], is a popular technique for image processing. This technique relies on orientation-selective convolution kernels to highlight edges in digital images. STF is highly helpful for the task of analyzing patterns existing on the surface of asphalt pavements; this technique has been successfully employed in crack classification [17, 29, 32] as well as other types of pavement distress [40].

To implement the SF technique, a linear combination of the Gaussian second derivatives is employed as the basic filter. A 2D Gaussian at a certain pixel coordination  $(x, y)$  within an image  $I$  is demonstrated in the following equation:

$$G(x, y, r) = \frac{1}{\sqrt{2\pi r}} \exp\left(\frac{-(x^2 + y^2)}{2r^2}\right), \quad (5)$$

where  $r$  is a free parameter which is the variance of the Gaussian function.

Applying the STF technique with different values of the angle  $\theta$ , a set of different filters can be obtained as follows:

$$F(x, y, r, \theta) = G_{xx} \cos^2(\theta) + 2G_{xy} \cos(\theta) \sin(\theta) + G_{yy} \sin^2(\theta), \quad (6)$$

where  $G_{xx}$ ,  $G_{xy}$ , and  $G_{yy}$  denote the Gaussian second derivatives. The formulas of these derivatives are presented as follows [32]:

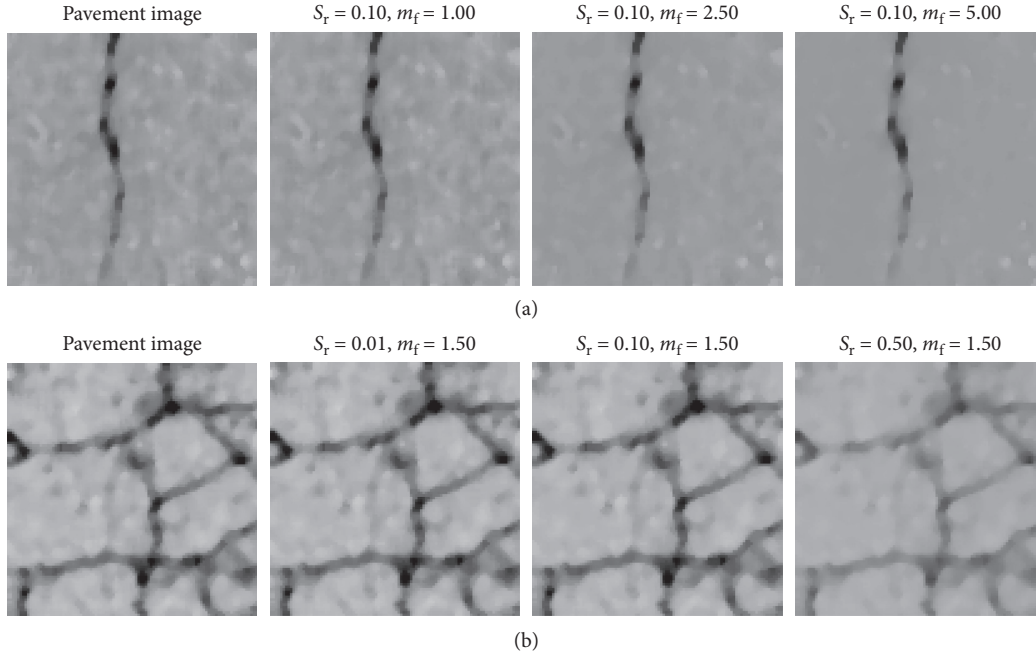


FIGURE 1: Image processed by FLLF with different values of parameters.

$$\begin{aligned}
 G_{xx}(x, y, r) &= \frac{(x^2 - r^2) \exp(-(x^2 + y^2)/2r^2)}{\sqrt{2\pi}r^5}, \\
 G_{yy}(x, y, r) &= \frac{(y^2 - r^2) \exp(-(x^2 + y^2)/2r^2)}{\sqrt{2\pi}r^5}, \\
 G_{xy}(x, y, r) &= G_{yx}(x, y, r) = \frac{xy \exp(-(x^2 + y^2)/2r^2)}{\sqrt{2\pi}r^5}.
 \end{aligned} \tag{7}$$

It is noted that the value of  $\theta$  is often varied from  $0^\circ$  to  $360^\circ$ . Figure 2 provides examples of STF responses of a pavement image with different selections of  $r$ . In this figure, the original image has been preprocessed by the median filter with the window size of  $5 \times 5$  pixels. As can be seen from the examples, a too small value of  $r$  leads to very weak signal of crack patterns. On the contrary, if  $r$  is too large (e.g.,  $r = 2.0$ ), the background texture of the asphalt pavement becomes more visible and this may hinder the crack detection and classification process.

In addition, the resulting STF response of a digital image  $I$  is calculated compactly in the following equation:

$$R(x, y) = F(x, y, \sigma, \theta) * I(x, y), \tag{8}$$

where “\*” denotes the convolution operator.

**2.1.3. Sobel Filter for Edge Detection.** As described in the previous work of Sobel [41], the Sobel filter (SBF) is a widely used technique for detecting edges in digital images. This technique reveals edges in an image by smoothing the image before computing the derivatives in the direction which is perpendicular to the derivative. To implement SBF, the filter  $h_x$  is employed to smooth the image in the  $x$  direction:

$$h_x = \begin{bmatrix} 1 & 1 \\ 2 & 2 \\ 1 & 1 \end{bmatrix}. \tag{9}$$

The convolution and the smoothing operators are both linear and can be combined in the following way:

$$h_{\text{Sobel},x} = \begin{bmatrix} 1 & 0 & -1 \\ 2 & 0 & -2 \\ 1 & 0 & -1 \end{bmatrix}. \tag{10}$$

In the same manner, the filter that computes the partial derivative in the  $y$  direction is computed as follows:

$$h_{\text{Sobel},y} = \begin{bmatrix} 1 & 2 & 1 \\ 0 & 0 & 0 \\ -1 & -2 & -1 \end{bmatrix}. \tag{11}$$

At each pixel within a digital image, the resulting gradient approximations are combined to yield the gradient magnitude which is calculated in the following way:

$$h_{\text{Sobel}} = \sqrt{h_{\text{Sobel},x}^2 + h_{\text{Sobel},y}^2}. \tag{12}$$

It is worth noticing that a threshold value  $T_s$  must be prespecified to obtain the image with detected edges. If the Sobel gradient values of pixels are smaller than the threshold value  $T_s$ , they are replaced by these threshold values [42]. Figure 3 presents the analysis results of edge detection using the Sobel algorithm of a pavement image in which different values of the threshold  $T_s$  are attempted. As can be seen from the examples, if  $T_s = 0.01$ , the resulting image is filled with edges detected from the background texture. On the contrary, if  $T_s > 0.1$ , virtually no signal of edges are captured by

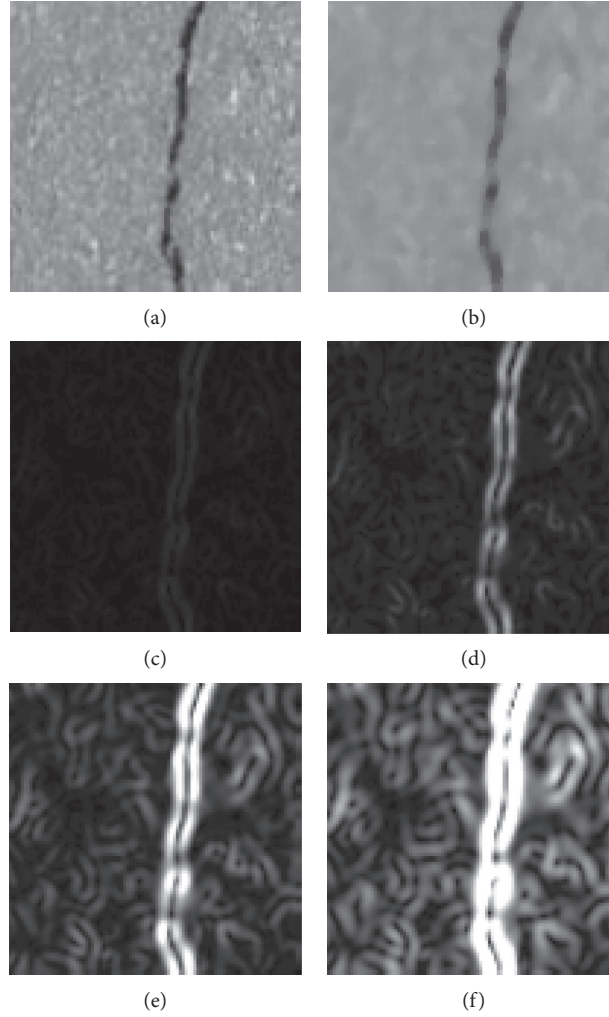


FIGURE 2: Examples of image enhancement with STF. (a) Pavement image. (b) Median filter enhancement. (c) GTF with  $r=0.5$ . (d) GTF with  $r=1.0$ . (e) GTF with  $r=1.5$ . (f) GTF with  $r=2.0$ .

the algorithm. It deems that  $T_s=0.05$  is the right value because the edges of the true crack existing in the image has been revealed.

**2.1.4. Projection Integral Technique.** The projection integral technique (PIT) is an effective technique used in shape and texture recognition [43]. This image analysis technique has been recently successfully employed in pavement crack classification [29, 32]. Using this method, the image is first converted from color image to grayscale image. The average value of gray intensity at each location of the image along an axis is computed to obtain a projection integral (PI). Therefore, PI is always associated with a certain axis. PIs along the horizontal and vertical axes are often computed and employed in object recognition. Horizontal PI (HPI) and vertical PI (VPI) are calculated in the following way:

$$\begin{aligned} \text{HPI}(y) &= \sum_{i \in x_y} I(i, y), \\ \text{VPI}(x) &= \sum_{j \in y_x} I(x, j), \end{aligned} \quad (13)$$

where HPI and VPI are the horizontal and vertical PIs, respectively.  $x_y$  and  $y_x$  represents the set of horizontal pixels at the vertical pixel  $y$  and the set of vertical pixels at the horizontal pixel  $x$  of an image  $I(x, y)$ , respectively.

Besides the two commonly employed HPI and VPI, the diagonal PI (DPI) can also be helpful in the task of pavement crack classification. It is noted that, for each image of pavement, there are two DPIs. To compute these two DPIs, the map of the SF response is rotated with the angles of  $+45$  and  $-45$  to create two rotated SF maps. The two DPI1 and DPI2 are obtained by computing the HPIs of the two rotated SF maps. The illustrations of PIs of the pavement images are provided in Figures 4 and 5. It is noted that, in Figure 4, the four PIs of an image are produced from the STF response. In Figure 5, the salient crack map created by SBF is employed to compute the four PIs.

**2.2. Adaptive Boosting Classification Tree.** Classification tree (CTree), developed by Breiman et al. [44], is an effective data

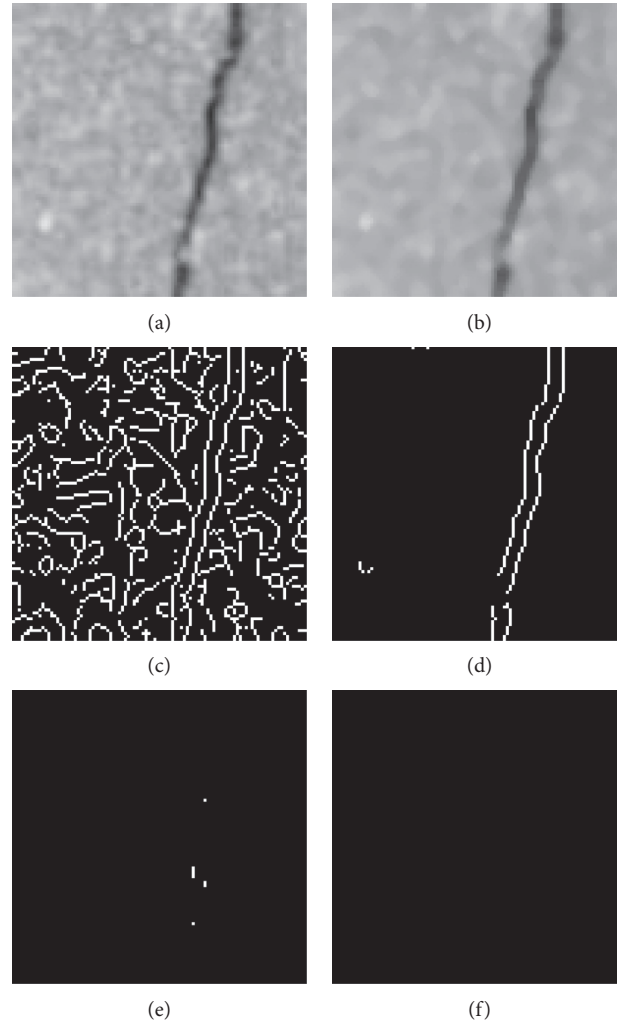


FIGURE 3: Examples of image enhancement with SBF. (a) Original image. (b) Median filter enhancement. (c) SBF:  $T_S = 0.01$ . (d) SBF:  $T_S = 0.05$ . (e) SBF:  $T_S = 0.10$ . (f) SBF:  $T_S = 0.50$ .

mining approach widely employed for data categorization [45, 46]. The CTree algorithm automatically reveals the hidden structural patterns in data and expresses the discovered patterns of the data as tree-like structures [47, 48]. CTree belongs to the group of supervised learning methods. Therefore, a training phase that requires a set of labeled data must be performed to construct the data categorization model. During the training phase of CTree, the training dataset is splitted into subsets using all predictor variables to create two child nodes in the tree-like structure [44]. It is noted that the most suitable predictor variables used for splitting operation is chosen by computing the value of an impurity function.

The data splitting process occurred in the training phase has the purpose of putting data into subsets that are as homogeneous as possible for each data category. The Gini impurity function is widely used to quantify the data homogeneous property; the Gini impurity is shown in the below equation [47]:

$$P = G_1 G_2, \quad (14)$$

where a Gini impurity index of data subset  $k$  is computed as follows [49]:

$$G_k = 1 - \sum_{i=1}^{n_{kc}} p_{ki}^2, \quad (15)$$

where  $n_{kc}$  represents the number of data categories and  $p_{ki}$  denotes the ratio of present of class  $i$  in this set.

When the training phase is successfully accomplished, a CTree model is represented by a root node, a set of internal nodes, and a set of terminal nodes. It is noticed that each node in the tree is essentially a binary decision that categorizes the predictor variable into either one of the two class labels. Thus, CTree carries out the data classification process in a top-down manner from the root node to the terminal node.

Moreover, in data mining, adaptive boosting [50], or AdaBoost for short, is a well-known ensemble learning strategy for enhancing the classification accuracy of a classifier through the process of adaptive reweighting and combining a set of individual models [51]. AdaBoost

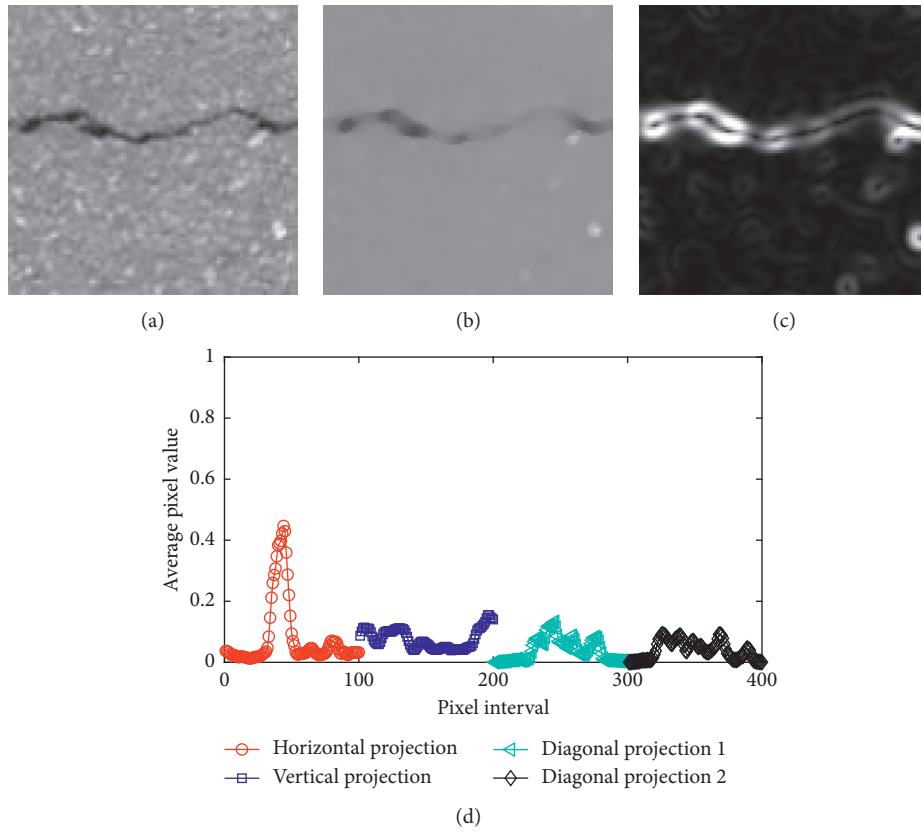


FIGURE 4: PIs of an image yielded from the STF response. (a) Pavement image. (b) FLLF. (c) STF. (d) Projective integrals.

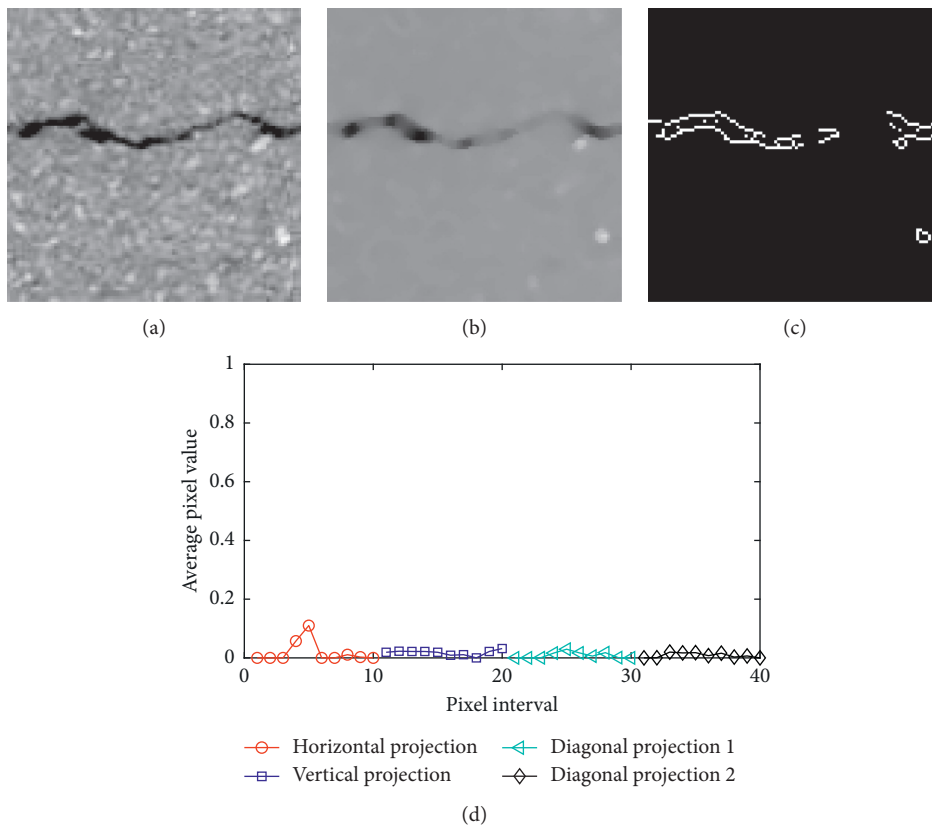


FIGURE 5: PIs of an image yielded from the SBF response. (a) Pavement image. (b) FBF. (c) STF. (d) Projective integrals.

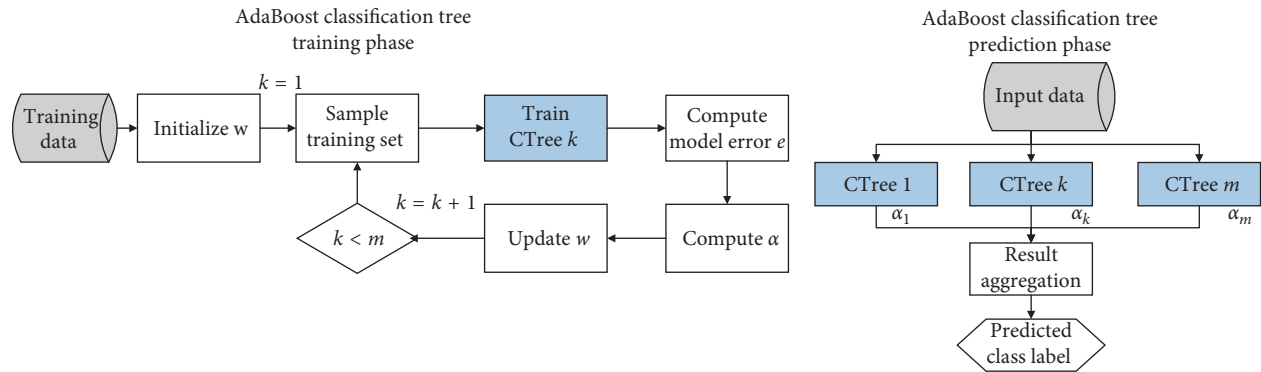


FIGURE 6: Adaboost CTree training and prediction phases.

ensemble of CTrees can be defined as a combination of multiple CTrees in which the final prediction result is obtained by combining the outputs of individual trees. Based on previous works [52–56], ensemble models have demonstrated better performance than individual models in a wide range of applications. The AdaBoost algorithm is demonstrated in Figure 6.

### 3. The Dataset of Asphalt Pavement Images

Since Adaboost CTree is a supervised learning approach, a dataset of pavement images with the prespecified ground truth categories must be prepared for the model construction and testing phases. To achieve this goal, the current study has collected pavement images in Da Nang city (Vietnam). The images are acquired with the employment of the digital camera held at the distance of about 1.2 m above the road surface. To speed up the phases of data processing and data classification, the images are resized to be  $100 \times 100$  pixels. There are five classes of pavement conditions; they are alligator crack (AC), diagonal crack (DC), longitudinal crack (LC), noncrack (NC), and transverse crack (TC). Each group of images has 400 samples; hence, the total number of data samples in the collected dataset set is 2000. The image dataset are demonstrated in Figure 7. It is noted that each pixel represents an area of approximately  $3.6 \times 3.6$  mm; therefore, the pavement area contained in each image sample is about  $360 \times 360$  mm.

### 4. Automatic Pavement Crack Recognition Using Fast Local Laplacian-Based Steerable and Sobel Filters Integrated with Adaptive Boosting Classification Tree

This section describes the structure of the proposed automatic model for pavement crack categorization. The proposed model combines the advanced image processing techniques and the machine learning method of Adaboost CTree. Advanced image processing techniques consist of FLLF, STF, SBF, and PIs. It is noted that the original pavement images have been preprocessed by the commonly used median filter to remove dot noise of the image background. FLLF is then used to concurrently smooth the image and highlight the edges. After being processed by FLLF, the enhanced image is either manipulated by STF or SBF to

create a salient map of cracks. Based on such salient map, PIs of the image are computed to serve as input features used by Adaboost CTree to classify the image into AC, DC, NC, LC, and TC categories. The overall picture of the proposed model is presented in Figure 8.

The model basically includes two modules: feature extraction based on the image processing technique and data classification based on Adaboost CTree. It is noted that the proposed model including the two modules has been constructed in the MATLAB environment with the employment of the Image Processing Toolbox [38] and the Statistics and Machine Learning Toolbox [57].

It is noted that in the feature extraction step, the maps created by the STF and SBF responses are used to compute four PIs, namely, HPI, VPI, and two DPIs (DPI1 and DPI2). The PIs of the pavement images yielded from STF and SBF are illustrated in Figures 9 and 10, respectively. Based on these figures, it can be shown that an image with a longitudinal crack generally produces a distinctive peak in its VPI. On the contrary, an image with a transverse crack yields a distinctive peak in its HPI. Moreover, the average values of PIs of images containing alligator cracks are higher than those of images containing no cracks. Notably, the two DPIs are especially useful in recognizing diagonal cracks. To compute these two DPIs, the maps of the STF and SBF responses are rotated with the angles of  $+45$  and  $-45$  to generate two rotated crack maps. The two DPIs are attained by calculating the HPIs of the two rotated crack maps.

As mentioned earlier, with the image size of  $100 \times 100$  pixels, the number of features generated by the four PIs is 400. With this size of features, the predictive capability of the Adaboost CTree model may be hindered due to the problem of the curse of dimensionality [58]. Thus, it can be of great usefulness if the feature size can be reduced. To do so, this study employs a simple moving average approach within which the average value of  $W$  consecutive values along a PI is calculated to create PIs with sampled data points. This process of feature reduction is illustrated in Figure 11. With  $W = 10$ , the total number of features in the reduced PIs is reduced from 400 to 40. Compared with the original PIs, the smoothed PIs have fewer data points and most importantly still present essential features of the original PIs.

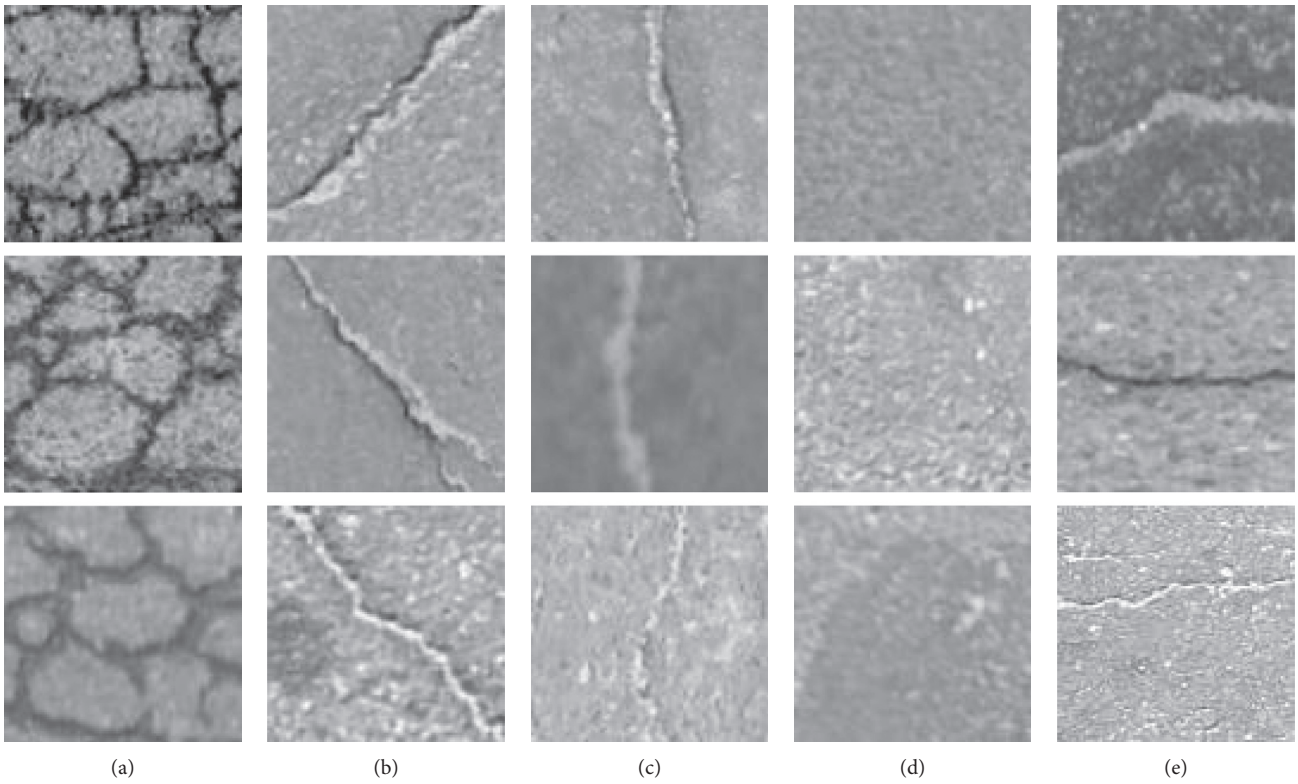


FIGURE 7: The collected dataset of pavement images. (a) AC, (b) DC, (c) LC, (d) NC, and (e) TC.

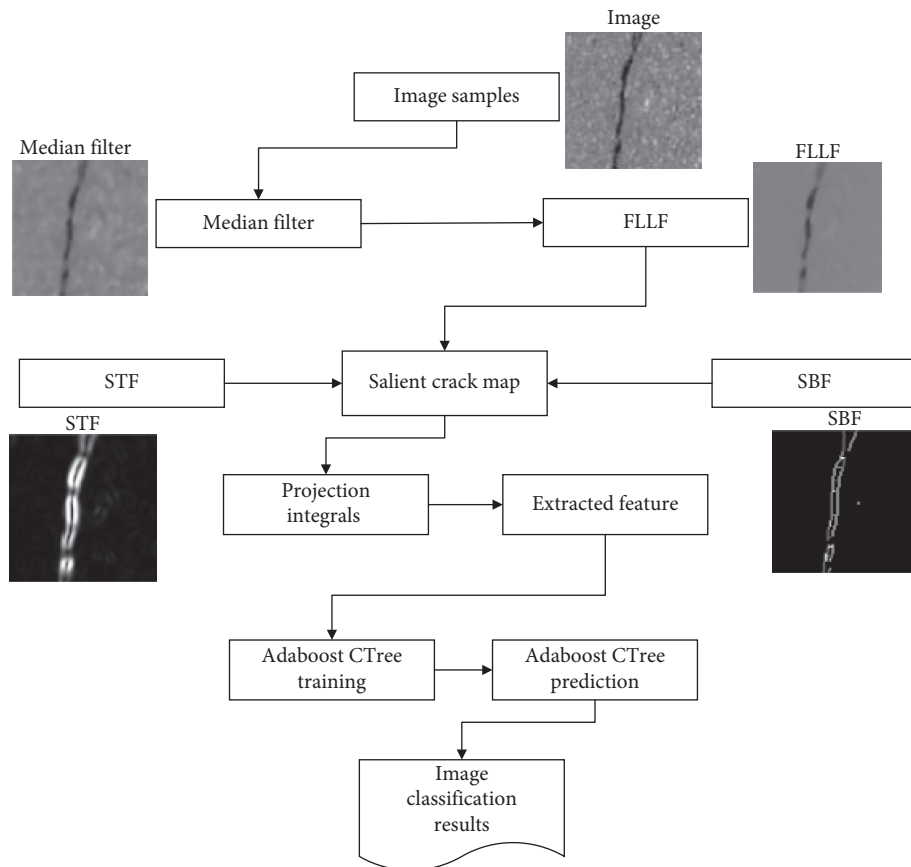
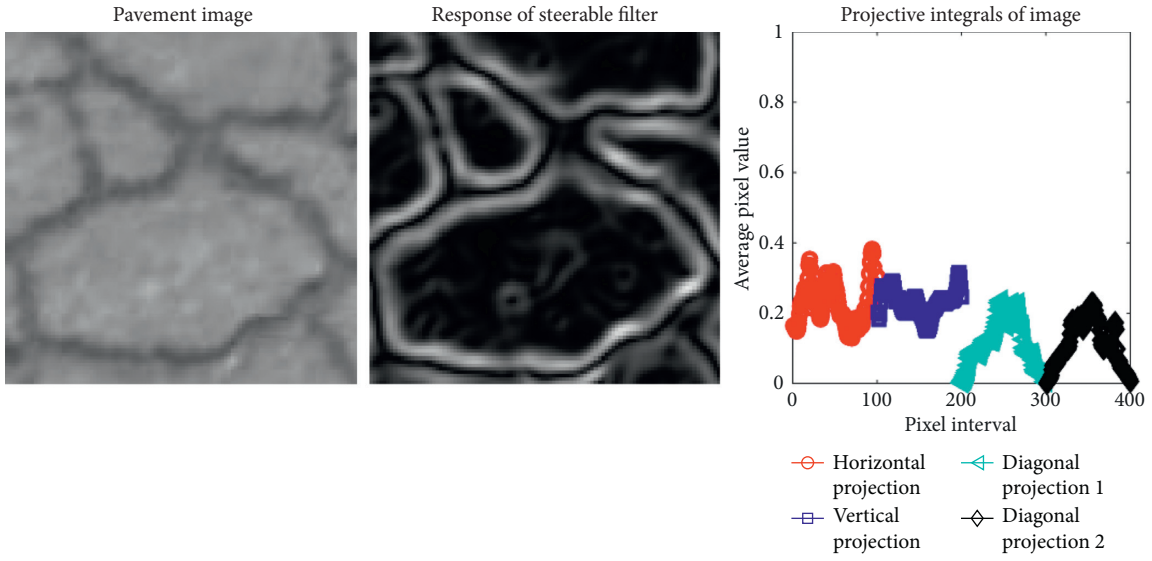
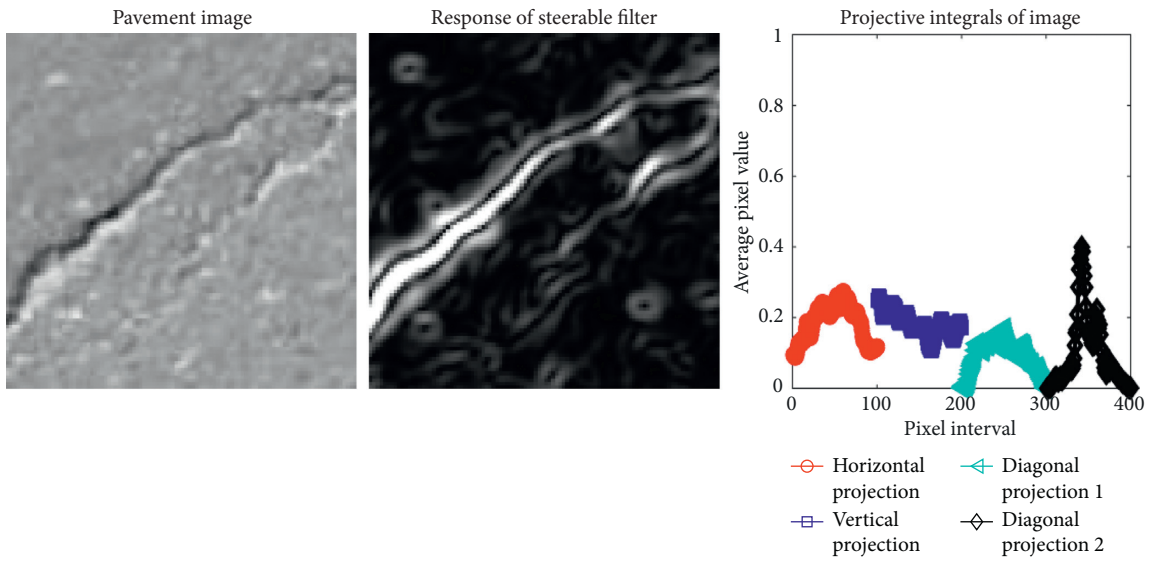


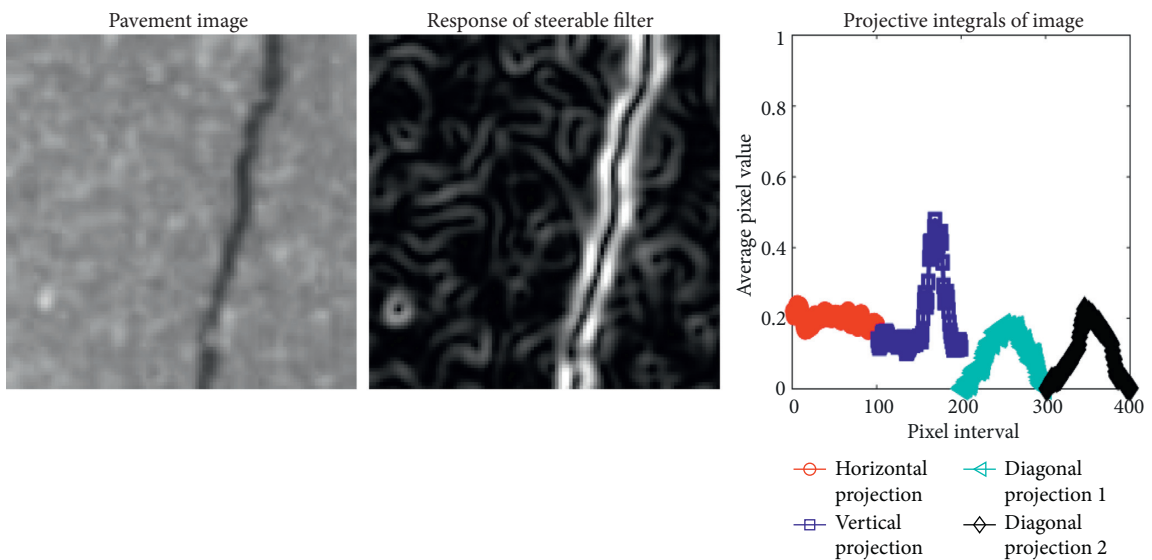
FIGURE 8: The proposed pavement crack classification model.



(a)



(b)



(c)

FIGURE 9: Continued.

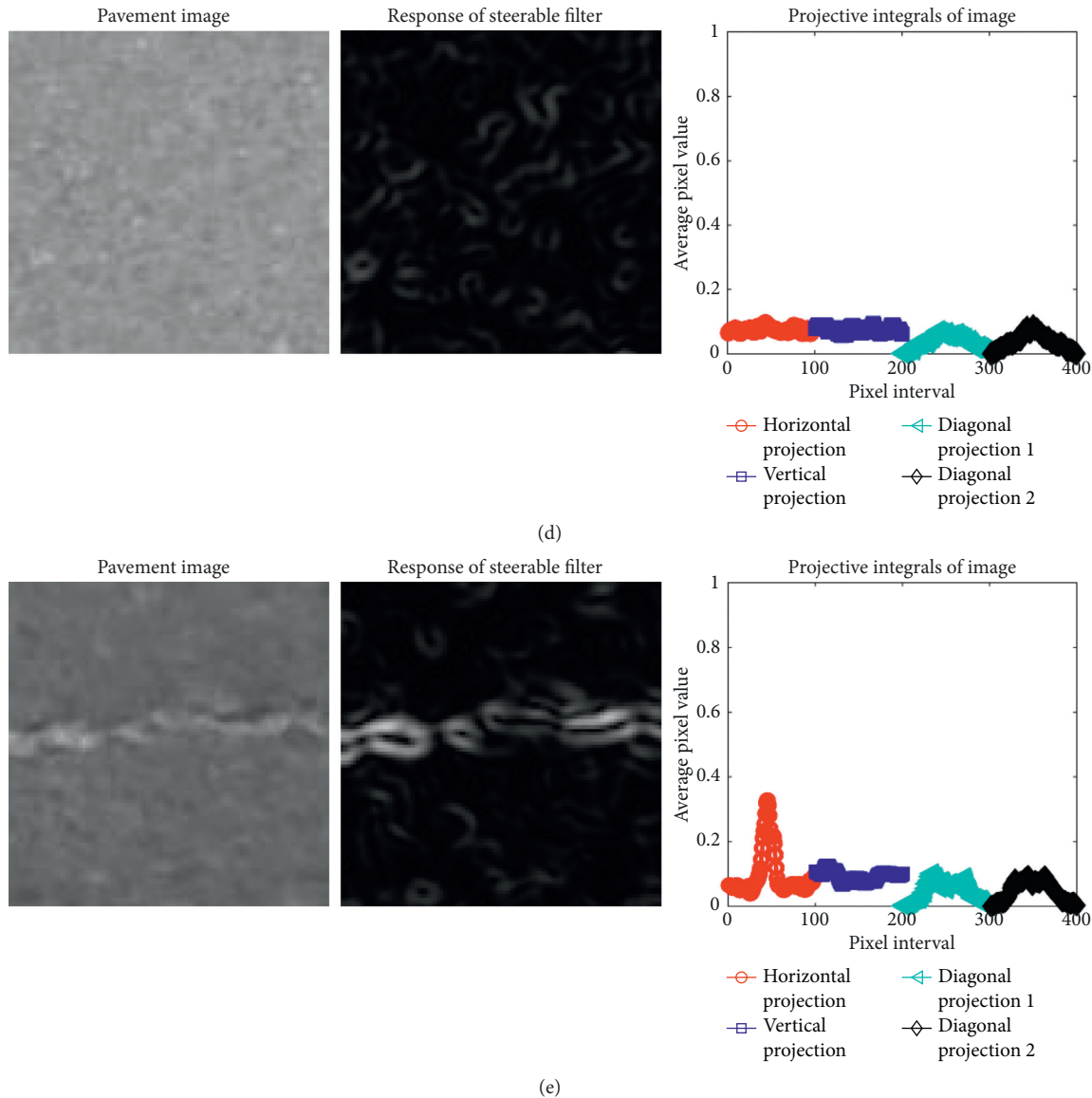


FIGURE 9: Projection integrals of asphalt pavement images using STF response: (a) alligator crack; (b) diagonal crack; (c) longitudinal crack; (d) noncrack; (e) transverse crack.

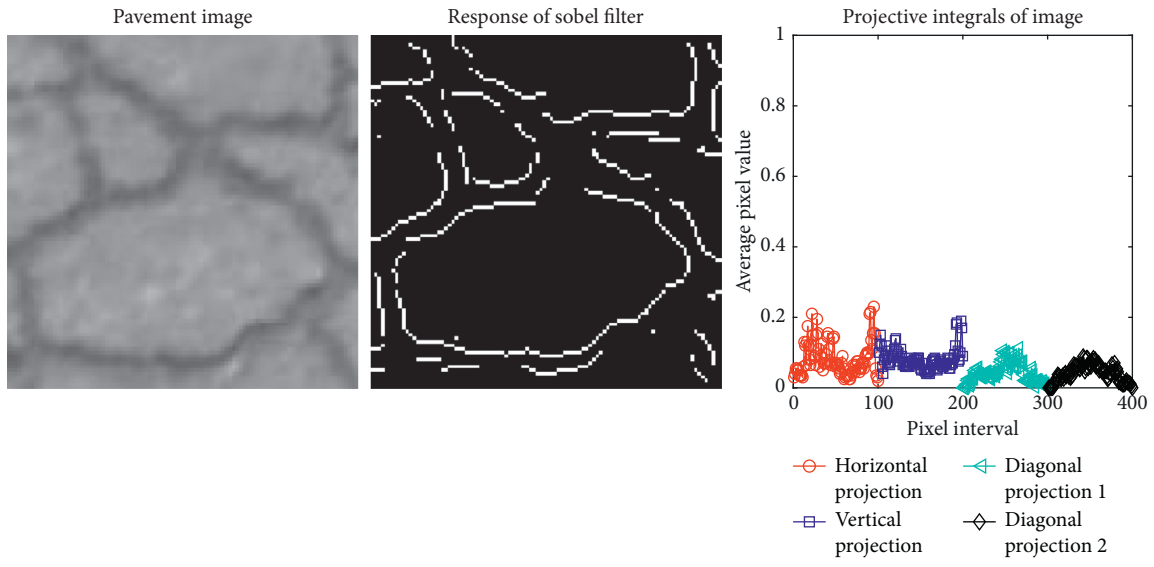
Accordingly, the reduced PIs are employed to general numerical features as input patterns which are used by Adaboost CTree to recognize the types of cracks (AC, DC, LC, and TC) as well as the condition of intact pavement (NC). It is noted that, in this study, the Adaboost CTree model has been used with the one-versus-one (OvO) strategy [59] to cope with the multilabel data classification. The reason of selecting OvO is that this strategy can deliver good prediction performance and can help us to avoid the imbalanced data classification problem [58, 60].

### 5. Experimental Results

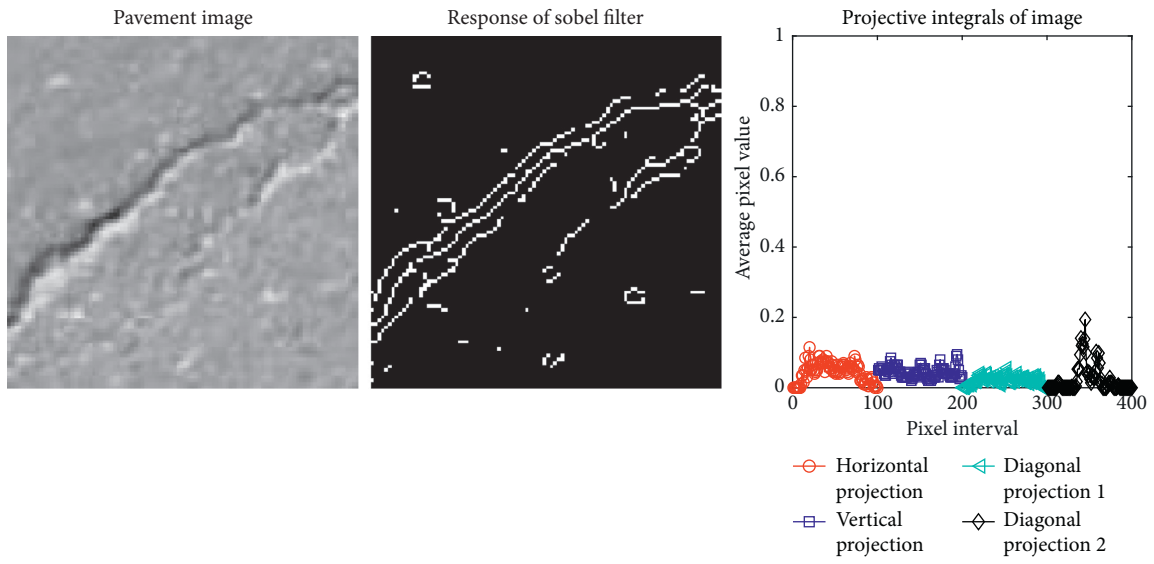
To construct and verify Adaboost CTree, the collected image dataset has been separated into two sets: the training set (70%) and the testing set (30%). The first set is used to

establish the learning model, and the second set is employed to inspect the predictive performance of the Adaboost CTree-based crack categorization model. Moreover, because one time of training and testing may not express the true predictive capability of the newly developed approach due to the problem of randomness in the selecting data, a repetitive data subsampling has been carried 20 times. The Adaboost CTree performance is assessed by averaging the prediction results attained from the 20 times of training and testing phases.

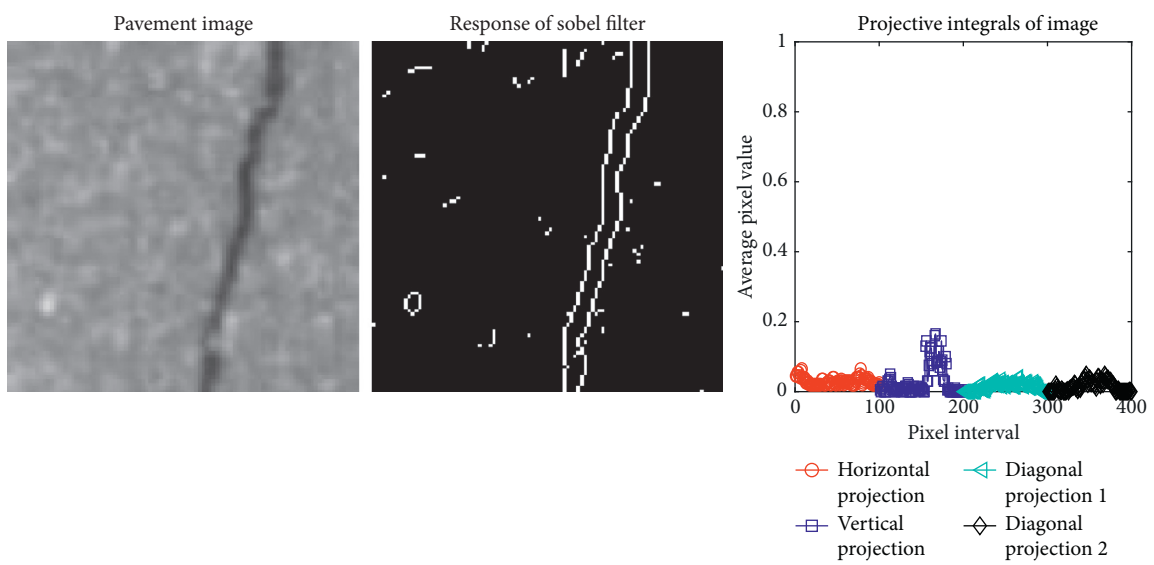
Moreover, the image processing techniques used in the feature extraction phase require the specification of several tuning parameters. In this study, these parameters are selected via several trial and error experiments with the collected pavement images. The setting of the parameter of the image processing techniques is as follows:



(a)



(b)



(c)

FIGURE 10: Continued.

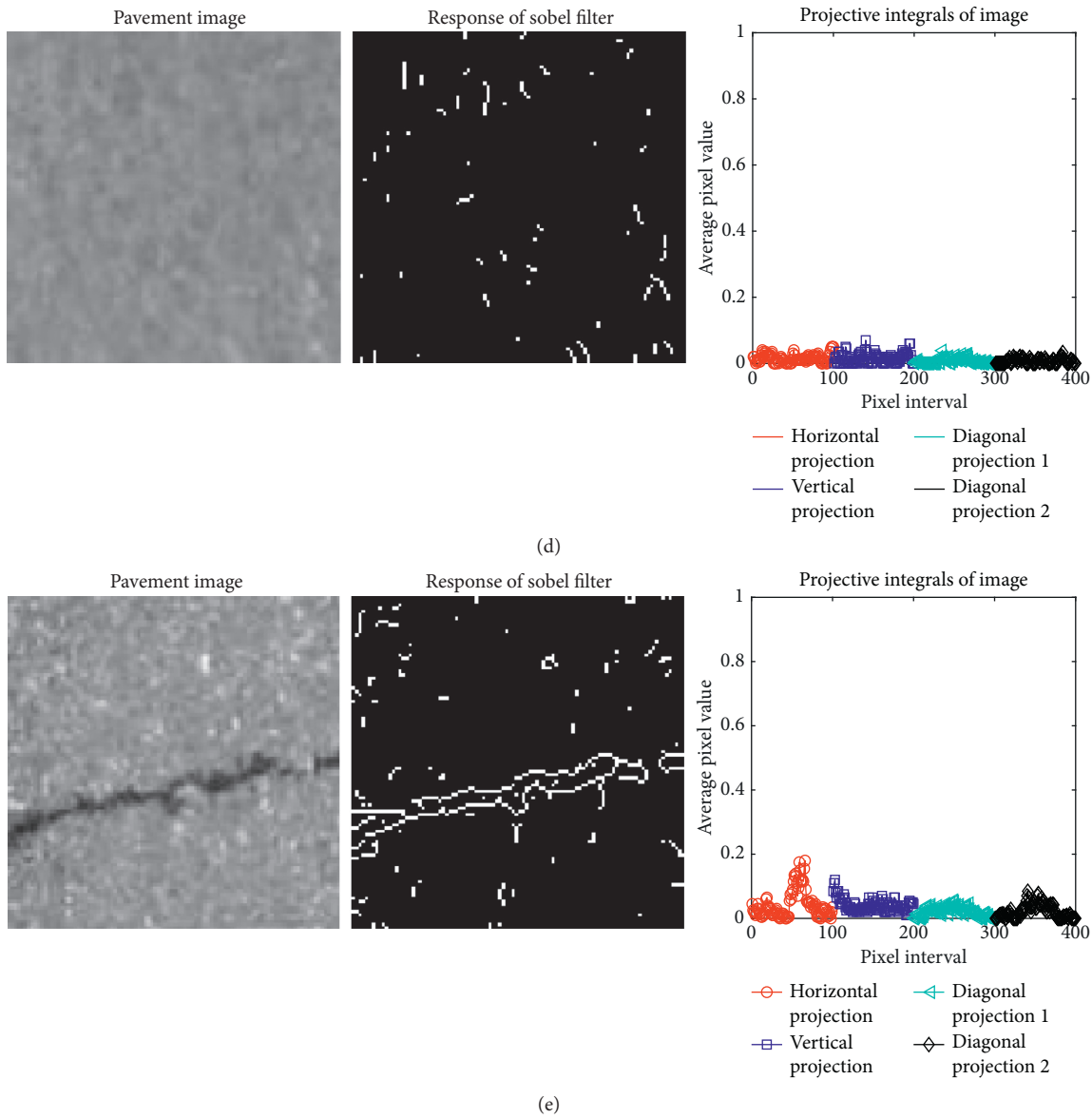


FIGURE 10: Projection integrals of asphalt pavement images using SBF response: (a) alligator crack; (b) diagonal crack; (c) longitudinal crack; (d) noncrack; (e) transverse crack.

- (i) The window size of the median filter is  $5 \times 5$  pixels
- (ii) The amplitude magnification factor  $m_f = 3$  and the intensity threshold  $S_r = 0.15$
- (iii) The variance of the Gaussian function used in STF is 1.5
- (iv) The threshold value  $T_s$  of SBF is 0.02
- (v) The window size ( $W$ ) used to smooth the PIs is 10

In addition, to express the predictive capability of the Adaboost CTree-based crack recognition model, the classification accuracy rate (CAR) for a class label  $i$  is computed by the following equation:

$$CAR_i = \frac{R_C^i}{R_A^i} \times 100(\%), \quad (16)$$

where  $R_C^i$  and  $R_A^i$  denote the number of data samples in the class  $i$ th being correctly recognized and the total number of data samples in the class  $i$ th, respectively.

The overall classification accuracy rate ( $CAR_{Overall}$ ) for all the five class labels is calculated by the following equation:

$$CAR_{Overall} = \sum_{i=1}^5 \frac{CAR_i}{5}. \quad (17)$$

The prediction accuracy of the Adaboost CTree models with the two employed SBF and STF for creating the salient crack maps is reported in Table 1. These two models are denoted as Adaboost CTree-SBF and Adaboost CTree-STF. As can be seen from this table, Adaboost CTree-STF has the CARs of the AC class (93.17%), DC class (89.54%), LC class (89.58%), NC (84.92%), and TC class (91.38%). These

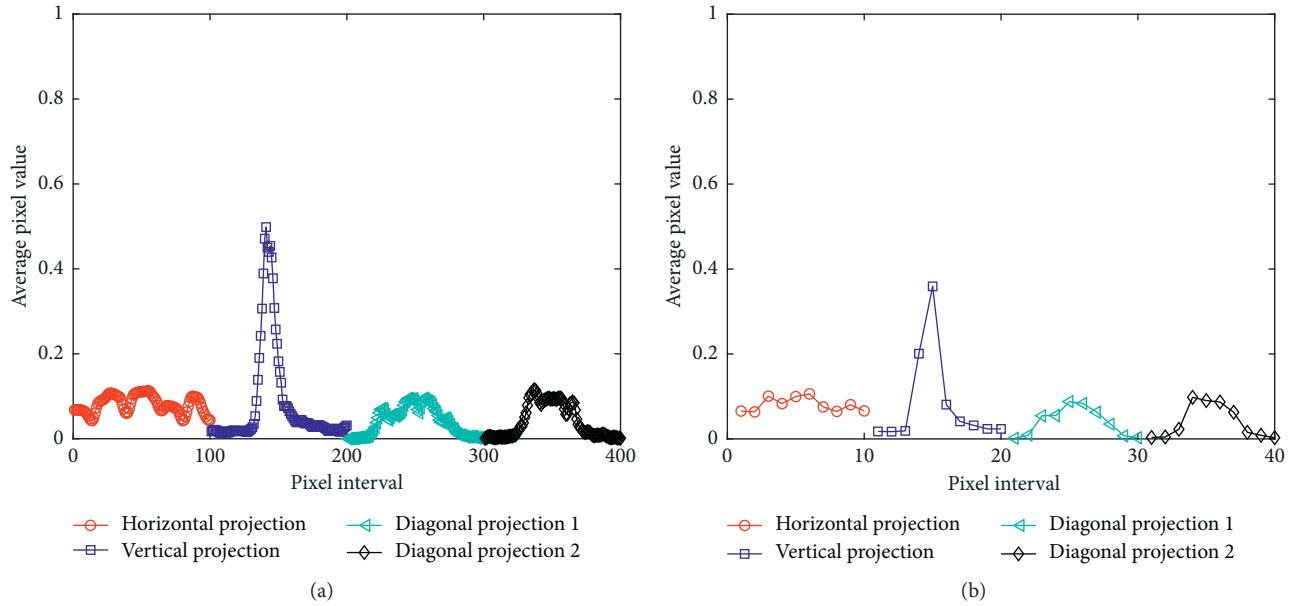


FIGURE 11: Projection integrals (PIs) of a pavement image: (a) the original PIs; (b) the reduced PIs.

TABLE 1: Classification results of Adaboost CTree.

Image filtering approach	Statistic	CAR of each class label					Overall CAR
		AC	DC	LC	NC	TC	
SBF	Average	90.50	80.83	83.71	79.38	88.08	84.50
	Std.	2.64	4.26	3.56	3.63	2.84	1.47
STF	Average	93.17	89.54	89.58	84.92	91.38	89.72
	Std.	3.03	2.64	4.14	4.02	3.28	1.32

outcomes are better than those yielded by the Adaboost CTree-SBF with the CARs of the AC class (90.50%), DC class (80.83%), LC class (83.71%), NC (79.38%), and TC class (88.08%). The overall CAR of Adaboost CTree-STF (89.72%) is also higher than that of Adaboost CTree-SBF (84.50%).

Furthermore, Figure 12 demonstrates the box plots of prediction results of the Adaboost CTree-SBF and Adaboost CTree-STF classification approaches. To further validate the statistical difference of the Adaboost CTree-SBF and Adaboost CTree-STF, the Wilcoxon signed-rank test (WSRT) is employed in this section. WSRT is a popular nonparametric statistical hypothesis test which is often employed for result comparison [61]. In this study, the significance level of WSRT is chosen to be 0.05. If the  $p$  value computed from the test is smaller than 0.05, it is able to confirm that the pavement crack classification results of the Adaboost CTree-SBF and Adaboost CTree-STF are statistically different. With  $p$  value = 0.00008, it is confident to state that Adaboost CTree-STF is significantly better than Adaboost CTree-SBF.

## 6. Conclusion

This study proposes an integration of image processing and machine learning approaches for automatic pavement crack

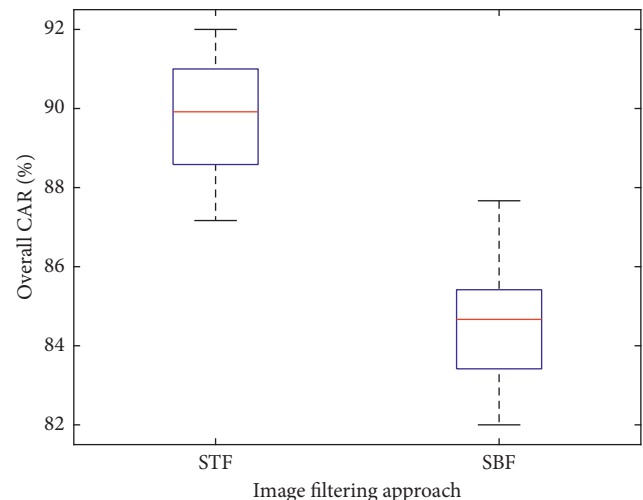


FIGURE 12: Box plots of prediction results of Adaboost CTree-SBF and Adaboost CTree-STF.

recognition. Advanced image processing techniques including FLLF, SBF, STF, and PI are employed to extract numerical features from digital images. The Adaboost CTree utilizes the extracted features to perform crack recognition tasks. A dataset of 2000 image samples with five classes of asphalt pavement conditions (AC, DC, LC, NC, and TC) has

been collected to train and validate the proposed integrated approach. An experiment using a random subsampling process and WSRT points out that Adaboost CTree-STF is significantly better than Adaboost CTree-SBF.

Since the current practice of pavement survey in Vietnam still heavily relies on the survey of human inspectors and manual data analysis processes, the new approach based on the Adaboost CTree classification model integrated with STF can provide a helpful tool to accelerate the periodic surveys of roads by boosting the productivity of the data acquisition and analysis processes. Thus, the newly constructed model can be highly useful for the local transportation agencies and authorities to manage their road sections effectively.

Based on the collected image samples, the smallest crack opening that the Adaboost CTree-STF model can detect is about 8 mm. Since the ability to detect small cracks can be essential for early warning of pavement deterioration, image samples with thinner crack opening should be collected in a future work to enhance the applicability of the current model. Moreover, since the current stage of the study is performing preliminary survey on pavement conditions. The details of crack length and opening have not yet been available for analysis. Therefore, the current model can be extended by employing image thresholding and image segmentation techniques to separate the crack objects from the pavement background. Accordingly, information regarding the length and the opening of cracks can be measured. In addition, other developments of the current study may include the investigation of other novel machine learning approaches in the task of asphalt pavement crack recognition and the extension of the current dataset to include other type of cracks (e.g., reflective cracks or block cracks) as well as other forms of pavement defects (such as potholes, ruts, depression, upheaval, and raveling) to enhance the applicability of the current prediction model.

## Data Availability

The dataset used in the study is provided in the supplementary file.

## Conflicts of Interest

The authors confirm that there are no conflicts of interest regarding the publication of this manuscript.

## Supplementary Materials

The supplementary file contains the dataset used in this study. In this file, the first 40 columns are the input features of the data (which are the projection integrals); the last column is the class labels (1 = alligator crack, 2 = diagonal crack, 3 = longitudinal crack, 4 = noncrack, and 5 = transverse crack). (*Supplementary Materials*)

## References

- [1] A. S. El-Wakeel, J. Li, A. Noureldin, H. S. Hassanein, and N. Zorba, "Towards a practical crowdsensing system for road surface conditions monitoring," *IEEE Internet of Things Journal*, p. 1, 2018.
- [2] K. Zhang, H. D. Cheng, and B. Zhang, "Unified approach to pavement crack and sealed crack detection using pre-classification based on transfer learning," *Journal of Computing in Civil Engineering*, vol. 32, no. 2, article 04018001, 2018.
- [3] GSO, *Transport, Postal Services and Telecommunications, Some Main Indicators on Capacity of Transportation General Statistics Office of Viet Nam*, GSO, Hanoi, Vietnam, 2010, [http://www.gso.gov.vn/default\\_en.aspx?tabid=473&idmid=&ItemID=12788](http://www.gso.gov.vn/default_en.aspx?tabid=473&idmid=&ItemID=12788).
- [4] T. I. Al-Suleiman, Z. M. Hamici, S. M. Bazlamit, and H. S. Ahmad, "Assessment of the effect of alligator cracking on pavement condition using WSN-image processing," in *Lecture Notes in Mechanical Engineering*, pp. 265–274, Springer International Publishing, Berlin, Germany, 2018.
- [5] W. Kaddah, M. Elbouz, Y. Ouerhani, V. Baltazart, M. Desthieux, and A. Alfalou, "Optimized minimal path selection (OMPS) method for automatic and unsupervised crack segmentation within two-dimensional pavement images," *Visual Computer*, 2018.
- [6] W. Wang, A. Zhang, K. C. P. Wang, A. F. Braham, and S. Qiu, "Pavement crack width measurement based on laplace's equation for continuity and unambiguity," *Computer-Aided Civil and Infrastructure Engineering*, vol. 33, no. 2, pp. 110–123, 2018.
- [7] D. Ai, G. Jiang, S. K. Lam, and C. Li, "Automatic pixel-level pavement crack detection using information of multi-scale neighborhoods," *IEEE Access*, vol. 6, pp. 24452–24463, 2018.
- [8] D. S. Mahler, Z. B. Kharoufa, E. K. Wong, and L. G. Shaw, "Pavement distress analysis using image processing techniques," *Computer-Aided Civil and Infrastructure Engineering*, vol. 6, no. 1, pp. 1–14, 1991.
- [9] K. R. Kirschke and S. A. Velinsky, "Histogram-based approach for automated," *Pavement-Crack Sensing Journal of Transportation Engineering*, vol. 118, no. 5, pp. 700–710, 1992.
- [10] H. D. Cheng, X. J. Shi, and C. Glazier, "Real-time image thresholding based on sample space reduction and interpolation approach," *Journal of Computing in Civil Engineering*, vol. 17, no. 4, pp. 264–272, 2003.
- [11] H. Lee and J. Kim, "Development of a crack type index transportation research record," *Journal of the Transportation Research Board*, vol. 1940, no. 1, pp. 99–109, 2005.
- [12] H. Zhao, G. Qin, and X. Wang, "Improvement of canny algorithm based on pavement edge detection," in *Proceedings of 2010 3rd International Congress on Image and Signal Processing*, pp. 964–967, October 2010.
- [13] Q. Zou, Y. Cao, Q. Li, Q. Mao, and S. Wang, "CrackTree: automatic crack detection from pavement images," *Pattern Recognition Letters*, vol. 33, no. 3, pp. 227–238, 2012.
- [14] A. Zhang, Q. Li, K. Wang, and S. Qiu, "Matched filtering algorithm for pavement cracking detection transportation research record," *Journal of the Transportation Research Board*, vol. 2367, no. 1, pp. 30–42, 2013.
- [15] M. Salman, S. Mathavan, K. Kamal, and M. Rahman, "Pavement crack detection using the Gabor filter," in *Proceedings of 16th International IEEE Conference on Intelligent Transportation Systems (ITSC 2013)*, pp. 2039–2044, The Hague, Netherlands, October 2013.
- [16] Z. Eduardo, G. G. B. Jaime, M. Roberto, and L. José, "Road crack detection using visual features extracted by Gabor filters," *Computer-Aided Civil and Infrastructure Engineering*, vol. 29, no. 5, pp. 342–358, 2014.

- [17] S. Li, Y. Cao, and H. Cai, "Automatic pavement-crack detection and segmentation based on steerable matched filtering and an active contour," *Model Journal of Computing in Civil Engineering*, vol. 31, no. 5, article 04017045, 2017.
- [18] K. Wang, Q. Li, and W. Gong, "Wavelet-based pavement distress image edge detection with à Troust algorithm transportation research record," *Journal of the Transportation Research Board*, vol. 2024, no. 1, pp. 73–81, 2008.
- [19] L. Ying and E. Salari, "Beamlet transform-based technique for pavement crack detection and classification," *Computer-Aided Civil and Infrastructure Engineering*, vol. 25, no. 8, pp. 572–580, 2010.
- [20] Y. O. Ouma and M. Hahn, "Wavelet-morphology based detection of incipient linear cracks in asphalt pavements from RGB camera imagery and classification using circular," *Radon Transform Advanced Engineering Informatics*, vol. 30, no. 3, pp. 481–499, 2016.
- [21] L. Sun, M. Kamaliardakani, and Y. Zhang, "Weighted neighborhood pixels segmentation method for automated detection of cracks on pavement surface images," *Journal of Computing in Civil Engineering*, vol. 30, no. 2, article 04015021, 2016.
- [22] S. Gao, Z. Jie, Z. Pan, F. Qin, and R. Li, "Automatic recognition of pavement crack via convolutional neural network," in *Transactions on Edutainment XIV*, Springer, Berlin, Heidelberg, Germany, pp. 82–89, 2018.
- [23] K. Gopalakrishnan, S. K. Khaitan, A. Choudhary, and A. Agrawal, "Deep convolutional neural networks with transfer learning for computer vision-based data-driven pavement distress detection," *Construction and Building Materials*, vol. 157, pp. 322–330, 2017.
- [24] N. D. Hoang, Q. L. Nguyen, and V. D. Tran, "Automatic recognition of asphalt pavement cracks using metaheuristic optimized edge detection algorithms and convolution neural network," *Automation in Construction*, vol. 94, pp. 203–213, 2018.
- [25] S. Mathavan, K. Vaheesan, A. Kumar et al., "Detection of pavement cracks using tiled fuzzy Hough transform," in *Proceedings of SPIE*, p. 15, Rochester, NY, USA, 2017.
- [26] H. Rababaah, "Asphalt pavement crack classification: a comparative study of three AI approaches: multilayer perceptron, genetic algorithms, and self-organizing maps," Ph.D. thesis, Indiana University South Bend, South Bend, IN, USA, 2005.
- [27] S. Mokhtari, L. Wu, and H. B. Yun, "Comparison of supervised classification techniques for vision-based pavement crack detection transportation research record," *Journal of the Transportation Research Board*, vol. 2595, pp. 119–127, 2016.
- [28] A. Banharsakun, "Hybrid ABC-ANN for pavement surface distress detection and classification," *International Journal of Machine Learning and Cybernetics*, vol. 8, no. 2, pp. 699–710, 2017.
- [29] A. Cubero-Fernandez, F. J. Rodriguez-Lozano, R. Villatoro, J. Olivares, and J. M. Palomares, "Efficient pavement crack detection and classification," *EURASIP Journal on Image and Video Processing*, vol. 2017, no. 1, 2017.
- [30] Y. Fujita, K. Shimada, M. Ichihara, and Y. Hamamoto, "A method based on machine learning using hand-crafted features for crack detection from asphalt pavement surface images," in *Proceedings of International Conference on Quality Control by Artificial Vision 2017*, p. 8, Tokyo, Japan, May 2017.
- [31] S. Wang, S. Qiu, W. Wang, D. Xiao, and K. C. P. Wang, "Cracking classification using minimum rectangular cover-based support vector machine," *Journal of Computing in Civil Engineering*, vol. 31, no. 5, article 04017027, 2017.
- [32] N. D. Hoang and Q. L. Nguyen, "A novel method for asphalt pavement crack classification based on image processing and machine learning," *Engineering with Computers*, 2018.
- [33] T. B. J. Coenen and A. Golroo, "A review on automated pavement distress detection methods," *Cogent Engineering*, vol. 4, no. 1, 2017.
- [34] H. Zakeri, F. M. Nejad, and A. Fahimifar, "Image based techniques for crack detection, classification and quantification in asphalt pavement," *A Review Archives of Computational Methods in Engineering*, vol. 24, no. 4, pp. 935–977, 2017.
- [35] M. Aubry, S. Paris, S. W. Hasinoff, J. Kautz, and F. Durand, "Fast local laplacian filters: theory and applications," *ACM Transactions on Graphics*, vol. 33, no. 5, pp. 1–14, 2014.
- [36] S. Paris, S. W. Hasinoff, and J. Kautz, "Local Laplacian filters: edge-aware image processing with a Laplacian pyramid," *Communications of the ACM*, vol. 58, no. 3, pp. 81–91, 2015.
- [37] Z. Qiang, L. He, Y. Chen, X. Chen, and D. Xu, "Adaptive fast local Laplacian filters and its edge-aware application," *Multimedia Tools and Applications*, 2017.
- [38] Mathworks, *Image Processing Toolbox User's Guide*, MathWorks, Inc., Natick, MA, USA, 2017, [https://www.mathworks.com/help/pdf\\_doc/images/images\\_tb.pdf](https://www.mathworks.com/help/pdf_doc/images/images_tb.pdf).
- [39] W. T. Freeman and E. H. Adelson, "Steerable filters for early vision, image analysis, and wavelet decomposition," in *Proceedings of Third International Conference on Computer Vision*, pp. 406–415, Osaka, Japan, December 1990.
- [40] N. D. Hoang, "An artificial intelligence method for asphalt pavement pothole detection using least squares support vector machine and neural network with steerable filter-based feature," *Extraction Advances in Civil Engineering*, vol. 2018, Article ID 7419058, 12 pages, 2018.
- [41] I. Sobel, "Neighborhood coding of binary images for fast contour following and general binary array processing," *Computer Graphics and Image Processing*, vol. 8, no. 1, pp. 127–135, 1978.
- [42] T. Bose, *Digital Signal and Image Processing*, Wiley, Hoboken, NJ, USA, 2003.
- [43] A. Chouchane, M. Belahcene, and S. Bourennane, "3D and 2D face recognition using integral projection curves based depth and intensity images," *International Journal of Intelligent Systems Technologies and Applications*, vol. 14, no. 1, pp. 50–69, 2015.
- [44] L. Breiman, J. H. Friedman, R. A. Olshen, and C. J. Stone, *Classification and Regression Trees*, Wadsworth and Brooks, Monterey, CA, USA, 1984.
- [45] M. S. Alkhasawneh, U. K. Ngah, L. T. Tay, N. A. M. Isa, and M. S. Al-Batah, "Modeling and testing landslide hazard using decision tree," *Journal of Applied Mathematics*, vol. 2014, Article ID 929768, 9 pages, 2014.
- [46] H. Hong, J. Liu, D. T. Bui et al., "Landslide susceptibility mapping using J48 decision tree with AdaBoost, bagging and rotation forest ensembles in the Guangchang area (China)," *CATENA*, vol. 163, pp. 399–413, 2018.
- [47] V. H. Dang, T. B. Dieu, X. L. Tran, and N. D. Hoang, "Enhancing the accuracy of rainfall-induced landslide prediction along mountain roads with a GIS-based random forest classifier," *Bulletin of Engineering Geology and the Environment*, 2018.
- [48] Y. Xia, C. Liu, Y. Li, and N. Liu, "A boosted decision tree approach using Bayesian hyper-parameter optimization for

- credit scoring,” *Expert Systems with Applications*, vol. 78, pp. 225–241, 2017.
- [49] L. Rokach and O. Maimon, *Datamining and Knowledge Discovery Handbook*, Springer, Berlin, Germany, 2010.
- [50] Y. Freund and R. E. Schapire, “A decision-theoretic generalization of on-line learning and an application to boosting,” *Journal of Computer and System Sciences*, vol. 55, no. 1, pp. 119–139, 1997.
- [51] S. A. Naghibi, D. D. Moghaddam, B. Kalantar, B. Pradhan, and O. Kisi, “A comparative assessment of GIS-based data mining models and a novel ensemble model in groundwater well potential mapping,” *Journal of Hydrology*, vol. 548, pp. 471–483, 2017.
- [52] A. O. M. Abuassba, D. Zhang, X. Luo, A. Shaheryar, and H. Ali, “Improving classification performance through an advanced ensemble based heterogeneous extreme learning machines,” *Computational Intelligence and Neuroscience*, vol. 2017, Article ID 3405463, 11 pages, 2017.
- [53] J. S. Chou, K. H. Yang, and J. Y. Lin, “Peak shear strength of discrete fiber-reinforced soils computed by machine learning and metaensemble methods,” *Journal of Computing in Civil Engineering*, vol. 30, no. 6, article 04016036, 2016.
- [54] L. I. Kuncheva, *Combining Pattern Classifiers: Methods and Algorithms*, John Wiley & Sons, Inc., Hoboken, NJ, USA, 2014.
- [55] B. T. Pham, D. T. Bui, M. B. Dholakia et al., “A novel ensemble classifier of rotation forest and Naïve Bayer for landslide susceptibility assessment at the Luc Yen district, Yen Bai Province (Viet Nam) using GIS Geomatics,” *Natural Hazards and Risk*, vol. 8, no. 2, pp. 649–671, 2017.
- [56] D. Yang, H. Mu, Z. Xu, Z. Wang, C. Yi, and C. Liu, “Based on soft competition ART neural network ensemble and its application to the fault diagnosis of bearing,” *Mathematical Problems in Engineering*, vol. 2017, Article ID 2641546, 11 pages, 2017.
- [57] Mathworks, *Statistics and Machine Learning Toolbox User’s Guide*, Mathworks, Inc., Natick, MA, USA, 2017, [https://www.mathworks.com/help/pdf\\_doc/stats/stats.pdf](https://www.mathworks.com/help/pdf_doc/stats/stats.pdf).
- [58] C. M. Bishop, *Pattern Recognition and Machine Learning (Information Science and Statistics)*, Springer, Berlin, Germany, 2011.
- [59] A. Rocha and S. K. Goldenstein, “Multiclass from binary: expanding one-versus-all, one-versus-one and ECOC-based approaches,” *IEEE Transactions on Neural Networks and Learning Systems*, vol. 25, no. 2, pp. 289–302, 2014.
- [60] K. B. Duan, J. C. Rajapakse, and M. N. Nguyen, “One-versus-one and one-versus-all multiclass SVM-RFE for gene selection in cancer classification,” in *Evolutionary Computation, Machine Learning and Data Mining in Bioinformatics*, pp. 47–56, Springer, Berlin, Heidelberg, Germany, 2007.
- [61] N. D. Hoang and D. T. Bui, “Predicting earthquake-induced soil liquefaction based on a hybridization of kernel Fisher discriminant analysis and a least squares support vector machine: a multi-dataset study,” *Bulletin of Engineering Geology and the Environment*, vol. 77, no. 1, pp. 191–204, 2018.

## Research Article

# An Artificial Intelligence Method for Asphalt Pavement Pothole Detection Using Least Squares Support Vector Machine and Neural Network with Steerable Filter-Based Feature Extraction

Nhat-Duc Hoang 

*Faculty of Civil Engineering, Institute of Research and Development, Duy Tan University, R.809–No. 03 Quang Trung, Da Nang 550000, Vietnam*

Correspondence should be addressed to Nhat-Duc Hoang; [hoangnhatduc@dtu.edu.vn](mailto:hoangnhatduc@dtu.edu.vn)

Received 19 March 2018; Accepted 30 April 2018; Published 6 June 2018

Academic Editor: Maksym Grzywinski

Copyright © 2018 Nhat-Duc Hoang. This is an open access article distributed under the Creative Commons Attribution License, which permits unrestricted use, distribution, and reproduction in any medium, provided the original work is properly cited.

This study establishes an artificial intelligence (AI) model for detecting pothole on asphalt pavement surface. Image processing methods including Gaussian filter, steerable filter, and integral projection are utilized for extracting features from digital images. A data set consisting of 200 image samples has been collected to train and validate the predictive performance of two machine learning algorithms including the least squares support vector machine (LS-SVM) and the artificial neural network (ANN). Experimental results obtained from a repeated subsampling process with 20 runs show that both LS-SVM and ANN are capable methods for pothole detection with classification accuracy rate larger than 85%. In addition, the LS-SVM has achieved the highest classification accuracy rate (roughly 89%) and the area under the curve (0.96). Accordingly, the proposed AI approach used with LS-SVM can be very potential to assist transportation agencies and road inspectors in the task of pavement pothole detection.

## 1. Introduction

Roads are essential components of the national infrastructure. Evaluating road condition is a crucial task of transportation agencies that are responsible for establishing maintenance schedules and allocating maintenance budgets [1]. The correlation of road deterioration and the increasing number of traffic accidents leads to the fact that road safety has become a common concern in many countries [2]. The problem of asphalt road degradation has a very negative impact on the economic development for developing countries where financial resource for pavement maintenance is often insufficient. Therefore, it is of practical need to improve the effectiveness of the asphalt pavement maintenance process.

The process of road safety survey generally consists of the detection of the defects (e.g., cracks and potholes) existing on the road section and evaluation of the magnitude of the defects [3]. Among several forms of pavement distresses, potholes are important indicators of the road defects, and they should be detected in a timely manner for the tasks of asphalt-surfaced pavement maintenance and rehabilitation

[4]. The reason is that this form of defect significantly delays traffic and brings about a hazardous condition for drivers.

A pothole is commonly defined as a bowl-shaped depression on the pavement surface with a minimum plane diameter of 150 mm [5]. Generally, structure aging, heavy traffic condition, poor drainage, thin asphalt layer substructure, and weak substructure can be the causes of pothole appearance [6]. In developing countries, the pavement pothole is often detected manually by inspectors of local transportation agencies during periodical field surveys. Although this conventional method can help to acquire accurate evaluation of potholes, it also features low productivity in both data collection and data processing. The reason is that one pavement inspector can only inspect less than 10 km per day [7]. With a large number of road sections needed to be inspected routinely, the automation of the pothole detection becomes a pressing need for transportation agencies. Moreover, the productive pavement surveying process significantly leads to economic gain. It is because, if rehabilitation process is performed timely, pavement restoration cost can be saved by up to 80% [8].

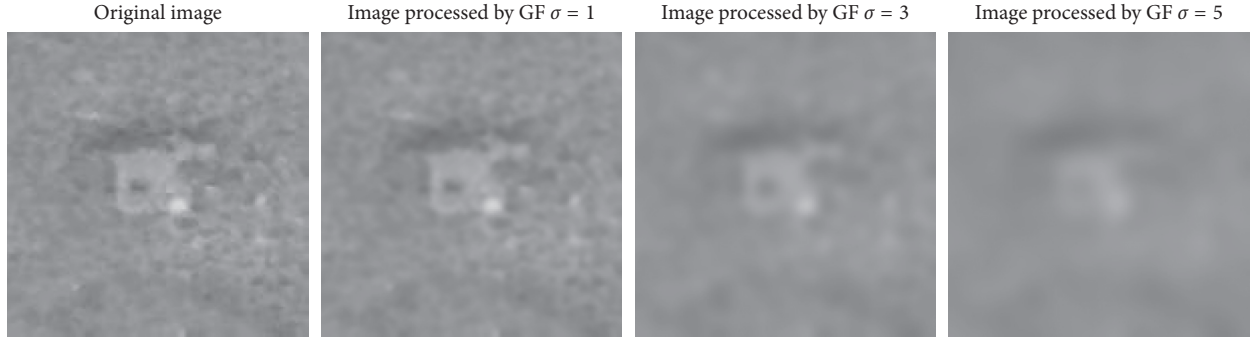


FIGURE 1: Image smoothing with the Gaussian filter.

In recent years, the advancement of image processing techniques and the availability of low-cost visual sensing equipment have paved the way for various methods of automatic pothole detection. The feasibility of automatic pothole detection approaches stems from the fact that the textures of potholes are recognizably different from the background of the pavement surface. Generally, computer-based pothole detection can be divided into 3D reconstruction-based and 2D vision-based approaches [3]. The 3D reconstruction-based methods are established by 3D point clouds that are provided by stereovision algorithms with the employment of a pair of video cameras [9]. As stated by Koch et al. [3], the stereovision-based methods require a complete 3D reconstruction of the asphalt pavement surface. These methods also necessitate expensive equipment which is significant hindrances for researchers in developing countries. Furthermore, irregular texture and color of the asphalt pavement create a significant challenge to the performance of 3D reconstruction-based approaches [3].

Accordingly, two-dimensional (2D) pavement images are widely used in practice for pavement pothole detection. Karuppuswamy et al. [10] proposed an integration of a vision and motion system to detect simulated potholes. Koch and Brilakis [11] relied on the elliptic shape, grain surface texture, and image segmentation to identify potholes in 2D images. Computer vision-based models that employ median filtering and morphological operations have been put forward by Lokeshwor et al. [12] and Radopoulou and Brilakis [13]. Koch et al. [14] established a pothole detection model that relies on the techniques of texture extraction and comparison between pothole pixels and healthy pavement pixels. Lokeshwor et al. [15] proposed an adaptive thresholding technique for segmenting distress pixels from the background pixels. The histogram shape-based thresholding and maximum entropy method have been employed in the previous works of Ryu et al. [6]. Ouma and Hahn [16] rely on wavelet transform and fuzzy *c*-means clustering to separate defect and nondefect pavement pixels.

Recent review works [3, 17, 18] have pointed out an increasing trend of applying image processing technique and artificial intelligence (AI) method for enhancing the accuracy and productivity of the task of interest. Moreover, irregular background illumination and complex pavement texture/color are still major challenges that computer vision-based methods have to overcome. Hence, other advanced approaches of image processing and AI should be investigated to construct automatic pothole recognition models.

The current study is dedicated to establishing a new AI-based model for automatically recognizing pothole objects in asphalt pavement images. The steerable filter is employed to create a salient map for distress detection. In addition, the Gaussian filter is utilized for image denoising, and the integral projection is employed to exhibit the characteristics of the salient map constructed by the steerable filter. The features extracted by the aforementioned image processing techniques are used by the artificial neural network and the least squares support vector machine. A data set of image samples with two class labels (nonpothole and pothole) has been collected and used to train and validate the performance of the two supervised learning algorithms.

The rest of the paper is organized in the following way: The second section presents the research methodology. The next section describes the structure of the proposed model for pavement pothole recognition. Experimental results and performance comparison are reported in the fourth section, followed by conclusions of the study in the final section.

## 2. Methodology

### 2.1. Image Processing Techniques

**2.1.1. Gaussian Filter (GF).** In image processing field, GF is a widely used preprocessing technique to reduce image noise and remove redundant details [19]. Particularly for the task of pothole detection, GF can be helpful to blur the asphalt background texture and facilitate further analysis of the digital image. The GF is essentially a 2D convolution operator that uses the kernel that represents the shape of a Gaussian function. The formula of a Gaussian function in a 2D space is given as follows:

$$G(x, y) = \frac{1}{2\pi\sigma^2} \exp\left(-\frac{x^2 + y^2}{2\sigma^2}\right), \quad (1)$$

where  $\sigma$  denotes the standard deviation of the GF.

Since the image is stored as a collection of discrete pixels, it is necessary to employ a discrete approximation of the Gaussian function before performing the convolution operator on the image. For more details of the discrete approximation of the GF, readers are guided to the previous works of Gonzalez et al. [19]. Figure 1 illustrates the effect of image smoothing using the GF with different values of standard deviation parameters.

**2.1.2. Steerable Filter (SF).** A SF is an orientation-selective convolution kernel image processing algorithm put forward by Adelson and Freeman [20]. SF is highly useful for the task of image enhancement because this algorithm is able to distinguish the objects of interest and the surrounding background [21]. SF has been successfully employed in various fields including recognition of object tracking, road crack detection, and many computer vision problems [22–26]. In this current study, a linear combination of Gaussian second derivatives is used as a basic filter.

The equation of the 2D Gaussian at coordination  $(x, y)$  in the digital image is provided as follows:

$$G(x, y, \sigma) = \frac{1}{\sqrt{2\pi r}} \exp\left(\frac{-(x^2 + y^2)}{2\sigma^2}\right), \quad (2)$$

where  $r$  is the variance of the 2D Gaussian function.

The second derivative of the function  $G$  is shown as follows:

$$\begin{aligned} G_{xx}(x, y, r) &= \frac{(x^2 - r^2)\exp(-(x^2 + y^2)/2r^2)}{\sqrt{2\pi r^5}}, \\ G_{yy}(x, y, r) &= \frac{(y^2 - r^2)\exp(-(x^2 + y^2)/2r^2)}{\sqrt{2\pi r^5}}, \\ G_{xy}(x, y, r) &= G_{yx}(x, y, r) = \frac{xy \exp(-(x^2 + y^2)/2r^2)}{\sqrt{2\pi r^5}}. \end{aligned} \quad (3)$$

The formulation of the steerable filter is given in the following equation:

$$\begin{aligned} F(x, y, r, \theta) &= G_{xx} \cos^2(\theta) + 2G_{xy} \cos(\theta) \sin(\theta) \\ &\quad + G_{yy} \sin^2(\theta), \end{aligned} \quad (4)$$

where  $\theta$  denotes the orientation of the filter.

The filter response for a whole digital image  $I$  is graphically presented in Figure 2 with  $\theta = [0 : 45 : 360]$  and  $r = 1.0, 1.5,$  and  $2.0$ . It is noted that the response at coordination  $(x, y)$  is attained by the convolution operator as follows:

$$R(x, y) = F(x, y, \sigma, \theta) * I(x, y), \quad (5)$$

where “\*” is the image convolution operator.

**2.1.3. Integral Projection (IP).** IP is a commonly used image processing technique in the field of automatic face recognition system [27]. Due to its simplicity and discriminative power, this technique is very potential to be applied to the task of pothole detection. Given a grayscale image  $I(x, y)$ , the horizontal and vertical IPs are defined as follows:

$$\begin{aligned} \text{HP}(y) &= \sum_{i \in x_y} I(i, y), \\ \text{VP}(x) &= \sum_{j \in y_x} I(x, j), \end{aligned} \quad (6)$$

where HP and VP are the horizontal and vertical IPs, respectively.  $x_y$  and  $y_x$  denote the set of horizontal pixels at

the vertical pixel  $y$  and the set of vertical pixels at the horizontal pixel  $x$ , respectively.

The results of IP analysis for several pavement images with the size of  $150 \times 150$  pixels are presented in Figure 3. As can be observed from these images, a healthy pavement image is characterized by recognizably stable signals of both horizontal and vertical IPs. On the other hand, each IP of an image containing a pothole features a peak; moreover, the location of these two peaks should be relatively close to each other. It is noted that if an image contains a crack pattern, the IPs are not stable. In this case, there should be a peak of intensity along one axis as shown in Figure 3(b). Based on such observations, IP can be effective in characterizing images with and without the pothole.

## 2.2. Artificial Intelligence Approaches

**2.2.1. Artificial Neural Network (ANN).** ANN is a popular AI approach for pattern recognition. This approach stems from biological neural networks in the natural world [28]. Through the supervised training process, an ANN model is capable of making inference via a large aggregation of neural units called artificial neurons. ANN is very similar to the way a biological brain solves pattern recognition problems with a large number of connected biological neurons [29]. An ANN model consists of multiple nodes, which simulate biological neurons of the human brain.

A neuron can process information and exchange information with other neurons through axons. Each link or axon is featured by a weight value. Thus, ANN is able to learn a discrimination function by adapting the values of these weights. An ANN model typically includes an input, a hidden, and an output layer (Figure 4).

Providing that the learning task is to approximate a classification function  $f: X \in R^D \rightarrow Y \in R^C$ , where  $D$  denotes the number of input attributes and  $C = 2$  represents the number of class labels, the ANN structure is shown in the following equation [30]:

$$f(X) = b_2 + W_2 \times (f_A(b_1 + W_1 \times X)), \quad (7)$$

where  $W_1$  and  $W_2$  denote weight matrices of the hidden layer and the output layer, respectively.  $b_1 = [b_{11}, b_{12}, \dots, b_{1N}]$  represents a bias vector of the hidden layer;  $b_2$  is a bias vector of the output layer;  $f_A$  denotes an activation function (e.g., log-sigmoid). Generally, the weight matrices and the bias vectors of the ANN can be effectively trained using the error backpropagation framework [28, 31].

**2.2.2. Least Squares Support Vector Machine (LS-SVM).** LS-SVM, proposed by Suykens et al. [32], is a least squares version of the standard support vector machine (SVM) algorithm. A notable advantage of LS-SVM is that the model structure of LS-SVM is learned by solving a linear system instead of a nonlinear optimization problem in SVM. During the learning process, LS-SVM first maps the data

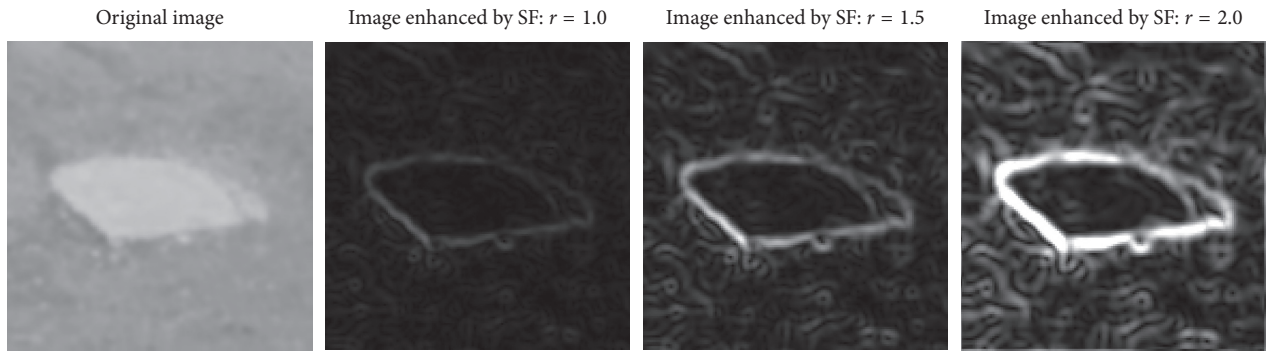
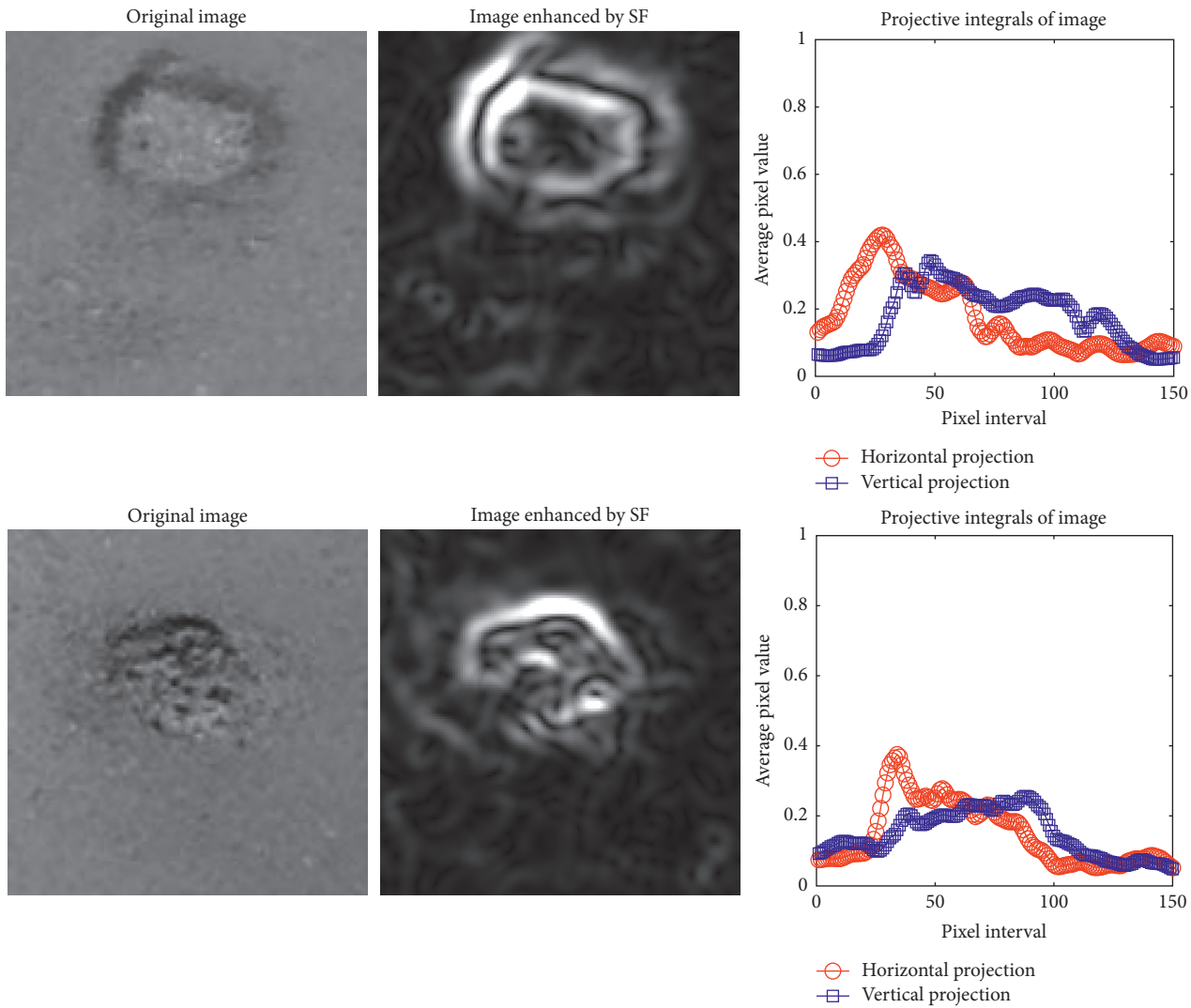


FIGURE 2: Image enhancement using the steerable filter with different value of  $r$ .



(a)

FIGURE 3: Continued.

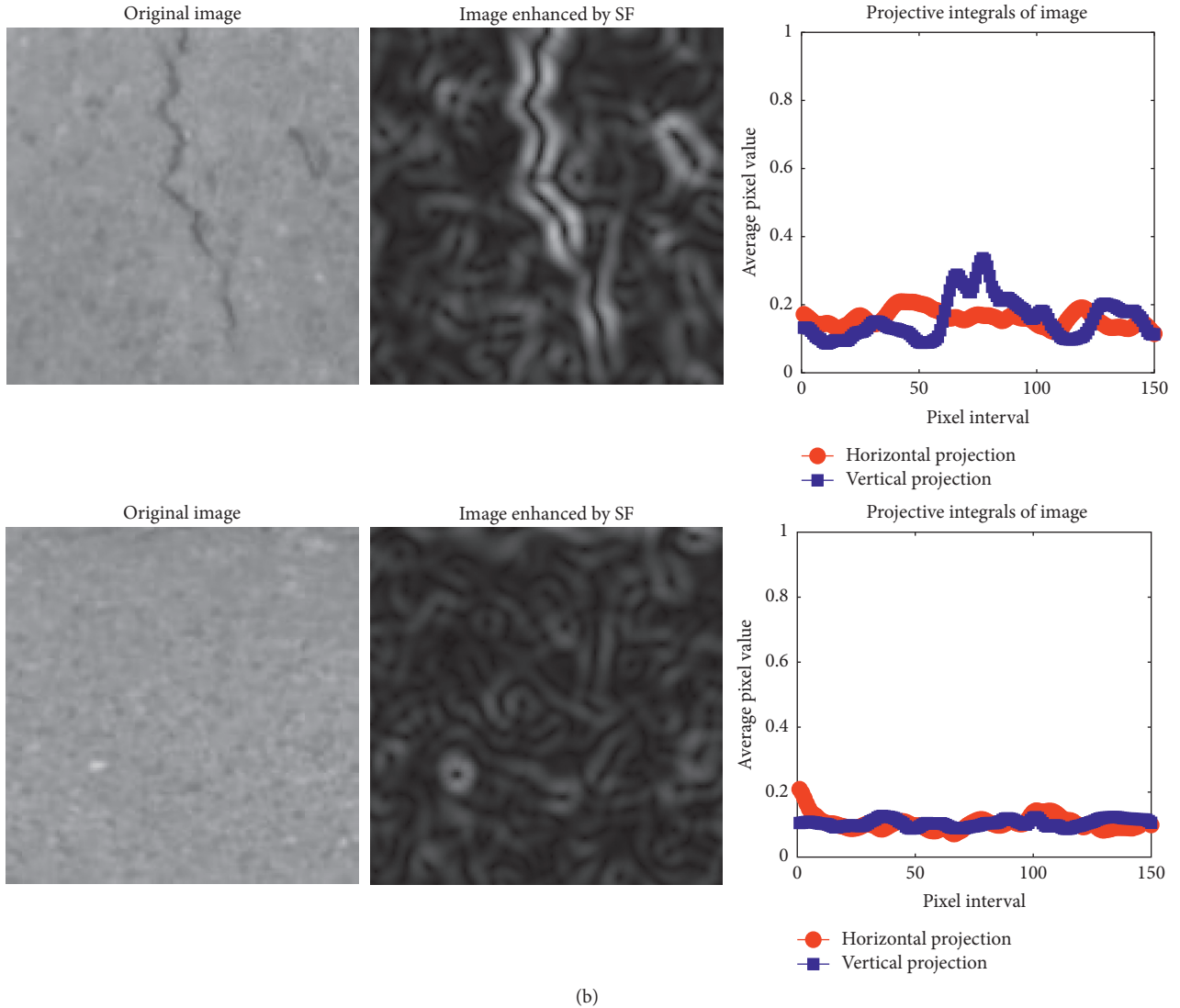


FIGURE 3: Integral projection of images: (a) pothole class and (b) nonpothole class.

from the original space to a high-dimensional feature space via a mapping function  $\varphi(\cdot)$  [33, 34]. The LS-SVM method then constructs an optimal separating hyperplane by adapting the parameters of its normal vector and bias. A typical learning process of a LS-SVM classifier is displayed in Figure 5.

Given a training data set of  $\{x_k, y_k\}_{k=1}^N$  where  $N$  represents the number of training data points,  $n$  denotes the data dimension,  $y_k \in \{-1, +1\}$  is the two class labels of interest, the LS-SVM for a 2-class pattern recognition can be stated as follows [35, 36]:

$$\text{minimize} \quad J_p(w, e) = \frac{1}{2}w^T w + \gamma \frac{1}{2} \sum_{k=1}^N e_k^2, \quad (8)$$

$$\text{subjected to} \quad y_k(w^T \varphi(x_k) + b) = 1 - e_k \quad k = 1, \dots, N, \quad (9)$$

where  $w \in R^n$  denotes the normal vector to the classification hyperplane and  $b \in R$  is the bias;  $e_k \in R$  represents error variables;  $\gamma > 0$  denotes a regularization constant.

Accordingly, the Lagrangian is given by the following equation [32]:

$$L(w, b, e; \alpha) = J_p(w, e) - \sum_{k=1}^N \alpha_k \{y_k(w^T \varphi(x_k) + b) - 1 + e_k\}, \quad (10)$$

where  $\alpha_k$  is a Lagrange multiplier;  $\varphi(x_k)$  denotes a kernel function.

After the KKT conditions for optimality are applied, the optimization described in (9) corresponds to solving the following linear system [32]:

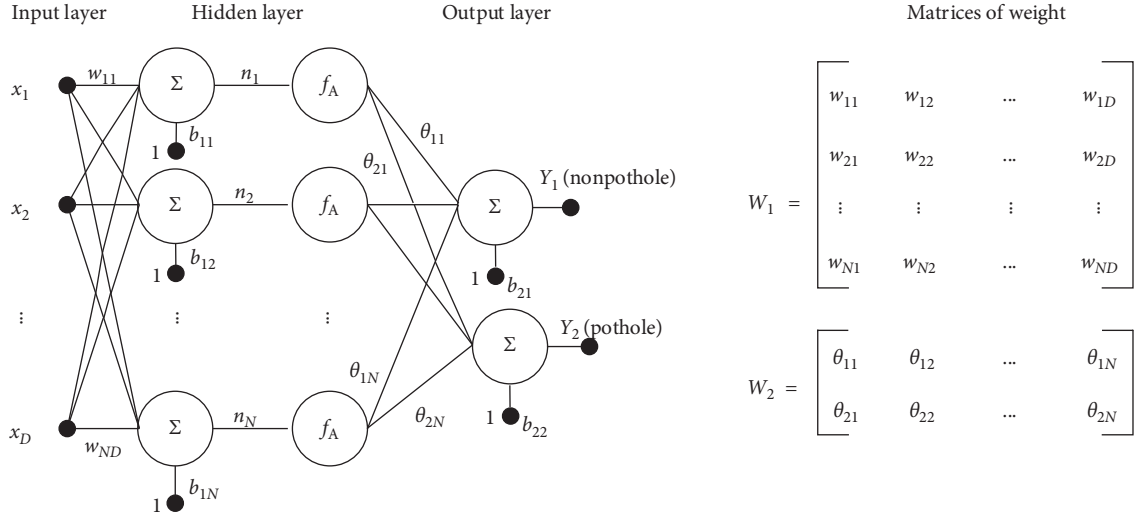


FIGURE 4: The ANN model structure used for pothole detection.

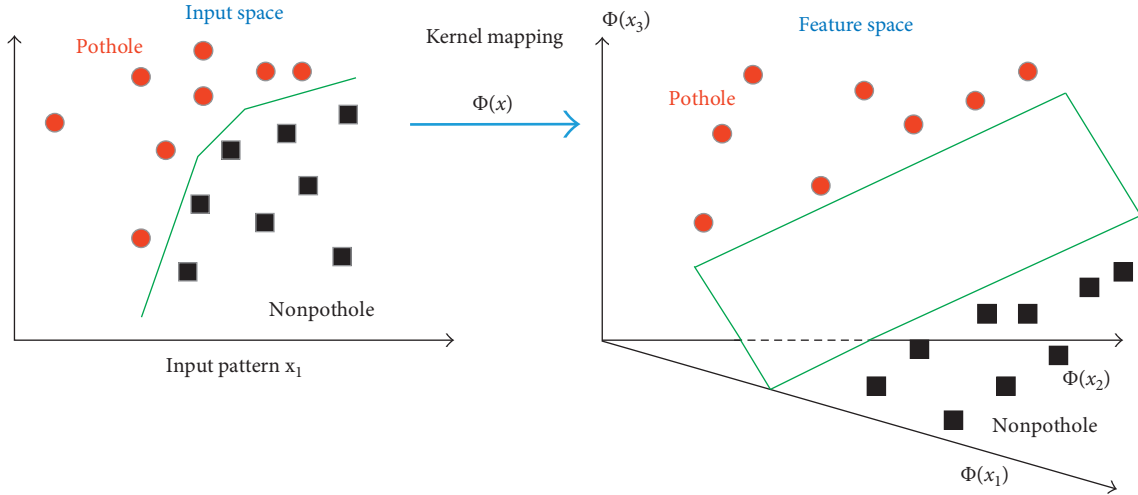


FIGURE 5: The LS-SVM classification model's learning process.

$$\begin{bmatrix} 0 & y^T \\ y & \Omega + \gamma^{-1}I \end{bmatrix} \begin{bmatrix} b \\ \alpha \end{bmatrix} = \begin{bmatrix} 0 \\ 1^v \end{bmatrix}, \quad (11)$$

where  $y = y_1, \dots, y_N$ ;  $1^v = [1; \dots; 1]$ ; and  $\alpha = [\alpha_1; \dots; \alpha_N]$ . Additionally, the kernel function is applied as follows:

$$\Omega[i, j] = y_i y_j \phi(x_k)^T \phi(x_l) = y_i y_j K(x_k, x_l). \quad (12)$$

Finally, the LS-SVM classification model can be obtained as follows:

$$y(x) = \text{sign} \left( \sum_{k=1}^N \alpha_k y_i K(x_k, x_l) + b \right), \quad (13)$$

where  $\alpha_k$  and  $b$  denote the solution to the linear system shown in (11). In addition, the kernel function that is often used in LS-SVM is the radial basis function (RBF) kernel [37].

**2.3. The Collected Data Set of Pavement Images.** Because ANN and LS-SVM are supervised learning algorithms, a data set of asphalt pavement images with ground truth conditions of pothole and nonpothole has to be collected for model training and validation. This study has collected images of asphalt pavement using a digital camera during field surveys. The two class labels of nonpothole and pothole are assigned by the inspector. To facilitate the speed of image processing steps, the image size of each sample is determined to be  $150 \times 150$  pixels. Thus, image cropping and resizing are applied if necessary.

In total, 200 image samples are prepared within which each class label has 100 samples. In order to establish and verify the prediction models, the collected data set has been divided into two subsets: the training set (80%) and the testing set (20%). The training set is employed in the model construction phase. The testing set is reserved to examine the predictive capability of the trained models. The collected image data set is illustrated in Figure 6.

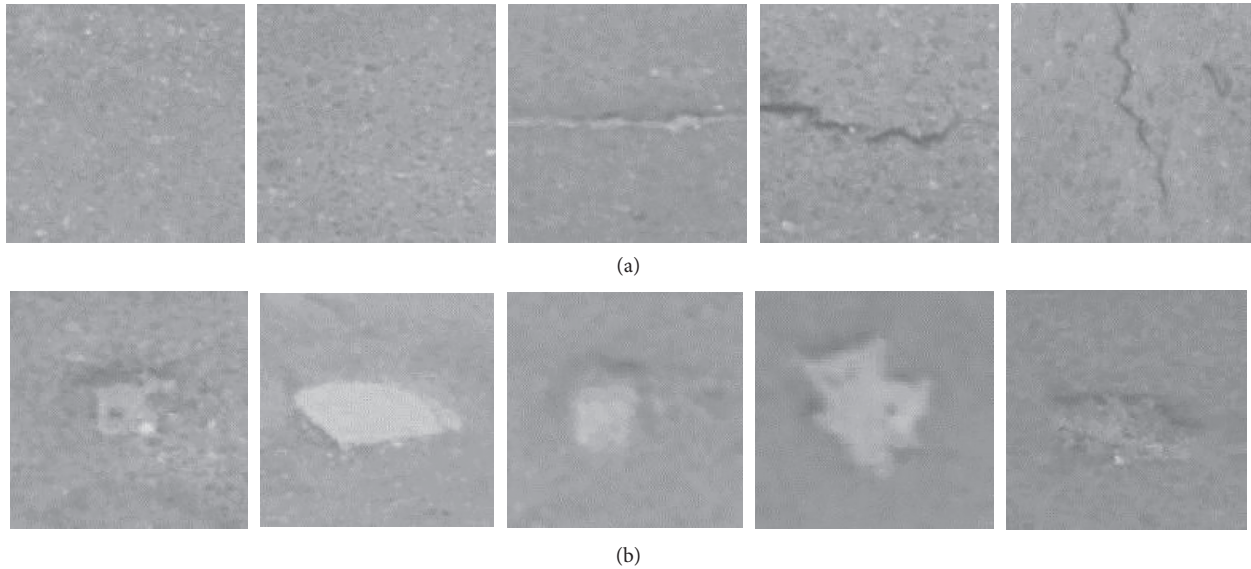


FIGURE 6: The collected image data set.

### 3. The Proposed Approach for Asphalt Pavement Pothole Detection

This section describes the overall structure of the proposed approach (Figure 7) which is named as steerable filter and artificial intelligence-based pothole detection model (SF-AI-PDM). The model includes three main modules: (1) image acquisition and feature extraction, (2) data set construction, and (3) AI model training and prediction. SF is an essential part of the first step.

Besides the SF algorithm, the GF is used as a method of image denoising and IP is employed to extract the properties of the salient map computed by the SF. It is noted that the GF is applied to denoise both the original image (GF level 1) and the SF-based salient map (GF level 2). The GF level 1 aims at removing irregular texture on the asphalt pavement background. Meanwhile, the GF level 2 is dedicated to enhance the SF-based salient map by reducing the noisy feature. In the third module, ANN and LS-SVM are employed to generalize a classification boundary used to recognize pothole patterns. It is noted that SF-AI-PDM has been programmed in MATLAB environment with the support of the MATLAB image processing toolbox [38].

At the first step of the first module, the proposed approach employs the GF to denoise the original digital image. Herein, the parameter  $\sigma_1$  which is the standard deviation of the GF used at level 1 should be selected. Based on several trial-and-error runs with the collected image samples, the value of  $\sigma_1 = 3$  is found to be the appropriate one. In the next step, the SF is used to create a response map. With the orientation of the filter  $\theta = [0 : 45 : 360]$ , the parameter  $r$  of SF is experimentally set to be 2. The parameter  $r = 2$  is found to sufficiently separate the pothole pattern out of the pavement background.

To enhance the quality of the SF-based response map, GF is applied. The value of the standard deviation of GF ( $\sigma_2$ ) at the second level is also selected to be 3. Based on the

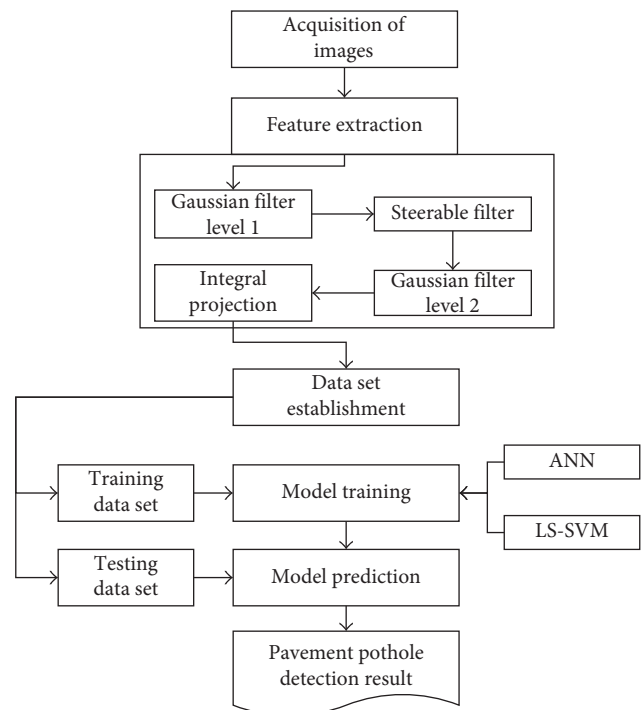


FIGURE 7: The proposed pavement pothole detection model (SF-AI-PDM).

smoothed response map, the IPs of the image are calculated. As stated earlier, the image size is  $150 \times 150$  pixels. Thus, if no simplification measure is employed, the number of IP-based features can be quite large (i.e., 300 features). To reduce the number of features, a method which is similar to the moving average technique is applied. In detail, the average value of 5 consecutive pixels along the horizontal and vertical axes of an image is computed to establish the contracted IP. This moving average technique can help to alleviate local fluctuations in the original IPs. Another

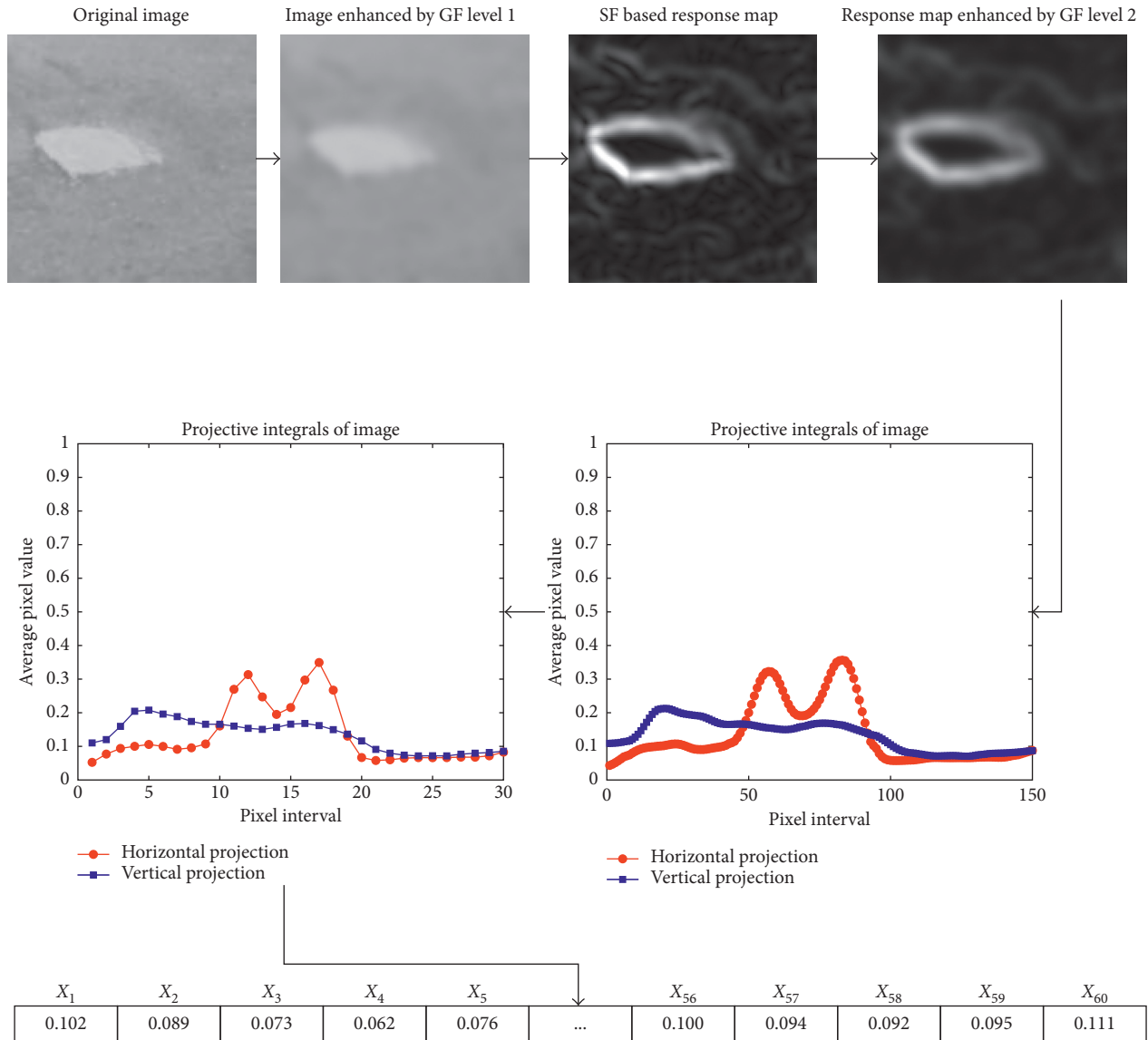


FIGURE 8: The feature extraction process of SF-AI-PDM.

benefit of this technique is that the number of features is reduced from 300 to 60. This reduction of the number of features is very helpful for the machine learning algorithms since they can avoid the curse of dimensionality [28].

The whole process of feature extraction is illustrated in Figure 8. It can be observed that the contracted IPs with 60 features ( $X_1, X_2, \dots, X_{60}$ ) still preserve the distinctive characteristics of the original IPs with 300 features. Another observation is that both GF level 1 and level 2 have critically diminished the noisy patterns in the original digital image and the SF-based response map. Particularly for the second level of the GF, this technique helps to highlight the pattern of the pothole. Consequently, the features extracted from the IPs can have high discriminative power to distinguish pothole and nonpothole classes.

After the feature set is determined, the data set of image samples is established in the second module. Accordingly, the data set is separated into two sets: training set (80%) and

testing set (20%). The training set is used for model establishment; the testing set is employed for model verification. With the separated data sets, the AI methods of ANN and LS-SVM are employed to generalize a decision boundary that classifies the instances of nonpothole and pothole classes. The training phases of ANN and LS-SVM require the setting of several model parameters. In addition, to quantify the classification performance of these two AI approaches, evaluation metrics must be employed. These two issues are going to be addressed in the next section of the study.

#### 4. Experimental Result and Comparison

As aforementioned, the data set consists of 200 image samples with the size of  $150 \times 150$  pixels. The data set is separated into the training set which occupies 80% of the data and the testing set which contains 20% of the data.

The first set is used to establish the model; the second set is reserved for investigating the predictive performance of the models. It is noted that a single run of the experiment may not reliably reveal the model predictive performance due to the problem of randomness in data separation. Hence, the performances of the AI approaches (ANN and LS-SVM) are evaluated via a repeated subsampling process which includes 20 runs. In each run, 20% of the data set is randomly taken out to form the testing data set; the rest of the data set is used as the training set.

It is also proper to note that, before the training and predicting phase, the Z-score transformation has been employed to normalize the whole data set. The data normalization aims at fending off the situation in which input variables with large magnitude dominate ones with small values. Moreover, the implementations of the two AI methods necessitate the specification of several tuning parameters. For the purpose of setting those parameters, the original data set is divided into a training set (80%) and a verification set (20%). The model's tuning parameters corresponding to the best predictive performance on the verification set is selected as the optimal ones.

The implementation of ANN requires determining the number of neurons in the hidden layer and the learning rate. As suggested by Heaton [39], the number of neurons is roughly selected to be  $N_L = (2/3)D_i + D_o$ . Herein,  $D_i$  and  $D_o$  represent the number of neurons in the input and output layers, respectively. In addition, the number of neurons in the hidden layer should not larger than  $1.5 \times N_L$  since overfitting often happens with an ANN with a surplus number of neurons. The second tuning parameter of ANN is the learning rate in which values can be selected from a set of [0.001, 0.01, 0.1, 1]. Other parameters of ANN including the type of the activation function and the number training epochs are selected to be log-sigmoid function and 3000, respectively. For the case of LS-SVM, this AI method necessitates an appropriate determination of the penalty constant and the kernel function parameters. In this study, these two tuning parameters of LS-SVM are determined via a grid search algorithm described in the previous research work of Hoang and Tien Bui [40].

Moreover, to quantify the predictive capability of AI models used for pothole detection, the classification accuracy rate (CAR) is calculated as follows:

$$CAR = \frac{R_C}{R_A} \times 100(\%), \quad (14)$$

where  $R_C$  and  $R_A$  represent the number of image samples being correctly classified and the total number of image samples, respectively.

Besides CAR, the true positive rate (TPR) (the percentage of positive instances correctly classified), the false positive rate (FPR) (the percentage of negative instances misclassified), the false negative rate (FNR) (the percentage of positive instances misclassified), and the true negative rate (TNR) (the percentage of negative instances correctly classified) should also be used [41]. The four indices are computed in the following way:

TABLE 1: Result comparison between ANN and LS-SVM.

Model	BPANN				LS-SVM			
	Training		Testing		Training		Testing	
Statistics	Mean	SD	Mean	SD	Mean	SD	Mean	SD
CAR	95.33	7.49	<b>85.25</b>	9.10	94.63	0.68	<b>88.75</b>	3.49
AUC	0.99	0.03	<b>0.92</b>	0.08	0.99	0.00	<b>0.96</b>	0.02
TPR	0.95	0.02	0.81	0.11	0.90	0.01	0.82	0.07
FPR	0.04	0.14	0.10	0.15	0.01	0.01	0.04	0.03
FNR	0.05	0.02	0.20	0.02	0.10	0.01	0.19	0.01
TNR	0.96	0.14	0.90	0.15	0.99	0.01	0.96	0.03

$$\begin{aligned} TPR &= \frac{TP}{TP + FN}, \\ FPR &= \frac{FP}{FP + TN}, \\ FNR &= \frac{FN}{TP + FN}, \\ TNR &= \frac{TN}{TN + FP}, \end{aligned} \quad (15)$$

where TP, TN, FP, and FN are the values of true positive, true negative, false positive, and false negative, respectively.

Furthermore, the four rates of TP, FP, FN, and TN can be graphically summarized in the form of a receiver operating characteristic (ROC) curve. The ROC curve is drawn based on the sensitivity (true positive rate) and the specificity (false negative rate). Using the ROC curve, an index called the area under the curve (AUC) can be calculated to express the model classification capability. It is noted that AUC ranges from 0.5 to 1. AUC=1 indicates a perfect classification model, and AUC=0.5 indicates an incapable classifier with random predictions [42].

Experiments with various settings of model parameters indicate that ANN with the number of neurons of 40 and the learning rate of 0.01 delivers the most desirable outcome. In addition, the regularization parameter of 500 and the kernel function parameter of 100 are found to be appropriate for the LS-SVM model. With such parameter settings, the model prediction performances obtained from 20 runs are summarized in Table 1 with the average (mean) and standard deviation (SD) values of each performance metric. It is observable that LS-SVM (CAR=88.75% and AUC=0.96) has achieved a better prediction accuracy than ANN (CAR=85.25% and AUC=0.92). The TPR and TNR of LS-SVM (0.82 and 0.96) are also superior to those of the ANN (0.81 and 0.90). The prediction capabilities of the two AI models in the form of ROCs are graphically presented in Figure 9. Experimental results indicate that LS-SVM is a more suitable AI approach for the collected image data set of asphalt pavement.

## 5. Conclusion

This research establishes an automatic approach for asphalt pavement pothole detection. Image processing techniques including GF, SF, and IP are used synergistically to extract features from pavement digital images. Two levels of GF are

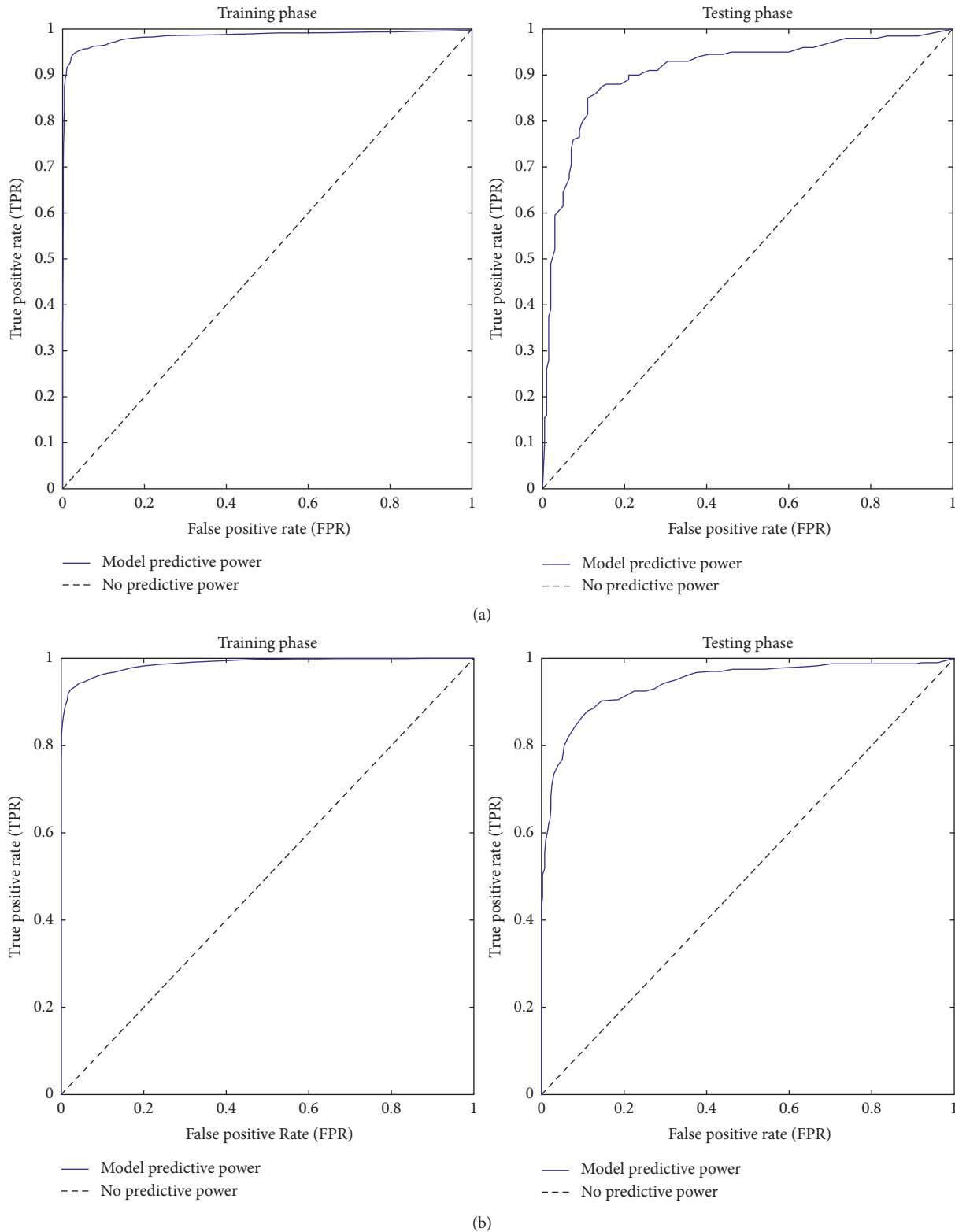


FIGURE 9: ROC of the ANN and LS-SVM models: (a) ANN results and (b) LS-SVM results.

utilized as an image denoising technique. SF assisted by GF is used to generate a pothole resilient map. IP analysis based on such map is performed to numerically present the feature of an image with the particular interest in pothole recognition.

A simple moving average technique is put forward to reduce the number of the extracted features from 300 to 60. Based on the image features, two AI approaches of ANN and LS-SVM have been employed to construct classification

models to predict the existence of pothole on the pavement surface. Experimental results with a repeated subsampling procedure with 20 runs confirm that ANN and LS-SVM are capable AI methods for pothole detection. It is because the CARs of both methods are higher than 85% and AUC values surpass 0.9. Moreover, LS-SVM has been identified as the better approach for the task of pothole detection with a desired accuracy of approximately 89%.

With good predictive accuracy, the proposed AI model is very potential to be employed by transportation agencies and road inspectors to enhance the productivity of pavement inspection tasks with the specific focus on the pothole. The first future direction of the current study may include the evaluation of other advanced AI methods and their ensemble learning strategy to meliorate the pothole detection accuracy rate. The second future direction of the current model is to utilize advanced image processing methods for estimating the size of potholes. In addition, the integration of the current AI model with other sophisticated image analysis techniques to enhance the feature extraction stage is also worth investigating.

### Data Availability

The data can be sent if requested by contacting the author at hoanghatduc@dtu.edu.vn.

### Conflicts of Interest

The author declares that there are no conflicts of interest regarding the publication of this manuscript.

### References

- [1] A. Cubero-Fernandez, F. J. Rodriguez-Lozano, R. Villatoro, J. Olivares, and J. M. Palomares, "Efficient pavement crack detection and classification EURASIP," *Journal on Image and Video Processing*, vol. 2017, no. 1, p. 39, 2017.
- [2] A. Tedeschi and F. Benedetto, "A real-time automatic pavement crack and pothole recognition system for mobile Android-based devices," *Advanced Engineering Informatics*, vol. 32, pp. 11–25, 2017.
- [3] C. Koch, K. Georgieva, V. Kasireddy, B. Akinci, and P. Fieguth, "A review on computer vision based defect detection and condition assessment of concrete and asphalt civil infrastructure," *Advanced Engineering Informatics*, vol. 29, no. 2, pp. 196–210, 2015.
- [4] FHWA, *Variability of Pavement Distress Data From Manual Surveys*, FHWA, Washington, DC, USA, 2000.
- [5] FHWA, "Distress identification manual for the long-term pavement performance program Federal Highway Administration," Tech. Rep. FHWA-RD-03-031, FHWA, Washington, DC, USA, 2003.
- [6] S. K. Ryu, T. Kim, and Y. R. Kim, "Image-based pothole detection system for its service and road management system," *Mathematical Problems in Engineering*, vol. 2015, Article ID 968361, 10 pages, 2015.
- [7] H. Oliveira and P. L. Correia, "Supervised crack detection and classification in images of road pavement flexible surfaces," in *Recent Advances in Signal Processing*, A. A. Zaher, Ed., InTech, Rijeka, Croatia, 2009.
- [8] Y. O. Ouma and M. Hahn, "Wavelet-morphology based detection of incipient linear cracks in asphalt pavements from RGB camera imagery and classification using circular Radon transform," *Advanced Engineering Informatics*, vol. 30, no. 3, pp. 481–499, 2016.
- [9] Z. Hou, K. C. P. Wang, and W. Gong, "Experimentation of 3D pavement imaging through stereovision," in *Proceedings of the First International Conference on Transportation Engineering*, Chengdu, China, July 2007.
- [10] J. Karuppuswamy, V. Selvaraj, M. M. Ganesh, and E. L. Hall, "Detection and avoidance of simulated potholes in autonomous vehicle navigation in an unstructured environment," in *Proceedings of the Intelligent Systems and Smart Manufacturing*, p. 11, Boston, MA, USA, October 2000.
- [11] C. Koch and I. Brilakis, "Pothole detection in asphalt pavement images," *Advanced Engineering Informatics*, vol. 25, no. 3, pp. 507–515, 2011.
- [12] H. Lokeshwor, L. K. Das, and S. K. Sud, "Method for automated assessment of potholes, cracks and patches from road surface video clips," *Procedia-Social and Behavioral Sciences*, vol. 104, pp. 312–321, 2013.
- [13] S. C. Radopoulou and I. Brilakis, "Improving patch distress detection using vision tracking on video data," in *Proceedings of the 21st International Workshop on Intelligent Computing in Engineering*, Cardiff, UK, July 2014.
- [14] C. Koch, G. M. Jog, and I. Brilakis, "Automated pothole distress assessment using asphalt pavement video data," *Journal of Computing in Civil Engineering*, vol. 27, no. 4, pp. 370–378, 2013.
- [15] H. Lokeshwor, L. K. Das, and G. Savita, "Robust method for automated segmentation of frames with/without distress from road surface video clips," *Journal of Transportation Engineering*, vol. 140, no. 1, pp. 31–41, 2014.
- [16] Y. O. Ouma and M. Hahn, "Pothole detection on asphalt pavements from 2D-colour pothole images using fuzzy c-means clustering and morphological reconstruction," *Automation in Construction*, vol. 83, pp. 196–211, 2017.
- [17] T. B. J. Coenen and A. Golroo, "A review on automated pavement distress detection methods," *Cogent Engineering*, vol. 4, no. 1, p. 1374822, 2017.
- [18] H. Zakeri, F. M. Nejad, and A. Fahimifar, "Image based techniques for crack detection, classification and quantification in asphalt pavement: a review," *Archives of Computational Methods in Engineering*, vol. 24, no. 4, pp. 935–977, 2017.
- [19] R. C. Gonzalez, R. E. Woods, and S. L. Eddins, *Digital Image Processing Using MATLAB*, Pearson Prentice-Hall, Upper Saddle River, NJ, USA, 2004.
- [20] E. H. Adelson and W. T. Freeman, "The design and use of steerable filters," *IEEE Transactions on Pattern Analysis and Machine Intelligence*, vol. 13, no. 9, pp. 891–906, 1991.
- [21] P. Perona, "Deformable kernels for early vision," *IEEE Transactions on Pattern Analysis and Machine Intelligence*, vol. 17, no. 5, pp. 488–499, 1995.
- [22] D. S. Alexiadis, N. Mitianoudis, and T. Stathaki, "Multidimensional directional steerable filters—theory and application to 3D flow estimation," *Image and Vision Computing*, vol. 71, pp. 38–67, 2018.
- [23] J. Braz, A. Ranchordas, H. Araújo, and J. Jorge, *Advances in Computer Graphics and Computer Vision*, Springer-Verlag, Berlin, Heidelberg, Germany, 2007.
- [24] W. T. Freeman and E. H. Adelson, "Steerable filters for early vision, image analysis, and wavelet decomposition," in

- Proceedings Third International Conference on Computer Vision*, pp. 406–415, Osaka, Japan, December 1990.
- [25] M. Jacob and M. Unser, “Design of steerable filters for feature detection using canny-like criteria,” *IEEE Transactions on Pattern Analysis and Machine Intelligence*, vol. 26, no. 8, pp. 1007–1019, 2004.
- [26] S. Li, Y. Cao, and H. Cai, “Automatic pavement-crack detection and segmentation based on steerable matched filtering and an active contour model,” *Journal of Computing in Civil Engineering*, vol. 31, no. 5, p. 04017045, 2017.
- [27] A. Chouchane, M. Belahcene, and S. Bourennane, “3D and 2D face recognition using integral projection curves based depth and intensity images,” *International Journal of Intelligent Systems Technologies and Applications*, vol. 14, no. 1, pp. 50–69, 2015.
- [28] C. Bishop, *Pattern Recognition and Machine Learning*, Springer Science+Business Media, Singapore, 2006.
- [29] B. T. Pham, D. Tien Bui, I. Prakash, and M. B. Dholakia, “Hybrid integration of multilayer perceptron neural networks and machine learning ensembles for landslide susceptibility assessment at Himalayan area (India) using GIS,” *Catena*, vol. 149, pp. 52–63, 2017.
- [30] T. H. Tran and N. D. Hoang, “Predicting colonization growth of algae on mortar surface with artificial neural network,” *Journal of Computing in Civil Engineering*, vol. 30, no. 6, p. 04016030, 2016.
- [31] N. D. Hoang, D. T. Vu, X. L. Tran, and V. D. Tran, “Modeling punching shear capacity of fiber-reinforced polymer concrete slabs: a comparative study of instance-based and neural network learning,” *Applied Computational Intelligence and Soft Computing*, vol. 2017, Article ID 9897078, 11 pages, 2017.
- [32] J. Suykens, J. V. Gestel, J. D. Brabanter, B. D. Moor, and J. Vandewalle, *Least Square Support Vector Machines*, World Scientific Publishing Co. Pte. Ltd., Singapore, 2002.
- [33] D. Tien Bui, T. A. Tuan, N. D. Hoang et al., “Spatial prediction of rainfall-induced landslides for the Lao Cai area (Vietnam) using a hybrid intelligent approach of least squares support vector machines inference model and artificial bee colony optimization,” *Landslides*, vol. 14, no. 2, pp. 447–458, 2016.
- [34] X. Xue, “Prediction of slope stability based on hybrid PSO and LSSVM,” *Journal of Computing in Civil Engineering*, vol. 31, no. 1, p. 04016041, 2017.
- [35] T. V. Gestel, J. A. K. Suykens, B. Baesens et al., “Benchmarking least squares support vector machine classifiers,” *Machine Learning*, vol. 54, no. 1, pp. 5–32, 2004.
- [36] W. Sun and M. Ye, “Short-term load forecasting based on wavelet transform and least squares support vector machine optimized by fruit fly optimization algorithm,” *Journal of Electrical and Computer Engineering*, vol. 2015, Article ID 862185, 9 pages, 2015.
- [37] Z. B. Chen, “Research on application of regression least squares support vector machine on performance prediction of hydraulic excavator,” *Journal of Control Science and Engineering*, vol. 2014, Article ID 686130, 4 pages, 2014.
- [38] MathWorks, *Image Processing Toolbox User's Guide*, The MathWorks Inc., Natick, MA, USA, 2016, [https://www.mathworks.com/help/pdf\\_doc/images/images\\_tbpdf](https://www.mathworks.com/help/pdf_doc/images/images_tbpdf).
- [39] J. Heaton, *Introduction to Neural Networks for C#*, Heaton Research, Inc., St. Louis, MO, USA, 2008.
- [40] N. D. Hoang and D. Tien Bui, “Predicting earthquake-induced soil liquefaction based on a hybridization of kernel Fisher discriminant analysis and a least squares support vector machine: a multi-dataset study,” *Bulletin of Engineering Geology and the Environment*, vol. 9, pp. 1077–1097, 2018.
- [41] V. López, A. Fernández, S. García, V. Palade, and F. Herrera, “An insight into classification with imbalanced data: empirical results and current trends on using data intrinsic characteristics,” *Information Sciences*, vol. 250, pp. 113–141, 2013.
- [42] N. D. Hoang and D. Tien-Bui, “A novel relevance vector machine classifier with cuckoo search optimization for spatial prediction of landslides,” *Journal of Computing in Civil Engineering*, vol. 30, no. 5, p. 04016001, 2016.